UNIVERSITY OF CAMBRIDGE
Department of Materials Science and Metallurgy

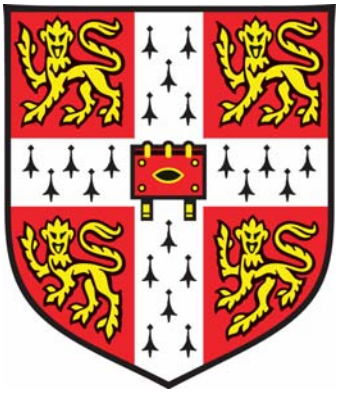

THERMO-ELECTRICAL PROPERTIES OF METALLIC SANDWICH SHEETS AND THEIR RESISTANCE WELDING CHARACTERISTICS

JIN CHONG TAN
Downing College

March 2005

A dissertation submitted for the degree of Doctor of Philosophy

PREFACE

This dissertation is submitted for the degree of Doctor of Philosophy in the University of Cambridge, U.K. The research described in this work was carried out by the author in the period October 2001 to March 2005, under the supervision of Prof. T.W. Clyne, in the Department of Materials Science and Metallurgy at the University of Cambridge.

To the best of my knowledge, the work described in this dissertation is original, except where due reference has been made to the work of others, and nothing has been included that is the outcome of work done in collaboration with others, except where noted. No part of this dissertation, or any similar to it, has been, or is currently being submitted for any degree at this, or any other university. This dissertation is less than 60,000 words in length.

Jin Chong Tan
Cambridge
March, 2005

ABSTRACT

The core architecture, thermo-electrical transport properties and welding characteristics of a novel metallic sandwich sheet material, termed a Hybrid Stainless Steel Assembly (HSSA) have been investigated. This lightweight material has an overall thickness of the order of 1 mm and incorporates a highly porous fibre network core. Several variants of this material have been produced employing different processing techniques.

The complex architecture of bonded metallic fibre networks has been characterised using a computed X-ray micro-tomography technique. The 3-D reconstructions provide a visual impression of the internal networks. To obtain useful geometrical statistics, such as fibre segment lengths and orientation distributions, the tomography images were analysed using a skeletonisation algorithm. The cores were found to be transversely isotropic, with fibres tending to lie on the in-plane directions.

The effective thermal and electrical conductivities of sintered fibre felts and assembled sandwich sheets have been measured and modelled. A steady-state bi-substrate thermal conductivity technique has been developed to measure the through-thickness conductivity. Low conductivities were measured, due to the high core porosity of above 80 vol.%. Three types of models are proposed to predict the conductivities: (i) a simple analytical model, based on an idealised unit cell structure and assumes all fibres are lying at the same inclination angle, (ii) an orientation distribution model that takes into account the actual fibre orientation distribution and (iii) a 3-D finite-element model constructed from micro-tomography images. The predictions were compared with experimental data and each model was found to have advantages and limitations.

A sequentially-coupled 2-D axisymmetric finite-element model for resistance spot welding has been developed to simulate mechanical and thermo-electrical interactions occurring during welding of lightweight sandwich sheets. The numerical model can predict the interplay of mechanical, electrical, thermal and metallurgical effects. The welding characteristics of sandwich materials have been investigated through experiments and subsequently compared with model predictions. During welding, the porous core sustains large plastic deformation, which changes its thermo-electrical properties. In order to obtain good quality weld nuggets, a suitable combination of welding parameters (electrode force, current and time) is required. It was found that excessive Joule heating due to high current levels can lead to melt expulsion and undesirable weld defects.

ACKNOWLEDGEMENTS

I gratefully acknowledge the financial funding provided by the Schlumberger & Malaysian Commonwealth Scholarship (Cambridge Commonwealth Trust), Overseas Research Students Award (ORS) and TWI (UK). Thanks to Prof. D.J. Fray for provision of office, laboratory and workshop facilities at the Department of Materials Science and Metallurgy, University of Cambridge.

I would particularly like to thank my supervisor, Prof. Bill Clyne, for his intellectual and moral support throughout my research. Special thanks go to Steve Westgate, the welding expert at TWI, for helping me with the welding experiments and sharing his expert knowledge.

Many thanks also go to all the technical staffs in this department, especially to Robert Stearn, for his help in designing and constructing new experimental setups; Kevin Roberts, for ensuring all the equipment in the process lab are up and running; and Dave Volwes, for his expertise in scanning electron microscopy. I must also thank the Biomaterials Group for allowing me to use their Skyscan X-ray Microtomograph.

Without a doubt, it is the people who have transformed the otherwise dull and boring Gordon Laboratory, into a pleasant and productive workplace. Thanks to those who have left:- Russell (for introducing me to Guinness® and showing me the wonders of Barrikade®), Dave (for *not* labelling all my stuffs and showing me his foams), Steve (for the ginger hair), Katy (for the 5-pint beer challenge), Helen (for being my quieter desk-neighbour), Thomas (for finishing up all the cakes), Vlado (for all the squash and tennis games), Tom(M) (for letting me become the new Mac-monitor) and Debu (for the proper curry, introducing me to loads of Indian mafias, sharing the George Nuttall *Close* flat and not turning it into a B&B†!). Thanks also go to those who are about to leave:- Tom(I) (for the introductory skiing lessons and staying cool *most* of the time), Sofia (for constantly fighting with me over the tiny bit of deskspace! And, teaching me some Greek dance moves) and Yi (for the Chinese food). A big thank you to all the current members:- Athina (for offering all the proper *advice* and eating the seafood I cooked!), Igor (for the advanced skiing lessons and proper drinks afterwards), Martin (for the Swiss 'jokes'), Andrew (for fixing my bike), James(C) (for keeping the penguins and hamsters safe), Jamie (for letting me become the new poster monitor), Chris (for not giving up on overclocking), Shila (I'm just wondering, when you'll be a *Saifuddin* again? And, for stopping being stingy.), Aikaterini (for ensuring the lab's fresh milk supply), James(D) (for being an active social monitor), Amaia (for joining me in the mind-boggling Argentinean tango lessons), Finn (for Friday nights' 5pm pub calls), Derek (for showing me how interesting drying is!) and Kirsten (for reminding me of Kikuchi lines).

Outside the department, there are always friends from Downing and other colleges – Joanna (thanks for the Zubrowka!), Ya-Ching (for all those fine food), Mario (for those Bavarian sausages), Monica (for the free Polish vodka), Carol, Arman, Gabriella, Edward, Elena … who are always happy to join me for (at least) a drink and mess around. Of course, I must acknowledge all my salsa partners (past and present) – Ariane, Milja, Sofia, Angelica, Ivana, Gabriela, Claire(s), Liz, Lorraine … for not failing to turn up on the dance floor (almost) every week! Last but not least, I would like to thank my Mom and Dad, my sister and brother, whom this thesis is dedicated to, for their unwavering support and encouragement!

† Bed & Breakfast

TABLE OF CONTENTS

NOMENCLATURE

Symbols	Description	Units
A	Area	m^2
A_C	Apparent contact area	m^2
a	Average radius of contacting asperities	m
b	Width	m
C_p	Specific heat capacity	$J\ kg^{-1}\ K^{-1}$
D	Fibre diameter	m
d	Centre-to-centre distance between two asperities	m
E	Young's modulus	$N\ m^{-2}$
E_c	Young's modulus of core	$N\ m^{-2}$
E_{fp}	Young's modulus of faceplate	$N\ m^{-2}$
F	Yield function	$N\ m^{-2}$
Gr	Grashof number	-
f	Fibre volume fraction	-
f_j	Joule dissipation weight factor	-
f_q	Fraction of electric dissipated energy	-
H	Total thickness of sandwich sheet	m
h	Thickness	m
h_b	Thickness of adhesive/braze layer	m
h_c	Thickness of sandwich core	m
h_f	Thickness of flocked fibre core	m
h_{fp}	Thickness of faceplate	m
h_m	Thickness of fibre mesh core	m
h	Heat transfer coefficient	$W\ m^{-2}\ K^{-1}$
h	Interfacial thermal conductance	$W\ m^{-2}\ K^{-1}$
$\hat{h}$	Specific enthalpy	$J\ m^{-3}$
I	Electrical current	A
I	Moment of inertia	$kg\ m^2$
J	Electrical charge flux (current density)	$A\ m^{-2}$
K	Extinction coefficient	m^{-1}
k	Thermal conductivity	$W\ m^{-1}\ K^{-1}$
k_a	Thermal conductivity of air	$W\ m^{-1}\ K^{-1}$

k_b	Thermal conductivity of braze or adhesive	W m^{-1} K^{-1}
k_c	Thermal conductivity of core	W m^{-1} K^{-1}
k_e	Effective thermal conductivity	W m^{-1} K^{-1}
k_f	Thermal conductivity of fibre	W m^{-1} K^{-1}
k_{f+a}	Combined thermal conductivity of fibre and air	W m^{-1} K^{-1}
k_g	Thermal conductivity of gas phase	W m^{-1} K^{-1}
k_s	Thermal conductivity of solid phase	W m^{-1} K^{-1}
k_{true}	Actual thermal conductivity	W m^{-1} K^{-1}
k_w	Thermal conductivity of water	W m^{-1} K^{-1}
k_x, k_y	Thermal conductivity in in-plane directions	W m^{-1} K^{-1}
k_z	Thermal conductivity in through-thickness direction	W m^{-1} K^{-1}
L	Fibre segment length	m
ΔL	Distance across sample	m
L/D	Fibre aspect ratio	-
m	Mass	kg
N_θ	Number of fibre segments at an angle θ to vertical	-
n	Number of contacting asperities	-
P	Pressure	Pa
P	Porosity	-
$P(\theta)$	Orientation distribution function	rad^{-1}
p	Hydrostatic stress	N m^{-2}
p_c	Yield stress in hydrostatic compression	N m^{-2}
Q	Heat	W
$\dot{Q}$	Heat generated in the body	W m^{-3}
q	Heat flux	W m^{-2}
q	Mises stress	N m^{-2}
R	Resistance	Ω
R_D	Dynamic resistance	Ω
R_E	Resistance of electrode	Ω
R_S	Static resistance	Ω
R_W	Resistance of workpiece	Ω
$R_{E\text{-}W}$	Resistance at electrode-to-workpiece interface	Ω
$R_{W\text{-}W}$	Resistance at workpiece-to-workpiece (faying) interface	Ω
R_a	Resistance of air	Ω
R_b	Resistance of adhesive/braze layer	Ω

R_f	Resistance of fibre	Ω
R_{tc}	Thermal contact resistance	m^2 K W^{-1}
R_*	Resistance of epoxy adhesive	Ω
r	Radius	m
T	Temperature	K
T_L	Liquidus temperature	K
T_S	Solidus temperature	K
T_s	Temperature of surface	K
T_{sur}	Temperature of surrounding	K
ΔT	Total temperature drop	K
ΔT_i	Temperature drop across interface	K
ΔT_s	Temperature drop across sample	K
t	Time	s
u	Displacement	m
u_r	Radial displacement	m
u_z	Axial displacement	m
V	Volume	m^3
V	Voltage	V
ΔV	Voltage drop	V
x, y, z	Cartesian coordinate directions	m
Δx	Sample thickness	m

Greek symbols:

α	Thermal diffusivity	m^2 s^{-1}
α	Shape factor of yield function	-
ε	Emissivity	-
ε	Strain	-
$\bar{\varepsilon}^{pl}$	Equivalent plastic strain	-
ε_{axial}^{pl}	Axial plastic strain	-
Φ	Electrical potential	V
γ	Empirical coefficient	-
η	Number density of contacting asperities	m^{-2}
Λ	Euclidean path length	m
λ	Shortest path length	m

μ	Coefficient of friction	-
θ	Mean fibre inclination angle (to the vertical axis)	º
θ_{tol}	Minimum kink angle tolerance	º
$\Delta\theta$	Bin size	º
ρ	Density	kg m^{-3}
ρ_c	Density of sandwich core	kg m^{-3}
ρ	Electrical resistivity	Ω m
ρ_e	Effective electrical resistivity	Ω m
ρ_b	Electrical resistivity of adhesive/braze layer	Ω m
ρ_f	Electrical resistivity of fibre	Ω m
ρ_x, ρ_x	Electrical resistivity in in-plane directions	Ω m
ρ_z	Electrical resistivity in through-thickness direction	Ω m
Σ	Beam stiffness	N m^{-2}
σ	Electrical conductivity	Ω^{-1} m^{-1}
σ_c	Yield stress in uniaxial compression	N m^{-2}
σ_Y	Yield strength	N m^{-2}
σ_{ecc}	Electrical contact conductance	Ω^{-1} m^{-2}
σ_{tcc}	Thermal contact conductance	W m^{-2} K^{-1}
τ	Tortuosity	-
ν	Poisson ratio	-
$\bar{v}$	Principle axis unit vector	-
ω	Compression yield strength ratio	-
ψ	Fitting parameter	-
ξ	Degree of anisotropy	-

Common subscripts and superscripts:

0	initial condition
1, 2, 3	corresponds to *x*, *y* and *z* axes
a	air
b	braze or adhesive layer
c	core
e	effective
f	fibre
f+*a*	fibre and air

fp	faceplate
m	Fibre mesh/ felt
tot	total
x, y	in-plane directions
z	through-thickness/ transverse/ axial direction

Physical constants:

e	Electronic charge	1.602×10^{-19} C
σ	Stefan-Boltzmann constant	5.67×10^{-8} W m^{-2} K^{-4}
k_B	Boltzmann's constant	1.381×10^{-23} J K^{-1}

Common Acronyms and Abbreviations:

AC	Alternating Current
BIW	Body In White
DC	Direct Current
EDS	Energy Dispersive X-ray Spectrometer
FD	Finite-Difference Method
FG	Flocked and Glued sandwich sheet
FEM	Finite-Element Method
LVDT	Linear Variable Differential Transformer
MB	long fibre in-plane Mesh – Brazed sheet
MG	long fibre in-plane Mesh – Glued sheet
NVH	Noise, Vibration and Harshness
PEEQ	Equivalent Plastic Strain
RMS	Root Mean Square
RSW	Resistance Spot Welding
SEM	Scanning Electron Microscope
SF	Short Fibre 3-D array sandwich sheet
VDSS	Vibration Damping Steel Sheets
μCT	Computed X-ray micro-Tomography

Chapter 1: Introduction

In recent years, there has been increasing interest in the development of lightweight metallic sandwich materials incorporating a porous core, for high performance engineering applications. The current work concerns a newly developed thin sandwich sheet material, termed a Hybrid Stainless Steel Assembly (HSSA) [1]. It is composed of twin stainless steel faceplates (200 μm), separated by a stainless steel fibre core, containing porosity of above 80 vol.%. The bonded metallic fibre core is produced via either a liquid- or solid-phase sintering process. The overall thickness is of the order of 1 mm. By combining stiff outer faceplates with a thicker and highly porous core, a structure exhibiting an attractive combination of properties can be constructed. These include low areal density, high beam stiffness, good corrosion resistance, thermal insulation and good vibration damping capacity. In addition, to gain commercial exploitation in transportation applications, criteria such as weldability and formability are also important.

Resistance spot welding (RSW) is in widespread commercial use in today's automotive assembly lines. It is a complex joining process, which involves the coupling of mechanical, electrical, thermal and metallurgical interactions. Flow of heat and electricity are central to weld nugget formation and are governed by the thermal and electrical conductivities of the material. In the case of highly porous materials, the mechanical deformation caused by electrode compression has pronounced effects. The conductivities of porous materials are known to be lower than monolithic materials. These changes affect the welding characteristics and weld pool development. To date, the weldability of monolithic sheets has been widely studied, but very limited work [2] has been done on the welding characteristics of either porous materials or sandwich sheets and most of the RSW models found in the literature [3] are limited to welding of monolithic materials.

In this work, the architecture of the bonded fibre cores was first characterised by employing both qualitative and quantitative techniques (Chapter 6). X-ray micro-tomography is shown to be a very useful non-destructive method for investigating the internal core structure and to obtain statistical distribution data on fibre segment length and orientation. These studies provide a clear picture of the complex fibre network architecture, vital for explaining their thermo-electrical properties. Subsequently, the thermal and electrical properties of the fibrous cores were measured and modelled (Chapter 7). Three types of models are proposed for the prediction of transport properties as a function of core architecture, namely (i) a simple analytical model which assumes an idealised unit cell structure, (ii) an orientation distribution model which takes into account the actual fibre

orientation distribution and (iii) three-dimensional finite-element models generated by meshing the reconstructed fibres obtained from X-ray micro-tomography. Each type of model has its own advantages and limitations.

A RSW finite-element process model has been developed to simulate the welding of thin stainless steel sandwich sheets (Chapter 8). It employs a sequential-coupling formulation to model the mechanical and thermo-electrical responses. This model takes into account the collapsible core structure and low core conductivities. The welding characteristics of two variants of lightweight sandwich sheets have been investigated through experiments and results were compared with model predictions (Chapter 9).

Chapter 2: Sandwich Materials

There is an increasing interest in the development of lightweight structural sandwich materials, especially for high performance engineering applications. Sandwich construction is efficient in utilising two different materials to attain superior performance, with stiff outer faceplates and a lightweight core conferring high bending stiffness and a low overall density. In fully metallic sandwich sheets, the porous core can be either periodic (honeycomb, struts assembly, shell elements etc) or stochastic (most metallic foams, fibres etc) in nature. Recently, a new kind of sandwich sheet, termed Hybrid Stainless Steel Assembly (HSSA) has been developed - composed of twin stainless steel faceplates (~200 μm) separated by a highly porous stainless steel fibrous core. It has an overall thickness of 1 mm and exhibits an attractive combination of properties.

2.1 A Brief History of Sandwich Construction

Although the idea of sandwich construction can be traced back to as early as the mid 19th century [4], its application as a structural material first appeared only in the 1940s in the aircraft industry [5]. The World War II Mosquito bomber, designed and built by Havilland Airplane Company is often quoted as the first structure to incorporate sandwich panels [6]. Its excellent performance convinced aircraft designers of the superiority of sandwich construction and instigated greater research interests in developing new sandwich materials. The landing of Apollo on the moon on 20th July 1969 marked another prominent breakthrough in the advancement of sandwich technology. Figure 2-1 illustrates the two interconnected sandwich shells which formed the wall structure of the capsule. The chosen sandwich construction was lightweight, but exhibited the high strength-to-weight ratios and stiffness needed to withstand the stresses induced by landing and atmospheric re-entry.

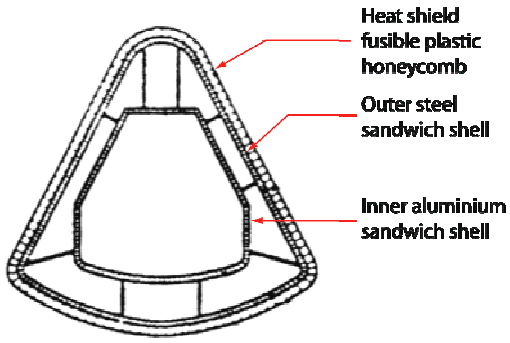

Figure 2-1. Sandwich construction of the Apollo capsule [7].

Nowadays, the use of sandwich constructions is widespread in various structural applications, especially in aircraft and spacecraft [8], racing cars, high-speed marine vessels [9], building constructions [7] and sports equipment. Besides structural applications, sandwich materials have also been employed in non-structural or semi-structural purposes, such as for energy absorption, air flow directionalisation, acoustical and thermal control, radio frequency shielding and aircraft nose radomes [6, 10, 11].

2.2 Basic Principles of Sandwich Construction

All sandwich materials (Figure 2-2) comprise two faceplates (relatively thin, but of high strength and stiffness), enclosing a core structure, which is thicker and less dense. To act as a composite load-bearing unit, these components are held together using adhesive, braze, mechanical fasteners (screws, rivets etc) or other joining techniques (diffusion bonding, resistance welding etc). By separating the faceplates with a lightweight core, the moment of inertia in bending of the sandwich panel is substantially increased. This will result in improved beam stiffness, compared with a monolithic plate having the same total weight.

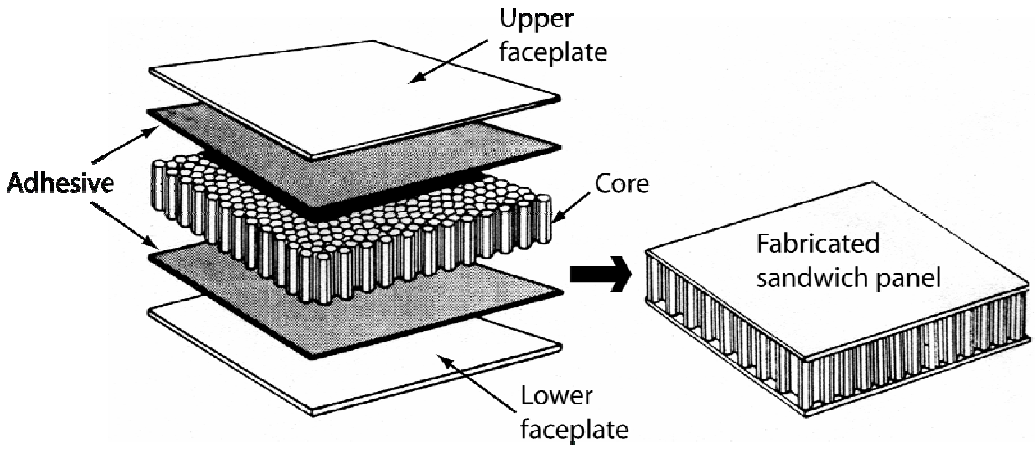

Figure 2-2. A typical sandwich structure, consisting of a porous core (honeycomb), bonded using adhesives to a pair of faceplates [5].

An effective sandwich construction has to satisfy a few basic design criteria, concerning the faceplates, core and faceplate-to-core bonding [4, 5]. The faceplates must have sufficient thickness and strength to withstand the tensile, compressive and shear stresses generated by external loads. Due to its density, the core contributes little to the overall beam stiffness. However, the core has several important functions, to ensure that the sandwich panel performs as expected. It must possess adequate stiffness in the direction normal to the faceplates to keep them at the correct distance apart (Figure 2-3(a)). Furthermore, the core should have sufficient shear stiffness to prevent sliding of faceplates over each other when a bending moment is applied. Otherwise, the faceplates will respond like two independent beams and the sandwich effect is lost (Figure 2-3(b)). Good core shear stiffness is also crucial to avoid overall buckling and crimping of the sandwich (Figure 2-3(c)). Finally, the compressive strengths of core and faceplates should be sufficiently high to prevent wrinkling of faceplates (Figure 2-3(d)). Good core compressive strength also helps to resist crushing by loads acting normal to the faceplates or by compressive stresses induced through flexure (Figure 2-3(e)). The faceplate-to-core bonding must also demonstrate adequate strength, to enable effective transmission of shear stresses between faceplates and core.

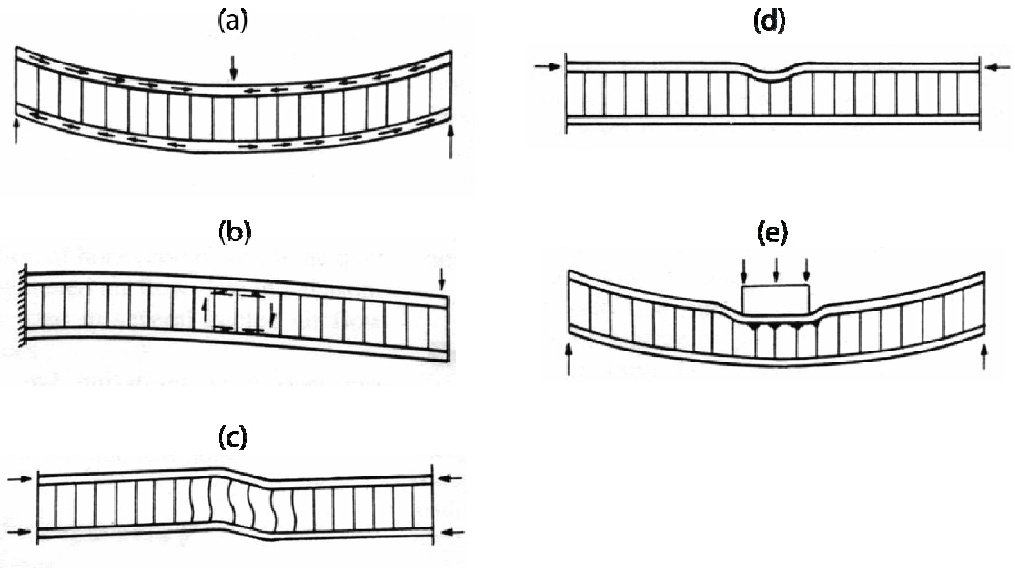

Figure 2-3. Basic sandwich construction criteria [5].

A well constructed sandwich panel generally exhibits the following favourable properties:

- High beam stiffness at low areal density.
- Good acoustic and vibration damping capacity.
- Excellent thermal insulation.
- Good resistance to aggressive environments (through the use of corrosion-resistant coatings or stainless steel faceplates).

2.3 Components of Sandwich Materials

2.3.1 Faceplates

In general, any material available in sheet form, with good stiffness and strength, can be used as faceplates. The choice of material may also depend on other factors, such as weight, cost, corrosion resistance, wear resistance, surface finish, radar transparency, humidity resistance and elevated temperature properties. Common faceplate materials can be grouped into two, namely, monolithic and composite materials [10].

2.3.1.1 Monolithic faceplates

Monolithic faceplates generally comprise of sheet metals or unreinforced polymers. These faceplates are normally pre-manufactured and bonded onto the core in separate processes. Sheet metals, such as carbon steel, stainless steel, aluminium or copper, are commonly used. They offer good mechanical properties at reasonable cost, but an inherent drawback lies in their weight penalty. Unreinforced polymers have low stiffnesses, which result in poorer structural performance.

2.3.1.2 Composite faceplates

Most composite faceplates are fibre-reinforced polymer composites, although natural composites such as wood are also used. Polymer composites may either be laminated directly onto the core, or first pre-manufactured and later bonded onto the core in another process. For fibre-reinforced polymers, all constituent materials commonly used in composite applications can be employed as faceplates. These include glass, carbon and aramid reinforcement and various types of thermoset resins and thermoplastics as matrices. For higher performance faceplates, prepregs composed of glass or carbon fibre-reinforced epoxy may be used. Composite faceplates can also be pre-manufactured through a compression moulding process, using moulding compounds which contain glass fibre reinforcement (e.g. sheet-moulding compound, bulk-moulding compound and glass-mat-reinforced thermoplastic).

2.3.2 Cores

Pore-free materials, although less widely used, have been employed as cores for sandwich panels. One better known example is the vibration damping steel sheet (VDSS), which combines a pair of steel faceplates with a visco-elastic synthetic resin core [12-14]. This material exhibits good vibration damping characteristics, making it suitable for automotive applications. However, the lack of formability and weldability has inhibited their widespread application. More recently, a laminated material consisting of alternating thin aluminium alloy sheets and glass/epoxy composite plies, known as GLARE® (GLAssfibre REinforced laminate) [15] has been specially developed for aircraft structures. It shortly will make its first appearance in the world's largest airliner – Airbus A380. Although this material is lightweight, it has limited formability and is difficult to join. Also, it is not a true sandwich material.

Porous cores are by far the more popular choice, mainly due to their relatively low density. Porosity levels up to over 90% are not uncommon. Therefore, a thicker core can be incorporated into the panel without additional weight penalty. Porous cores can be classified, according to the distribution of the pores, into periodic and stochastic (random) types.

2.3.2.1 Periodic cores

Periodic cores exhibit a repeating array of cellular patterns, and encompasses [16]:

- Prismatic elements (honeycomb, corrugation, truss etc).
- An assembly of struts (tetrahedral, pyramidal, Kagomé).
- Shell elements (egg-box).

The most widely used periodic core is no doubt the honeycomb, produced by joining thin sheets of material (aluminium, Kevlar, fibreglass, Nomex, graphite etc) to form connecting cells. Today, almost all of the sandwich panels for commercial and military aircrafts incorporate honeycomb cores. Honeycombs are available in three basic cell configurations: hexagonal, overexpanded and flexible (Figure 2-4). To maximise the bending stiffness of the sandwich panel, the prismatic axis of the cell is aligned perpendicular to the plane of the faceplates. Hexagonal cell honeycomb has limited formability and cannot be formed into compound curvatures. The overexpanded cell configuration has rectangular cells, and can be easily formed in the planar direction but its shear stiffness is slightly reduced in this direction. Flexible core configuration offers the best formability and suited for structures with compound curvatures [5].

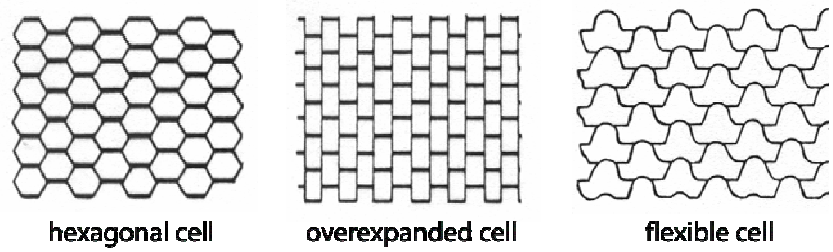

Figure 2-4. Honeycomb cell configurations (plan view) [5].

A corrugated core sandwich panel is composed of a fluted metal sheet attached alternatively to the faceplates. The metal sheet can have different geometries, including parallel strips, cylindrical tubes and trusses (Figure 2-5). Unlike honeycomb cores, its prismatic axis is aligned parallel to the plane of the faceplates.

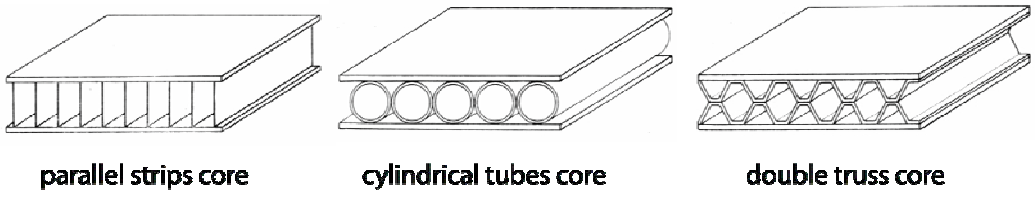

Figure 2-5. Different variants of sandwich panels employing corrugated cores [4].

Recently, a textile-based approach has been employed to produce woven metal fabric, bonded at the nodes using transient liquid phase technique [17]. In principle, this approach is applicable to any alloy that can be drawn into wires. The metal wires can be oriented at any angle to the faceplate normal, such as 0º/90º and ±45º configurations (Figure 2-6). Plies of woven laminates are then stacked onto each other and brazed to form an open-cell periodic sandwich core. Due to its architecture, the core exhibits anisotropic mechanical and transport properties.

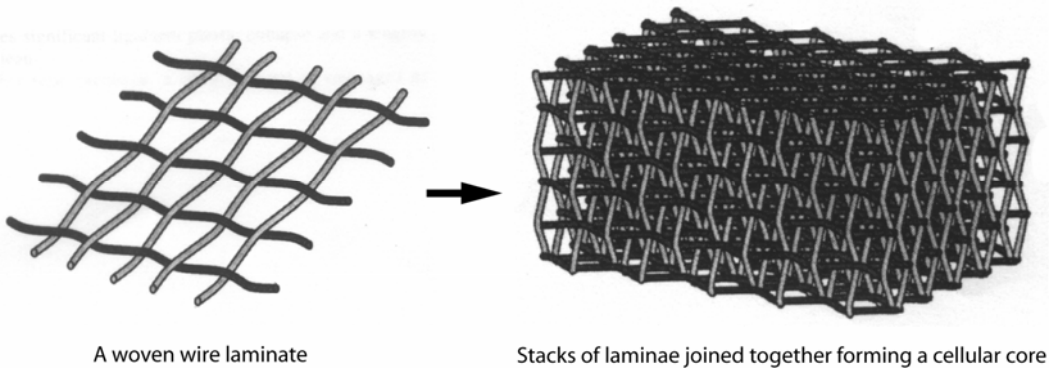

Figure 2-6. A periodic metal core produced by sintering plies of woven fabric laminates [17].

Periodical sandwich cores which consist of an assembly of struts (Figure 2-7) have been manufactured through various casting and forming techniques [16]. Investment casting has been used to produce 3-D Kagomé sandwich panel with attached faceplates, but casting defects remain a standing issue. Cores with tetrahedral and pyramidal struts can be manufactured by bending the nodes of a perforated metal sheet. These strut layers can be further stacked together and bonded to form a periodic cellular lattice.

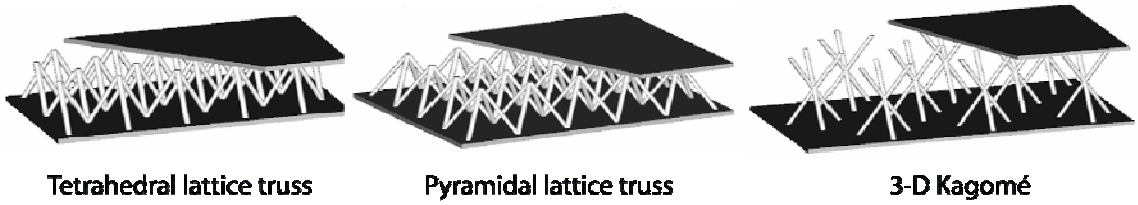

Figure 2-7. Periodic cellular metal core comprising of an assembly of struts [18].

2.3.2.2 Stochastic cores

Stochastic cores do not have a periodic structure and cannot be directly represented using a repeated unit cell. One of the better known stochastic cores is cellular foam (open-cell, closed-cell or mixed-cell). Foam cores consist of either metallic (mainly aluminium) or polymeric cellular structures, filling three-dimensional space. Sandwich panels can be constructed by bonding the faceplates to the foam, using an adhesive. Pure metallic bonding can also be attained by roll-cladding the faceplates to a piece of foamable precursor material, before subjecting it to a heat treatment, causing expansion to the desired thickness (Figure 2-8) [19].

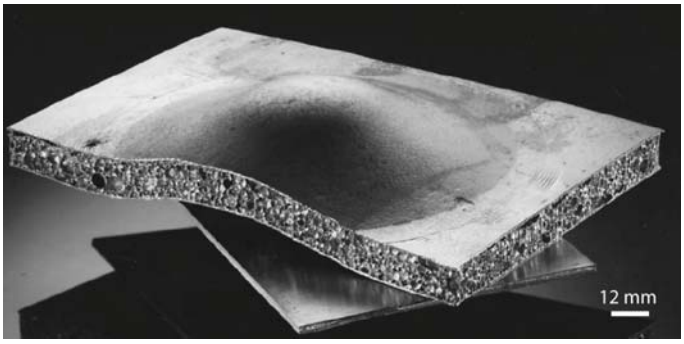

Figure 2-8. A sandwich panel with aluminium foam core and steel faceplates [19].

Expanded thermoset and thermoplastic foams are the most commonly used core materials for all applications, except in the aerospace industry. Almost any polymer can be foamed, but the most common ones are polyurethanes (PUR), polystyrenes (PS), polyvinylchloride (PVC), polymethacrylimides (PMI), polyetherimides (PEI) and polyphenolics (PF). Sandwich panels having complex geometries can be obtained using polymers (e.g. PUR), which can be foamed in-situ between the faceplates [10].

The use of mineral fibres as core materials is well known for their high-temperature thermal insulation, but the drawback lies in their poor mechanical properties. So, they are mainly employed in less mechanically demanding applications, such as for fire doors and panels in the building industry. More critical applications involve the use of sintered high purity silica fibres coated with borosilicate glass layer, as heat-resistant tiles for space shuttle orbiters, to counter re-entry aerodynamic heating [20, 21]. Other metallic thermal protection system consists of high temperature metallic alloy shell panels (e.g. Inconel), filled with alumina fibres [22, 23].

Porous sandwich cores can also be made of metallic fibres [24]. Recently, stainless steel fibres in various aspect ratios have been used to fabricate thin stainless steel sandwich sheets [25, 26]. The highly porous cores have fibre volume fractions ranging from 8 to 20%. Bonding at the fibre contact points is achieved by liquid [27] or solid phase sintering. The sintered fibre felt (mesh) can later be adhesively bonded or brazed onto the faceplates. The distribution of fibres within the core can be either random or preferentially oriented. More details on fibrous core sandwich materials are presented in §2.4.

2.3.3 Faceplate-to-core bonding

To attain good mechanical properties, the faceplates must be well bonded to the thicker and weaker core, enabling effective load transfer between the components. Bonding techniques that have been

used include adhesive joints, brazing, transient liquid phase (TLP) process, resistance welding etc [16, 28]. Among these, the more widely employed are adhesive bonding and brazing.

2.3.3.1 Adhesive bonding

Adhesive bonding of faceplates and core is straightforward and independent of the faceplate and core materials. Adhesive layers are interleaved between the faces and the core (Figure 2-2), the whole stack is then put under a specified pressure and temperature required for curing the adhesive resin. Curing of the adhesive can be carried out in a hydraulic press or, for more demanding applications, in an autoclave.

The most widely used adhesives for bonding sandwich systems are structural adhesives, mostly thermosets, due to their high strength, good elevated temperature resistance, creep resistance and solvent resistance. Structural adhesive is used to transfer loads between adherents in service environments, in which the bond can be stressed to a high proportion of its ultimate strength for long periods without failure [29]. They can be grouped into one-component and two-component systems. A one-component heat-activated system composed of two components that are premixed. This system eliminates the metering and mixing requirements of the two-component systems; however, they require special storage conditions (i.e. 0 °C or below). Chemical families in this group include epoxies and epoxy-nylons, polyurethanes, polyimides, polybenzimidazoles, and phenolics. For the two-component mix-in systems, the chemical families consist of epoxies, modified acrylics, polyurethanes, silicones, and phenolics. Curing of structural adhesives is often performed at elevated temperatures and under pressure to acquire better bond quality and to shorten curing time [30].

2.3.3.2 Brazing

Brazing is a process of joining solid metals (either of similar or dissimilar types) in close proximity, by introducing a brazing filler metal that melts above 450 ºC [31]. Since brazing does not result in melting of parent materials, their mechanical properties are not affected when the right type of filler metal is used. Filler metals of different compositions have been developed to achieve compatibility, strength, corrosion resistance and other desirable properties when joining dissimilar metals [32]. Nickel-based brazing filler metals are normally used for brazing stainless steels. They provide high temperature capabilities, good corrosion resistance and improved mechanical properties compared to silver- and copper-based filler metals. However, in the context of stainless steels, certain braze alloys which contain phosphorous or elements of small atomic radii, may lead to embrittlement. Brazing

can be performed under vacuum or in a controlled atmosphere furnace (argon, dry hydrogen etc), at temperatures of 930 ºC to 1200 ºC, depending on the type of filler metal used [33].

Brazing is suitable for producing multiple joints in one operation, which is usually needed for bonding a porous core material to a pair of faceplates. It also results in low warping, low contamination and is capable of producing joints of different dimensions [34]. In addition, since brazing is a liquid phase sintering technique, for which the rate is controlled by viscous flow, rather than by diffusion (as in solid state sintering), well-consolidated joints can be formed quickly, minimising any deleterious changes to the base materials microstructures [26]. However, a drawback lies in the expensive furnaces required. In addition, excessive use of braze material can also add parasitic weight to the assembled sandwich panels.

2.4 New Lightweight Stainless Steel Sandwich Sheets with Fibrous Metallic Cores

A novel type of lightweight sandwich material has been proposed by Roland Gustafsson, of Volvo Technological Development [1, 25]. It is composed of a pair of thin stainless steel faceplates (200 μm), separated by a stainless steel fibre core, and has an overall thickness of about 1 mm. This type of material is designated as a Hybrid Stainless Steel Assembly (HSSA). Unlike other conventional sandwich materials with thicknesses of the order of 10 mm [35-37], this panel can be handled and formed like monolithic sheet. In addition, it has the potential for offering an attractive combination of properties, including low areal density, high beam stiffness [38], good corrosion resistance, thermal insulation and good acoustic and vibration damping capacity. Besides the original design, several other variants have also been developed and tested in Cambridge [26, 38-40], aimed primarily at improving certain properties, such as stiffness, weldability and formability.

2.4.1 Production and structure

2.4.1.1 Flocked sheet

The original structure of HSSA sandwich sheet, as conceived by Gustaffson [1], is depicted in Figure 2-9. Short 316L stainless steel fibres of about 1 mm length and 25 μm diameter, are electrostatically deposited (the process is known as flocking) onto the 316L faceplates, each of 200 μm thickness. The fibres in the core were produced by a bundle drawing process (Bekaert S.A.), and are magnetic due to the formation of martensite. The work-hardened surface feature (grooves produced due to drawing) can be clearly seen in Figure 2-10. The faceplate-to-core bonding is attained using an epoxy adhesive (Gurit Essex Betamate® – a one-component heat cured epoxy). Since HSSA is a

generic name, the material produced in this way is now termed the flocked and glued (FG) sheet, to distinguish it from other variants of thin sandwich sheets developed in Cambridge.

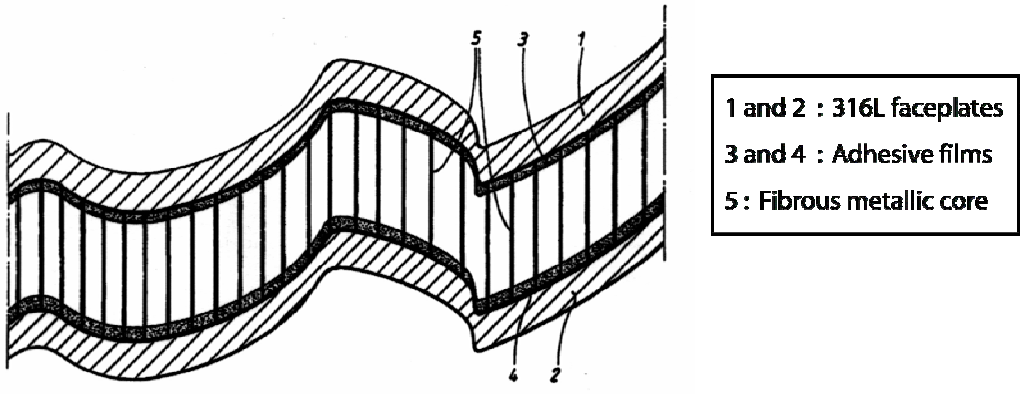

Figure 2-9. Schematic depiction of the flocked and glued (FG) sandwich sheet, as outlined in the original patent [1].

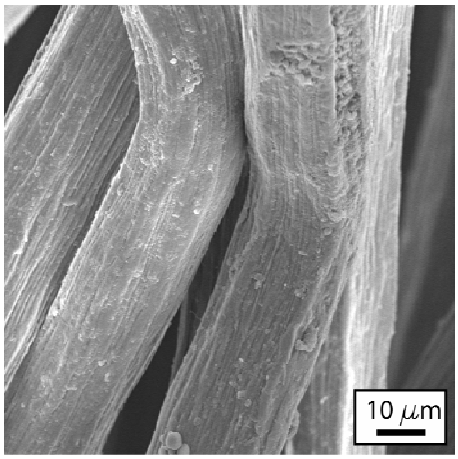

Figure 2-10. Scanning electron micrograph showing the surface morphology of as-drawn 316L fibres [38].

During flocking process, the short fibres are introduced into an electrical field, making them positively charged, and hence attracted towards the lower faceplate that has been covered with an adhesive film. The fibre ends are embedded into the adhesive and discharged upon touching the faceplate, hence enabling more charged fibres to be added until the required volume fraction (~8 vol.%) is attained. The upper faceplate, which is also epoxy coated, is later added to the assembly and cured to obtain the complete sandwich construction. A cross-sectional view of the produced material and its corresponding schematic, are shown in Figure 2-11(a) and (b), respectively. It can be seen that the actual fibres are inclined over a range of angles (between about 0° to 30°) to the faceplate vertical axis, instead of being perfectly perpendicular (i.e. $\theta = 0^{o}$), as outlined in the original patent (Figure 2-9). The cured epoxy has a thickness of about 100-150 μm.

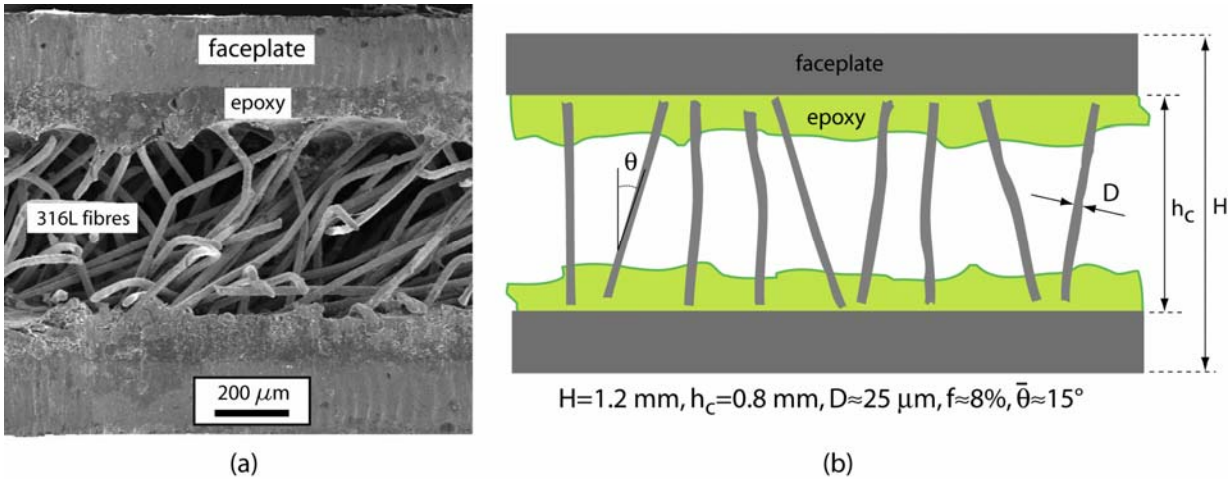

Figure 2-11. (a) SEM micrograph showing the cross-sectional view of flocked and glued sheet, and (b) schematic representation of the actual structure [38].

2.4.1.2 Long fibre in-plane mesh sheets

Based on the original concept of HSSA (§2.4.1.1), two other variants of sandwich sheets have been developed by Markaki and Clyne [38, 41] in Cambridge. Both the faceplates and fibres are still made of 316L stainless steel, but the core is in the form of a pre-manufactured fibre mesh (Bekaert S.A.), containing about 19 vol.% of 25 μm diameter fibres, about 16 mm in length. The structures of both variants are illustrated in Figure 2-12.

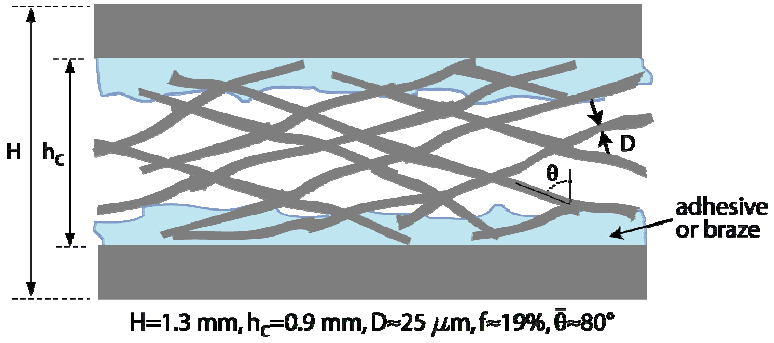

Figure 2-12. Schematic depiction of the structure of long fibre in-plane mesh sheets [38].

The faceplate-to-core bonding is obtained either by adhesive bonding (Araldite 420A/B – a two-component heat cured epoxy) or by brazing (Ni-14Cr-4Fe-2.8B-3.3Si-0.6C braze alloy, at 1000 ºC for 5 minutes in a controlled atmosphere). Micrographs in Figure 2-13 show sections through the sheets and the two different bonds (braze and adhesive). It can be seen that the long fibres are inclined at high angles to the faceplate vertical axis.

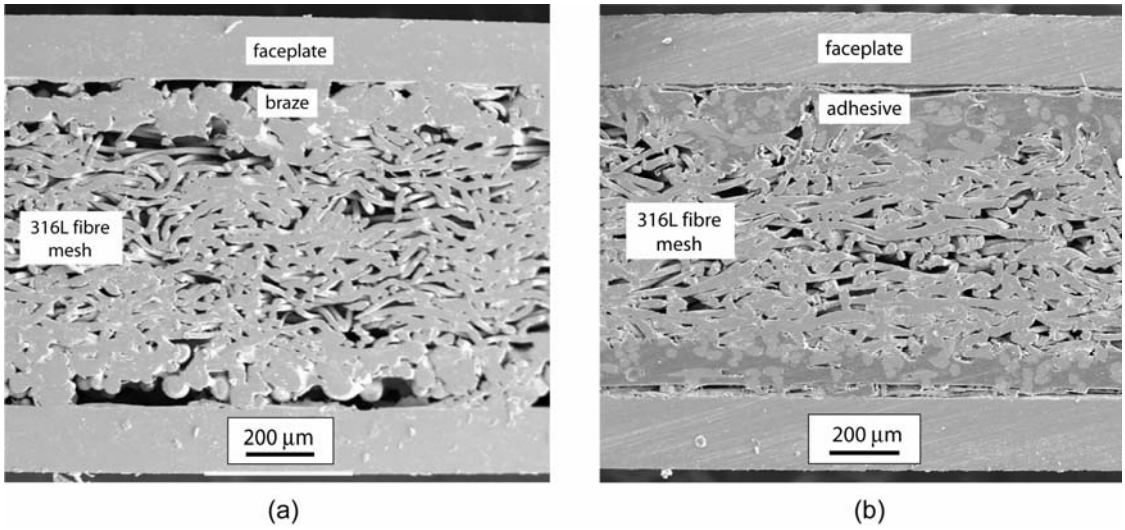

Figure 2-13. Scanning electron micrographs showing the cross-sectional views of (a) brazed (MB) and (b) glued long fibre in-plane mesh sandwich sheets. Both incorporated a pre-manufactured fibre mesh and 316L faceplates [42].

Because solid-state sintering was used in manufacturing the sintered mesh, the fibres have a coarse and recrystallised microstructure (Figure 2-14), which is fully austenitic (non-magnetic).

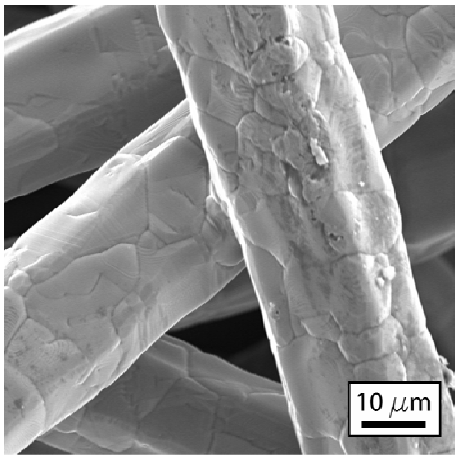

Figure 2-14. Scanning electron micrographs showing the recystallised microstructure of sintered fibre mesh, and the formation of a sintered joint (neck) [38].

2.4.1.3 Short fibre 3-D array (SF) sheet

More recently, another variant of lightweight stainless steel sandwich sheet has been developed in Cambridge, using a brazing technique [40]. This new variant is designed to improve the stiffness, formability and weldability. The produced material and the envisaged structure are as illustrated in Figure 2-15(a) and (b), respectively.

The core consists of 446 ferritic stainless steel fibres (~10 vol.%), produced by Fibretech Ltd., through a melt-overflow technique (a grooved wheel is dipped into the surface of the melt and the fibres solidify on the wheel as it turns). The 446 fibre has a diameter of ~100 μm and length of ~2 mm. In the brazed core, fibres are thought to be oriented at a mean angle of ~60º to the faceplate vertical axis. The use of fibres with lower aspect ratio (i.e. length/diameter or *L*/*D*) and fibre orientation produces a stiffer core. Also, it has been reported [40] that the brazed joints obtained using brazing technique are likely to be stronger than those found in solid-state sintered mesh (Figure 2-14), since fibre fractures were observed along the fibres rather than at the joints.

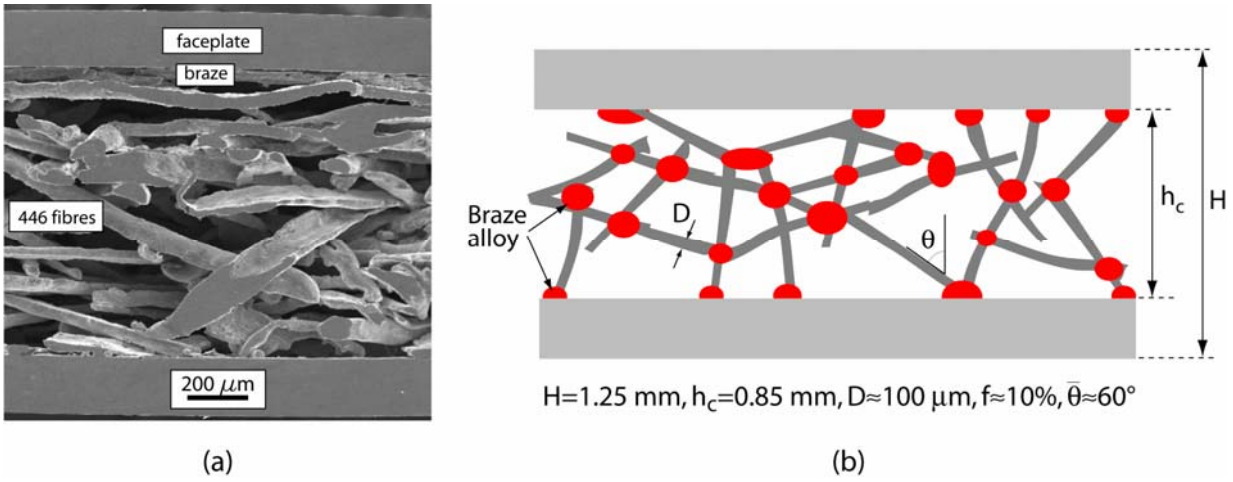

Figure 2-15. (a) Scanning electron micrograph of the produced 3-D array sandwich sheet [42] and (b) schematic depiction of the sandwich sheet [26, 40].

2.4.2 Mechanical properties of fibrous core

The review presented in this section is mainly from the published work of Markaki and Clyne [2, 26, 38, 39]. Results concerning the crushing behaviour of sandwich profiles are based on the work of Mohr and Wierzbicki [43].

2.4.2.1 Single fibre tensile tests

Single fibre tensile tests were performed to understand the deformation and fracture behaviour of individual fibres within the fibrous core [26]. Figure 2-16 shows the different responses obtained from 316L and 446 fibres. The as-received (drawn) 316L fibre (flocked and glued sheet) does not exhibit clear signs of yielding prior to fracture, mainly attributed to its martensitic microstructure. Failure occurs at a tensile strength of 1.2 GPa and a nominal strain of about 1%. The heat-treated 316L fibre (long fibre in-plane mesh) has a yield strength of about 200 MPa, while the strength and ductility are 0.4 GPa and 7%, respectively. The improved ductility is clearly due to the recrystallised

microstructure. Compared with both 316L fibres, the heat-treated 446 fibre (short fibre 3-D array) exhibits higher tensile (~1.3 GPa) and yield strengths (1 GPa). Also, the ductility (~3%) is between the as-received and heat-treated 316L fibres.

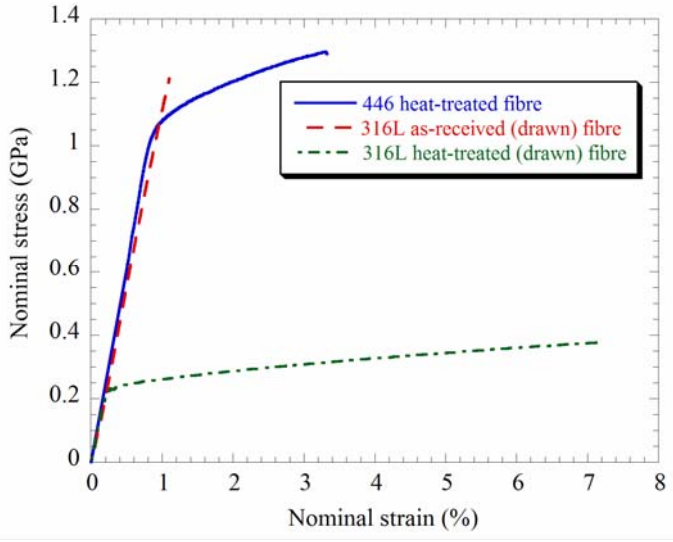

Figure 2-16. Typical single fibre tensile test data for (a) as-received (drawn) 316L (flocked and glued sheet), (b) heat-treated 316L (long fibre in-plane mesh) and (c) heat-treated 446 (short fibre 3-D array) fibres [26].

2.4.2.2 Beam stiffness

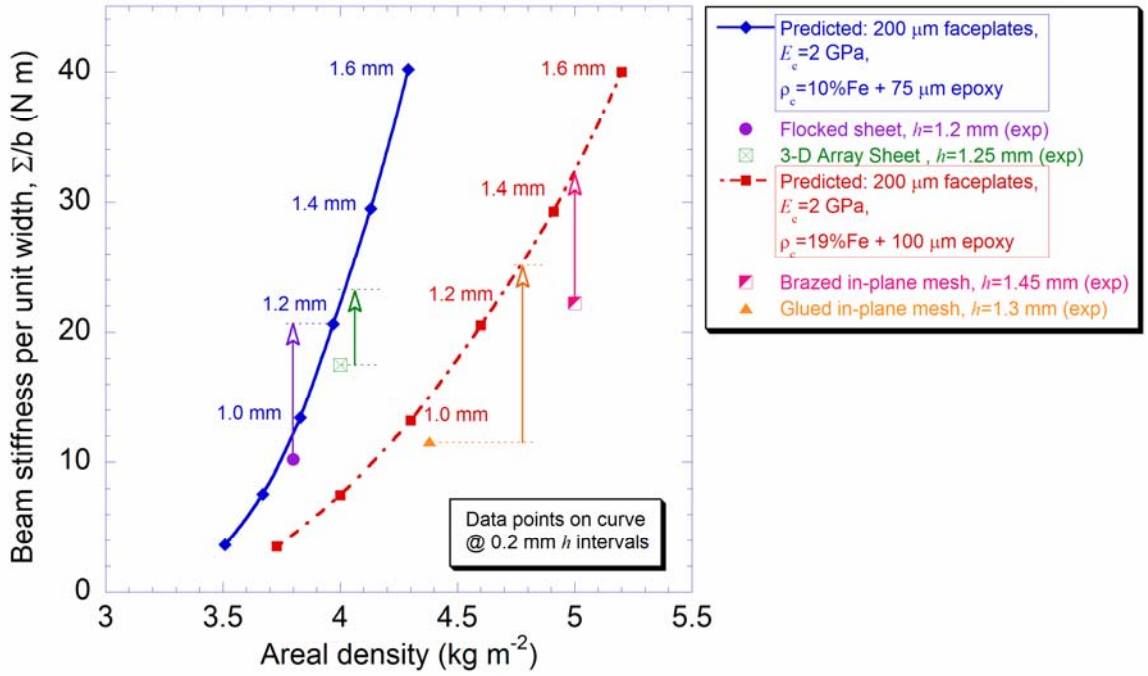

Figure 2-17. Predicted beam stiffness as a function of areal density for four different sandwich sheets, compared with predictions obtained by assuming simple beam bending for a sandwich beam incorporating 200 μm faceplates (E_{fp} = 200 GPa) and an epoxy core (E_c = 2 GPa, ρ = 1.56 Mg m^{-3}). The arrows indicate the expected stiffness, following predictions made for sandwich sheets of the same thickness (after Markaki and Clyne [38] and [40]).

The beam stiffnesses of sandwich sheets were measured using a cantilever bending technique [38, 40]. Figure 2-17 shows the experimental data, compared with predictions for a sandwich sheet with a typical isotropic epoxy core, generated using the standard expression of beam stiffness per unit width (Σ / b) of a doubly symmetric, prismatic sandwich beam:

$$\frac{\Sigma}{b} = \frac{E_{fp}\left(h^3 - h_c^3\right) + E_c h_c^3}{12} \tag{2.1}$$

where E is the Young's modulus and h is the thickness, while the subscripts fp and c designate the faceplate and core, respectively. The contribution of core shearing in cantilever bending has not been taken into account, since the shear moduli of the cores are not known.

For all materials, the experimental stiffnesses are lower than predicted values, at the corresponding sheet thicknesses. For both flocked (FG) and glued long in-plane mesh sheets, the measured stiffnesses are about 50% less than predictions. Although the brazed long in-plane mesh sheet is about 70% as stiff as predicted, the material has much higher areal density, due to the presence of the braze. For the 3-D array sheet, the measured stiffness is relatively higher than flocked sheet, but is still lower than predicted. This is because the core has poor resistance to in-plane shear, so that additional deflections come from the shear strain. It can be seen that the significant improvement in stiffness expected from the 3-D array core architecture (intermediate fibre orientation and strong fibre joints) is not fully achieved.

2.4.2.3 Through-thickness stiffness

The through-thickness Young's moduli of fibrous cores have been measured using a microindenter fitted with a cylindrical flat-head [26, 38]. The samples consisted of sandwich sheets, rather than free standing cores. However, due to the fact that the faceplate stiffness (E_{fp}: 200 GPa) is orders of magnitude higher than that of the core (E_c: 10-100 MPa), the measured displacement can be assumed to be from that of the core alone. The flocked and 3-D array sheets have through-thickness moduli of about 100 MPa, while it is about 30 MPa for the in-plane mesh. The lower modulus of in-plane mesh core can be attributed to the higher mean fibre inclination angles (with respect to the vertical axis).

2.4.2.4 Resistance to interfacial delamination

The delamination resistance of sandwich sheets for mode-I loading has been investigated [26]. The fracture energy and mode of failure is summarised in Table 2-1. The flocked sheets delaminate primarily by fibres being pulled out of their sockets in the adhesive layer. The long in-plane mesh

material fails at the sintered fibre necks (joints) and exhibits the lowest fracture energy. On the other hand, short fibre 3-D array sheets delaminate by fibre fracture within the core, so the fracture energy is substantially higher. It is generally difficult to produce strong joints by solid-state sintering technique (Figure 2-14), since prolonged heating may cause grain coarsening and carbide precipitation, reducing the fibre strength. In contrast, brazing is a much faster process, so that deleterious changes to the fibre microstructure can be prevented.

Table 2-1. Delamination resistance of different sandwich cores [26].

Sandwich core	Interfacial fracture energy, J m^{-2}	Delamination mode
Flocked and glued (FG)	~340	Fibre pull-out
Long in-plane mesh	~30	Sintered neck fracture
Short fibre 3-D array (SF)	~675	Fibre fracture

2.4.2.5 Energy absorption

The crushing of sandwich columns made of flocked sheets has been investigated, to evaluate the influence of core material on energy absorption [43]. As expected, the shear strength of the flocked core (FG sheets) was found to be small (~0.85 MPa), compared with the faceplates. It has been reported that the weak faceplate-to-core bonding caused the core to deform independently from the two faceplates, losing its sandwich effect.

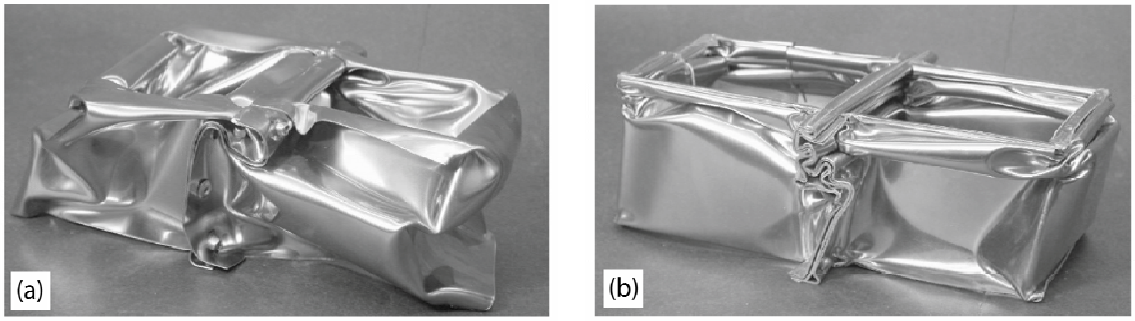

Figure 2-18. Deformed double-cell columns after crushing: (a) solid section of stainless steel sheets, and (b) flocked and glued (FG) sheets. Both columns had similar dimensions and were crushed over the same distance [43].

Figure 2-18 shows a comparison between the crushing behaviour of double-cell columns made of monolithic and flocked (FG) sheets. It can be seen that the collapsed sandwich shows a greater number and much shorter folding wavelengths, which are good indications of high energy absorption by the porous core. The mean crushing force was also found to be ~60% higher than monolithic sheets. Unfortunately, this study was limited to the flocked sheets alone; the crushing behaviour of other variants has yet been investigated, so no comparison can be made at this stage.

2.4.3 Electrical resistivity and resistance weldability

The effective electrical resistivity of the porous core and how it affects resistance weldability, are presented in detail in §3.3 and §4.6.1, respectively. At this point, it is sufficient to mention that the flocked and glued (FG) sheet has relatively higher core resistivity, making it difficult to weld. However, brazed sandwich sheets (long in-plane mesh and 3-D array sheets), were found to exhibit lower resistivity and are therefore more weldable.

2.4.4 Potential applications

Based on the reviews of mechanical and electrical properties outlined in §2.4.2 and §2.4.3, it can be concluded that stainless steel sandwich sheets can offer a good combination of properties – lightweight, high beam stiffness, good interfacial toughness, weldable and good energy absorption during crushing. Clearly, these characteristics make them well suited for various applications in the transportation industry, as summarised in Table 2-2.

Table 2-2. Potential applications and gains for employing fibrous core sandwich sheets in the transportation sector (after [25]).

Sector	Driving forces	Potential applications
Cars, trucks, buses etc	Fuel economy, safety, NVH*, transport efficiency, appearance.	BIW** components, floor panels, hatches, spoilers, shelves, tailgates, tonneau covers, seat frames, chassis components.
High speed train	Weight reduction, safety, appearance, NVH*.	Interior and exterior body panels, seats etc. Safety performance, appearance and weight reduction are important for this type of trains. Stainless steel is a common material for these applications.
Airfreight	Weight reduction, ease of maintenance.	Air cargo containers – today both insulated and normal containers used are made out of different lightweight materials.
Shipbuilding	Weight reduction, ease of maintenance.	The demand for faster and lighter ships has increased the needs for light and efficient marine structural arrangements.
Mobile homes	Appearance, transport efficiency, NVH*.	Exterior body panels, floor and roof panels, engine encapsulations.

*NVH: Noise, Vibration and Harshness
**BIW: Body In White

Chapter 3: Thermal and Electrical Conductivities of Highly Porous Materials

The thermal and electrical transport properties of highly porous materials, such as foams, sintered fibre felts, wood etc, are very different from those of fully dense materials. Both their effective thermal and electrical conductivities can be sharply reduced at low solid fractions (≤ 20%) depending on their architecture. Three mechanisms (solid and gas conduction, convection and radiation) can contribute to heat transfer in porous materials, but only solid conduction is effective in electrical conduction. For high porosity sintered fibre materials, prediction of transport properties are not straightforward, since many additional parameters, such as fibre orientation, fibre segment aspect ratio and tortuosity may need to be taken into consideration.

3.1 Thermal and Electrical Conductivities

Heat conduction in a solid material is governed by its thermal conductivity, k (W m^{-1} K^{-1}) and thermal diffusivity, α (m^2 s^{-1}). The heat flux, q (W m^{-2}), induced by a temperature gradient, $\partial T/\partial x$ (K m^{-1}), is given by Fourier's law [44]:

$$q_i = -k_{ij}\frac{\partial T}{\partial x_j} \qquad i, j = 1,2,3 \tag{3.1}$$

The heat flux, q_i, is the rate of heat flow through unit cross-sectional area. The negative sign indicates that heat flows from a higher to a lower temperature region. The thermal conductivity, k_{ij}, is a second-rank tensor. For a transversely isotropic material, $k_{in-plane} = k_{11} = k_{22}$ and $k_{transverse} = k_{33}$. For an isotropic material, $k_{11} = k_{22} = k_{33} = k$ and $k_{ij} = 0$ for $i \neq j$. Therefore, for unidirectional heat flow in an isotropic material, eqn.(3.1) can be simply written as:

$$q = -k\frac{\partial T}{\partial x} \tag{3.2}$$

In some cases, heat generated ($\dot{Q}$, in W m^{-3}) within a body must be taken into account and the net energy may cause the temperature to change with time ($\partial T/\partial t$) at particular locations. For an isotropic material subject to one-dimensional heat flow, this can be expressed as [44]:

$$\frac{\partial}{\partial x}k\left(\frac{\partial T}{\partial x}\right) + \dot{Q} = \rho C_p\frac{\partial T}{\partial t} \tag{3.3}$$

The product of density and specific heat capacity, ρC_p (J m^{-3} K^{-1}), is the volumetric heat capacity. The ratio of thermal conductivity to the volumetric heat capacity is the thermal diffusivity, α (m^2 s^{-1}):

$$\alpha = \frac{k}{\rho C_p} \tag{3.4}$$

Thermal diffusivity is a measure of how readily a material comes into thermal equilibrium with its environment.

Since the conduction of heat and electrical charge are mathematically analogous, from eqn.(3.1), the current density, J (A m^{-2}), can be written as:

$$J_i = \sigma_{ij} \frac{\partial \Phi}{\partial x_j} \qquad i, j = 1, 2, 3 \tag{3.5}$$

where σ (Ω^{-1} m^{-1}) is the electrical conductivity and $\partial \Phi / \partial x$ (V m^{-1}) is the electrical potential gradient (electrical field). The electrical conduction of a material is commonly characterised by its electrical resistivity, ρ (Ω m), which is the reciprocal of conductivity, σ.

In fully dense materials, both thermal and electrical conductivities are dependent on the concentration of carriers and their mobility. For thermal conduction, possible carriers include free electrons and phonons. A good thermal conduction is conferred by the presence of free electrons (metals) or by high phonon velocities (light, stiff lattices) and large phonon mean free paths (few defects acting as scattering centres). Materials with free electrons (metals) generally exhibit high electrical conductivities [45]. With the exception of (relatively rare) materials and liquids with highly mobile ions, materials without free electrons are very poor electrical conductors, even though they may be good thermal conductors (via phonons). In fact, the electrical and thermal conductivities of metals are linked and their ratio is predicted to be constant at a given temperature (Wiedemann-Franz Law) [46]: the ratio $k/(\sigma T)$, the Lorenz number, is given by $3k_B^2/e^2$, which has a value of about 22 W nΩ K^{-2}.

3.2 Heat Transport in Highly Porous Materials

Highly porous materials (porosity, $P \geq 80\%$), such as foams, fibrous media and wood, are well known for their low effective thermal conductivities and have been exploited as insulating materials.

Compared with a fully dense material, the effective conductivity not only depends on the solid phase (parent material) conductivity, but also on its volume fraction (*f*) and structure (geometry, tortuosity, distribution and connectivity).

3.2.1 Heat Transport Mechanisms

In general, heat transmission can occur via three mechanisms: conduction, convection and radiation. The contribution from each mechanism to the overall effective conductivity may differ according to the structure and property of a particular material and also its working environment (temperature, pressure, fluid flow conditions etc).

3.2.1.1 Conduction

For a porous material, heat transfer by conduction takes place via conduction in the solid phase (foam cell walls, cell ligaments, struts, fibres etc), or through the fluid (gas or liquid) filling the pores.

Compared with a fully dense solid, solid conduction in highly porous material is significantly lowered due to several factors. The relatively low volume fraction of solid phase present greatly reduces the cross-sectional area available for heat flow. The intricate structure of the solid phase, consisting of a complex array of interconnected cell walls (e.g. foams) [47] or tortuous fibres of various orientations [23, 48], can increase the heat conduction paths. In addition, thermal constriction resistances from the joints of contacting fibres or foam ligaments [49] may further reduce the contribution of solid conduction.

Besides solid conduction, heat conduction can also take place through a stagnant fluid phase within the pores. But, its overall contribution will be small if the solid phase is metallic, since the thermal conductivity of gases (commonly air) is normally orders of magnitude lower than metals. In principal, solid phase conductivity will dominate when the solid to fluid conductivity ratio is high, even at high porosity levels. Experimental and modelling work by Boomsma and Poulikakos [47] has clearly pointed out that, for an open-cell aluminium foam (solid conduction, $k_s = 218$ W m^{-1} K^{-1}) of f=0.05, changing the fluid conductivity has a small effect on increasing the effective thermal conductivity (Figure 3-1). By replacing the vacuum in the pores with air ($k_a = 0.0265$ W m^{-1} K^{-1}), the effective conductivity was found to increase from 3.82 to 3.85 W m^{-1} K^{-1} ($k_s / k_a \approx 8200$). When using water ($k_w = 0.613$ W m^{-1} K^{-1}) as the fluid phase, the conductivity was increased to

4.69 W m^{-1} K^{-1} ($k_s / k_w \approx 356$). It can be seen that, despite a ~2200% increase in fluid conductivity, the effective conductivity has improved by only ~22%. However, their work involved only stagnant fluid phase. If the fluid filling the open-cell pores is actively flowing, changing the fluid conductivity may have a more significant effect, since the contribution from convective heat transfer will become important.

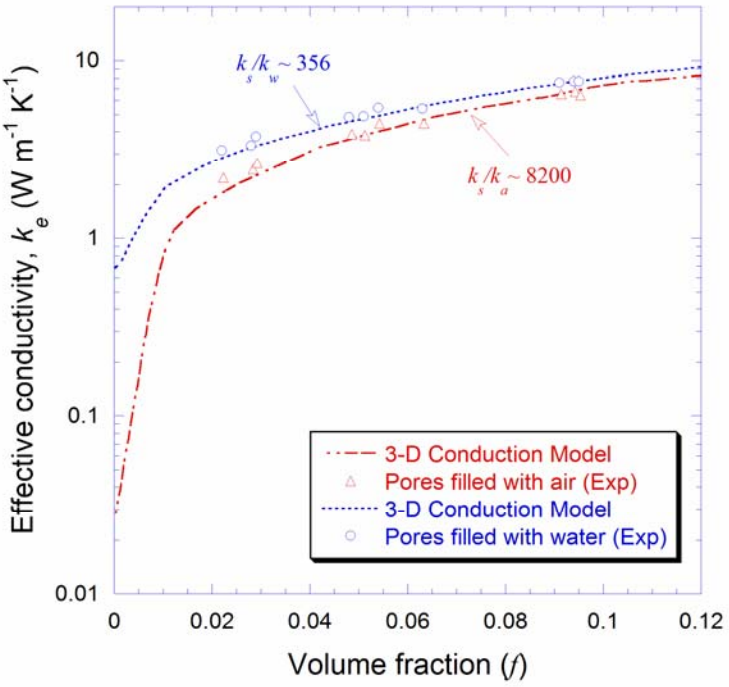

Figure 3-1. Effective thermal conductivities of fluid-saturated aluminium foams, filled with either water or air. The curves are predictions obtained using by the 3-D conduction model of Boomsma and Poulikakos (after [47]).

However, gas conduction becomes a major mechanism for porous materials with lower solid to fluid conductivity ratio, which is the case for high porosity polymeric foams. For closed-cell polyurethane foams filled with CFC-11 gas ($k_s = 0.25$ W m^{-1} K^{-1}, $k_g = 0.013$ W m^{-1} K^{-1}, $k_s / k_g \approx 19.2$), at a relative density ($\rho_{foam} / \rho_{solid}$) of between 0.03 and 0.07, gas conduction contributes more than 60% towards the overall conductivity [50]. Where fluid phase conduction is dominant, the effective conductivity can be reduced by filling the pores with a lower conductivity gas phase (e.g. CCl_4F, $k_g = 0.008$ W m^{-1} K^{-1}) [51].

When heat flow through a two-phase porous material is primarily by conductive transfer, its effective thermal conductivity (k_e) can be estimated by averaging the conductivities of the constituent phases [52]. By assuming the orientation of heat flow is parallel to both phases, the parallel rule of mixtures gives the upper bound of k_e:

$$k_e = fk_s + (1-f)k_g \tag{3.6}$$

where f $(=1-P)$ is the volume fraction of the solid phase, while subscripts s and g represent solid and gas, respectively. On the other hand, the lower bound is given by the inverse rule of mixtures (transverse conductivity):

$$k_e = \left(\frac{f}{k_s} + \frac{1-f}{k_g} \right)^{-1} \tag{3.7}$$

Both equations are effectively based on a 'slab model', which assumes the material to have a layered structure. They agree well with layered materials, such as long fibre composites and laminates, but do not provide good predictions for materials with random pore distribution. Eqn.(3.7) can seriously under-predict the transverse conductivity when the structure is not, in fact, layered (e.g. if k_g=0, then k_e=0).

In fact, random pores result in microscopic distortion of temperature field in their vicinity. This can cause deviation in heat flow from the apparent direction of macroscopic flow, hence increasing the microscopic (actual) path length. Eqn.(3.6) is exact only when both microscopic and macroscopic heat flow are parallel to each other ($k_s \approx k_g$). However, this is usually not the case for most porous materials. When k_s and k_g differs significantly from each other, microscopic heat flow may either bend towards the pore ($k_s < k_g$) or away from the pore ($k_s > k_g$). In 2-D heat flow problems, the average cosine of the angle between microscopic (local) and macroscopic (global) heat flow is given by [53]:

$$\langle \cos\theta \rangle = \frac{k_e}{fk_s + (1-f)k_g} \tag{3.8}$$

Many other expressions for k_e have been derived for porous materials, especially for polymeric foams and particulate beds. These can be found in the reviews of Collishaw and Evans [54], and Dawson and Briggs [55]. They consist of empirical correlations and semi-empirical models, while others are valid only within certain volume fractions. Several workers [47, 49, 56] have also developed models based on three-dimensional description of high porosity (P > 90%) open-cell foam geometry that are consistent with experiments. In general, better predictions are obtained from models which closely resemble the actual material structure.

For bonded metallic fibres, the major transport mechanism is conduction when the fluid phase is stagnant (no convection). To date, only limited data are available in the literature for the effective conductivity of sintered metal fibres (stainless steel, copper, nickel) [48, 57]. While several workers have proposed expressions for predicting conductivity, there are difficulties. The effects of the constituent conductivity ratio (k_f / k_g), porosity (*P*), fibre aspect ratio (*L/D*), tortuosity and orientation distribution may all be important. Since the distribution of fibres in a sintered felt is either in a random or preferred orientation, a repeating unit cell may be difficult to identify, so an 'average unit cell' is normally assumed for modelling purposes.

The first group of models accounts only for the effects of fibre volume fraction, $f\left(=1-P\right)$ and the constituent conductivity (k_f and k_g). Koh and Fortini [57] applied an equation formulated earlier by Aivazov and Domashnev [58] (originally for predicting the effective conductivity of porous media under vacuum) to experimental data of sintered fibres (felts), and concluded that:

$$k_e \simeq \frac{fk_f}{1+11\,(1-f)^2} \tag{3.9}$$

Acton [59] assumed a simplified unit cell and square fibre cross-sections and arrived at the following equation:

$$k_e \simeq (1-f)^2 k_g + f^2 k_f + \left[\frac{4f(1-f)k_f k_g}{k_f + k_g}\right] \tag{3.10}$$

Koh *et al* [60] formulated the following expression by taking into consideration the contact resistance and fibre network resistance in series:

$$k_e \simeq \frac{f^2 k_f}{f\left[1+2(1-f)\right]+1.5(1-f)} \tag{3.11}$$

Other expressions can be found which incorporate the fibre aspect ratio $\left(L/D\right)$ term, although are for cell geometries such that it can be expressed in terms of volume fraction. Semena and Zaripov [61] derived the following empirical equation for sintered metal fibres ($0 < f < 0.35$) under a vacuum:

$$k_e \simeq f^2 k_f \exp\left\{-[\pi + \log_{10}(D/L)]\right\} \tag{3.12}$$

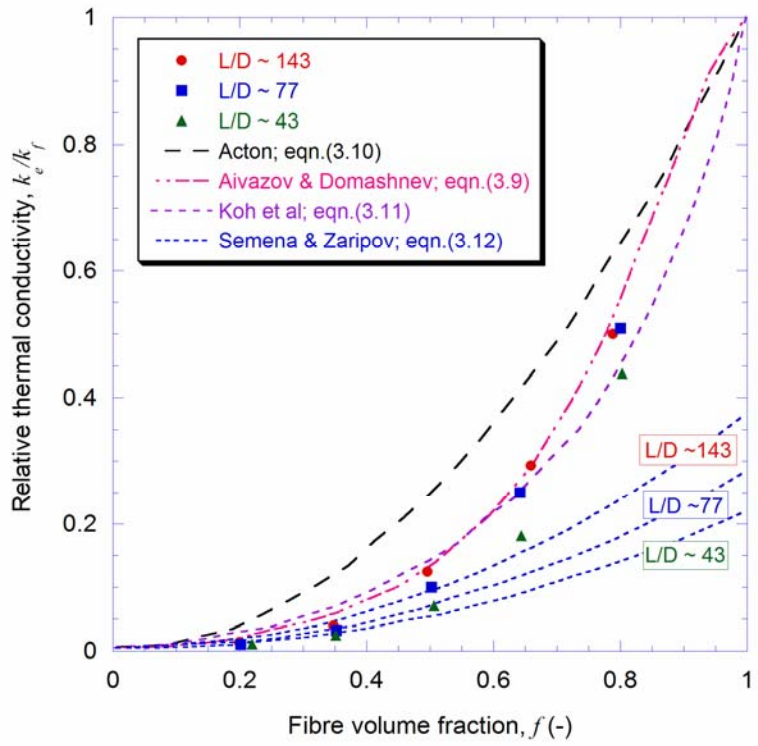

Figure 3-2. Comparison between effective thermal conductivity predictions, using eqns.(3.9) to (3.12), and experimental data for sintered copper fibre felts of different fibre aspect ratio (*L/D*). The fibre aspect ratios were obtained from the original fibres ($20 \le D \le 70$ μm and $3000 \le L \le 10000$ μm) [48, 61].

Figure 3-2 shows a comparison between predictions from these analytical expressions and experimental data of Semena and Zaripov [61], for copper fibre felts of three different fibre aspect ratio, and fibre volume fraction ranging from 0.2 to 0.8. It can be seen that Acton's equation (eqn.(3.10)) consistently overpredicts the conductivity. Eqns.(3.9) and (3.11) generally provide better predictions. Although eqn.(3.12) directly incorporates the aspect ratio term, satisfactory agreement was obtained only at volume fraction less than 0.5, for the corresponding *L/D* ratios. It seems to be difficult to identify which is reliable over a wide volume fraction range. This may be due to the fact that the fibre aspect ratios were determined from the original fibres, rather than from the sintered fibre segments found on the felts.

Bauer [53] formulated an expression that accounts for the average fibre orientation, θ:

$$\left(\frac{k_e - k_g}{k_f - k_g}\right)\left\{\frac{k_e + k_g[(1-\sin^2\theta)/(1+\sin^2\theta)}{k_f + k_g[(1-\sin^2\theta)/(1+\sin^2\theta)}\right\}^{\left(\frac{-\sin^2\theta}{1+\sin^2\theta}\right)} = f \qquad (3.13)$$

where $\sin^2\theta$ signifies the average orientation of fibres in the direction relative to macroscopic heat flow. In eqn.(3.13), θ can serve as an adjustable parameter for experimental data analysis, since

average orientation is not easily measured. At the extreme of $\sin^2\theta = 0$, heat flows along the longitudinal axis of fibre; when $\sin^2\theta = 1$, heat flow direction is transverse to the fibre longitudinal axis; whilst for a random distribution ($\sin^2\theta = 2/3$), heat flows preferentially across fibres. Figure 3-3 shows predictions from this model, compared with experimental data compiled from different workers [60-64]. It can be seen that the normalised data show a large scatter and do not fit well with predictions for any specific orientation. Bauer [53] claimed that better agreement can be obtained by assuming $\sin^2\theta > 0.667$, implying that most fibres are more preferentially oriented in the felt plane and heat flow direction tends to be across the fibres. However, this does not seem to be well justified by the data depicted in Figure 3-3.

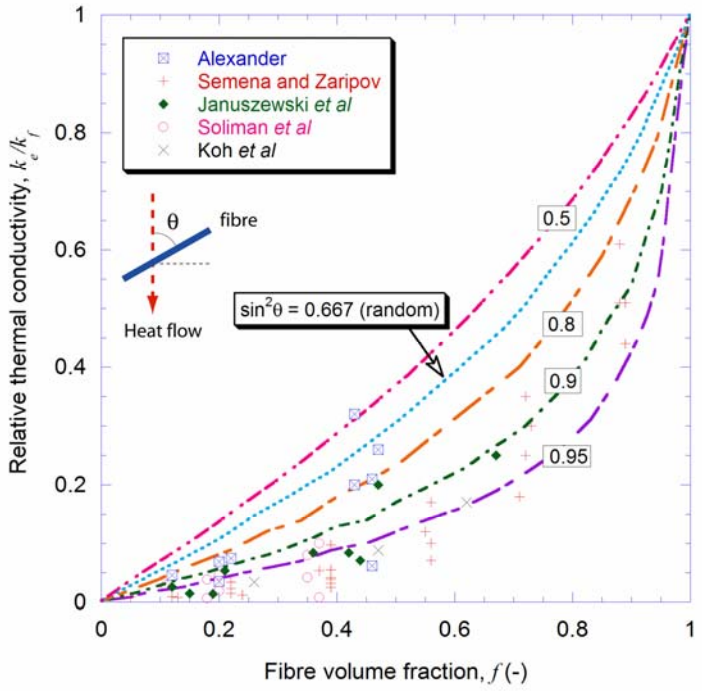

Figure 3-3. Relative thermal conductivity of sintered metal fibres of various porosity and fibre orientation. Experimental data are from different sources, while the curves are predictions obtained by employing different values of $\sin^2\theta$ in eqn.(3.13). The angle θ is measured relative to the heat flow direction [53]. (Data sources: Alexander [63], Semena and Zaripov [61], Januszewski *et al* [64], Soliman *et al* [62] and Koh *et al* [60]).

3.2.1.2 Convection

In porous materials, convective heat transfer takes place within the fluid and then to surrounding solid, under the influence of a temperature gradient. This can occur either by free or forced convection. The heat flux transmitted by convection is often represented by an equation of the form:

$$q = h\,(T_s - T_{sur}) \tag{3.14}$$

where h (W m^{-2} K^{-1}) is the heat transfer coefficient. T_s and T_{sur} are temperatures of the surface and surrounding, respectively.

A temperature gradient causes local density differences, producing buoyancy forces which lead to free convection. Convection in pores is low when the Grashof number, Gr (ratio of buoyant force driving convection to the viscous force opposing it), is less than about 10^3 [65]. By using this as a lower limit, the minimum cell size for convection in closed-cell foam has been found to be ~10 mm. In fact, real foams commonly have cell sizes at least a factor of 10 smaller, making convection ineffective [51]. Experiments by Skochdopole [66] confirmed that convection is negligible in polymeric foams with cell diameters below 4 mm. In fibrous media with density greater than 20 kg m^{-3}, it was found that convection is suppressed because the fibres subdivide the gas into sufficiently small pores [67]. Therefore, convective contribution is generally not taken into account when it comes to the analysis of heat transfer in materials containing fine, closed cells. However, it may become important at larger cell diameters or when the material has an open-cell structure [54].

Forced convection is caused by external means, such as fans or pumps. Several workers have investigated the use of open-cell porous materials, such as metal foams [68] and fibrous materials [69, 70] as heat exchangers under forced air convection. They were found to function as better heat dissipaters compared with plain flat plates, with improved efficiency at higher porosity levels.

3.2.1.3 Radiation

Radiant energy is transmitted by electromagnetic waves. The net radiant heat flux from an opaque surface of temperature T_s, to another at a lower temperature of T_0, can be written as:

$$q = \varepsilon\sigma\ (T_s^4 - T_0^4) \tag{3.15}$$

where ε is the emissivity ($0 \le \varepsilon \le 1$) and σ is the Stefan-Boltzmann constant. Since q is proportional to T^4, the radiation contribution becomes more significant at higher temperature. The heat flux transferred depends on the emissivity of the material for the radiant wavelength. Although gas filling pores is commonly transparent to radiation, the solid phase is often opaque to the wavelengths concerned. In a transient event, the net contribution of radiation may also be reduced due to repeated reflection and absorption at the surfaces [51]. In foams, the radiation contribution thus tends to increase with decreasing volume fraction of solid phase or with increasing cell size [54].

Several workers have studied the radiation contribution in fibrous media, made of alumina [23] and silica fibres [21, 71, 72], both of which are effectively transparent to the radiant wavelengths. So, eqn.(3.15) is not suitable for such materials. Experimental and modelling results indicated that radiation contribution is also strongly influenced by the orientation of these fibres [73]. However, limited information is available on the radiation contribution in metallic fibrous media, although in general, metals are rather opaque to radiation across a wide wavelength range, so radiation contributions are expected to be small.

3.2.1.4 Combination of Mechanisms

The approach that is normally taken to account for the contributions of different heat transport mechanisms in porous material involves additive superposition [50, 74], that is:

$$k_{total} = k_{conduction\ (s+g)} + k_{convection} + k_{radiation} \tag{3.16}$$

where $k_{conduction\ (s+g)}$ is the coupled conductivity of solid and gas phases, found using expressions such as eqns.(3.6) and (3.7). Although Eqn.(3.16) offers simplicity and appears to be consistent with experiments, it is far from exact [54]. This approach is incorrect because radiation does not depend on just the temperature gradient (dT/dx), but also on the absolute temperatures involved. It agrees with experimental observations when convection and radiation contributions are small, that is, for a fine porosity material operating at low temperatures.

When the convective term is small, the total flux can be treated as a sum of conductive and radiative terms:

$$q_{total} = q_{conduction\ (s+g)} + q_{radiation} \tag{3.17}$$

Eqn.(3.17) serves as a basis for several workers who investigated the combined conduction and radiation heat transfer in high temperature glass fibre insulations [75-77] and foams [78, 79]. For foams, Glicksman *et al* [78] proposed the following expression:

$$q_{total} = -k_{conduction\ (s+g)}\left(\frac{dT}{dx}\right) - \left(\frac{16\sigma T^3}{3K}\right)\left(\frac{dT}{dx}\right) \tag{3.18}$$

where K is the mean extinction coefficient, measured by infrared spectroscopy. The radiative term is treated as dependent on both the temperature gradient and absolute temperature.

3.3 Electrical Transport in Highly Porous Materials

Compared with fully dense materials, highly porous materials exhibit significantly lower electrical conductivities (higher electrical resistivities). Unlike heat transfer, which can occur through different mechanisms, electrical charge transport can only take place via solid conduction. The volume fraction of solid phase (or relative density) and its architecture, strongly affect electrical conduction. In principal, electrical resistance increases due to reduction in cross-sectional area, longer and tortuous conduction paths and additional constriction resistances introduced by fibre and ligament joints.

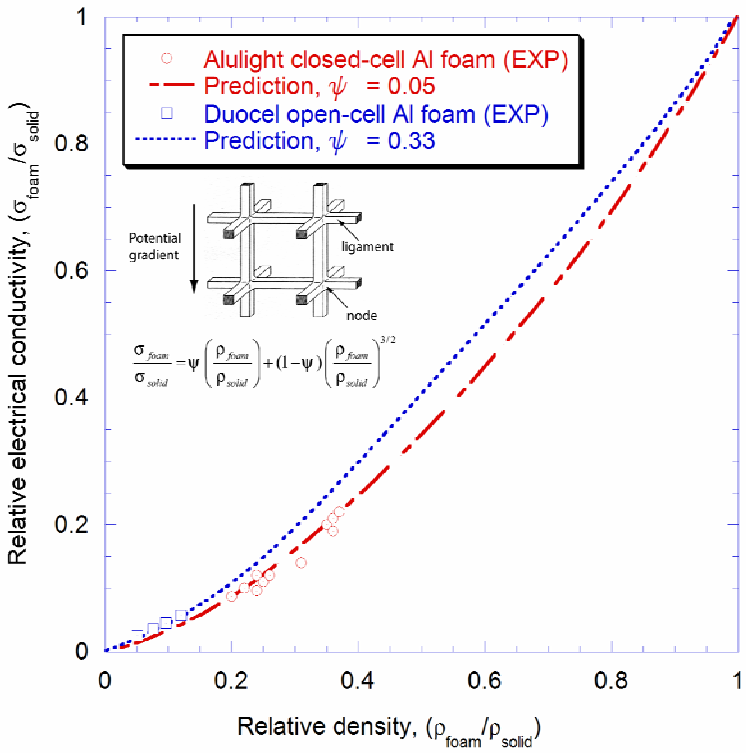

Figure 3-4. The relative electrical conductivity versus relative density of open- and closed-cell aluminium foams. The lines are predictions using the inset equation, where ψ is the fitting parameter (after[80]).

As pointed out earlier (§3.1), since electrical and thermal conductivities are mathematically analogous, most of the expressions developed for heat conduction [53-55] can equally be employed for predicting effective electrical conductivity. However, unlike heat conduction, limited data for electrical resistivity of porous materials have been reported, making model validation more difficult. Using an idealised unit-cell model (Figure 3-4), Ashby *et al* [80] showed that the effective electrical conductivity of open- and closed-cell foams varies non-linearly with relative density. It was pointed out that conductivity depends mainly on the distribution of solid phase between cell ligaments and nodes. The model also agrees well with open-cell foams, since the (relatively thin) cell walls actually make little contribution to the overall conductivity.

Dharmasena and Wadley [81] proposed a tetrakaidecahedral unit-cell model to predict the electrical conductivity of an open-cell aluminium foam. For low relative density foams (4 to 12%), the model predicts a linear dependence upon the relative density, although the limited experimental data points available show, trend of non-linearity. To attain better model predictions, they emphasized the need for a more detailed morphological representation of the real foam cellular structure.

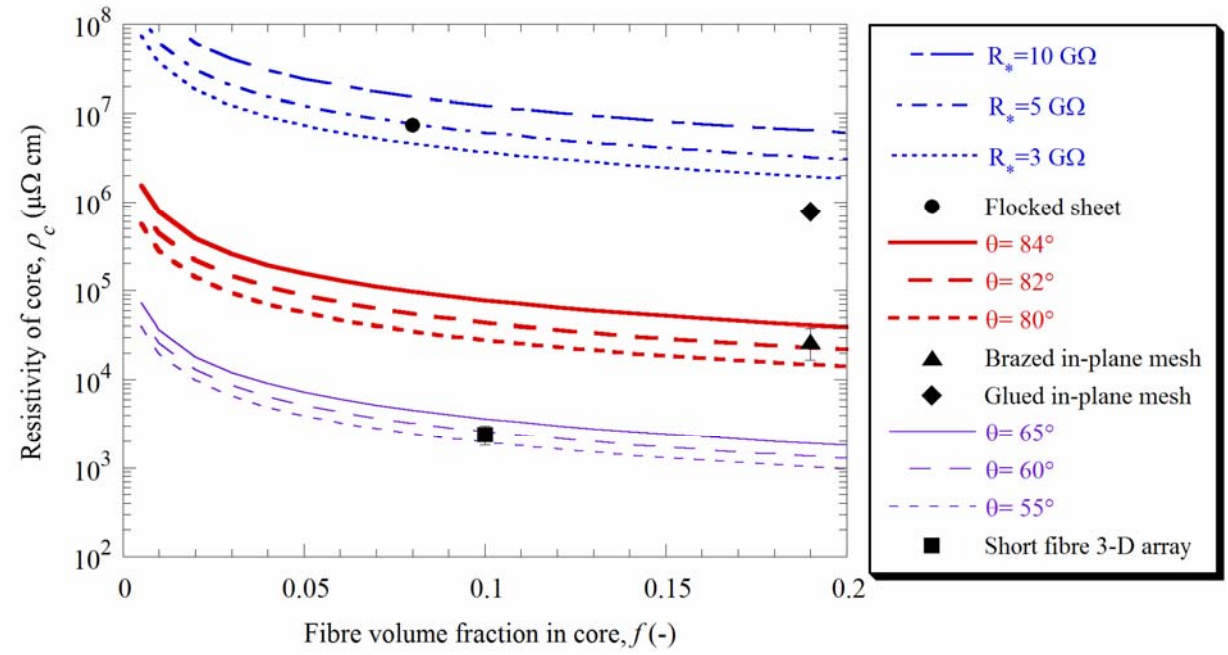

Figure 3-5. Core resistivity as a function of core fibre volume fraction. Experimental data are shown together with predictions from eqns.(3.19) and (3.20) [26].

The effective resistivities of fibre cores found in lightweight sandwich materials (§2.4) have been studied by Markaki *et al* [2, 26]. The experimental data are depicted in Figure 3-5, together with their analytical predictions. For bonded fibre array cores, the following expression relates the effective resistivity of the core, ρ_c, to the resistivity of the fibre, ρ_f; fibre volume fraction, f; and mean fibre orientation, θ (measured from the vertical axis):

$$\rho_c = \frac{\rho_f}{f \cos^2 \theta} \tag{3.19}$$

For a flocked fibre core, the effective resistivity can be predicted from:

$$\rho_c = \frac{1}{f}\left(\frac{\pi D^2 R_*}{2h_c} + \rho_f\right) \tag{3.20}$$

where R_* is the resistance of the epoxy adhesive joining fibre to faceplate.

The flocked fibre core has the highest electrical resistivity (~10 Ω cm), because of poor electrical contact between fibre ends and faceplates. As expected, the resistivities of the brazed in-plane mesh (~0.01 Ω cm) and 3-D array cores (~0.001 Ω cm) are orders of magnitude lower than the flocked core. The adhesively bonded in-plane mesh core (~1 Ω cm) has relatively higher resistivity, compared with its brazed counterpart, due to poor electrical contact with faceplates. However, it is still better than the flocked core, probably because of the pressure applied during curing, which promoted better electrical contact with the faceplates. The model predictions clearly show that the fibrous core resistivity has a non-linear dependence on fibre volume fraction and is strongly affected by mean fibre orientation.

Chapter 4: Resistance Spot Welding (RSW)

Resistance spot welding (RSW) is today's most widely used technique to join sheet metals in automotive manufacturing. However, the process itself is complicated, difficult to analyse and incompletely understood. Flow of electricity and heat determines weld nugget development. The mechanical deformation caused by electrode forces is also important. In addition, electrical and thermal contact resistances at the electrode-to-workpiece (E-W) and workpiece-to-workpiece (W-W) interfaces can affect weld nugget development. Various material properties, including thermal and electrical conductivities, mechanical properties, surface and metallurgical characteristics also affect weldability. Although the weldability of monolithic sheet materials (e.g. steel and aluminium) has been widely studied, very little work has been done on the welding characteristics of either porous materials or sandwich sheets. Since the 1960s, numerical models of increasing complexity have been formulated to investigate welding characteristics, but almost all were developed for monolithic sheet materials.

4.1 Basic Principles of RSW

Resistance spot welding (RSW) is a process where two faying surfaces are joined, using the heat generated by resistance to the flow of electric current through the workpieces, held under force by a pair of electrodes. The RSW process involves a complex interaction between mechanical, electrical, thermal and metallurgical phenomena, as illustrated in Figure 4-1. Two workpieces are compressed between a pair of water-cooled (copper alloy) electrodes, which apply a constant pressure onto the sheets, ensuring good contact. A high amperage current is then passed through the electrodes, to generate localised heating at the faying surfaces. Heat generation from interfacial contact resistance, and Joule heating, results in the formation of a molten nugget at the faying surfaces, within regions of high current concentration. The current flow is then discontinued, but pressure is maintained, in order to allow rapid heat dissipation and solidification of the weld nugget. During cooling, excessive electrode pressure is to be avoided, to prevent melt expulsion. The electrodes are then retracted once the nugget has fully solidified [3, 82].

RSW is today's most widely used joining technique for sheet metal fabrication, and has been extensively employed for automotive body-in-white (BIW) assemblies. Typically, 3000 to 4000 spot welds are present in an average passenger vehicle [83, 84]. Compared with other joining techniques, RSW is fast, cost effective, efficient and capable of producing high quality welds [85]. It is also preferred over other techniques when lap joints are permitted, and when gas- or liquid-tight seams are not essential. In addition, RSW can be fully automated and robotised, making it suitable for high production automotive assembly lines [82].

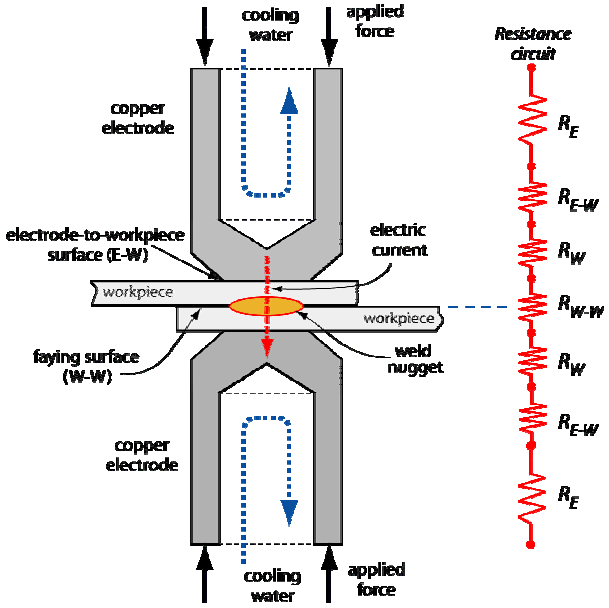

Figure 4-1. Schematic representation of resistance spot welding setup and its corresponding electrical resistance circuit. (Note: *E*: Electrode; *W*: Workpiece; *E-W*: Electrode-to-workpiece; *W-W*: Workpiece-to-workpiece or faying surface).

The welding cycle consists of four phases [86], as depicted in Figure 4-2.

(i) *Squeeze time* is the time interval between timer initiation and first application of current. This interval ensures that the required force is applied and good contact is established between electrodes and workpieces, prior to the application of current.

(ii) *Weld time* is the time interval when high amperage current is passed through the workpieces via the copper electrodes. This is normally a small fraction of a second.

(iii) *Hold time* is the time during which the electrode force is maintained on the workpieces after the current has been discontinued. Sufficient hold time is important to allow for the weld nugget to solidify.

(iv) *Off time* represents the time interval between the end of hold time and the start of another weld cycle.

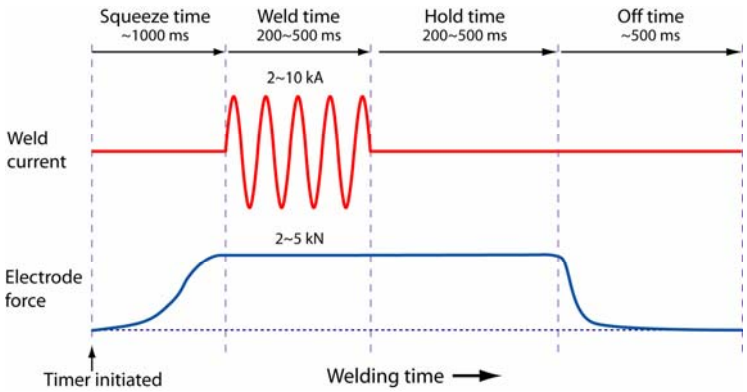

Figure 4-2. A typical welding cycle for single impulse resistance spot welding process of plain carbon steel sheets (after [86]).

4.2 Force Distribution across Electrodes

The compressive force applied by the pair of welding electrodes during the squeeze time determines the contact area at the E-W and W-W interfaces, which affects the electrical (§4.4.1) and thermal (§4.4.2) contact resistances. Since both heat generation and dissipation rates are dependent on these resistances, the development of the weld nugget is therefore directly affected. In general, by increasing the electrode force, the initial heating and average current density at the interfaces are reduced, as a result of lower electrical contact resistance. In addition, higher force improves the thermal contact conductance, leading to additional heat losses into the electrodes, further impeding weld nugget growth.

The non-uniform distribution of pressure across the E-W and W-W interfaces is dependent on the geometry of electrode used. Determination of local contact stress distribution is difficult to conduct through experiments and is normally predicted using mathematical models. Analytical models have been used by several investigators, such as Hill [87] and Ishlinsky [88], to calculate the pressure distribution. Figure 4-3 shows the different pressure distribution developed across the indentation surface for flat or spherical indenters. The calculation was done by taking into account surface frictional effects and assuming the material to be elastic-perfectly plastic. In the context of RSW, a flat indenter will be analogous to a truncated cone electrode, while a spherical punch corresponds to a hemispherical electrode. For both cases, maximum stresses develop directly under the centre of the indenter. The flat indenter has higher stresses at the periphery compared with a spherical indenter.

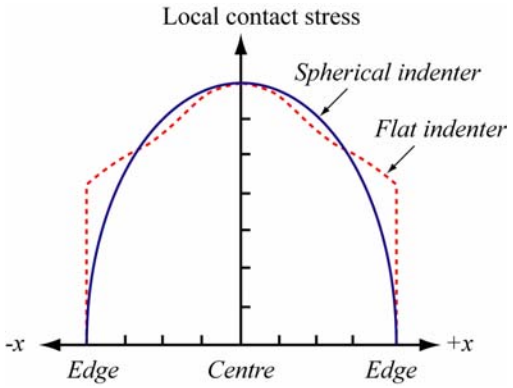

Figure 4-3. Pressure distribution generated across indentation, using a flat and spherical indenter [88] (after [3]).

Using finite-element methods, several workers [89-91] have predicted the evolution of interfacial contact pressure during welding of monolithic steel sheets. Most studies were conducted using truncated cone electrodes. The typical results are shown in Figure 4-4, based on the work of Feng *et al* [89]. It can be seen that significant changes in pressure and contact area take place during welding. Due to thermal expansion of workpieces and electrodes, the contact areas tend to shrink

during the first few weld cycles. But, for subsequent cycles, as a result of resistive heating, the sheets soften and contact area increases. It is interesting to see that, for both interfaces, pressure profiles at the 2nd cycle show some resemblance to the calculation of Ishlinsky [88] for a flat indenter (Figure 4-3). Relatively higher pressures are also predicted at the periphery after the initial first few cycles.

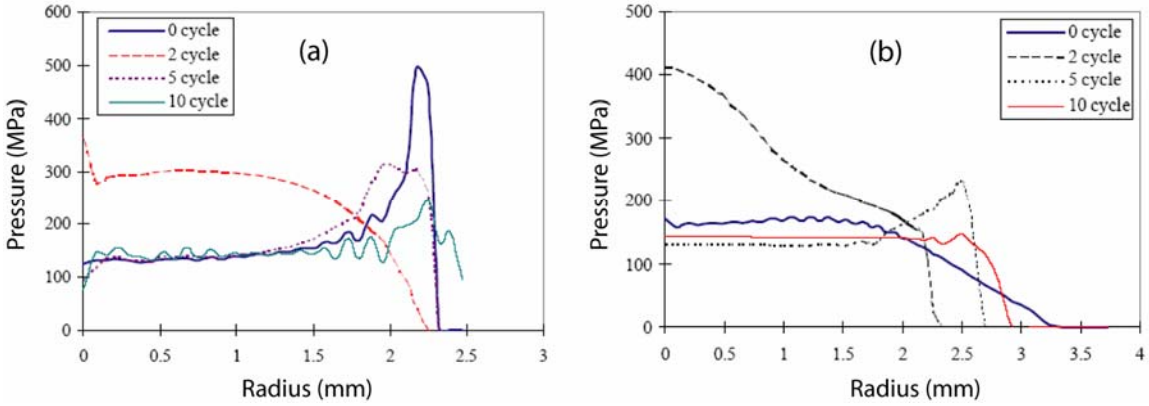

Figure 4-4. Interfacial contact pressure and contact area variation at the (a) electrode-to-workpiece (E-W) interface, and (b) faying (W-W) interface. The steel sheets were 1.6 mm thick and the truncated electrode has a face diameter of 4.5 mm [89]. (Note: 1 cycle=0.02 s)

4.3 Electricity and Heat Flow in RSW

4.3.1 Electrical current flow

During the weld time, the flow of (high amperage) current through the workpieces determines the overall weld nugget formation. In general, the distribution of current and potential is not uniform across the electrode face (Figure 4-5), which is mainly attributable to the electrode face geometry.

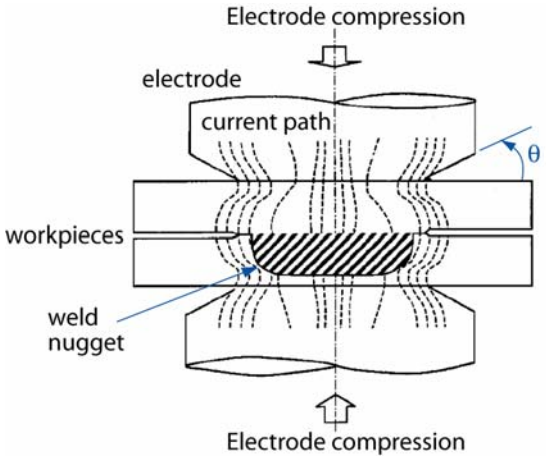

Figure 4-5. Schematic representation of current path in the electrode and workpieces during weld time, using a pair of truncated cone electrodes. (Only half of the weld nugget is depicted here) [3].

Using finite-element models, Bowers *et al* [92] investigated the effects of different electrode geometries on local current distribution. Their calculations show that more uniform current distribution at the electrode face can be attained when the electrode to sheet interface angle, θ, approaches 90°. For truncated cone electrodes ($\theta < 90^{\circ}$), higher current density can be found at regions located around the periphery of the contact area between the workpieces and electrode. This gives rise to uneven heating and promotes localised electrode wear. Similar conclusions were also reached by Nied [93]. Besides the geometrical effect, the maximum in current density at the periphery is caused partly by the higher pressures at this location. These issues may not be relevant for a hemispherical electrode.

4.3.2 Heat flow

4.3.2.1 Heat generation

In RSW, heat is generated as a result of localised resistive heating and is governed by three factors:

(i) the welding current, I (A);

(ii) the resistance of the conductors, R (Ω); and

(iii) the weld time, t (s).

The relationship between them is given by Joule's law:

$$Q = I^2 Rt \tag{4.1}$$

where Q is the heat energy generated, in Joules. The amount of heat generated is proportional to the square of welding current, and directly proportional to the resistance of workpieces and weld time. Clearly, the welding current has a relatively larger contribution towards overall heat generation, as compared with resistance and time. In fact, the resistance term, R, is made up of a series of resistances found within the electrodes, workpieces and different interfaces (Figure 4-1):

(i) the bulk resistance of copper electrodes, R_E;

(ii) the interfacial contact resistance between electrodes and workpieces, $R_{E\text{-}W}$;

(iii) the bulk resistance of workpieces, R_W; and

(iv) the interfacial contact resistance between the workpieces, $R_{W\text{-}W}$.

If all the other parameters are assumed to be constant, the arithmetical sum of the total resistance, R, determines the magnitude of the current, I. The heat generated at a specific location will be directly proportional to the resistance at that point. Part of the heat generated is used to produce the molten

nugget at the faying surface, while the rest will be conducted away and lost (§4.3.2.3). From eqn.(4.1), it is apparent that the welding current is inversely proportional to the square-root of time for a fixed total quantity of heat. Therefore, to compromise for a shorter weld time, a larger welding current is necessary in order to generate sufficient welding heat and produce an acceptable weld. However, very large currents can result in inhomogeneous distribution of heat within the weld zone, leading to severe surface melting and electrode deterioration [94, 95].

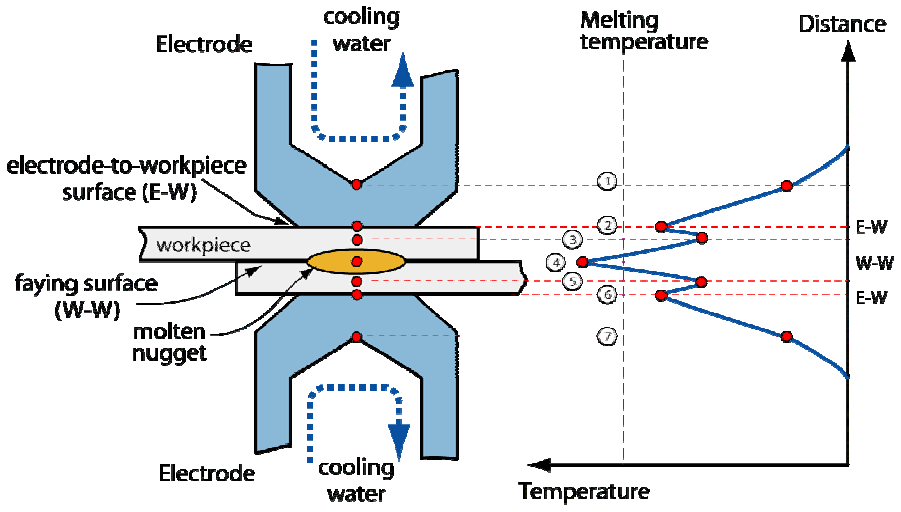

Figure 4-6. Temperature profile for various locations at the end of weld time, for the resistance welding of a pair of monolithic sheets [86].

Figure 4-6 illustrates the temperature profile developed in the workpieces and electrodes at the end of weld time. By assuming that the workpieces are of the same material and thickness, the resultant temperature profile will be symmetrical along the faying surface axis. In principle, the temperature distribution observed is the result of different locations having different electrical resistances, as described below:

(i) Positions 1 and 7 – the resistance of the electrode material, R_E. This resistance is relatively small because the electrodes are made of copper, which is a very good electrical and thermal conductor. In addition, water cooling creates effective heat dissipation, hence maintaining low temperatures at these locations.

(ii) Positions 2 and 6 – the interfacial contact resistance between electrode and workpiece interface, $R_{E\text{-}W}$, the magnitude of which depends on the surface condition of the electrode and workpiece, the size of the electrode face and the electrode force. A relatively high resistance is expected at these regions, due to imperfect contact between the conforming surfaces. However, it is generally presumed that the contact resistance should be lower than that at the faying surface

(point 4), because softer copper electrodes promote better surface contact with the workpieces [96]. In addition, other non-electrically conducting asperities and films present at the surface can also provide additional heat conduction routes across the interface [97]. Although a considerable amount of heat is generated at E-W interface, no fusion occurs there, due to rapid heat dissipation into the water-cooled electrodes.

(iii) Positions 3 and 5 – the resistance of the workpieces, R_W, which is proportional to its bulk resistivity and thickness, and inversely proportional to the cross-sectional area of the current path. For a fully dense material, R_W should be lower than $R_{E\text{-}W}$, which translates into lower temperatures at these locations.

(iv) Position 4 – the interfacial contact resistance at the faying surface, $R_{W\text{-}W}$, where resistance is usually very high compared with all other locations. Intense localised heating takes place here. Heat loss into the water-cooled electrodes is minimised, since large amounts of heat are also generated at the neighbouring locations 2 and 6, hence reducing the local temperature gradient. Heat loss at the faying surface occurs mainly by conduction into the surrounding workpieces, but at a much slower rate (§4.3.2.3). As current continues to flow, the rate of temperature increase at 4 will surpass that at positions 2 and 6, and eventually melting initiates when the melting temperature is reached [86]. Using a numerical model, Xu and Khan [98] showed that, for a pair of aluminium sheets, heat generated at the faying surface determines the overall nugget development.

Kaiser *et al* [99] studied the different stages of nugget growth and reported the occurrence of peripheral melting when using very high currents and short welding times; otherwise, radial nugget growth from the central axis was observed. Other experimental [100, 101] and numerical [89, 102, 103] studies indicated that weld nuggets initiate from the central axis and then expanding radially outwards. The site of nugget initiation is probably governed by the localised heat and electric current profiles produced under different welding conditions [104]. For normal (pore free) materials, it is generally observed that nugget growth rate and weld size are determined by the current and thickness of the workpieces. The rate of nugget growth can be increased by decreasing the contact area of electrodes, while the width of the weld nugget formed is primarily determined by electrode contact area [105].

4.3.2.2 Heat balance

Heat balance is attained when the depth of fusion in the two workpieces are the same, so that a symmetric weld is formed. Therefore, it occurs naturally when the two workpieces are of the same material, have similar thicknesses, and are welded using electrodes of the same alloy, shape and size. Various factors affecting heat balance include:

(i) Relative thermal and electrical conductivities of the materials to be joined;

(ii) Geometry of the weldment;

(iii) Thermal and electrical conductivities of the electrodes; and

(iv) Geometry of the electrodes (flat, truncated, hemispherical face etc).

Heat unbalance can occur during welding of workpieces with significantly different thermophysical properties, compositions or dimensions. However, this can be countered through careful part design, electrode material selection, and optimisation of welding current and time [86].

4.3.2.3 Heat dissipation

During welding, most of the heat loss takes place via conduction into adjacent parent materials (workpieces) and electrodes (Figure 4-7). While convection and radiation losses from workpiece surfaces may also occur, thermal analyses have shown that their effect on nugget formation is generally insignificant [106, 107].

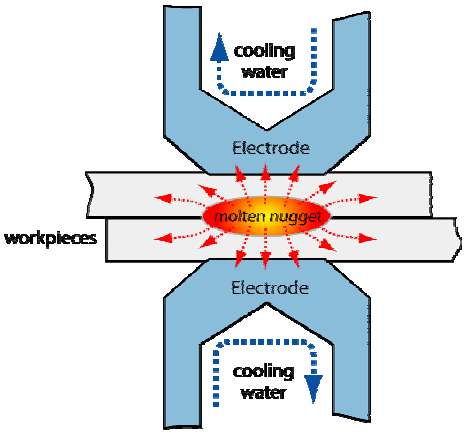

Figure 4-7. Primary modes of heat flow during RSW. Heat transfer from weld pool to (a) water-cooled copper alloy electrodes, and (b) surrounding base metals.

The rate of heat dissipation from the fusion zone varies during the welding process. Heat losses during the weld time are affected by the conductivities of the workpieces, weld time and the effectiveness of electrode water-cooling. Since the amount of heat generated is inversely

proportional to the electrical conductivity of the base material, its thermal conductivity and temperature gradient will determine the extent of heat dissipation. During the hold time, heat losses take place through the copper electrodes which act as heat sinks, ensuring rapid cooling of the molten nugget. During welding of thin sheets, a suitable rate of heat dissipation is necessary to prevent warpage. Heat is also dissipated into the surrounding base material, but this is reduced when a longer weld time is used, leading to a lower temperature gradient between the fusion zone and the neighbouring base metal [86].

4.4 Interfacial Contact Resistances

4.4.1 Electrical Contact Resistance

Electrical contact resistance has been extensively studied, in view of its importance for accurate simulation and monitoring of the initiation and growth of weld nuggets. Since the electrical contact resistance at the welding interface is time-dependent, the weld current changes throughout the welding process. Factors identified as affecting the magnitude of the contact resistance include the bulk material electrical resistivity, mechanical properties of the material at the faying surface, properties of any coatings on the surfaces, the pressure exerted at the interface, the average temperature of materials adjacent to the interface, the duration for which pressure and electricity is imposed, and the surface topography (i.e. surface roughness and flatness).

In RSW, two types of electrical contact resistances are involved, namely, static and dynamic contact resistances. In general, the static electrical resistance is associated with solid asperity metallic contact, in the absence of current flow, while dynamic contact resistance concerns molten metallic contact after the initiation of current flow.

4.4.1.1 Static contact resistance

Real surfaces in contact are never perfectly smooth and flat, but are composed of a large number of discrete contacting points, known as asperities (Figure 4-8). Initially, the conducting asperities for electrical contact are small in number and random in distribution. During the squeeze time, when the two workpieces are put under compressive loads, the faying surfaces in the region surrounding the contact interface will separate (Figure 4-5) due to elastic deformation [93, 108]. Hence, electrical contact is established only across the surface located directly between the electrodes. Since the number of surface asperities supporting the applied load increases with progressive yielding, the true contact area, which initially is only a small fraction of the apparent (macroscopic) contact area

increases to approach the apparent area [109, 110]. In addition, plastic deformation can also result in the rupture of any oxide film, or other contamination film, present on the surface, thus reducing the contact resistance. Crinon and Evans [111] showed that with symmetrical electrode pairs, the high contact resistance associated with oxide films is very resistant to damage by axial force. Instead, even a small degree of relative sliding at the faying surface is highly effective in breaking down oxide films, leading to a considerable drop in contact resistance.

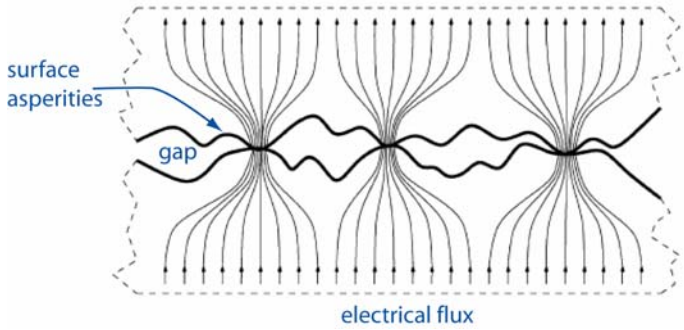

Figure 4-8. Surface asperities and constriction of electrical flow at the rough interface [112].

Thornton *et al* [97] found that the interfacial contact resistance at the electrode-to-workpiece interface, $R_{E\text{-}W}$, is not necessarily lower than the faying surface resistance, $R_{W\text{-}W}$, although the E-W interface has different metal combinations. They argued that the probability for the asperities to break through the contaminant and oxide films to establish metallic contact with the copper electrode, is essentially similar to what is taking place at the faying surface. However, evidently, the progression of melting and alloying of copper and workpiece material is prevented by effective electrode water-cooling (Figure 4-6).

Greenwood [113] derived an analytical expression to predict the magnitude of static electrical contact resistance between two clean and uncoated surfaces, R_S:

$$R_S = \left[\left(\rho_1 + \rho_2 \right) \left(\frac{1}{4na} + \frac{3\pi}{32nd} \right) \right] \tag{4.2}$$

where ρ_1 and ρ_2 are the bulk resistivities of the two contacting surfaces, n is the number of contacting asperities, a is the average radius of contacting asperities, and $2d$ is the average centre-to-centre distance between asperities. This equation only considers the constriction effects and neglects the contact resistance due to surface contaminants. In reality, the application of eqn.(4.2) is complicated, because information about the size, number and distribution of contacting asperities is difficult to obtain. Moreover, these parameters may be both load- and properties-dependent.

4.4.1.2 Dynamic contact resistance

Dynamic contact resistance is the sum of the bulk material resistance, faying surface contact resistance and electrode-workpiece (*E-W*) resistances, and its magnitude changes continuously throughout the RSW process. Wang and Wei [114] employed a numerical model to demonstrate that the dynamic resistance curve (R_D) can be divided into four distinct stages, as depicted in Figure 4-9. In stage I, the decrease in dynamic resistance at the faying surface and *E-W* interface is due to the breakdown of insulating layers or "fritting". During stage II, dynamic resistance increases, primarily from the increase in the bulk resistance of workpieces and interfacial contact resistances, as a result of temperature increase. Following that, the decrease of dynamic resistance in stage III results from competition between the increasing bulk resistance with temperature and the decreasing interfacial contact resistance at the faying surface caused by softening. In stage IV, the dynamic contact resistance decreases as molten nugget is initiated and mechanical collapse occurs. Experimental dynamic resistance curves similar to the one predicted have been reported by other investigators [97, 115, 116].

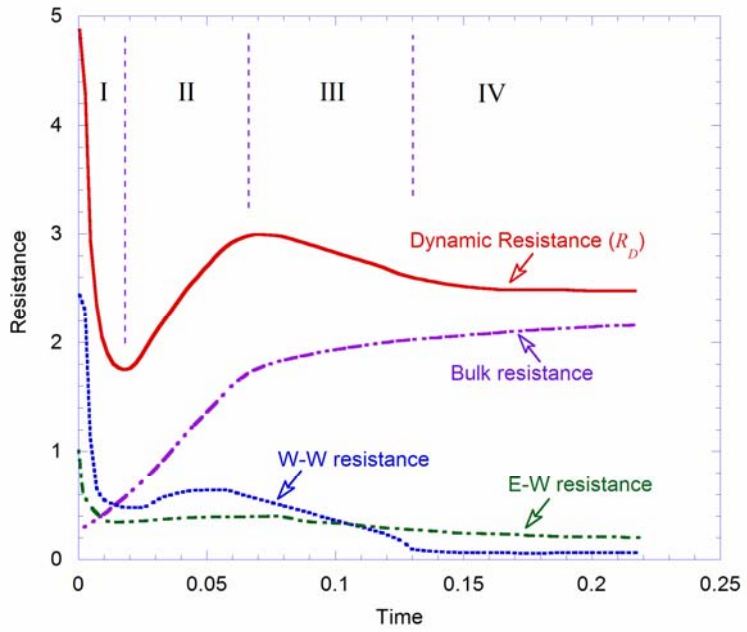

Figure 4-9. Predicted (dimensionless) dynamic resistance, bulk resistance and contact resistance at the faying surface and electrode-workpiece interface, expressed as a function of (dimensionless) time. The dimensionless parameters that served as inputs for Wang and Wei's model can be found in [114].

An extensive study of the dynamic resistance curve of uncoated and galvanised auto-body steels under different welding currents and electrode forces has been performed by Savage *et al* [115]. Different dynamic resistance curves were observed for different surface conditions and material combinations. However, in general, it was found that the initial rapid increase in resistance can be ascribed to the rapid rise of temperature, whereas the subsequent decrease in resistance is due to the

establishment of metal-to-metal contacts across a major portion of the faying surface. Expulsion was observed when high welding currents and long welding times were employed. This is attributed to the excessive growth of the molten nugget, so that it can no longer be contained by the surrounding base metal.

Thornton *et al* [97] showed that, essentially all the dynamic resistance change occurred within the first quarter cycle of the applied current, and the faying surface resistance is approximately 10 μΩ on completion of the weld cycle for aluminium and 30~40 μΩ for steel. The sheet samples were 50×25 mm, with an overall thickness of 25 mm. Furthermore, they reported the interesting finding that the electrode-to-workpiece contact resistance, $R_{E\text{-}W}$, can be higher or lower than that of the faying interface, $R_{W\text{-}W}$, but basically should be of the same order of magnitude. Similar observations were also made by Vogler and Sheppard [117], and by Lee and Nagel [118].

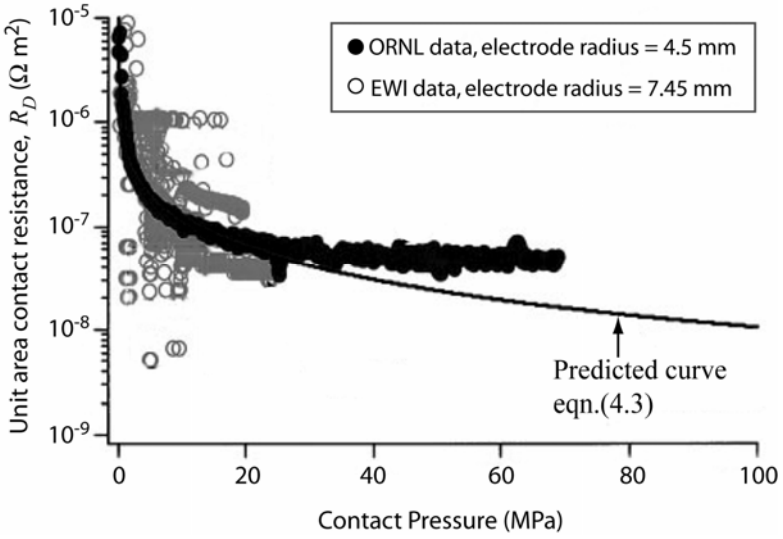

Figure 4-10. Unit area dynamic contact resistance predictions from eqn.(4.3), as a function of contact pressure. The experimental data were of DF140 steel samples, measured at Oak Ridge National Laboratory (ORNL) and Edison Welding Institute (EWI) [109].

More recently, Babu *et al* [109] presented a modified version of eqn.(4.2), tailored towards predicting the dynamic contact resistance, R_D, in RSW:

$$R_D = (\rho_1 + \rho_2)\left[\frac{1}{4}\left(\frac{\pi\sigma_Y}{\eta P}\right)^{1/2} + \frac{3\pi}{16\eta^{1/2}}\right] \tag{4.3}$$

where $\eta = n/A_C$ and A_C is the apparent contact area (face diameter of electrodes). This semi-empirical expression relates the contact resistance to the bulk resistivity (ρ), yield strength (σ_Y),

and the number density of contacting asperities (η). These vary with temperature (since σ_Y is temperature dependent) and pressure (P). Good correlation with experimental measurements was obtained at low contact pressures and temperatures (Figure 4-10), but discrepancies were observed at higher contact pressures, due to the fact that metal deformation other than yielding (such as creep, as a result of localised heating at contacting asperities) is not accounted for in this model.

4.4.2 Thermal Contact Resistance

As in the case of current, two surfaces in contact are never in perfect thermal contact (due to asperities), so heat transfer takes place via solid conduction through a limited number of actual contact points, and by gas conduction and radiation across the gaps (Figure 4-11). Due to imperfect contact, a temperature drop (ΔT) is generated across the interface.

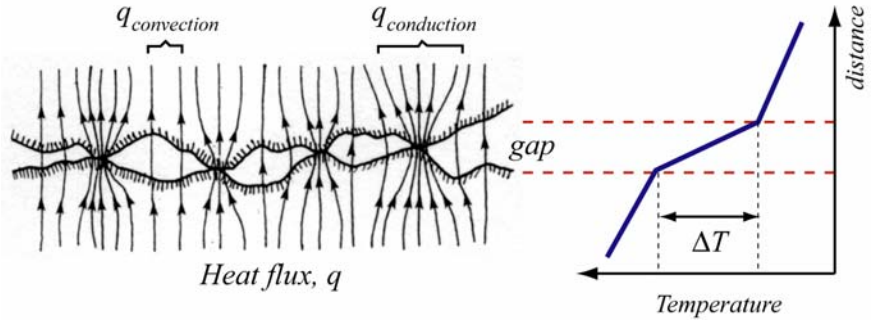

Figure 4-11. Temperature drop across an interface due to thermal contact resistance (after [119]).

Thermal contact resistance, R_{tc} ($m^2\,K\,W^{-1}$), is defined as the ratio of the temperature drop, ΔT, across an interface to the average heat flux, q:

$$R_{tc} = \frac{\Delta T}{q} \tag{4.4}$$

However, some studies reported are expressed in terms of thermal contact conductance, σ_{tcc} ($W\,m^{-2}\,K^{-1}$), which is simply the reciprocal of thermal contact resistance ($1/R_{tc}$). In general, the magnitude of the thermal contact resistance is dependent on the mechanical and thermophysical properties of the contacting materials, the characteristics of the contacting surfaces (roughness, flatness, cleanliness etc), the presence of an interstitial media (gas or fluid), the applied force and the overall environment of the junction [119]. For two flat interfaces, one way to reduce thermal contact resistance is by filling the interstitial gaps with soft metals (indium, tin, lead, silver etc) or silicone-based thermal greases, which have thermal conductivities orders of magnitude higher than air [44].

Loulou and Bardon [120] investigated the transient thermal contact conductance between the copper electrode and steel workpiece (E-W) interface during RSW. Figure 4-12 shows the transient contact conductance observed during the (from 0.7 to 0.9 s) 0.2 seconds weld time. Three different stages can be identified. The first region corresponds to a dry pressed contact established under electrode compressive forces (up to 0.71 s). The second stage shows a significant increase in contact conductance up to approximately half of weld time (0.8 s). This is attributed to the increasing metal-to-metal contact area, as the temperature of the workpieces rises and the weld zone start to develop. The thermal conductance later stabilised at a relatively high value of about 200~300 kW m^2K. The final stage showed a slight decrease in contact conductance, as a result of metal shrinkage due to weld nugget solidification.

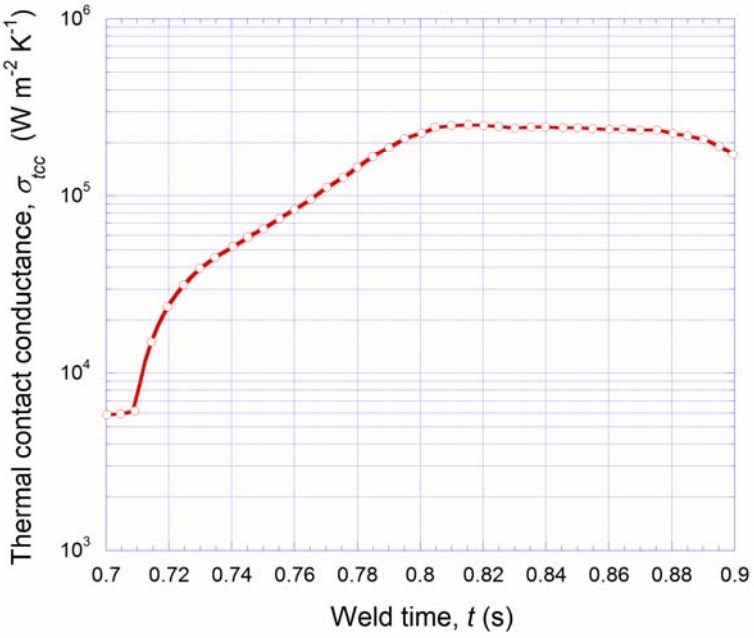

Figure 4-12. Thermal contact conductance measured at the electrode-to-workpiece (E-W) interface during weld time (0.2 s), using electrode force of 2.3 kN (~46 MPa) and welding current of 10 kA [120].

More recently, Le Meur *et al* [121] measured the thermal contact resistance of copper electrode to steel sheet interface, as a function of electrode force (average pressure) and current intensity. As shown in Figure 4-13(a), the contact conductance (reciprocal of resistance) seems to decrease with both pressure and current. However, since all measurements were conducted at pressure ratings ranging from 70-130 MPa (above 2 kN), it is thought that the measured conductances will be independent of electrode force. The apparent decrease in contact conductance with increasing current intensity can be explained, partly by the difference in dilatation between the sheet regions and electrode faces (Figure 4-13(b)). However, at higher current levels, the already dilated regions have a reduced electrode-to-workpiece nominal contact area, hence any contribution towards any

subsequent decrease will be small. This phenomenon is true as long as the hardness of the workpiece exceeds that of the electrode.

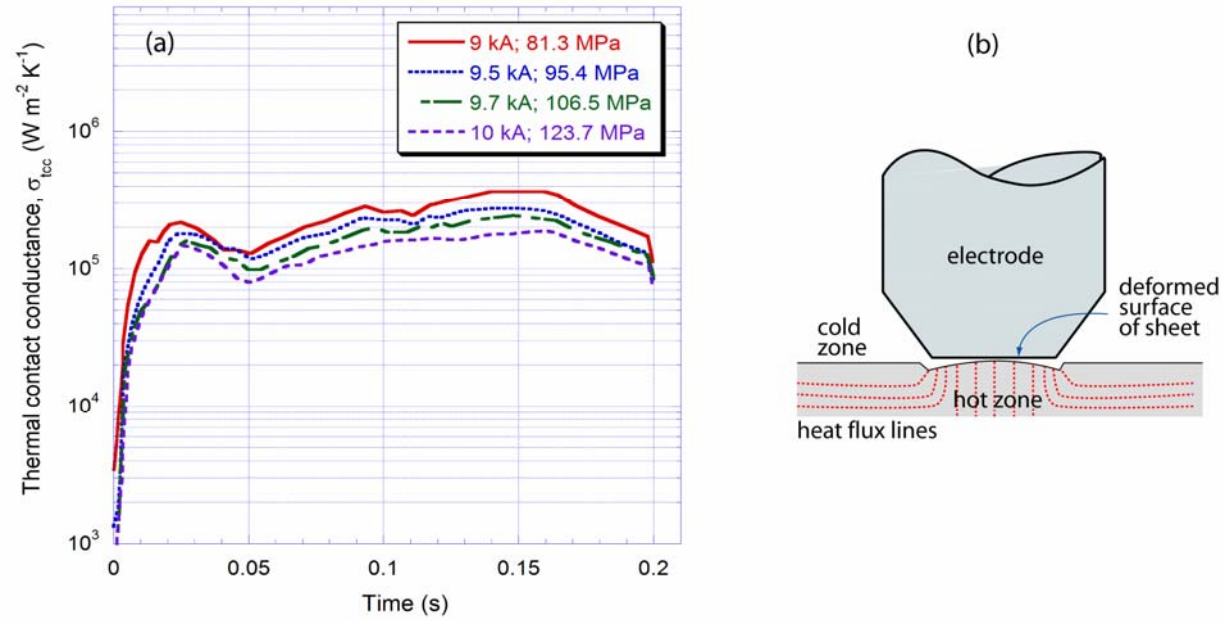

Figure 4-13. (a) Variation of thermal contact conductance with time, electrode average pressure and weld current (N.B. The original plot is presented as thermal contact resistance versus time), (b) schematic representation of dilatation effect on electrode face and workpiece (after [121]).

4.5 Sensitivity to Material Properties

Various material properties can have an impact on resistance weldability. During the welding cycle, the thermal conductivity and electrical resistivity of the parent material are the primary factors that govern heat generation and heat loss. In fact, electrical resistivity is one of the most vital properties. Since the amount of heat generated is directly proportional to resistance (§4.3.2.1), metals of high resistivity are generally more weldable than those of low resistivity. Furthermore, metals of high thermal conductivity (usually associated with low electrical resistivity) are difficult to weld, because greater power input is required to compensate for increasing heat loss. For a material with high thermal and electrical conductivities, such as aluminium, the welding current needed may be up to four times of an equivalent thickness of steel, in order to generate sufficient heat and compensate for heat losses [122].

Materials with high coefficient of thermal expansion (CTE) are less weldable, since warping and buckling of the welded assemblies can easily occur, resulting in weld cracking. To overcome the high thermal expansion and contraction, fast electrode follow-up (post-weld forge) is required during nugget solidification [122].

Resistance weldability is also affected by the hardness and strength of the materials to be joined. Metals that retain high strength and hardness at elevated temperatures (e.g. high strength steels) require higher electrode force to ensure good current flow across workpieces. Sufficient forging must also be applied on the molten weld to avoid expulsion (splash) [123]. In contrast, soft metals (e.g. aluminium) with lower stiffnesses are less resistant to electrode indentation, and the applied force must be carefully controlled to prevent surface damage.

The oxide forming characteristics of the parent material surface may also affect weldability [111, 124]. Thick oxide films, with high electrical resistivity, can influence heat generation during the welding process by preventing electrical flow through the workpieces. Conversely, if the oxide film is extremely thin, it may be insignificant to the surface contact resistance. For oxide film thickness within these two extremes, electrical current may flow, but localised heating at the faying surface may produce inconsistent weld strength.

Weldability also depends on the metallurgical characteristics of the workpieces. For the case of stainless steels, they can be divided into three groups, namely, ferritic, martensitic and austenitic types. Their hardenability is determined by the carbon, chromium, and nickel contents. Both the ferritic (non-hardenable) and martensitic (hardenable) types require special precautions to attain good weldability. The ferritic type has poor weldability, since the weld zone tends to have a coarse-grained structure and low ductility, which is not suitable when a ductile weld is required. For martensitic type, a post-weld heat treatment can be employed to improve weld ductility, but this treatment is ineffective for the ferritic type. Austenitic stainless steels are susceptible to carbide precipitation if heated for an appreciable time within 430 to 880°C, but this can be avoided by using shorter weld times [86].

4.6 Resistance Weldability of Thin Sandwich Materials

4.6.1 Lightweight stainless steel sandwich sheets

The magnitude of the through-thickness electrical resistivity (§3.3) has a direct influence on the resistance welding characteristics of sandwich sheets [2, 26]. The flocked sheet cannot be welded directly, due to its high core resistivity [26]. A weld can only be obtained using a shunt (Figure 4-14). The shunt creates a bypass circuit, allowing current to flow through the faceplates without passing through the core, hence leading to heating and softening of the adhesive at the faceplate-to-core interface. This causes reduction in the core resistance which subsequently allows a direct current to flow through the core, generating sufficient heat to initiate melting.

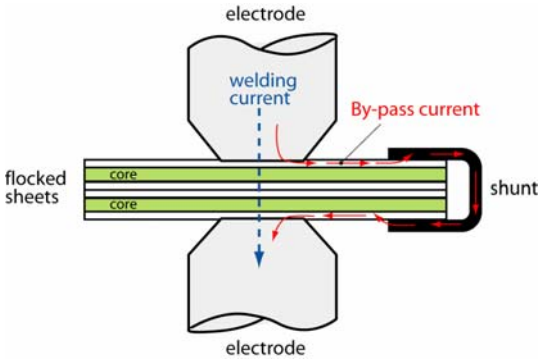

Figure 4-14. Resistance spot welding of a pair of flocked and glued (FG) sandwich sheets by employing a shunt, which acts as a bypass circuit.

The voltage and current history plots (Figure 4-15) indicate that breakthrough and high current occurred only near the end of the 10-cycle weld time. Furthermore, the irregular shape of the current waveform at the last cycle indicates intermittent current flow.

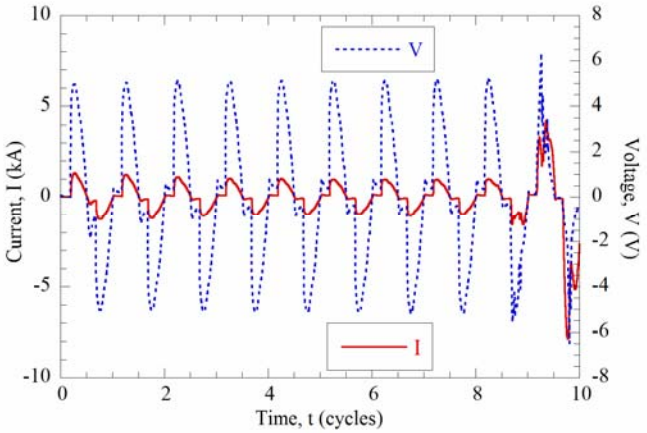

Figure 4-15. Voltage and current versus time plots obtained from welding of a pair of flocked sheets, with a weld time of 10 cycles (0.2 s) [26].

Although welding was possible using a shunt, the weld nugget produced was consistently of poor quality and mechanically inferior (Figure 4-16). The faceplates are susceptible to local burn-through due to the high shunt current, resulting in cracking and melt expulsion. The blow holes formed within the weld nugget are probably caused by vaporisation of the adhesive. Similar problems have also been encountered in the resistance welding of vibration damping steel sheets (VDSS) [125].

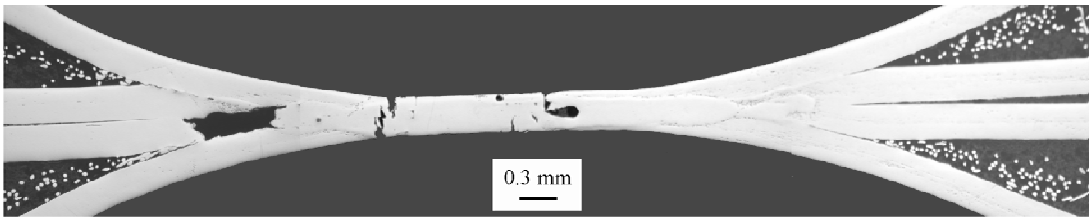

Figure 4-16. Optical micrograph showing the transverse cross-section of a spot weld for a pair of flocked and glued (FG) sheets [26].

The brazed in-plane mesh sheet, due to its relatively low through-thickness electrical resistivity, is more readily weldable. The voltage and current history plots in Figure 4-17 show good current flowing through the core from the start of weld time. As shown in Figure 4-18, the weld nugget formed was of good quality, with some lateral flow of melted fibres. The inner faceplates still retained their integrity and outer faceplates remained unmelted.

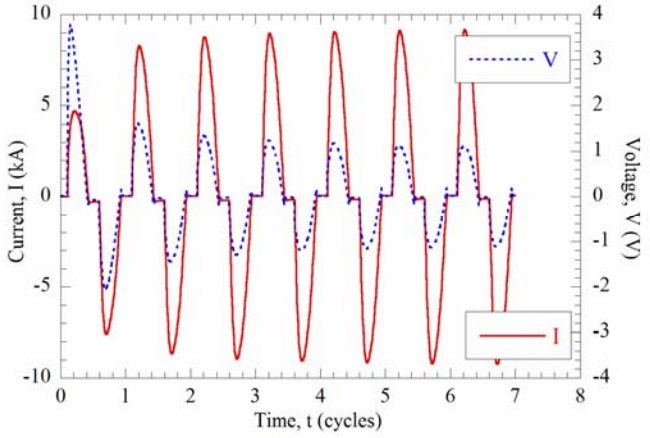

Figure 4-17. Voltage and current versus time plots obtained from welding of a pair of brazed in-plane mesh sheets, with a weld time of 7 cycles (0.14 s) [26].

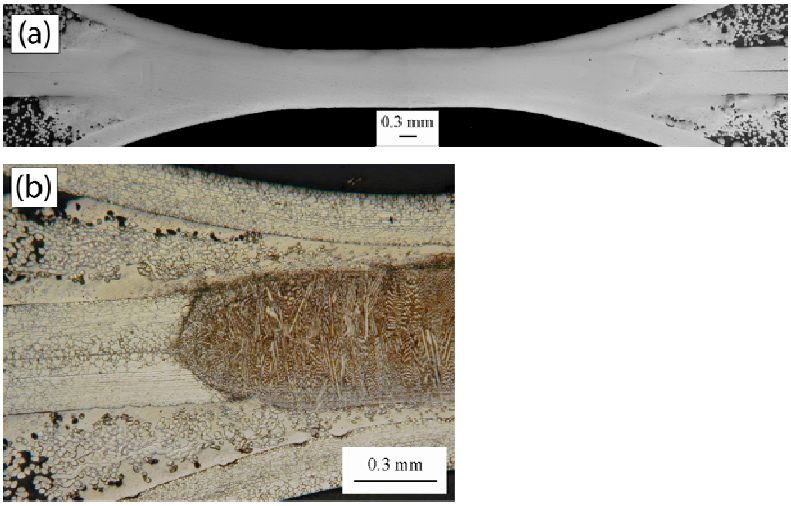

Figure 4-18. Optical micrographs depicting the transverse cross-sections of a welded pair of brazed long in-plane mesh sheets. (a) An as-polished complete section, and (b) higher magnification view of an etched weld nugget [26].

4.6.2 Vibration damping steel sheets (VDSS)

A typical vibration damping steel sheet consists of a pair of cold-rolled steel faceplates (0.4~0.6 mm) and a synthetic resin core (50 μm). The conventional type of VDSS is not directly weldable, due to the high electrical resistivity of resin. As in the case of FG sandwich sheets (§4.6.1), they can be welded using a bypass circuit to induce electricity flow [12, 13, 126].

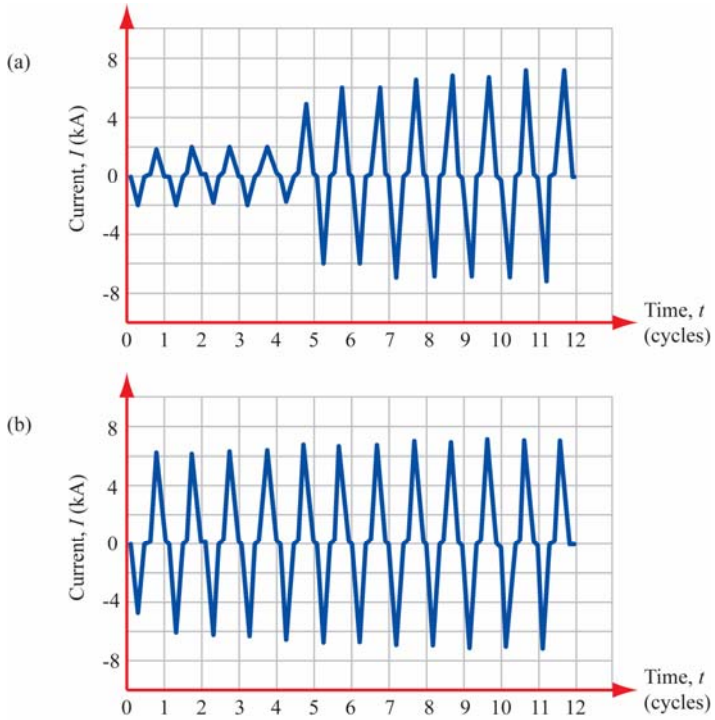

Figure 4-19. Comparison of typical welding current waveforms obtained from a pair of (a) conventional VDSS welded using a shunt and (b) conductive type VDSS which is directly welded. Note: 1 cycle = 0.02 s (after [126]).

However, since the bypass current is relatively low (Figure 4-19(a)), the resultant nugget has a reduced strength. The need to use a bypass circuit for each and every weld also makes welding a large quantity of points uneconomical. To overcome this problem, the non-conductive core has been replaced with a conductive type resin (with ~50 μm nickel powder). This conductive variant exhibited good resistance weldability under the same welding conditions as for that of normal steel sheets (Figure 4-19(b)). The weld nugget obtained (Figure 4-20) show good penetration into the faceplates, and has good mechanical properties [12, 13, 126]. It is interesting to see that the current waveform of the conventional VDSS exhibited some resemblance to the current response of flocked sheets without using a shunt (Figure 4-15), while the conductive VDSS is similar to that of brazed in-plane mesh sheets (Figure 4-17).

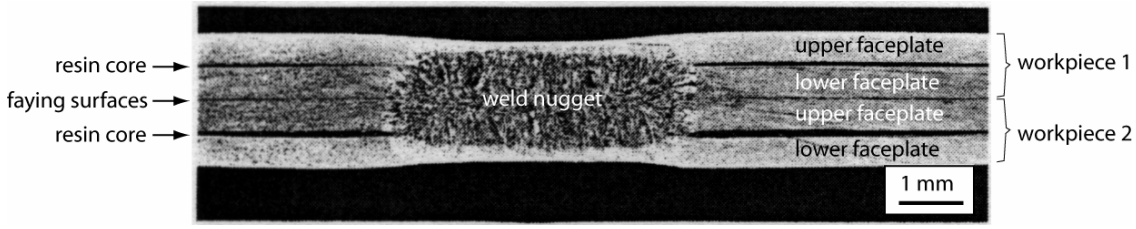

Figure 4-20. Cross-sectional view showing the weld nugget of conductive type vibration damping steel sheets (VDSS). Spot welding was performed at 8 kA for 200 ms and electrode force of 2.5 kN [126].

4.7 Numerical Modelling of RSW Process

In order to understand the relationships between different resistance welding parameters, it is essential to have a good knowledge of the changes taking place during the process. The mechanical, electrical, thermal and metallurgical interactions determine the stress state developed during squeeze, hold and weld cycles, electrical and thermal fields development, and weld nugget formation. This information is required for the development of an automation system equipped with a control mechanism, with sensors employed to monitor various welding parameters, such as electrode force, welding current, voltage and current responses, and nugget development during weld time [127, 128]. However, the existing experimental techniques for direct measurements of current and thermal profiles in the weld pool are inadequate, because of the high current involved (in the order of kA) and the relatively short weld time (typically less than 1 s) [129]. Due to these complications, numerical models of different levels of complexities have been developed, to provide insights into the welding process and to predict nugget development.

4.7.1 An Overview of RSW Numerical Models

4.7.1.1 One-dimensional models

Early numerical models developed to simulate RSW process had limited success, due to the limited computational capability available in the 1970s, which restrained the size and complexity of problems that could be solved. Most of these models were aimed at solving heat transfer problems, some neglecting interfacial contact resistances, and almost all incorporated little or no mechanical simulation.

In 1967, Rice and Funk [96] proposed a 1-D multilayer heat transfer model using the finite-difference (FD) method, capable of predicting the temperature profile in the workpieces. The model incorporated temperature-dependent material properties, heat generation from Joule heating and

energy generated at the interfaces, but excluded latent heat of fusion. The results obtained were limited to certain material types and sample dimensions.

Gould [130] (1987) formulated a 1-D model to predict weld nugget formation. Additional factors such as electrode geometry and latent heat of fusion were taken into account. The electrical contact resistance was assumed to vary linearly with temperature, and became zero at the melting point. Despite taking these into account, discrepancies were observed between predictions and experimental data for thicker steel sheets. Since the model did not incorporate the effects of radial heat transfer, it could not correctly predict the heating at the faying surfaces.

4.7.1.2 Two- and three-dimensional models

Greenwood [107] (1961) presented one of the first 2-D axisymmetric heat conduction models, solved using finite-difference method to simulate RSW process. It included internal Joule heating, but did not account for interfacial contact resistance and temperature-dependent material properties. Despite these shortcomings, some important results were obtained. Maximum temperatures were found to be located at the periphery of electrode-to-workpiece (E-W) interface at an early stage of the weld cycle. However, at longer times, the temperature distribution resembled the shape of an elliptical nugget and the maximum temperature shifted to the centre of the weld. Following that, Bentley *et al* [131] (1963) developed a metallographic technique to measure temperature distribution at various weld times and compared it with Greenwood's model [107]. Their experiments indicated that contact resistance played a major role during the initial stages of weld formation, but became less significant during subsequent stages. Since the model did not consider contact resistance effects, it was unable to correctly predict the temperature distribution during these early stages.

One step further was taken by Nied [93] (1984) and Tsai *et al* [132] (1992), who developed finite-element (FE) models that took into account mechanical behaviour and transient thermal responses (Figure 4-21). Surface effects at E-W and W-W interfaces were modelled using surface elements with a thickness equivalent to a typical oxide layer, which is about 50 μm. These elements were used to simulate interfacial electrical and thermal resistances, and to transfer compressive forces across the contacting interfaces. However, changes in contact resistances were not considered. Numerical predictions show stress concentration at the periphery of the truncated cone electrode, at the start of weld cycle. The weld nugget was initiated as a toroid (ring-like nugget) about the electrode axis, gradually expanding inwards and outwards during subsequent cycles, and eventually coalesced to

form a penny-shaped nugget. Tsai's predictions were also shown to exhibit good qualitative agreement with experimental data [132].

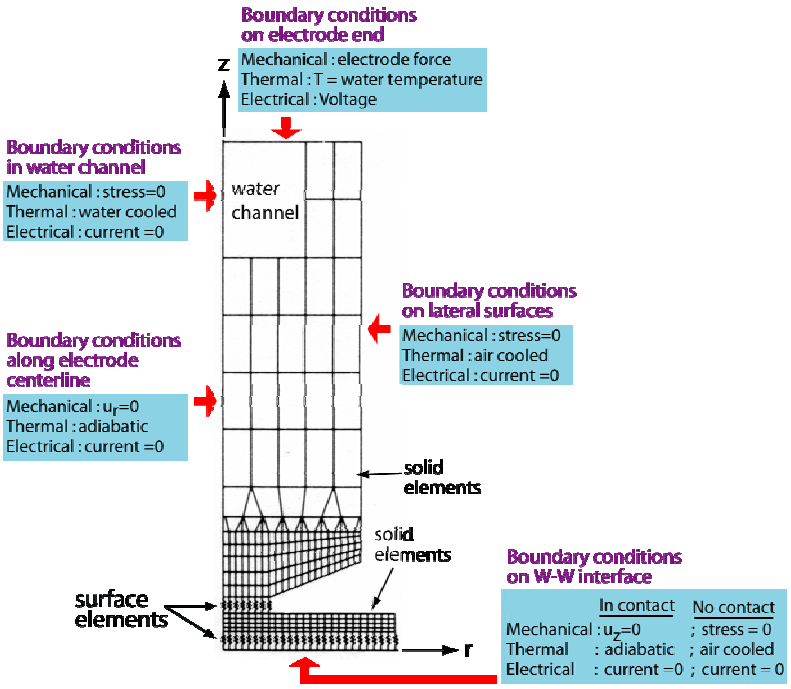

Figure 4-21. A 2-D axisymmetric finite-element model proposed by Nied [93], depicting the different element types and boundary conditions for mechanical and thermal-electrical analysis. (Note: u_r and u_z are radial and axial displacements, respectively.)

Two-dimensional axisymmetric heat transfer models based on finite-difference methods have been proposed by several investigators. Cho and Cho's model [133] (1989) incorporated the transient thermo-electrical interaction at the faying surface and its effects on internal heat generation. The model of Han *et al* [134] (1989) expressed the contact resistance at the faying surface as a function of electrode force. Both were reported to show good correlation in terms of temperature distribution and nugget size. Wei and Ho [105] (1990) formulated a transient thermo-electric model to study nugget growth for different weld currents, electrode face geometry, and workpiece thickness ratios. They emphasised the importance of considering radial heat losses for longer weld times and at higher weld currents. The nugget growth rate was found to increase with increasing weld current and workpiece thickness, or with decreasing electrode contact area. However, none of the finite-difference models found in the literature incorporate mechanical responses.

Later, Browne *et al* [135] (1995) formulated an integrated thermal-electrical-mechanical model for RSW of aluminium alloys, using domed (hemispherical face) electrodes. The mechanical analysis simulated elastic-plastic deformation and was solved using the finite-element method, while the thermo-electrical analysis was solved using the finite-difference method. The original model has also

being extended to incorporate the effect of shunts and expulsion at the faying surfaces [136]. Other finite-element models that consider thermal-electrical-mechanical interactions were developed by Feng *et al* [89] (1998), Khan *et al* [90, 137] (1999, 2000), Gupta and De [138] (2002), and Long and Khanna [139] (2003). These models can predict most of the RSW responses, which include electrode contact area, stress distribution, nugget diameter, depth of penetration, rate of heating and cooling etc.

All the models discussed so far do not account for the transport of mass and momentum in the mushy zone, and hence are unable to predict convection effects in the molten nugget. To investigate the importance of convection, Wei and Yeh [103] (1991) employed a continuum model accounting for momentum, heat and species transports in a binary solid-liquid phase change system, and found that convection in the weld nugget is in fact very small. The maximum velocity is predicted to be less than 5 mm s^{-1}, even at high welding currents (> 8 kA). Using an incrementally-coupled thermal-electrical-mechanical model, Khan *et al* [90] also found that convection effects in the weld pool are insignificant, with maximum liquid (aluminium) velocity of about 0.2 mm s^{-1}.

One of the most comprehensive RSW models published to date was developed by Khan *et al* [90] (2000), featuring a thorough heat transfer analysis, accounting for convection in the molten pool, electrical field analysis, thermoelastic-plastic deformation, temperature- and pressure-dependent electrical interfacial contact resistance, phase changes, and temperature-dependent material properties. A finite-element commercial code (ABAQUS ver.5.8) was used for solid mechanics modelling, while a control-volume based finite-difference code was employed for coupled thermo-electrical analysis. These two analyses were then incrementally-coupled. The thermo-mechanical analysis solves for the stress field developed, as the result of electrode force and changing material properties. Using this stress field, the contact areas at E-W and W-W interfaces were determined, and subsequently used to calculate the magnitude of electrical contact resistance. The value of thermal contact conductance was assumed constant. In their formulation, the contact resistances were treated as artificial interface elements and assigned reasonable material properties, to simulate a volumetric heat source. The model was used to study the effect of electrode geometry (truncated cone taper angle and face diameter) and applied pressure on nugget growth. The nugget growth was shown to be insensitive to the taper angle (within 20° to 40°), but largely determined by the contact area at the faying surface, which depends on face diameter and applied force. A similar incrementally-coupled model was reported by Sun and Dong [102] (2000), except both mechanical and thermo-electrical analyses were solved using the finite-element method. Both models had been validated by the corresponding authors, using experimental data acquired from RSW of aluminium alloys.

Despite the fact that, the state of the art RSW numerical models are capable of predicting many of the intricate interactions and phenomena involved, these models were formulated primarily for monolithic steel and aluminium sheets. Little or no work has been done in simulating the resistance welding of metallic sandwich sheets incorporating a fibrous and/or highly porous core. In addition, porous materials are well known to exhibit high thermal and electrical resistances (Chapter 3). In terms of mechanical deformation, more dramatic changes are expected during the process than occur with a dense sheet material. Evidently, these major differences must be incorporated into a successful RSW model for highly porous sandwich materials.

Chapter 5: Experimental Techniques

This chapter describes the experimental methods employed in manufacturing thin sandwich materials and subsequently investigating their properties. These include techniques for characterising the structures and chemical compositions of the fibrous cores. Techniques have also been developed for determining the thermal conductivity and electrical resistivity of sandwich materials. An industrial-scale resistance spot welding machine was used in studying the weldability of sandwich materials.

5.1 Sample Manufacture

5.1.1 Flocked and Glued Sheet (FG)

Flocked and glued (FG) sheets were provided by HSSA Sweden AB. These were manufactured by a flocking process, as described in §2.4.1.1. The as-received material had dimensions of 1 m × 1 m, and was cut into suitable specimens for testing using snips and a low-speed diamond saw.

5.1.2 Short Fibre 3-D Array Sheet (SF)

The short fibre 3-D array (SF) sheets were manufactured by a liquid phase sintering process, developed in Cambridge. The short 446 ferritic stainless steel fibres (100 μm diameter, 2 mm long) were produced by Fibretech Ltd., using a melt-overflow technique. A Ni-based braze alloy, BNi-1 {Ni-(13.0-15.0)Cr-(2.75-3.50)B-(4.0-5.0)Si-(4.0-5.0)Fe-(0.6-0.9)P-0.02S-0.05Al-0.05Ti-0.05Zr} (Brazing and Soldering Automation Ltd.), was used to join the fibre-to-fibre contact points, and to bond fibre ends onto 200 μm thick 316L faceplates (Advent Research Materials Ltd.).

A technique has been developed for distribution of braze powder onto fibres prior to sintering (Figure 5-1). The quantity of fibres required to produce a core with volume fraction of ~10% was determined by weighing. These were then carefully sieved onto the lower faceplate, placed in a graphite mould, to attain a uniform distribution and to prevent agglomeration. A coating of aerosol glue (3M Spray Mount® adhesive) was then sprayed onto the fibres, before distributing a measured amount of braze powder (10% of fibre weight) over the fibre array. The braze particles adhered to the fibres due to the presence of the glue. The upper faceplate was later added to complete the sandwich assembly. Sintering was performed in a tube furnace under 95% argon and 5% hydrogen atmosphere, at 1100 ºC, for a period of 5 minutes. The temperature of the sample was monitored via a K-type thermocouple inserted into the mould. To reduce surface deformation (wrinkling) at elevated temperature, a pair of 2 mm thick Al_2O_3 plates (Hybrid Laser Tech Ltd.) was used to

sandwich the 316L faceplates during sintering. By using this manufacturing route, sandwich sheets measuring up to 300 mm × 60 mm were produced.

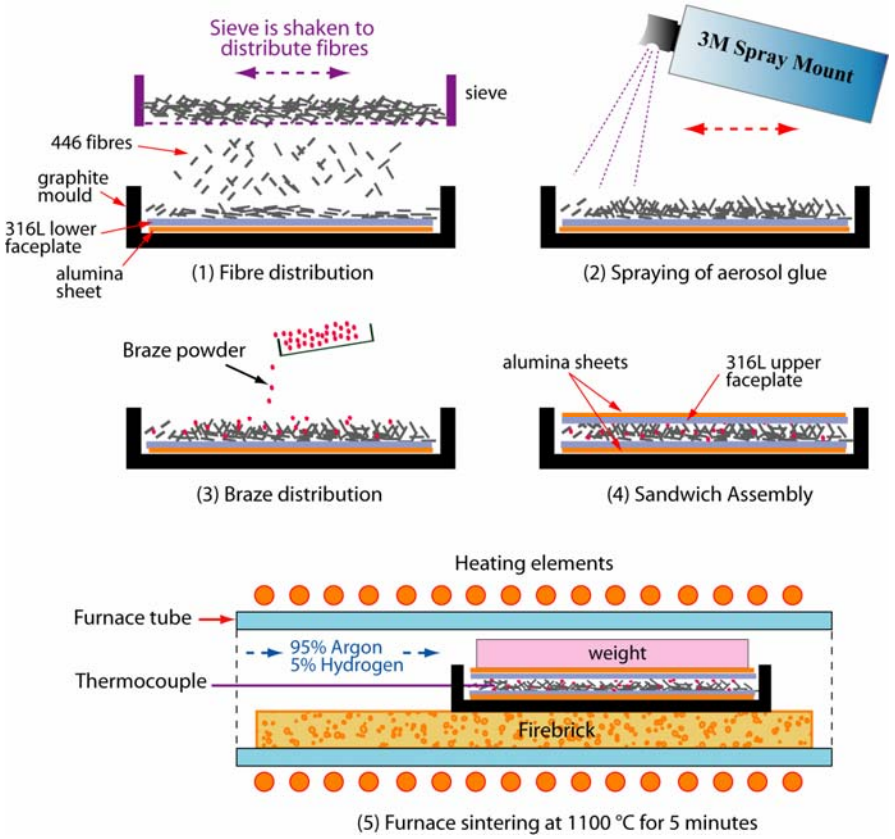

Figure 5-1. Schematic depiction of the stages involved in the production of short fibre 3-D array sandwich sheets (after [40]).

5.1.3 Long Fibre In-plane Mesh – Brazed (MB) or Glued (MG) Sheets

The long in-plane mesh brazed (MB) sheets were provided by Markaki and Clyne [38], and produced according to the description given in the literature (§2.4.1.2). A new variant of long in-plane mesh and glued (MG) sandwich sheet has also been manufactured. It incorporated a pre-sintered 446 stainless steel felt (~15 vol.%), made of 50 µm diameter and 10 mm long fibres produced via melt-overflow technique (Fibretech Ltd.). Faceplate-to-core bonding was achieved using a one-component heat-cured structural adhesive, containing di(benzothiazol-2-yl)disulphide and calcium oxide dispersed in oil (Bostik Findley Inc.). This adhesive has low viscosity and thin layers were applied onto the inner faces of faceplates coming into contact with the pre-sintered mesh. The assembled sandwich was then placed into an aluminium mould and curing was performed using a hydraulic hot press, at 200 °C for 20 minutes in air (Figure 5-2). A moderate pressure of 40 MPa was maintained throughout curing and the temperature of the sample was monitored using a K-type thermocouple.

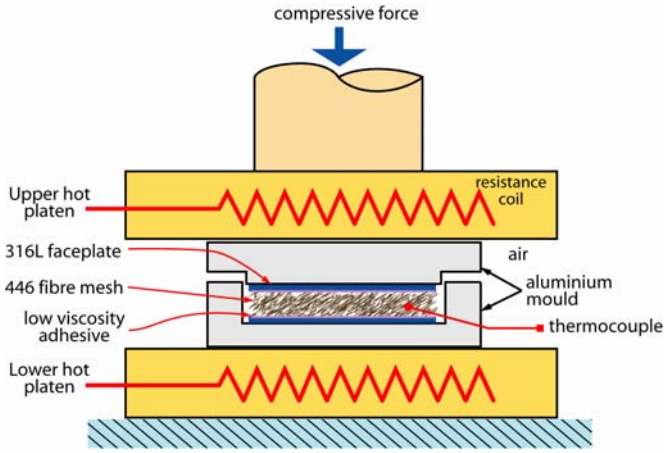

Figure 5-2. Schematic of the set-up used to cure the long in-plane mesh glued (MG) sandwich sheets.

5.2 Microstructural Characterisation

5.2.1 Optical Microscopy

Standard optical microscopy techniques were used to investigate the structures of the porous core and the weld nuggets. Samples were cut to the required dimensions using a low speed diamond saw. In order to avoid crushing and changes to the porous core structure, extra care was taken when securing the sample onto the saw fixture. The cut samples were then vacuum impregnated with a low viscosity Caldofix® (Struers) resin and hardener. To prepare the resin-hardener mixture, 10 parts (by weight) of resin were mixed with 3 parts of hardener, stirred for 3 minutes and then placed in a vacuum chamber for about 5 minutes to remove the entrapped air bubbles. The prepared mixture was carefully poured into a plastic mould containing the sectioned sample. Subsequently, the mould containing the sample and resin was put into a vacuum chamber and air was drawn out through a series of pumping cycles, forcing the resin to infiltrate the porous core. Curing of mounting resin was performed in a furnace, at 80 °C for 1 hour. The impregnated samples were successively ground using 400, 600, 800 and 1200 grit silicon carbide papers, followed by polishing using 6, 3 and 1 μm diamond pastes.

To reveal the microstructure of the weld nuggets, the polished samples were etched using Fry's Reagent (5 g $CuCl_2$, 40 ml HCl, 30 ml H_2O, 25 ml ethanol), for a period of 15 to 30 seconds, before washing in a stream of flowing water and subsequently ethanol. The prepared samples were examined and images were taken using a Carl Zeiss optical microscope, equipped with a Nikon 2-megapixel digital camera.

5.2.2 Scanning Electron Microscopy (SEM)

The JEOL-JSM5800 scanning electron microscope (SEM) was used when higher magnification images and greater depth of fields were necessary. This technique is useful in investigating the fibre and bond structures and faceplate-to-core interfaces. For sandwich materials which contain non-conducting adhesives, samples were gold sputtered to prevent charging-up in the SEM. Observation of topographical features was carried out using Secondary Electron (SE) imaging, at 15 to 20 kV. Besides functioning as an imaging tool, the SEM is also equipped with an Energy Dispersive X-ray Spectrometer (EDS), which was used to identify the chemical compositions of different stainless steel fibres.

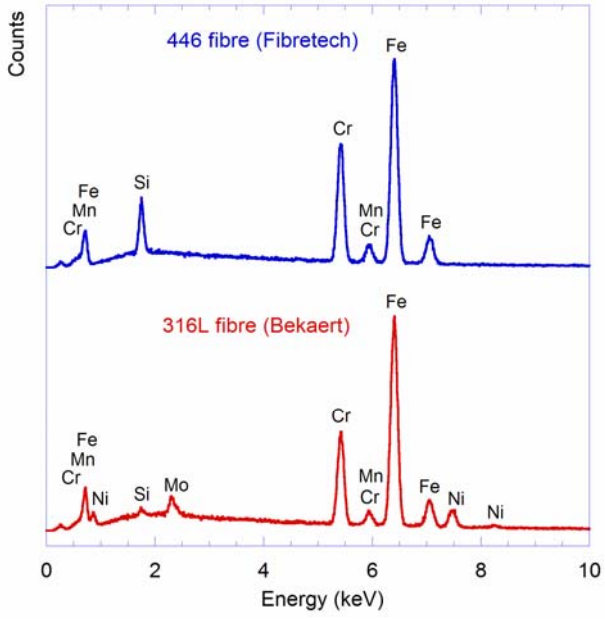

Figure 5-3. Typical EDS spectrums of 316L and 446 stainless steel fibres.

The EDS spectrums of 316L (Bekaert S.A.) and 446 (Fibretech Ltd.) stainless steel fibres are depicted in Figure 5-3. The element contents in weight percent (wt.%) are listed in Table 5-1. Clearly, 446 stainless steel fibres can be identified from the significantly higher chromium and silicon contents, which are important in increasing oxidation resistance and promoting a ferritic microstructure. Nickel and molybdenum are not added into 446 fibres, but form a major part in 316L fibres, to promote an austenitic microstructure.

Table 5-1. Chemical composition of 316L and 446 stainless steel fibres.

Element (wt %)	C*	Si	Mo	Cr	Mn	Ni	Fe
316L	≤0.03	0.33	2.33	16.58	0.62	9.98	Balance
446	≤0.20	3.04	-	23.19	0.73	-	Balance

*Reported by [140].

5.3 Computed X-ray micro-Tomography (μCT)

Computed X-ray micro-tomography technique had been used to investigate the three-dimensional structure of fibrous cores found within thin sandwich materials. It is a non-destructive method, based on the same principles as conventional medical CT-scanners. However, unlike medical CT-scanners, its spatial resolution is excellent down to a few microns. 3-D computer reconstructions, obtained from tomography scans were used to extract both qualitative and quantitative information of the core structure.

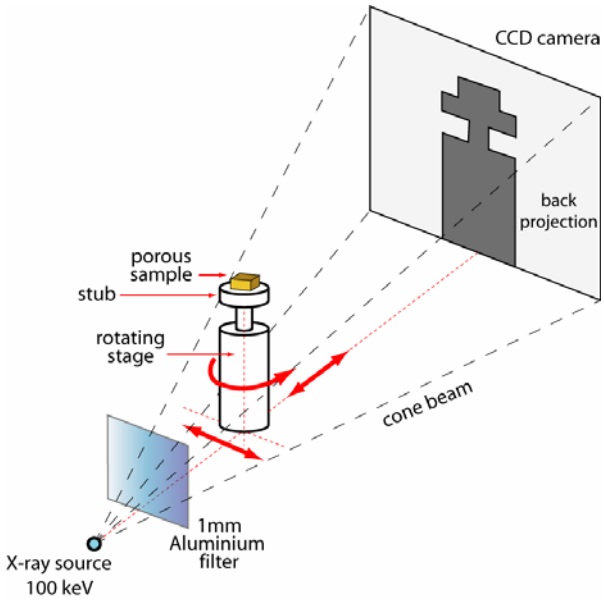

Figure 5-4. Schematic of experimental set-up for collecting two-dimensional radiographs of porous cores, using a cone-beam X-ray arrangement. The whole set-up resides within an enclosed X-ray compartment.

Tomography scans were performed using a high-resolution SkyScan-1072 desktop microtomograph (SkyScan, Belgium.), with a minimum spatial resolution of ~5 μm. The X-ray source was set at 100 keV (98 μA). A 1 mm thick aluminium filter was used to reduce beam hardening and to generate better contrast. The sample was a 5 mm × 5 mm square, mounted onto a stub, which was later secured onto the stage within the X-ray compartment (Figure 5-4). During scanning, the sample was rotated in steps of 0.45°, through 180°. At each position, an X-ray absorption radiograph was collected using a 1024 × 1024 × 12 bit CCD camera. The gain and exposure time were set at 1.0 and 6.5 seconds, respectively. Using these settings, the total scanning time was approximately 1 hour. The complete set of radiographs acquired at different angles was then used in 3-D reconstruction, employing the Feldkamp algorithm (back-projection algorithm) [141], with convolution and correction for cone-beam. These algorithms have been incorporated into the 'Cone-Beam Reconstruction' software developed by SkyScan. As for 3-D volume reconstruction and rendering, they were done using the 'AMIRA™' visualisation software.

Quantitative analyses were carried out on the tomographic scans, to characterise the spatial and orientation distribution of fibres. Spatial information such as 2-D areal fraction and 3-D fibre volume fraction, were acquired using SkyScan's 'CTAn+CTVol' software. In contrast, statistical data concerning fibre orientation, tortuosity, bond distribution and segment length distributions were obtained using the '3DMA' (3-D Medial Axis) code, written by Lindquist and co-workers [142-144]. The source code was compiled using the GNU compilers (gcc, g++ and g77), and executed under a Linux operating system. Further details are presented in §6.2.2.

5.4 Fibre Volume Fraction Measurements

The fibre volume fraction (f) of sintered fibre felts was determined via density measurement. To avoid the effects of inhomogeneity, large samples with cross-sections of at least 50 mm × 50 mm were used. For each variant of fibre felt, measurements were repeated on three different samples. The weights of the samples (m_f) were found using a balance. The volume of fibre contained within each volume of interest (V_{tot}) was then calculated from the known stainless steel density ($\rho_f(316) = 8000$ kg m^{-3} and $\rho_f(446) = 7500$ kg m^{-3} [145]). The fibre volume fraction is given by:

$$f = \frac{m_f}{\rho_f}\frac{1}{V_{tot}} \tag{5.1}$$

5.5 Thermal Conductivity Measurements

A new set-up, termed a steady-state bi-substrate technique, has been developed for measuring the through-thickness thermal conductivity of sheet materials, with thicknesses of the order of 1 mm. Figure 5-5 shows a schematic of the set-up. The sample, with cross section of 35 mm × 30 mm, was sandwiched between two Nimonic 80A alloy substrates (Special Metals Ltd.). These substrates acted as flux meters, each being instrumented with four K-type thermocouples (T_1 to T_8), inserted into holes at known heights, drilled to the centerline of each block. Since the (temperature-dependent) thermal conductivity of Nimonic 80A is well known over a wide temperature range (Figure 5-6), the heat flux through each substrate can be accurately determined.

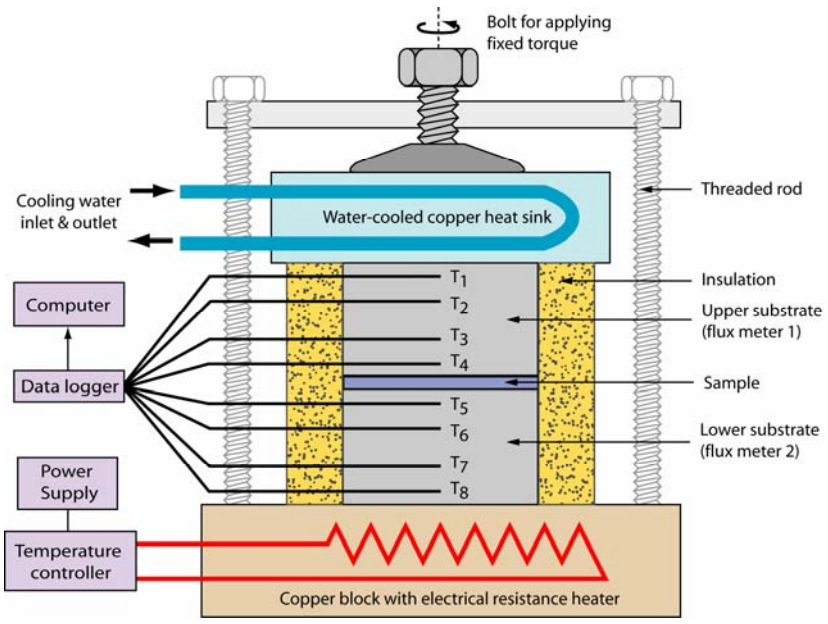

Figure 5-5. Schematic of the steady-state bi-substrate thermal conductivity set-up; T_1 to T_8 designate the eight thermocouples used for monitoring the temperature within the two substrates (flux meters).

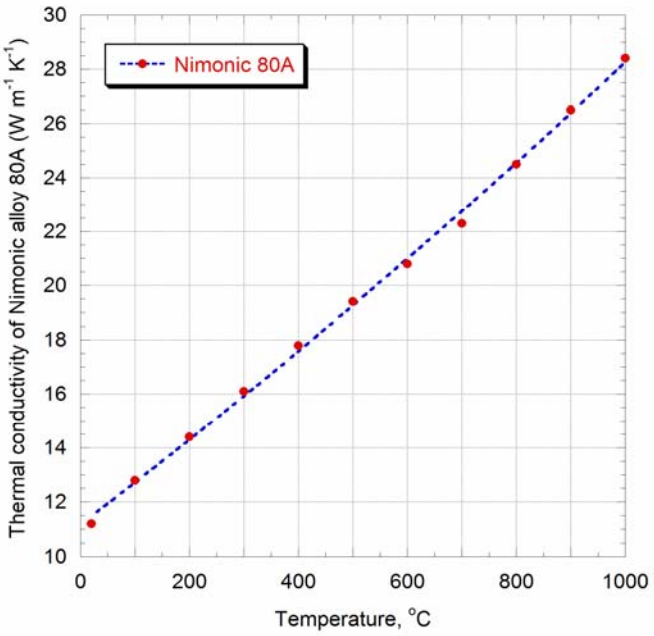

Figure 5-6. Temperature-dependent thermal conductivity of Nimonic 80A alloy [146].

The temperature gradients across the set-up were generated by heating the lower substrate with an electric resistance heater, while heat was continuously dissipated from the upper substrate via a water-cooled copper heat sink. To maintain consistent heat supply and removal, the heater power and cooling water flow rate were fixed throughout the experiment. The set-up was insulated with a low conductivity glass wool, to minimise lateral heat loss and ensure one-dimensional heat flow. A thin layer of silicone-based conductive compound (Servisol Silicone Grease, Ambersil Ltd.) was

carefully applied onto the sample and substrate interface, to eliminate air gaps and raise the interfacial thermal conductance. To ensure that the interface could be reproduced for different runs, a fixed torque of 2 N m was applied onto the test column by securing the bolt. It was established that this generated a force of 500 N, using a load cell set-up. This corresponds to a pressure of ~480 kPa (~5 bar).

During the experiment, the temperature readings (T_1 to T_8) were continuously monitored using a data logger. A steady-state was considered to have been established when the temperature fluctuations were within ±1 ºC, for more than 30 minutes. These readings were used in calculating the effective thermal conductivity (k_e) of the sample.

By assuming one-dimensional heat flow through the specimen and substrates, the mean heat flux, q, was found by taking into account the temperature-dependent thermal conductivity of the substrates, as given by eqns.(5.2) to (5.4):

$$q_{upper} = \frac{1}{6}\sum_{\substack{i=2 \\ i>j}}^{4}\sum_{j=1}^{3}\frac{T_i - T_j}{x_i - x_j}k_{substrate}\left(T_{ave}^{ij}\right), \quad T_{ave}^{ij} = \frac{T_i + T_j}{2} \tag{5.2}$$

$$q_{lower} = \frac{1}{6}\sum_{\substack{i=6 \\ i>j}}^{8}\sum_{j=5}^{7}\frac{T_i - T_j}{x_i - x_j}k_{substrate}\left(T_{ave}^{ij}\right), \quad T_{ave}^{ij} = \frac{T_i + T_j}{2} \tag{5.3}$$

where i and j designate locations of the thermocouples (Figure 5-5), while $k_{substrate}\left(T_{ave}^{ij}\right)$ is the temperature-dependent thermal conductivity of the substrate at an average temperature. The mean heat flux through the upper and lower substrates can then be written as:

$$q = \frac{1}{2}\left(q_{upper} + q_{lower}\right) \tag{5.4}$$

The measurement was presumed to satisfy one-dimensional heat flow when:

$$\frac{\left|q_{upper} - q_{lower}\right|}{q} \leq 10\% \tag{5.5}$$

For a well insulated set-up, the difference was typically less than 10%.

Figure 5-7 shows a schematic of the temperature profile established across the substrates and sample at steady-state. Assuming no lateral heat loss to the surrounding, the same heat flux (q) flows through the sample and interfaces (Figure 5-5), so we may write:

$$q = k_e \frac{\Delta T}{\Delta x} \tag{5.6}$$

$$q = h\Delta T_i \tag{5.7}$$

$$q = k_{true} \frac{\Delta T_s}{\Delta x} \tag{5.8}$$

where k_e is the effective thermal conductivity of sample, ΔT is the total temperature drop, Δx is the sample thickness, h is the interfacial thermal conductance (assumed to have the same magnitude for both interfaces), k_{true} is the actual sample thermal conductivity, while the subscripts i and s designate interface and sample, respectively.

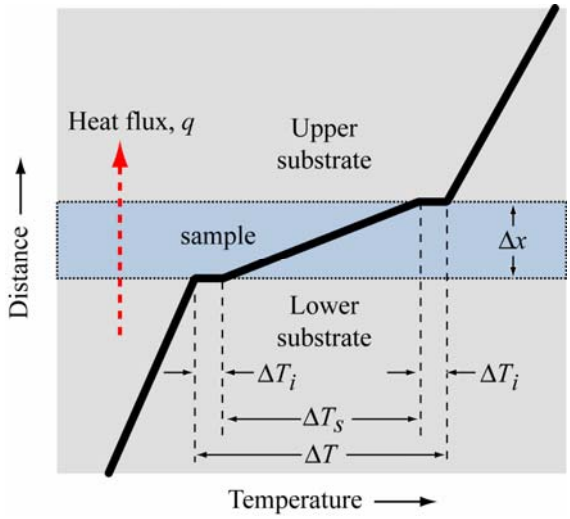

Figure 5-7. Schematic depicting the temperature drops across the substrates and sample.

The total temperature drop, ΔT, is made up of temperature drops across the sample and interface:

$$\Delta T = \Delta T_s + 2\Delta T_i \tag{5.9}$$

By substituting eqns.(5.7) and (5.8) into eqn.(5.9), and rearranging, we obtain the following linear equation:

$$\frac{\Delta T}{q} = \frac{\Delta x}{k_{true}} + \frac{2}{h} \tag{5.10}$$

Now, by plotting $\Delta T/q$ versus Δx, the slope and intercept are given by $1/k_{true}$ and $2/h$, respectively. Both the values of k_{true} and h can now be readily determined. It can be seen that, in order to obtain k_{true}, samples of different thicknesses (Δx) have to be tested.

This technique has been verified using a standard material of known thermal conductivity, i.e. fused silica (quartz glass) samples (Heraeus Quarglas, Germany). The manufacturer's material datasheet reports a thermal conductivity value of 1.46 W m^{-1} K^{-1} at 100 °C [147]. Samples with three different thicknesses, i.e. 0.567, 0.989 and 2.897 mm, were used. Polishing was performed on the as-received materials to ensure a consistent surface finish (~1 μm). Figure 5-8 shows the temperature versus distance plot for a silica sample with a thickness of 2.897 mm. The mean temperature of the sample was about 100 ºC and the total temperature drop (ΔT) across the sample was about 48 ºC. Similar profiles were observed for the thinner samples, but with smaller drops. Using eqns.(5.2) to (5.4), the mean heat flux was estimated as 26.36 kW m^{-2}. Subsequently, from eqn.(5.6), the effective thermal conductivity (k_e) was found to be 1.25 W m^{-1} K^{-1}.

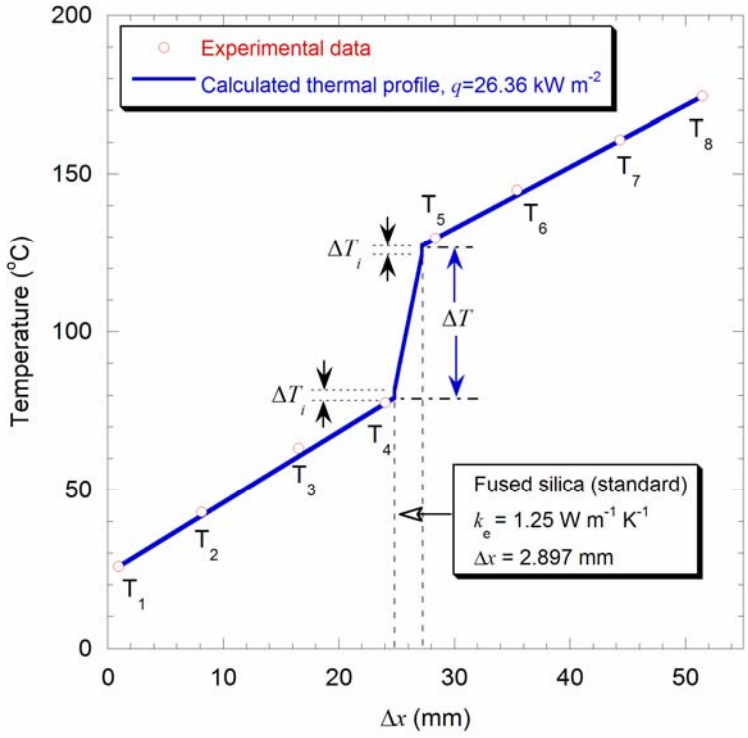

Figure 5-8. Temperature versus distance plot showing the temperature drop across a fused silica sample. The points (T_1 to T_8) are thermocouple measurements corresponding to locations depicted in Figure 5-5. The line is calculated using the average heat flux (q) and temperature-dependent thermal conductivities of Nimonic substrates (Figure 5-6).

Figure 5-9 shows experimental data for all the fused silica samples, along with the best linear fit, as given by eqn.(5.10). It can be seen that the data show relatively small scatter. The values of actual thermal conductivity (k_{true}) and interfacial thermal conductance (h) were found to be 1.54 W m^{-1} K^{-1} and 12.88 kW m^{-2} K^{-1}, respectively. Of course, k_{true} is higher than k_e, since temperature drops across the two interfaces ($2\Delta T_i$) have now been taken into account. The actual conductivity agrees well with the value quoted by the manufacturer [147]. Also, the interfacial contact conductance measured here

is of a similar order of magnitude to values reported elsewhere (for a similar surface finish and contact pressure) [44].

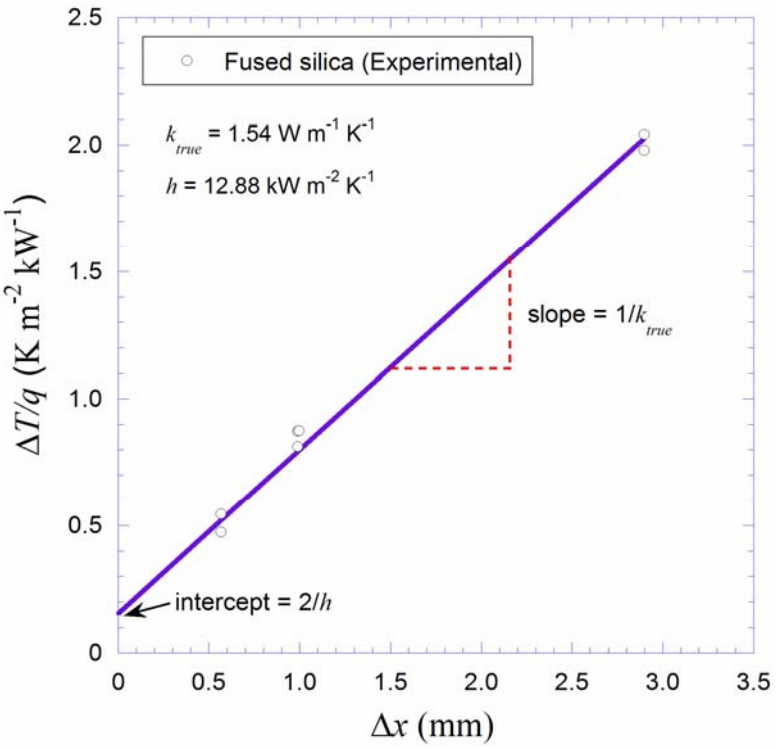

Figure 5-9. A plot of $\Delta T/q$ versus Δx for fused silica samples of three different thicknesses. The points are experimental data while the line is their best linear fit using eqn.(5.10). Conductive compound was applied at the interface and the mean temperature of the samples was about 100 ºC.

Unfortunately, this kind of treatment was not suitable for sandwich sheets and sintered fibre felts, since the samples were manufactured only at specific thicknesses. Changing the sandwich thickness may lead to a different core structure. So, for the case of sandwich materials, k_e was measured instead of k_{true}. However, for highly porous materials, the difference between the two should be small since the temperature drop expected at the contacting interfaces should be relatively small, compared with the overall temperature drop through the sample ($\Delta T \gg \Delta T_i$).

5.6 Electrical Resistivity Measurements

The effective electrical resistivity of sandwich sheets in the through-thickness and in-plane directions were measured using experimental set-ups as depicted in Figure 5-10. The fixture used for in-plane resistivity measurement has been previously used by Whitehouse *et al* [148]. The fixture for through-thickness measurement was specially constructed to accommodate sheet materials with thickness of the order of 1 mm. For through-thickness measurements, the sandwich sheets were cut into

15 mm × 10 mm rectangular coupons, while for in-plane measurements, samples measuring 80 mm × 10 mm were used.

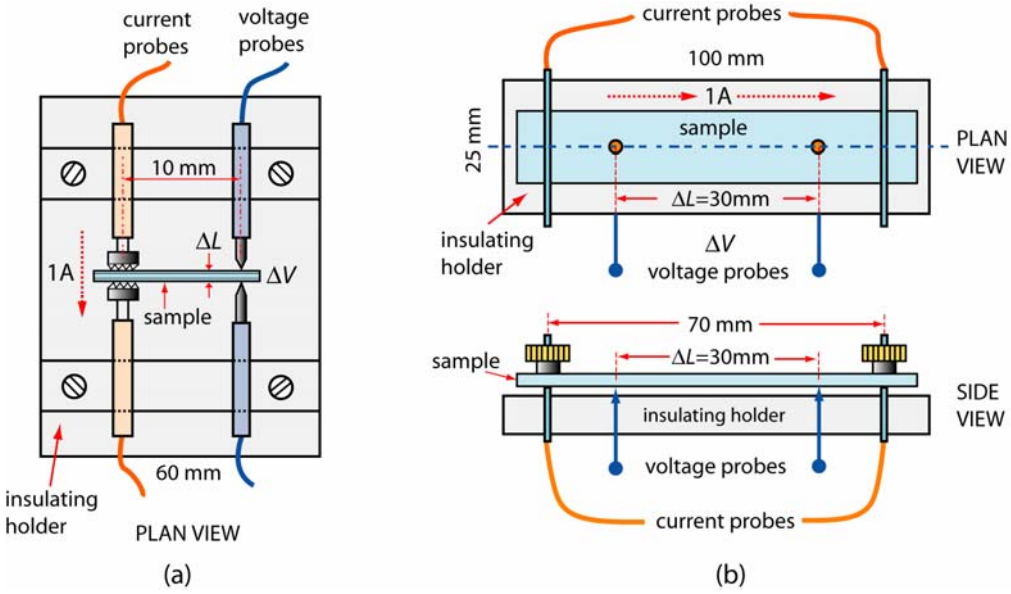

Figure 5-10. Schematic of the fixtures used in measuring the (a) through-thickness and (b) in-plane electrical resistivity of thin sandwich materials.

Both set-ups operate by passing a fixed current, I, through a specified distance of the sample, ΔL, while detecting the voltage drop, ΔV, through a pair of spring-loaded probes. Using Ohm's Law, the effective electrical resistivity, ρ_e, is given by:

$$\rho_e = \left(\frac{\Delta V}{I}\right)\left(\frac{A}{\Delta L}\right) \tag{5.11}$$

where A is the cross-sectional area perpendicular to the current flow.

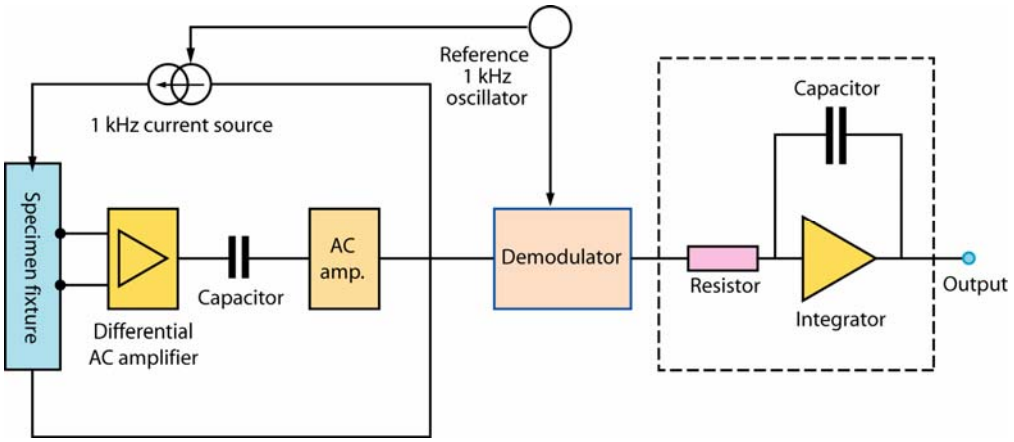

Figure 5-11. The alternating current circuit used in supplying modulated 1 A current and filtering noise.

An alternating current (AC) circuit, as shown in Figure 5-11, was used to supply a 1 A current, modulated at a fixed frequency of 1 kHz. In order to obtain reliable measurements, the potential drops attributed to other resistances in the sensing circuit must be eliminated. The direct current (DC) offset, generated by the drop in the mean voltage of the AC signal was removed by first passing the signal through an AC amplifier, followed by rectification via a demodulator. Subsequently, the rectified signal was passed through an integrator to remove noise, before being displayed as an output DC voltage, ΔV.

5.7 Compression Tests

To obtain the compressive stress-strain response of sandwich sheets in the through-thickness direction, uniaxial compression tests were performed using an ESH hydraulic-driven universal testing machine. The test coupons had dimensions of 15 mm × 15 mm, and the thickness of every individual sample was measured using a micrometer. All tests were carried out under a constant crosshead velocity of 1 mm min^{-1}. The behaviour of the porous core was assumed to be strain-rate independent. The compressive force was measured via a 10 kN load cell. Due to the small sample thickness (~1 mm), the crosshead displacement was found to be unsuitable in determining sample displacement. Therefore, displacement was obtained instead using a linear variable differential transformer (LVDT), attached to the compression platen. Force and displacement during compression were continuously monitored and recorded using LabVIEW data logging software (National Instruments). The samples with collapsed cores were later used for investigating the effects of core compression on effective thermal and electrical conductivities.

5.8 Resistance Spot Welding (RSW)

Resistance welding experiments were conducted at TWI, Great Abington (Cambridge). The RSW machine used consisted of a Martin welding gun, equipped with a Miyachi medium frequency (1000 Hz) inverter (DC power supply), as shown in Figure 5-12. The gun was fitted with ISO 5821, type-F (Cu-Cr-Zr) hemispherical electrodes with a dome radius of 8 mm (Figure 5-13).

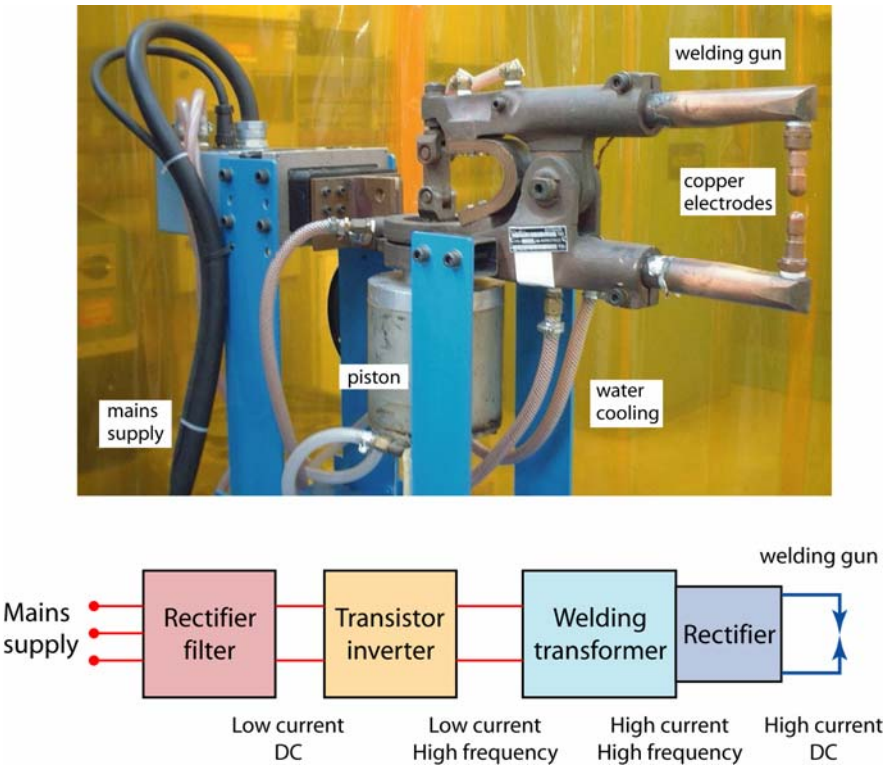

Figure 5-12. The resistance spot welding machine at TWI used for the experiments and its corresponding schematic.

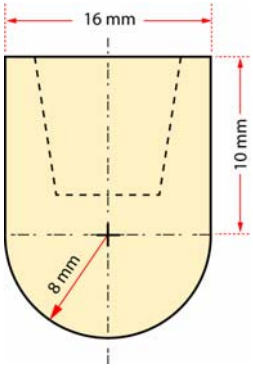

Figure 5-13. Schematic of type-F hemispherical face electrode (ISO 5821) used in the welding experiments of sandwich sheets.

The sandwich sheets were cut into 30 mm × 20 mm coupons and single welds were made on pairs of samples stacked on top of each other. The electrode force was set at 2.5 kN for all welds, while the

input current was varied from 4 to 6 kA (RMS[†]). Each weld cycle (Figure 5-14) was initiated with 1800 ms squeeze time, followed by 200 ms weld time and ended with 200 ms hold time. In order to study the cold collapse behaviour of the porous core, the same weld cycle was used, but without the passage of current during weld time. The voltage and current histories throughout weld time were continuously monitored and recorded using a Kontron transient recorder.

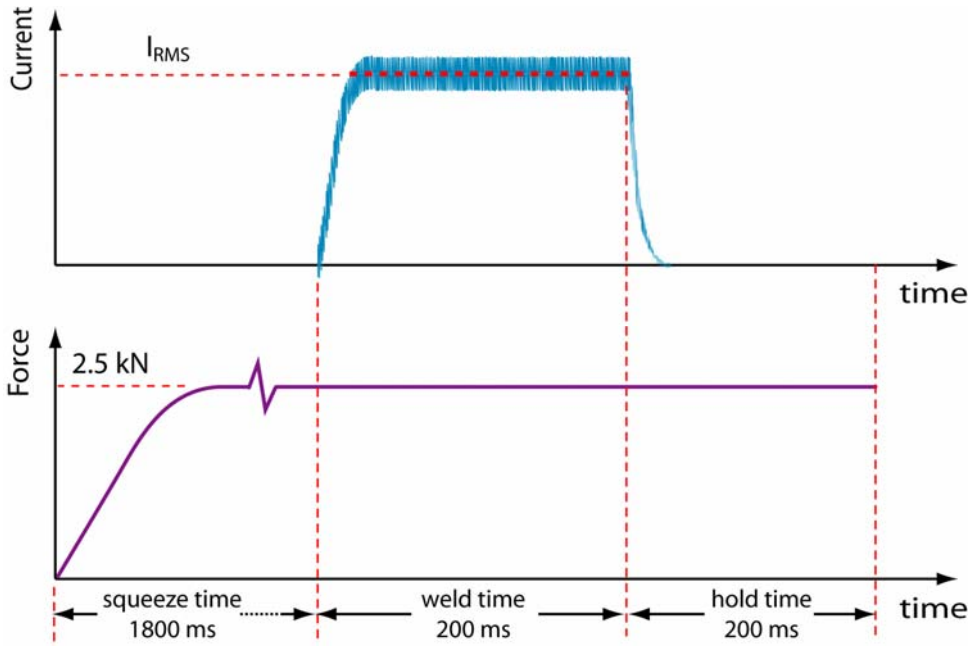

Figure 5-14. Typical weld current input from a DC power supply and the electrode force profile during squeeze time, weld time and hold time. The current used (I_{RMS}) ranged from 4 to 6 kA.

[†] RMS : Root mean square

Chapter 6: Architecture of Metallic Fibre Assemblies

The complex architecture of the bonded metallic fibre cores has been characterised via qualitative and quantitative techniques, since a clear understanding of the structure is important for explaining their properties. To obtain a qualitative view of the core structure, scanning electron microscopy (SEM) was used. Computed X-ray micro-tomography (μCT) was employed in investigating the internal core structure and for quantifying fibre segment lengths, fibre orientation distributions and tortuosity.

6.1 Core Characterisation using Scanning Electron Microscopy (SEM)

Figure 6-1 shows the general morphology of different core structures, as observed using the SEM. It can be seen from the cross-sectional views that the flocked core has a distinctly different fibre orientation distribution, as compared with pre-sintered felts (316L and 446) and brazed core (446). The flocked fibres have smaller inclination angles (measured from the vertical axis), while other cores show larger inclination angles (i.e. fibres are lying more in-plane).

Figure 6-2 depicts the fibre surface features and the bonds (necks) formed at fibre-to-fibre contacting points. The as-drawn (flocked) fibre has a surface topography showing grooves aligned along the fibre axis. In contrast, fibres in both pre-sintered felts (316L and 446) have recrystallised grain structures, as a result of solid-state sintering performed at elevated temperatures. For the 446 brazed fibres, the melted braze particles have been redistributed to the joints by capillary forces, forming bonds between contacting segments upon cooling. It can be seen that a relatively large amount of braze material is located at the joints, as compared with bonds formed by solid-state sintering.

Clearly, the SEM is a useful tool in providing a qualitative view of the overall fibre network structure, but rather limited when it comes to quantifying the core architecture.

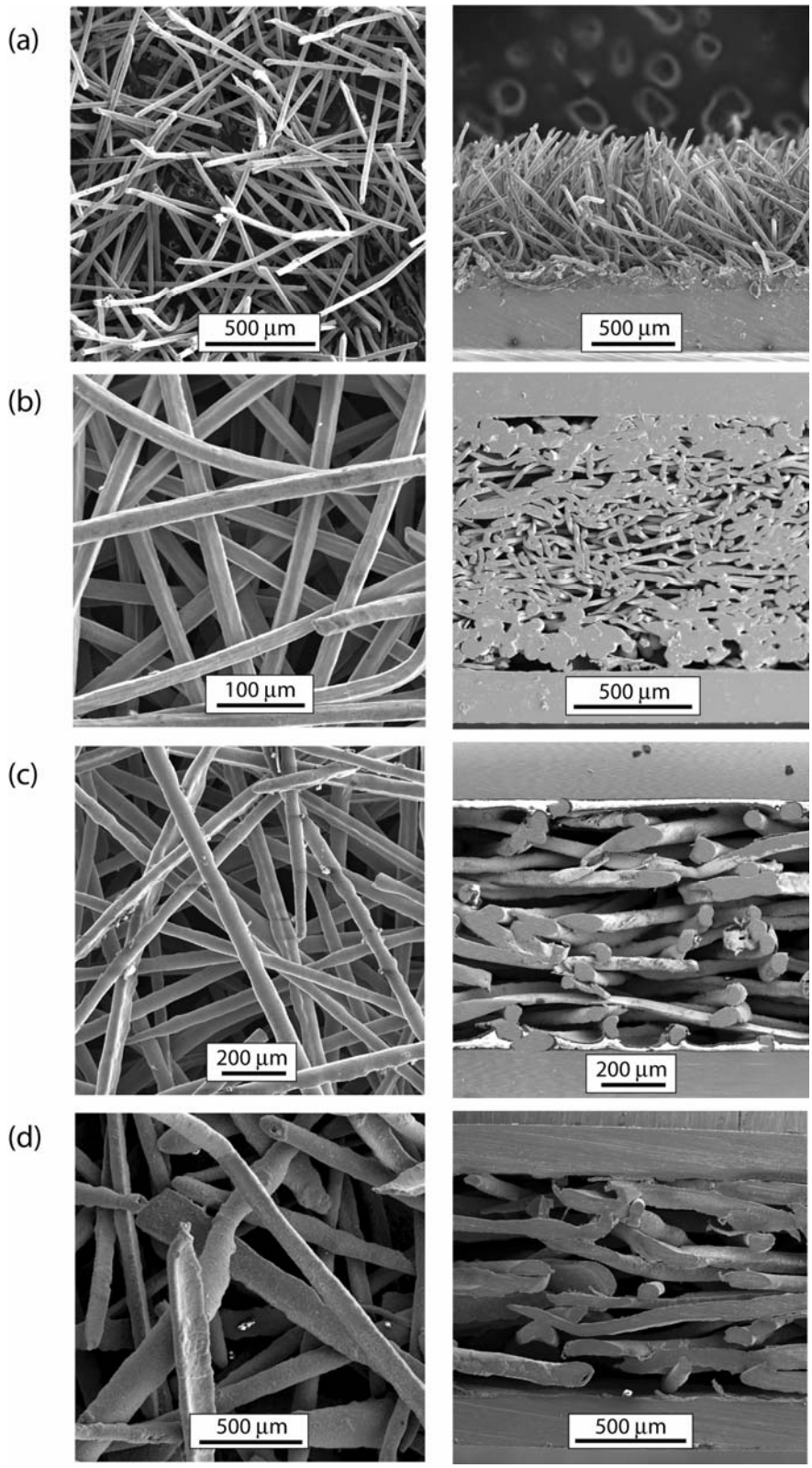

Figure 6-1. SEM micrographs showing the four different fibrous cores (plan and cross-sectional views) found in thin sandwich sheets: (a) 316L flocked fibre (FG sheet), (b) 316L pre-sintered felt (MB sheet), (c) 446 pre-sintered felt (MG sheet) and (d) 446 brazed fibres (SF sheet). Note: FG sheet is shown here with its upper faceplate detached.

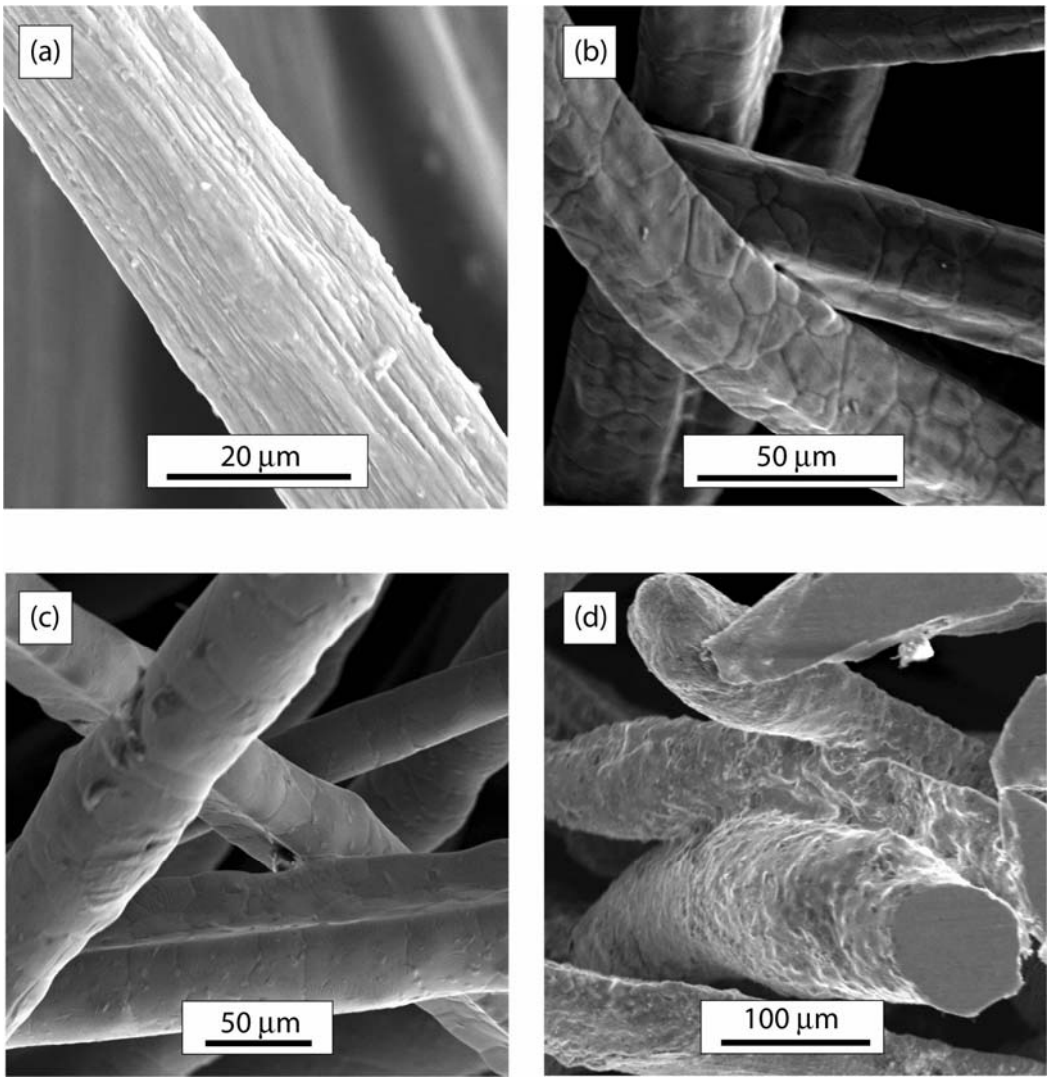

Figure 6-2. Higher magnification SEM micrographs showing the surface structures of fibres and fibre-to-fibre bonds (sintering necks), in (a) 316L flocked core, (b) 316L pre-sintered felt, (c) 446 pre-sintered felt and (d) 446 brazed fibres.

6.2 Core Characterisation using Computed X-ray micro-Tomography (µCT)

X-ray micro-tomography was used to examine the internal core structure and to obtain geometrical statistics of fibre distributions.

6.2.1 Qualitative Analysis

Figure 6-3(a) shows a typical X-ray absorption radiograph of a SF sandwich sheet, as recorded by the CCD camera. Four hundred such radiographs, taken in steps of 0.45°, through 180°, were used to reconstruct 2-D cross-sections (slices) of the core at different heights. The reconstructed slices are greyscale images, with intensity levels ranging from 0 to 255; one of such slices is depicted in Figure

6-3(b). The fibre phase appears as black (0), because of its higher X-ray attenuating coefficient; in contrast, a void is white (255), since it is the lower attenuating phase. However, due to noise and variations in intensity, the fibre phase cannot be easily identified. Therefore, anisotropic diffusion smoothing [149] was first performed, to obtain a smoother image and to sharpen the fibre phase edges (Figure 6-3(c)). Subsequently, segmentation was carried out via thresholding (Figure 6-3(d)).

Figure 6-4 shows radiographs of the other three cores and their segmented cross-sections. The internal structure of the bonded fibre network core was partly revealed by the 2-D reconstructed slices. It can be seen that each variant of sandwich sheet has different fibre volume fraction. However, the architecture of the cores can be more fully represented using 3-D tomographic reconstructions, as depicted in Figure 6-5. These 3-D renderings give a visual impression of the fibre orientation distributions of the core networks.

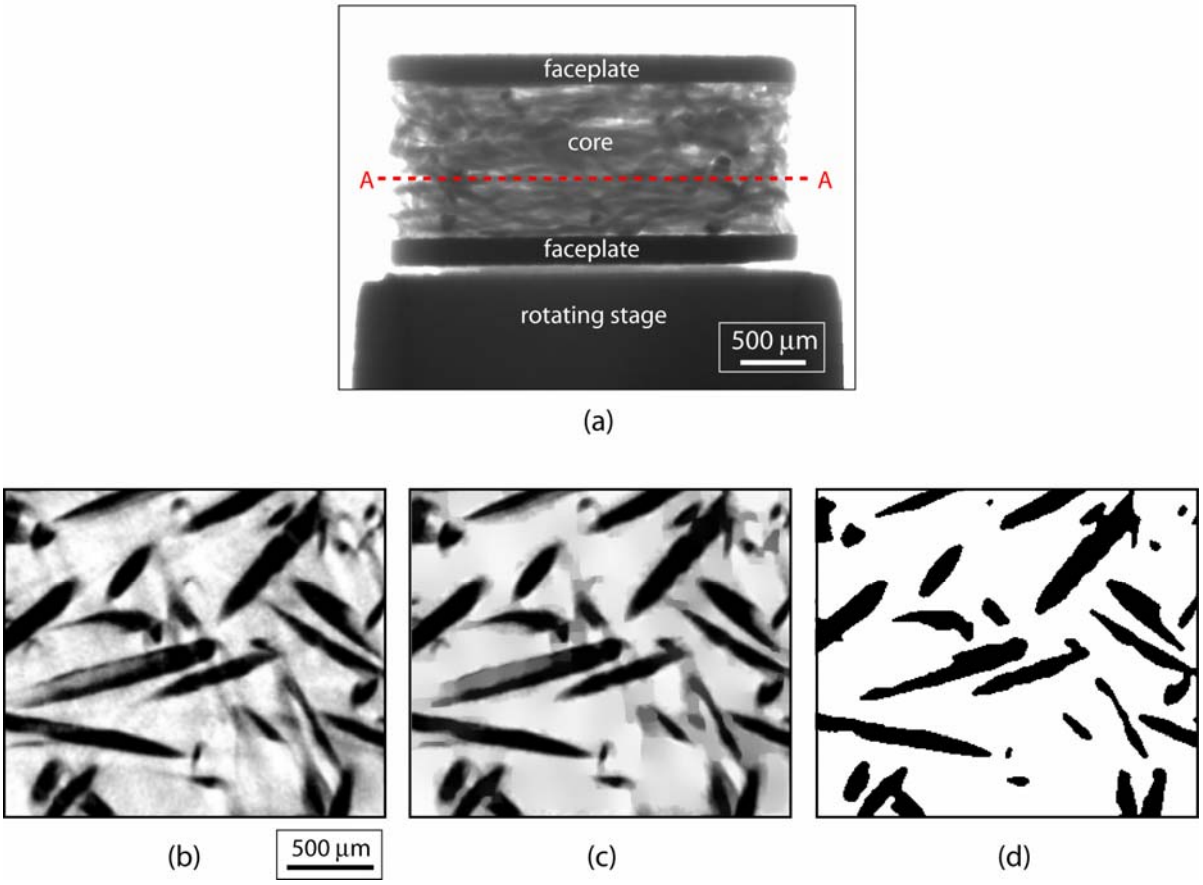

Figure 6-3. (a) A typical X-ray absorption radiograph of SF sandwich core structure, (b) a reconstructed 2-D slice through the core at position A-A, (c) the greyscale image after anisotropic diffusion smoothing, and (d) the segmented slice after thresholding.

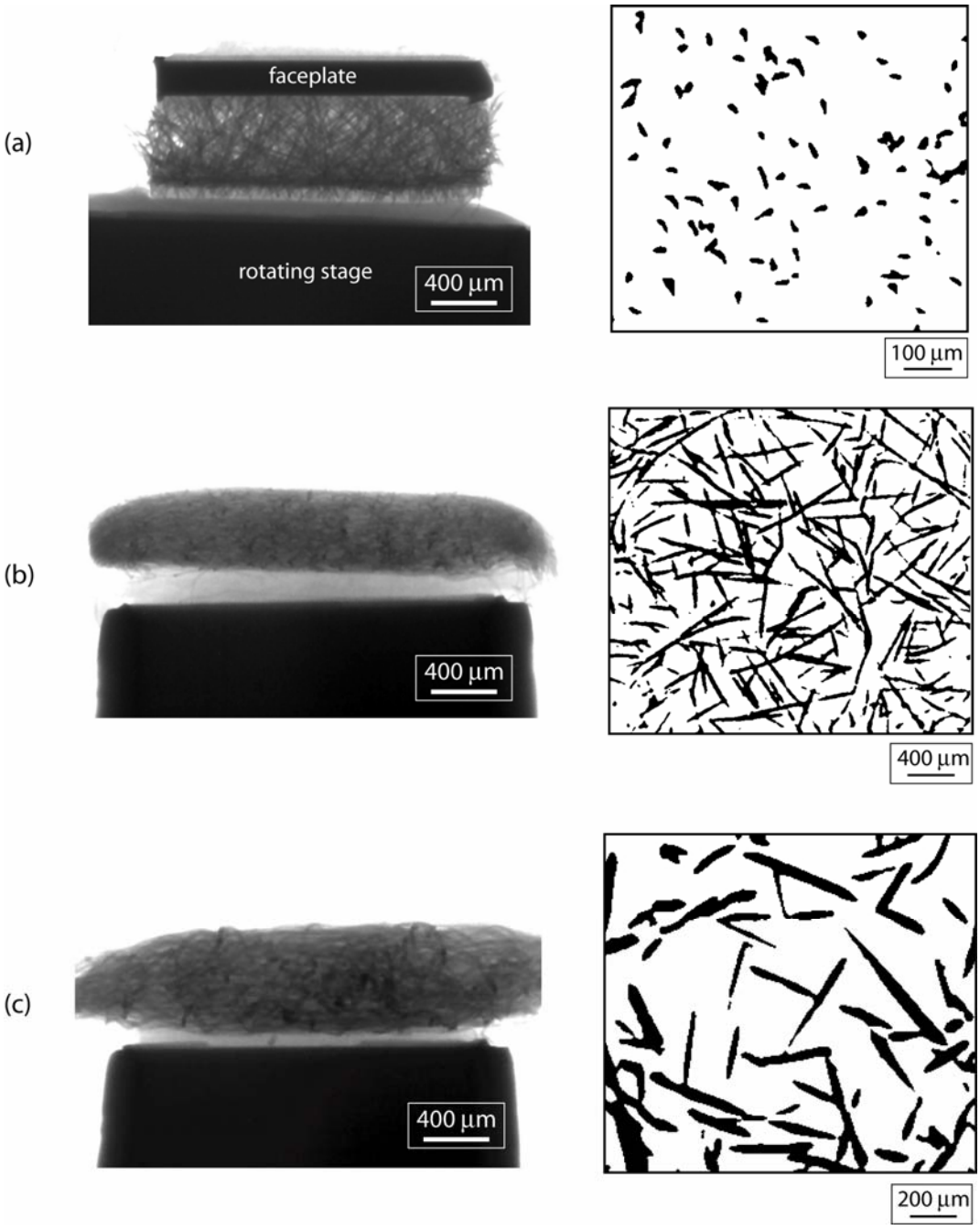

Figure 6-4. Radiographs of (a) FG (b) MB and (c) MG core structures, and their corresponding 2-D segmented tomographic slices (only a single slice at a specific height is shown here).

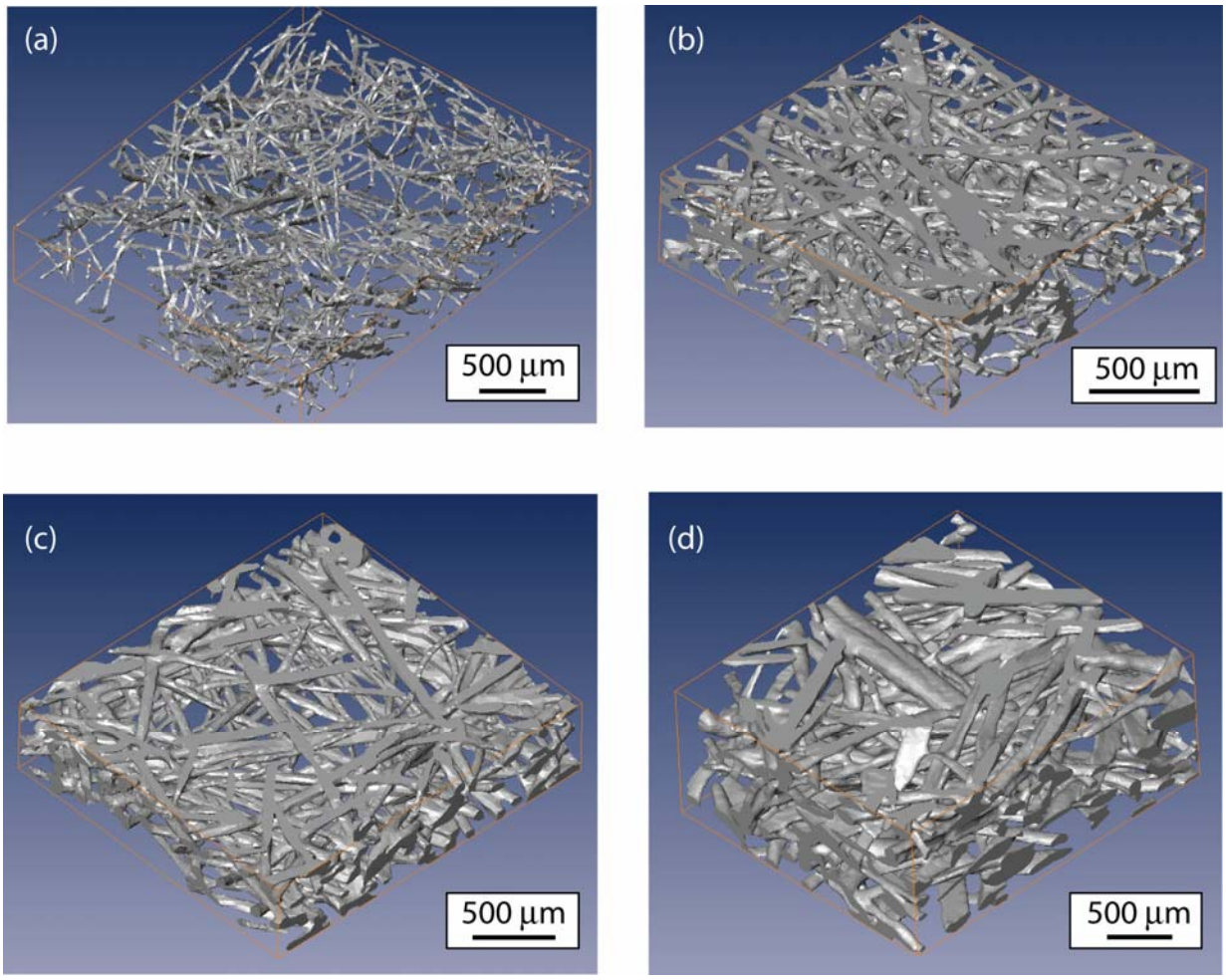

Figure 6-5. 3-D tomographic reconstructions of fibre cores, in (a) FG, (b) MB, (c) MG and (d) SF sandwich sheets. The 3-D renderings were generated using AMIRA™ visualisation software.

6.2.2 Quantitative Analysis using a Skeletonisation Algorithm

In order to extract geometrical statistics from the complicated 3-D fibre networks (Figure 6-5), the reconstructed fibre surfaces were simplified to their medial-axes or 'skeletons'. The medial-axis offers a skeletal representation of the surface, while preserving its original topology and geometry, so that the network geometry can be efficiently analysed. The skeletonisation algorithm used in this work was the '3DMA' code, developed by Lindquist and co-workers [142, 143]. Only a brief overview of the code and its relevant terminologies will be presented here; further details can be found in [144, 150].

For a digitised fibre network in 3-D space, the medial axis consists of a network of tortuous 'paths' and 'clusters' (Figure 6-6). A 'path' is defined as a connected *string* of filled voxels[‡], each voxel has

[‡] A voxel is a three-dimensional pixel.

exactly two filled neighbours. A 'cluster' is defined as a set of medial axis voxels, each with at least three neighbours lying in the same cluster. Therefore, in the actual fibre network, paths correspond to fibre segments, while clusters correspond to fibre bonds. The number of paths meeting at a cluster is termed the 'coordination number'. Each path on the medial axis can be classified as one of three types:

(i) a 'branch-branch' (B-B) path connects to a cluster at each end;

(ii) a 'branch-leaf' (B-L) path connects to a cluster only at one end, the other end being free;

(iii) a 'leaf-leaf' (L-L) path represents an isolated fibre.

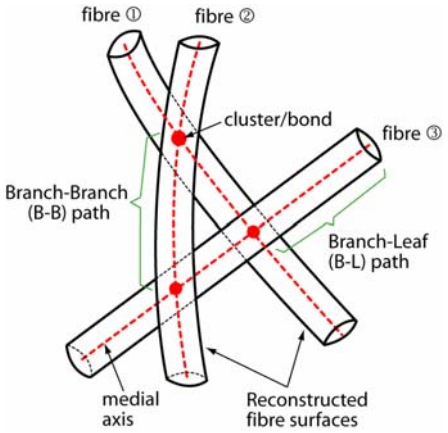

Figure 6-6. A schematic depiction of medial axis, paths (fibre segments) and clusters (fibre bonds) formed between three fibres. Each cluster shown here has a coordination number of four.

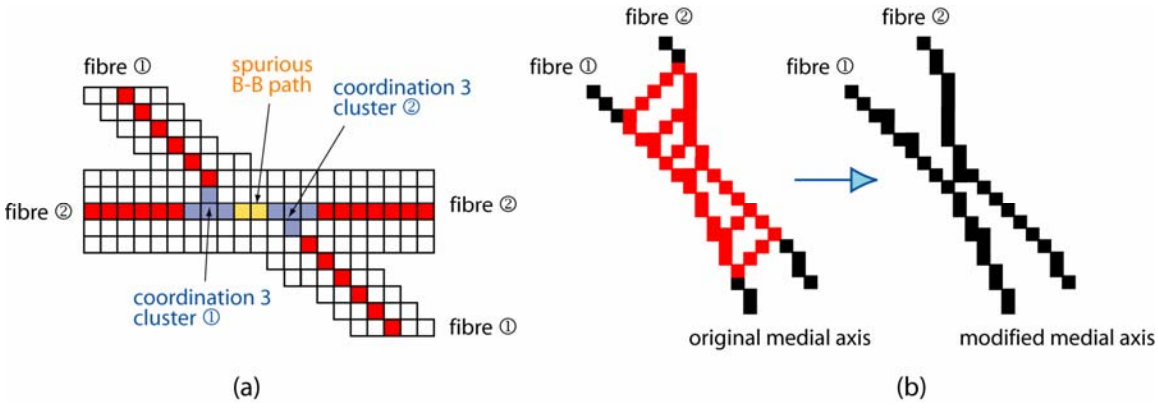

Figure 6-7. Medial axis modifications to remove spurious branch-branch (B-B) paths: (a) cluster-merge algorithm for two crossing fibres, and (b) surface remnant reduction algorithm for two closely lying fibres. This representation is in 2-D, whereas the algorithm is applied to a 3-D array of voxels (after [144]).

Special precautions were taken to extract reliable statistics from the medial axis. Due to finite volume discretisation, the skeletonisation algorithm generated a number of spurious B-B paths. For two fibres lying across and touching each other (Figure 6-7(a)), the 'cluster-merge algorithm' was used to join the two *close* clusters (with a coordination number 3) to produce a single coordination number 4 branch cluster. When two fibres were crossing at a very acute angle, the medial axis

appeared as ladder-shaped and contained a large number of spurious B-B paths (Figure 6-7(b)). In this case, the 'surface remnant reduction algorithm' was employed to delete the additional paths, leaving behind only the connecting route at the center of mass of the cluster. Moreover, surface noise (irregularities in the digitised surface) may resemble dead-end fibre segments, hence producing spurious B-L paths. These were eliminated by specifying a user defined B-L segment length threshold (100 μm). Also, L-L paths were not taken into account for the statistics, since they could have formed part of longer fibres exiting the imaged region.

The 3DMA code also incorporates a fibre tracing capability, which joins up the individual paths (fibre segments) through clusters (fibre crossing-points) to reconstruct the medial axis of a single fibre. It works by computing the optimal pairs of paths at all clusters, employing an 'optimal path-pairing algorithm'. In order to accommodate bending of fibres at crossings, a minimum kink-angle tolerance ($\theta_{tol} = 60°$) was specified, so that only paths forming angles less than this will be paired up.

Figure 6-8 shows the 3-D medial axis network in the SF core, extracted using the skeletonisation technique. Medial axis modification algorithms discussed above were applied to remove spurious B-B segments and to exclude all L-L segments. It can be seen that the medial axes have a clear relationship to the fibre surface. The medial axis networks of SF, MB and MG cores are depicted in Figure 6-9.

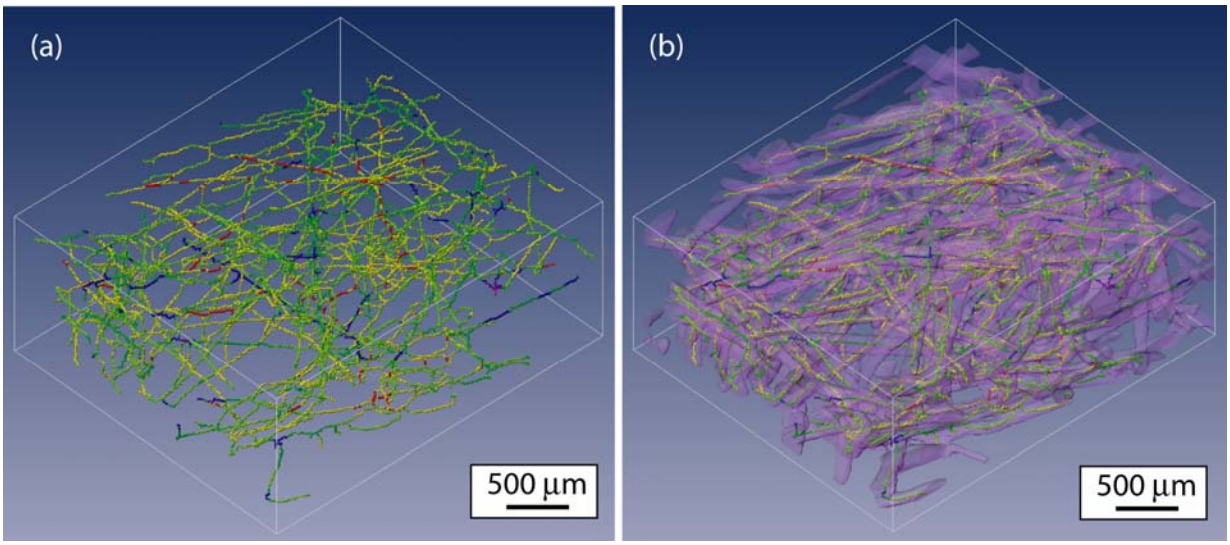

Figure 6-8. Skeletonised bonded fibre core in the SF sandwich sheet: (a) the medial axis network, (b) the medial axes are shown in relation with the fibre surfaces (transparent). The colour of each voxel on the medial axis designates the closest distance to the fibre surface, blue being the furthest away while red being the closest.

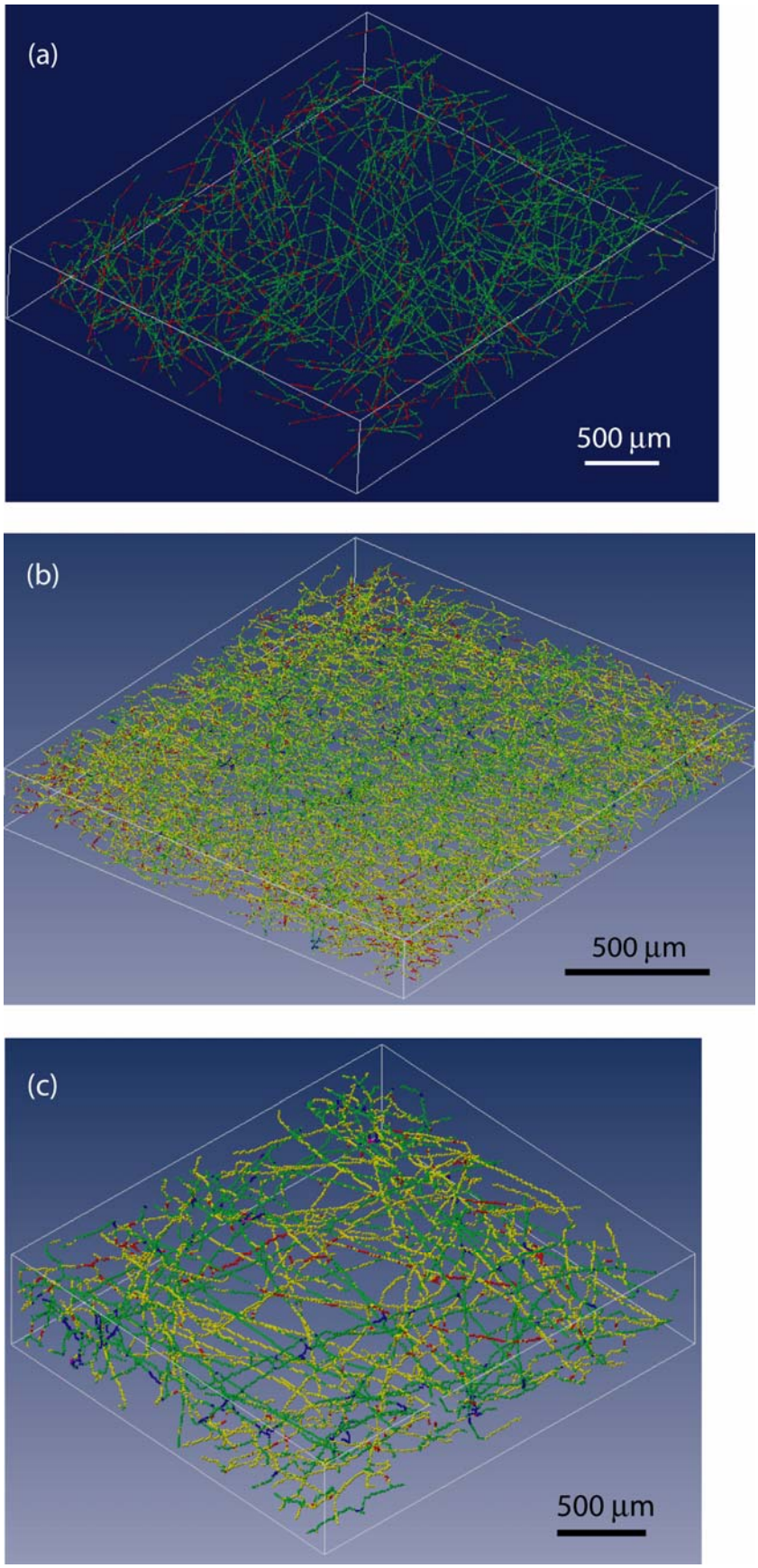

Figure 6-9. Medial axis networks of (a) SF (b) MB and (c) MG cores. The colour of each voxel designates the closest distance to the fibre surface, blue being the furthest away while red being the closest.

6.2.2.1 Fibre volume fraction

The core fibre volume fraction (f) was determined using 3-D image analysis of reconstructed fibres, by dividing the fibre volume by the total volume of interest, such as those shown in Figure 6-5. The results are presented in Table 6-1, together with values obtained from density measurements (§5.4). It should be noted that determination of fibre volume fraction from segmented tomography slices is prone to large errors (20% or more are not uncommon), so it is not recommended as a technique for obtaining this parameter. This is due to a couple of factors. Firstly, the small sample size used in tomography (5 mm × 5 mm) limits the accuracy. Secondly, the image analysis technique is very sensitive to segmentation errors, resulting in either over- or under-estimation of fibre fractions. So, obtaining volume fraction using density measurement is a more accurate method.

Table 6-1. Core fibre volume fractions, obtained from tomography and density measurements. The errors were based on the standard deviation of at least three different samples.

Core type	Measured fibre volume fraction, f	
	3-D image analysis of tomography slices	Density measurement
FG	0.06±0.02	0.08±0.01
MB	0.24±0.04	0.19±0.02
MG	0.21±0.04	0.15±0.02
SF	0.16±0.05	0.10±0.02

6.2.2.2 Fibre segment length distributions

The fibre segment lengths were obtained by extracting the lengths of medial axis paths (voxel strings) connecting two clusters (Figure 6-6). Branch-leaf (B-L) segments with lengths less than 100 μm were most likely to be artefacts generated by noise and were therefore excluded from the statistics. Figure 6-10 presents the distributions for the MB, MG and SF bonded fibre cores. Their mean segment lengths were found as 120 μm, 170 μm and 250 μm, respectively. It can be seen that the mean segment length increases with decreasing fibre length and fibre volume fraction. Such an increase is expected as the fibre fraction falls, but the expected effect of fibre length is less easy to predict. However, shorter fibres might be expected to lead to fewer entanglements. So, this observation is readily explicable. These segment lengths correspond to mean aspect ratios (L/D) of 4.8, 3.4 and 2.5, respectively.

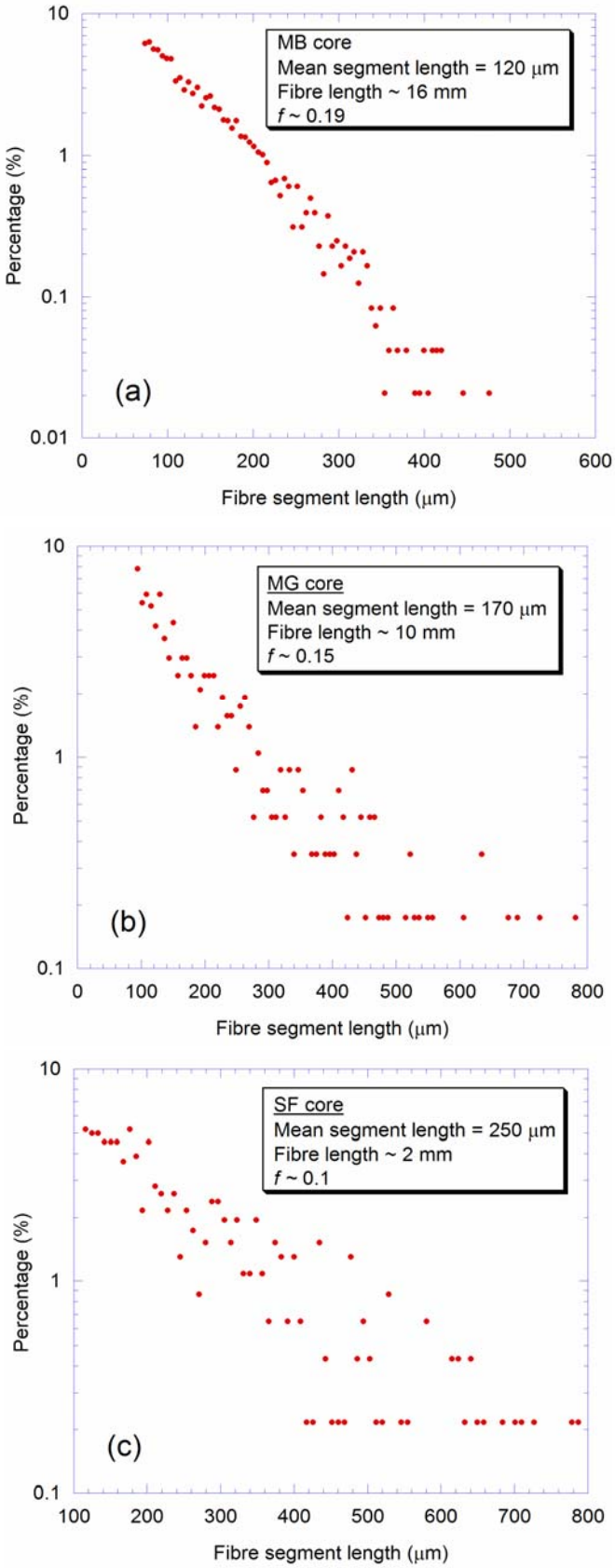

Figure 6-10. Fibre segment length distributions for (a) MB, (b) MG and (c) SF cores. The sample size was at least 300 fibre segments for each analysis. The distributions are truncated due to segment length thresholding (100 μm).

6.2.2.3 Fibre network tortuosity

The tortuosity of the fibre networks was quantified using a tortuosity algorithm. For each medial axis voxel on the 'entrance face' and for each voxel on the 'exit face' (Figure 6-11), the algorithm searches for the shortest path (if one exists), which connects them through the medial axis network [142].

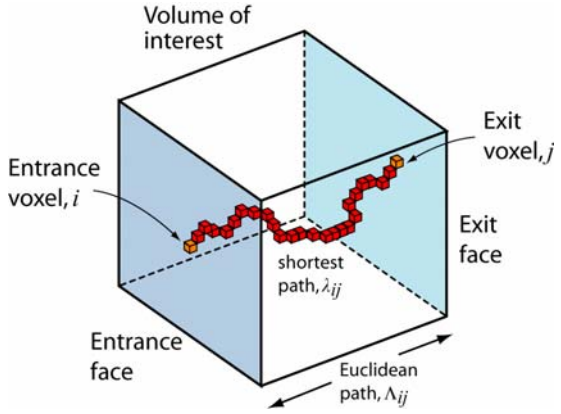

Figure 6-11. Schematic illustrating the entrance (*i*) and exit (*j*) voxels used in calculating tortuosity.

All possible entrance and exit voxel pairs (*i, j*) available in the network were taken into account. If the length of the shortest path is λ_{ij}, while the Euclidean distance between the voxel pairs is Λ_{ij}, the tortuosity, τ_{ij}, is defined as:

$$\tau_{ij} = \frac{\lambda_{ij}}{\Lambda_{ij}} \tag{6.1}$$

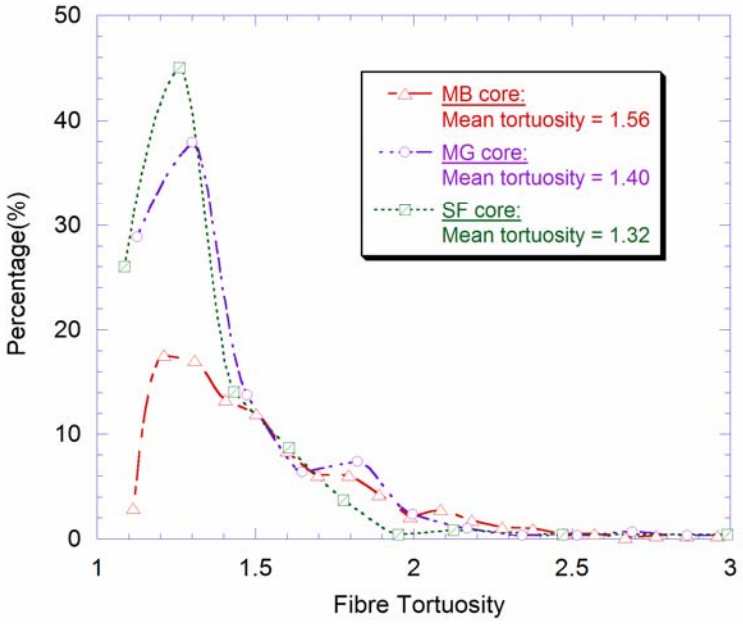

Figure 6-12. Fibre tortuosity distributions of (a) MB, (b) MG and (c) SF cores.

Hence, a tortuosity of unity implies λ_{ij} is equal to Λ_{ij}, i.e. a straight path from the entrance to the exit face. Figure 6-12 shows the fibre tortuosity distributions of the three bonded networks. The mean tortuosities of SF, MB and MG cores are 1.32, 1.40 and 1.56, respectively. Clearly, the SF core shows a tortuosity closer to unity. This may be associated with the shorter fibres in this core. In contrast, the MB core has higher tortuosity levels. The tortuosity distribution of the MG core is intermediate.

6.2.2.4 Fibre segment orientation distributions

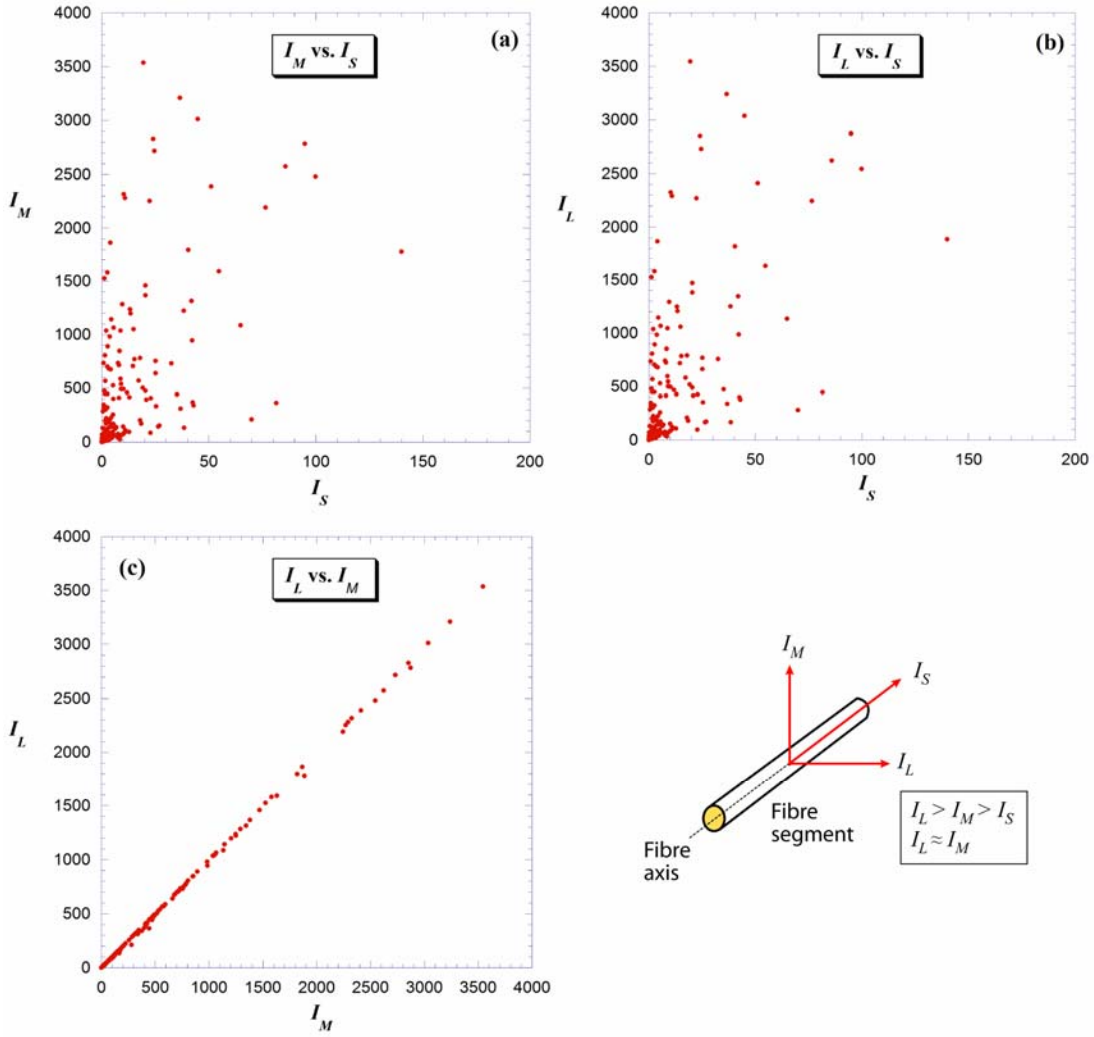

Figure 6-13. Cross-correlation plots for the small, medium and large moments of inertia (I_S, I_M, I_L) of a SF core. Each point on the plot corresponds to a fibre segment. The inset depicts the axes of the three moments of inertia, relative to the fibre axis. All the axes have units of mass × distance^2.

To establish the orientation of fibre segments, the 3DMA algorithm [142] treats each path as an isolated solid body and calculates its diagonalised moment of inertia tensor. The three eigenvectors correspond to the principal axes, while the eigenvalues correspond to the moments of inertia about

these axes. For a cylindrical body, such as that of a typical fibre segment, the larger (I_L) and intermediate (I_M) moments of inertia will have similar magnitudes, while the smallest moment of inertia (I_S) indicates the fibre axis. The cross-correlation plots of I_L, I_M and I_S are depicted for a SF core in Figure 6-13, where it can be seen that $I_L \approx I_M$. Similar correlation-plots were also obtained for the other fibre assemblies.

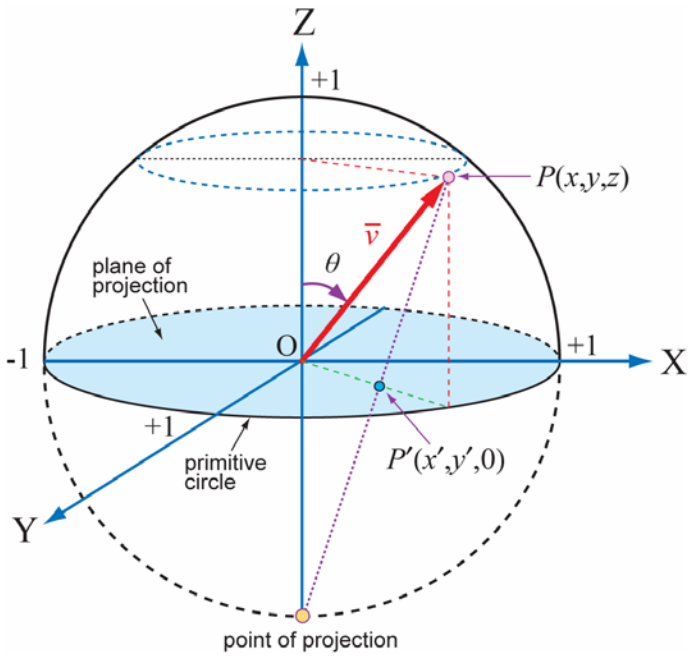

Figure 6-14. Schematic illustrating a normalised principle axis, $\bar{v}$ (a unit vector), and stereographic projection of its tip onto the XY plane (projection plane), using the south pole as the point of projection. The fibre segment inclination angle (θ) is measured from the +Z axis. The tip of the directional unit vector, $P(x,y,z)$, is located on the spherical surface, while its projection is $P'(x',y',0)$.

Each directional vector for I_S was normalised to unit length, $|\bar{v}|=1$, and re-plotted from the origin (Figure 6-14). All unit vectors from the lower hemisphere (-Z axis) were then reflected at the XY plane, so that only the upper hemisphere (+Z axis) was analysed. The fibre segment orientation distributions on the XY plane were represented by means of stereographic projection. Using the south pole as the point of projection, the tip of each unit vector was projected onto the projection plane (XY plane). The relationship between a point located on the spherical surface, $P(x,y,z)$, and that on the XY plane, $P'(x',y',z')$, can be expressed as:

$$x' = \frac{x}{z+1} \quad ; \quad y' = \frac{y}{z+1} \quad ; \quad z' = 0 \qquad (6.2)$$

The fibre segment inclination angle from the vertical axis, θ, can be calculated from:

$$\theta = \sin^{-1}\sqrt{x^2 + y^2} \tag{6.3}$$

In the context of fibre network assemblies, X- and Y- axes denote the in-plane reference directions, while Z-axis designates the through-thickness (transverse) direction. Orientation distributions on the YZ and XZ planes were also found via orthographic projection of the unit vector tips (from spherical surface perpendicular to the corresponding plane).

Figures 6-15 to 6-18 show the fibre segment orientation distributions on XY, YZ and XZ planes and inclination angles of the four fibre assemblies. The orientation distributions of a SF core verify that the flocked fibres are far from being orientated at 0º to the vertical axis, as claimed by the original patent (Figure 2-9) [1]. In fact, the fibres exhibit a mean inclination angle of about 60º to vertical. On the other hand, for bonded cores, statistics indicate that the fibre segments are oriented at much higher angles. It can be seen that, more fibres tend to lie closer to the in-plane (XY) directions. Furthermore, the projections on the YZ and XZ planes show clear signs of transverse isotropy. If the distributions were isotropic (random), then there should be a uniform distribution in the projection and inclination angle plots. Both MB and MG cores have mean inclination angles of about 75º to the vertical, which is apparent for a sintered fibre assembly made up of longer fibres (>10 mm). However, for a SF core, despite the shorter fibre length (~2 mm), the mean angle is at about 70º. This is due to the fact that, the assembled core has an overall thickness of ~0.85 mm (Figure 6-1(d)), so, to produce a core of lower inclination angle, it will be necessary to incorporate even shorter fibres (<1 mm).

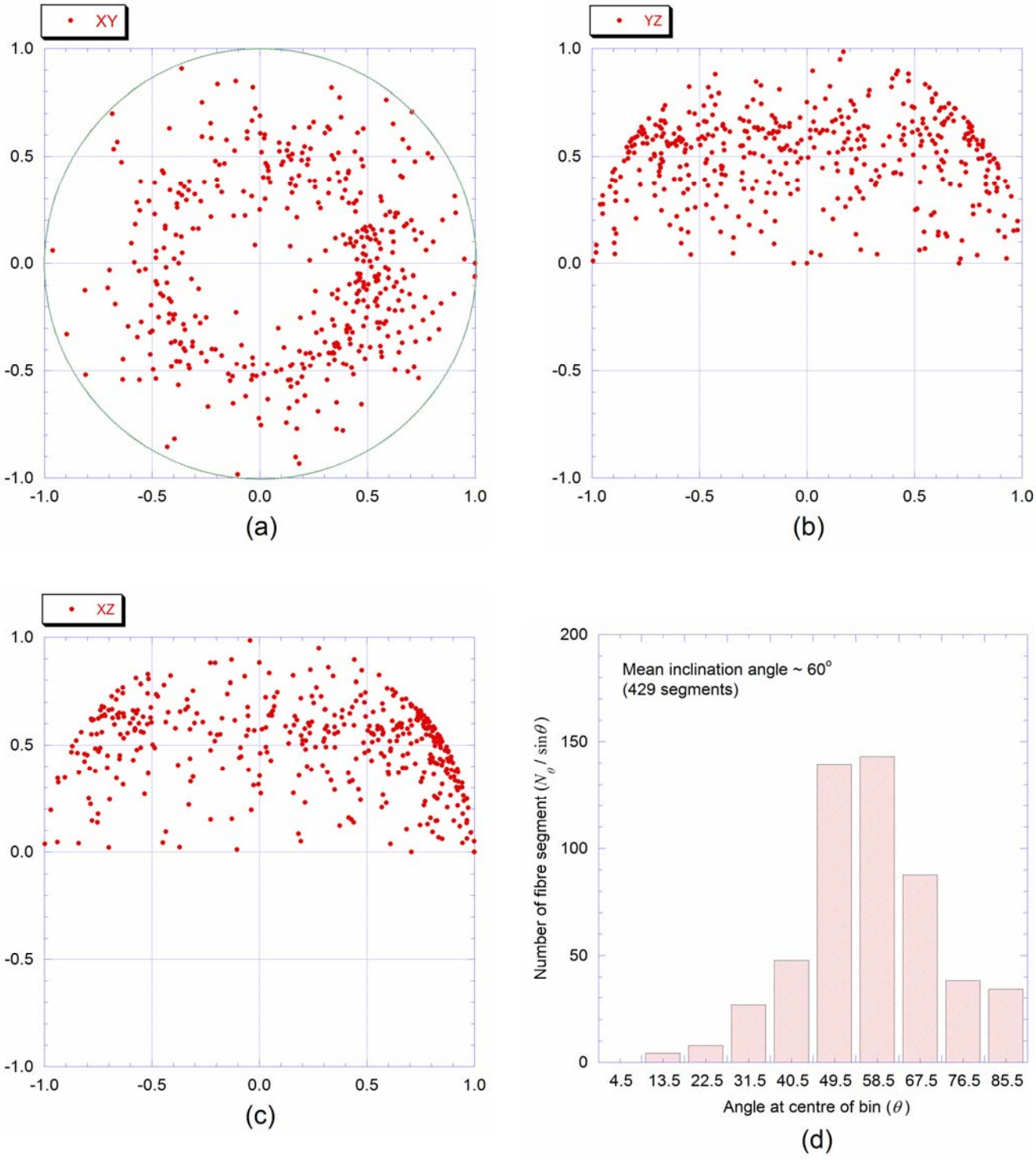

Figure 6-15. Orientation distribution plots and fibre segment inclination angles of a FG core. Projections of the tips of principal axis unit vector onto the (a) XY, (b) YZ and (c) XZ planes and (d) fibre segment inclination angles to the vertical axis. The green circle designates the primitive circle on the XY projection plane. The sample consisted of 429 fibre segments. (*N.B.* The number of fibre segment, N_θ, has been divided by sin θ to correct the bias towards larger angles.) The orientation raw data can be found in Appendix (A).

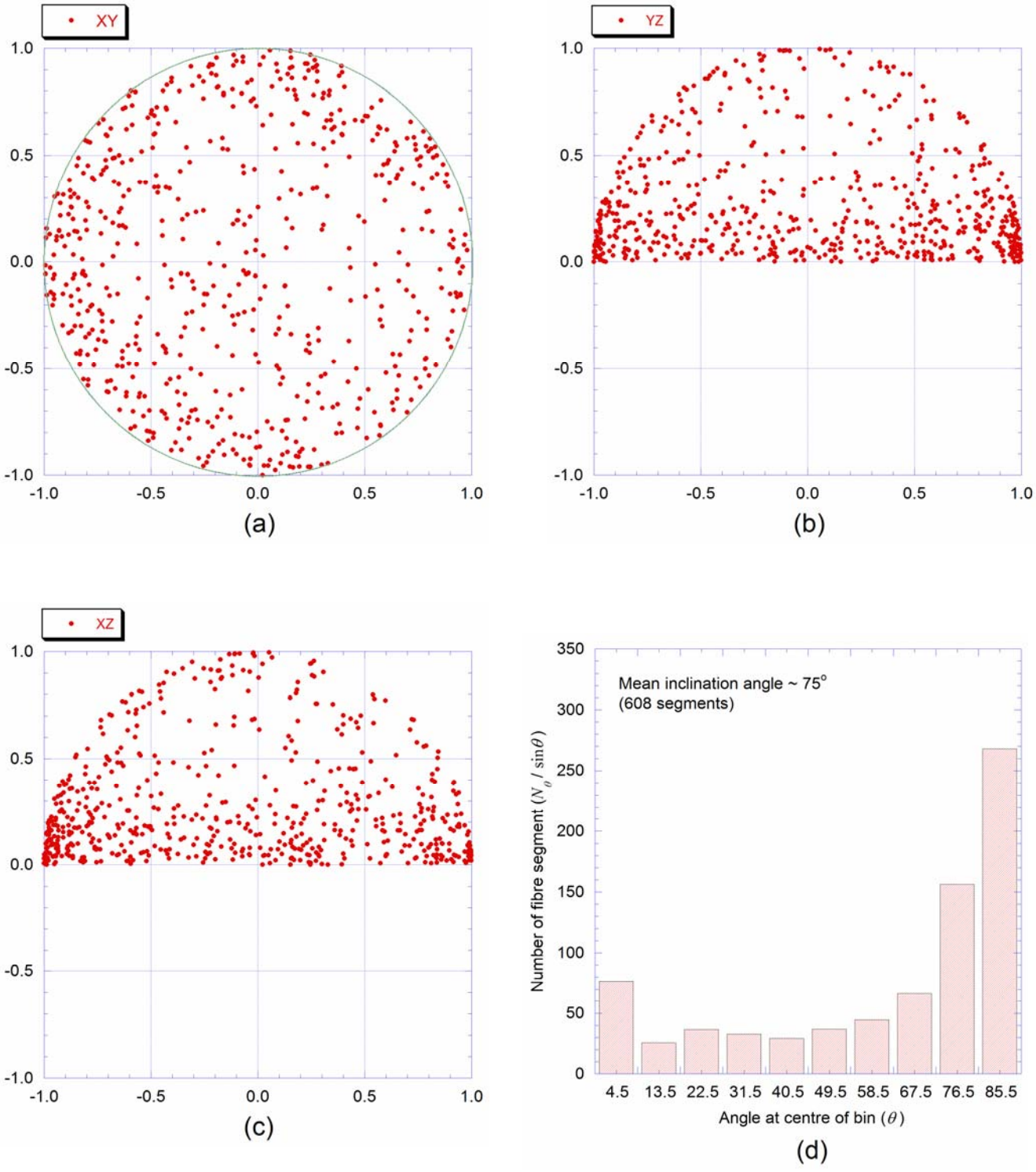

Figure 6-16. Orientation distribution plots and fibre segment inclination angles of a MB core. Projections of the tips of principal axis unit vector onto the (a) XY, (b) YZ and (c) XZ planes, while (d) fibre segment inclination angles to the vertical axis. The sample consisted of 608 fibre segments. The orientation raw data can be found in Appendix (B).

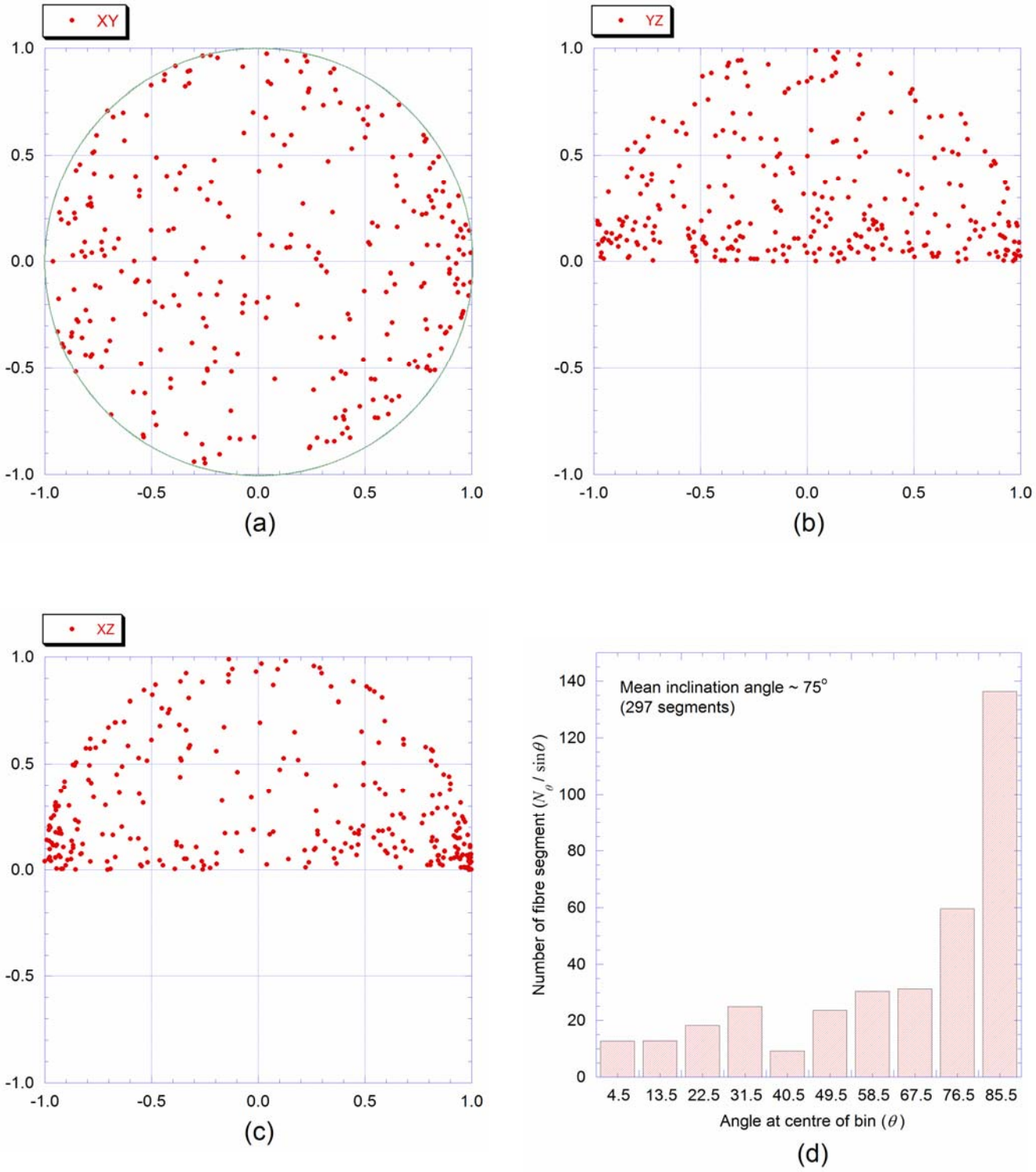

Figure 6-17. Orientation distribution plots and fibre segment inclination angles of a MG core. Projections of the tips of principal axis unit vector onto the (a) XY, (b) YZ and (c) XZ planes, while (d) fibre segment inclination angles to the vertical axis. The sample consisted of 297 fibre segments. The orientation raw data can be found in Appendix (C).

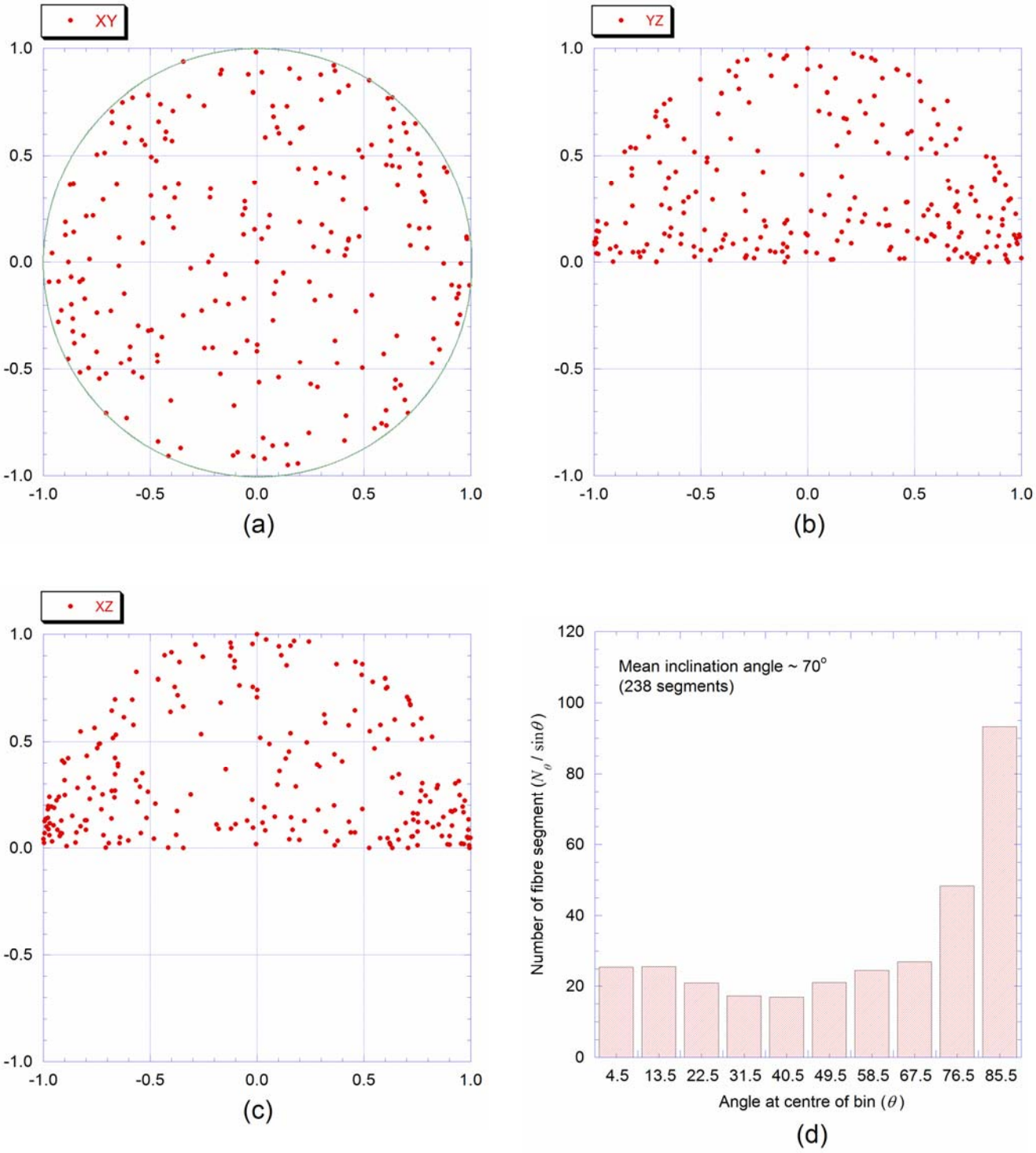

Figure 6-18. Orientation distribution plots and fibre segment inclination angles of a SF core. Projections of the tips of principal axis unit vector onto the (a) XY, (b) YZ and (c) XZ planes, while (d) fibre segment inclination angles to the vertical axis. The sample consisted of 238 fibre segments. The orientation raw data can be found in Appendix (D).

6.2.3 Summary

The statistics collected from the X-ray micro-tomography of metallic fibre cores are summarised in Table 6-2.

Table 6-2. Various fibre aspect ratio and orientation distributions obtained from X-ray micro-tomography.

Core type	Fibre volume fraction*	Fibre length** (mm)	Mean segment length (μm)	Fibre segment aspect ratio (L/D)	Mean inclination angle to the vertical axis (º)	Fibre tortuosity
FG	0.06±0.02	~1	-	-	~60	-
MB	0.24±0.04	~16	120	4.8	~75	1.6
MG	0.21±0.04	~10	170	3.4	~75	1.4
SF	0.16±0.05	~2	250	2.5	~70	1.3

* These values should serve only as estimates.
** As provided by the fibre manufacturers (Bekaert S.A. and Fibretech Ltd.).

Chapter 7: Thermal and Electrical Properties of Sandwich Sheets with Fibrous Cores

The thermal and electrical properties of thin sandwich sheets with a highly porous metallic fibrous core have been measured and modelled. The cores are transversely isotropic, with different conductivities in the through-thickness (transverse) and in-plane directions. A simple analytical model based on an idealised unit cell is proposed, to predict thermal and electrical properties. These predictions were strongly dependent on core fibre volume fraction and mean fibre inclination angle. However, this simple model does not allow incorporation of actual fibre orientation distributions. To take this into account, an orientation distribution model which predicts conductivities based on an orientation distribution function, P(θ), has been developed. A numerical model, using the finite-element (FE) method, has also been used to predict the conductivities. The three-dimensional finite-element mesh was generated from the reconstructed fibres obtained from X-ray micro-tomography.

7.1 Measured Conductivities

7.1.1 Thermal Conductivity

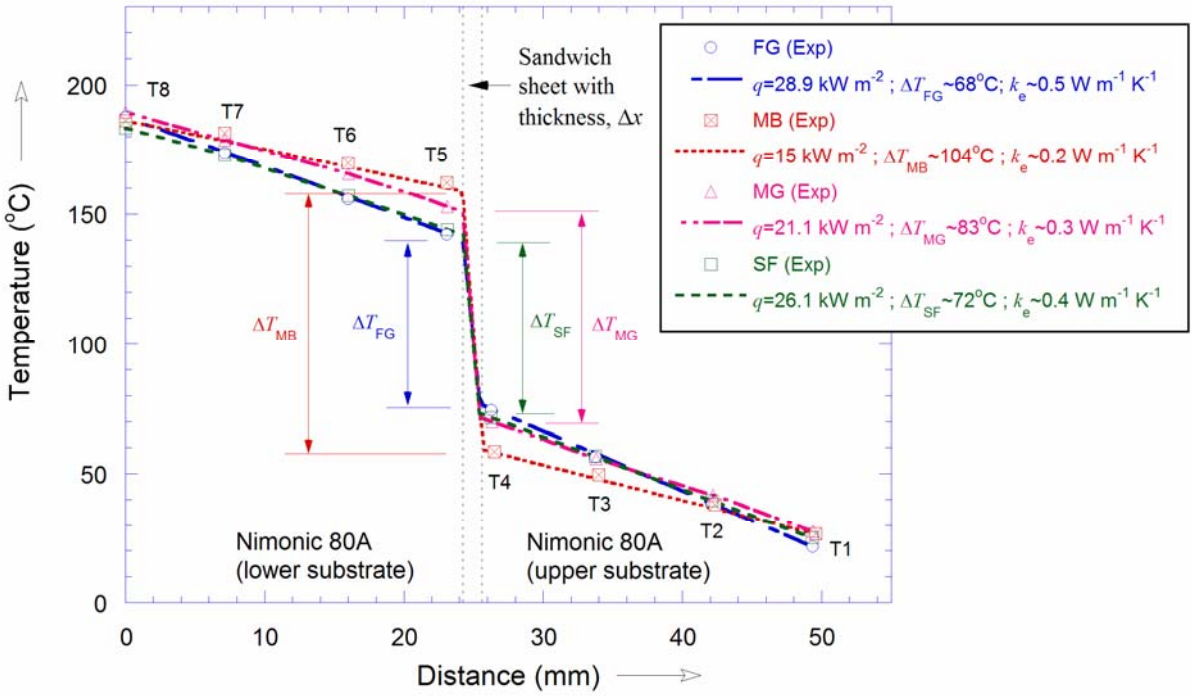

Figure 7-1. Typical temperature gradient plots, depicting the temperature drops (ΔT) in the through-thickness direction (Δx) of sandwich sheets. The points (T_1 to T_8) correspond to the eight thermocouple readings taken at steady-state conditions (Figure 5-5), while the curves were calculated based on eqns.(5.2) to (5.4). The effective conductivity (k_e) was found according to eqn.(5.6), by employing the average heat flux (q).

The effective thermal conductivities (k_e) of pre-sintered fibre felts and assembled sandwich sheets were measured, with a mean temperature of about 100 °C, using the steady-state bi-substrate technique described in §5.5. Figure 7-1 shows the temperature gradients established at steady-state conditions, through the upper and lower Nimonic substrates and pre-sintered felts/sandwich sheets.

Large temperature drops of 70 °C or more were observed across all samples and the through-thickness conductivities were measured to be of the order of 0.1 W m^{-1} K^{-1}. Clearly, such low conductivities are due to the highly porous core structures, with porosity levels exceeding 80 vol.% (Table 6-1). Moreover, the effective conductivity is further reduced in sandwich sheets (FG and MG) which incorporate (low conductivity) adhesives, instead of braze, for core-to-faceplate bonding.

Table 7-1 shows the average conductivities determined from at least three different samples. It can be seen that the experimental precision is ±10%, mainly attributable to the errors in heat flux measurements (eqn.(5.5)).

Table 7-1. Measured effective through-thickness thermal conductivities, at a mean temperature of 100 °C, for pre-sintered fibre felts and assembled sandwich sheets.

Material		Effective thermal conductivity, k_e (W m^{-1} K^{-1})
Core	316L pre-sintered felt (MB core)	0.14 ± 0.02
	446 pre-sintered felt (MG core)	0.17 ± 0.02
Sandwich sheet	Flocked and glued (FG)	0.48 ± 0.02
	Long in-plane mesh, brazed (MB)	0.22 ± 0.02
	Long in-plane mesh, glued (MG)	0.30 ± 0.03
	Short fibre 3-D array (SF)	0.42 ± 0.04

7.1.2 Electrical Resistivity

The effective electrical resistivities (reciprocal of conductivities) of pre-sintered felts and sandwich sheets, in both through-thickness and in-plane directions, were measured using the experimental setup described in §5.6. The results obtained are shown in Table 7-2.

Table 7-2. Measured effective electrical resistivities, in through-thickness and in-plane directions of pre-sintered fibre felts and sandwich sheets, measured at room temperature.

Material		Electrical resistivity (μΩ cm)	
		Through-thickness ($\pm 0.3\times10^3$)	In-plane* ($\pm 0.2\times10^3$)
Core	316L pre-sintered felt (MB core)	1.6×10^3	1.0×10^3
	446 pre-sintered felt (MG core)	1.8×10^3	1.2×10^3
Sandwich sheet	Flocked and glued (FG)	7×10^6	-
	Long in-plane mesh, brazed (MB)	3×10^4	-
	Long in-plane mesh, glued (MG)	5×10^4	-
	Short fibre 3-D array (SF)	3×10^3	-

*Only the in-plane resistivities of pre-sintered fibre felts (MB and MG cores) were measured, since it was not possible to detach the FG and SF cores from their faceplates without first destroying the original core structures.

It can be seen that the through-thickness resistivity of FG sheet is a few orders of magnitude higher than MB, MG and SF sandwich sheets. This is clearly caused by the thick epoxy adhesive, which

prevents the fibre ends from coming into good contact with the faceplates (Figure 7-2). In contrast, despite using an adhesive for faceplate bonding, the resistivity of MG sheet is about two orders of magnitude lower than FG. This is probably due to the use of a low viscosity adhesive and curing under pressure, which promote better contact with faceplates (Figure 7-3(a)). Also, it is interesting to note that, the resistivity of MG sheet is of the same order of magnitude as its brazed counterpart, MB sheet. Among the sandwich sheets, SF exhibits the lowest resistivity, because of the use of a braze metal for both fibre and faceplate bonding (Figure 7-3(b)).

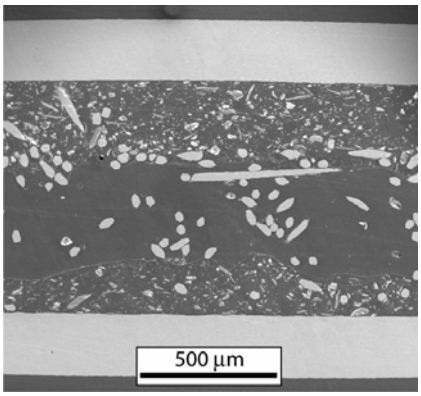

Figure 7-2. SEM micrograph showing the cross-sectional view of the FG core after being impregnated with resin. Only a small number of fibre ends are in direct contact with the 316L faceplates.

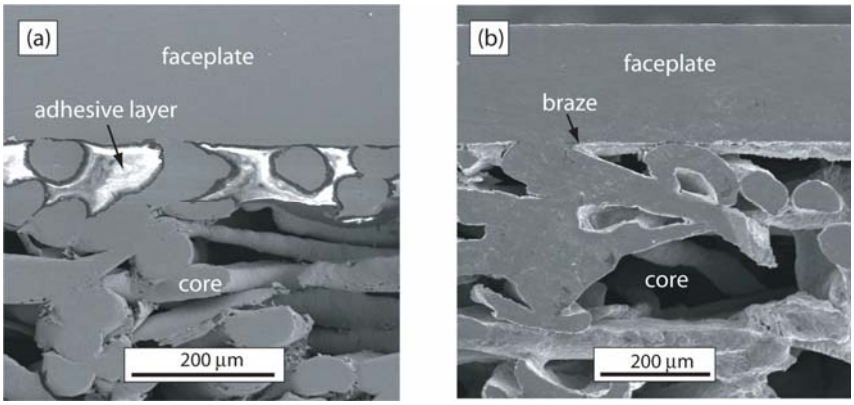

Figure 7-3. SEM micrographs showing the fibre-to-faceplate contacts in (a) MG and (b) SF sheets.

For both pre-sintered fibre felts, electrical resistivity in the in-plane direction was found to be about 40% lower than that measured in the through-thickness direction. The same effect is expected for thermal conductivity, i.e. in-plane conductivity will be higher than through-thickness conductivity. In fact, this is expected in view of the transversely isotropic core architecture. Evidently, a high proportion of fibres lying at high inclination angles (>70º) will favour in-plane transport of heat flux and electrical charge and inhibit through-thickness transport.

7.2 Modelling of Effective Conductivities using an Idealised Unit Cell Model

7.2.1 Thermal Conductivity

An analytical model is proposed to investigate the effects of mean fibre inclination angle (θ) and core fibre volume fraction (*f*), on the effective thermal conductivity of sandwich sheets with different core architectures. It can be regarded as a generic model for the treatment of sandwich materials incorporating sintered fibre assembly cores, such as those found in MB, MG and SF sheets. Moreover, it can also be applied to the flocked core found in the FG sheet.

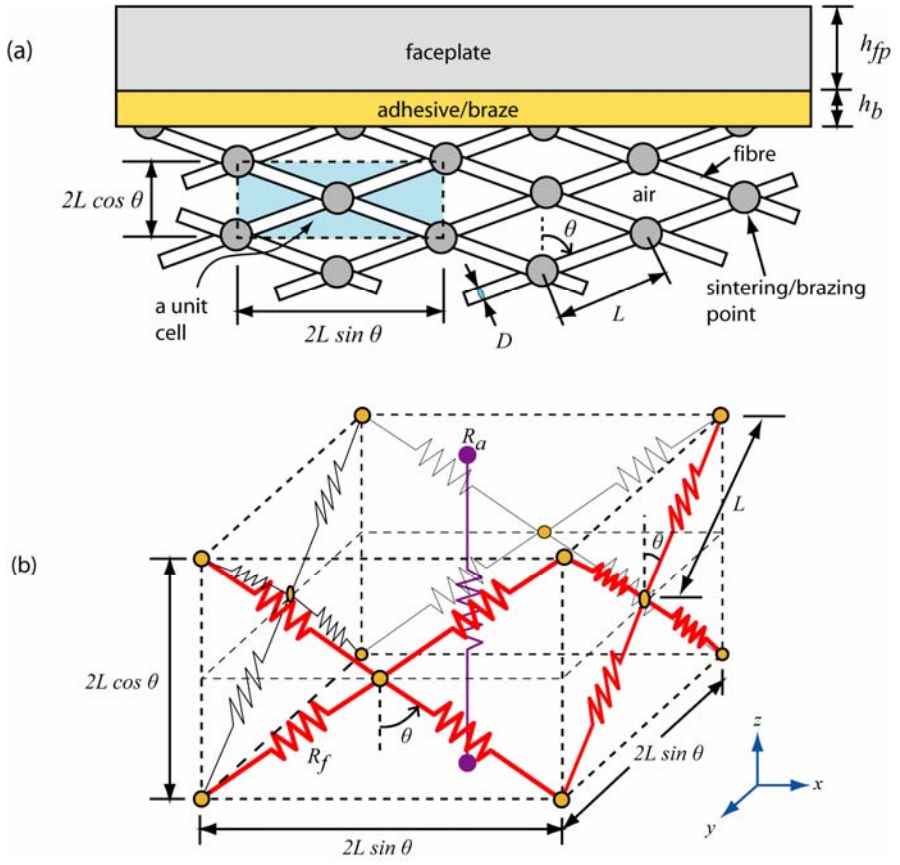

Figure 7-4. Schematic showing the (a) sintered fibre assembly model and the idealised unit cell (b) perspective view illustrating the resistance network model of the idealised unit cell. R_f and R_a are resistances of stainless steel fibre segment and air, respectively. L is the fibre segment length and θ is the mean fibre inclination angle, measured from the vertical axis. The through-thickness direction is designated as *z,* while in-plane directions are *x* and *y*.

The sintered felt (mesh) core is assumed to have an idealised unit cell structure, which is transversely isotropic ($k_x = k_y \neq k_z$), as depicted in Figure 7-4(a). The sintering or brazing points (necks) are spaced at a fixed interval of L and the fibres are inclined at a mean inclination angle of θ, to the through-thickness axis. The thermal resistance of a junction is assumed to be negligible. The unit cell

has sides of $2L\sin\theta$ and a height of $2L\cos\theta$ (Figure 7-4(b)). Since there are effectively eight fibres per unit cell, the fibre volume fraction of the unit cell (f) can be expressed as:

$$f = \frac{\pi D^2}{4L^2 \sin^2\theta \cos\theta} \tag{7.1}$$

7.2.1.1 Through-thickness (transverse) conductivity

In the through-thickness (z) direction, the resistances of the fibre segments (R_f) and air column (R_a) can be written as:

$$R_f = \frac{L}{\pi D^2 k_f} \tag{7.2}$$

$$R_a = \frac{L\cos\theta}{\pi D^2 k_a \left(\frac{1}{f\cos\theta} - 1\right)} \tag{7.3}$$

where k_f and k_a are the corresponding conductivities. For electrical conductivities, the air can be ignored (unless the breakdown field is exceeded), while for thermal conduction, it could be relevant when convective transport is insignificant.

Taking R_f and R_a as two resistances in parallel, the total resistance of the sintered felt in z-direction is given by:

$$R_z = \frac{L\cos\theta}{\pi D^2 \left\{k_f \cos\theta + k_a\left(\frac{1}{f\cos\theta} - 1\right)\right\}} \tag{7.4}$$

On the other hand, the effective conductivity of the fibre felt (k_z) can also be written as:

$$k_z = \frac{L\cos\theta}{4R_z L^2 \sin^2\theta} \tag{7.5}$$

By substituting eqn.(7.4) into (7.5), the sintered felt conductivity in the through-thickness direction can be expressed as:

$$k_z = fk_f \cos^2\theta + \left(1 - f\cos\theta\right)k_a \tag{7.6}$$

Figure 7-5 shows predicted through-thickness conductivities, as given by eqn.(7.6), together with experimental data for 316L and 446 pre-sintered fibre felts. In order to get good agreement with experiment, the mean inclination angle of 316L felt is required to be at about 77°~80°, while it is about 75°~77° for the 446 felt. This is broadly consistent with values obtained from X-ray micro-tomography analyses, which found mean inclination angles ranging from 70° to 80° for both felts (§6.2.2.4). As expected, the conductivity is predicted to increase with core fibre volume fraction (f). However, for a given fibre volume fraction, the conductivity of 446 felt is found to be higher. This is attributable to two factors. Firstly, as for the parent materials, the conductivity of stainless steel 446 is about 20% higher than 316L. Secondly, the lower fibre inclination angle in 446 felt results in higher conductivity, since conduction paths are effectively shortened.

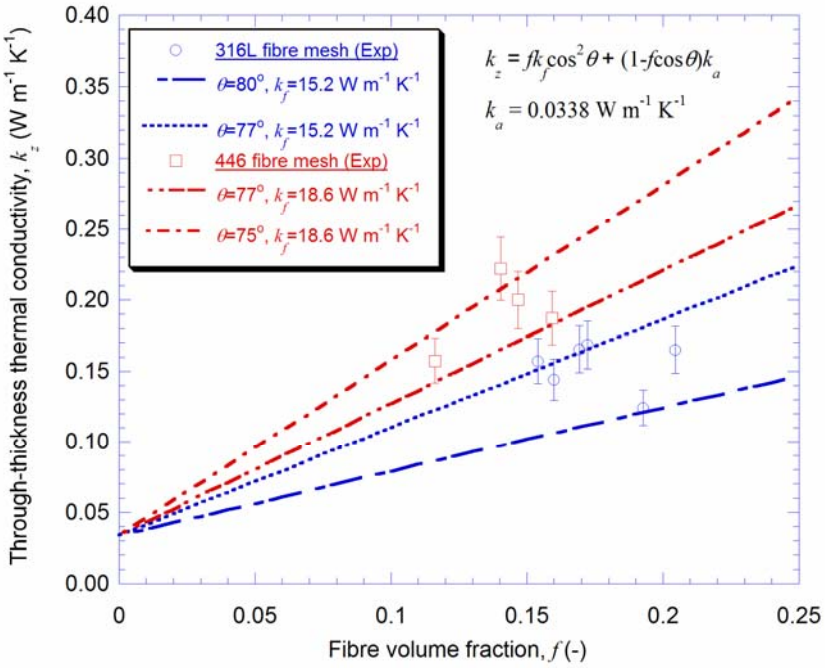

Figure 7-5. Effective thermal conductivities of pre-sintered 316L and 446 fibre felts. The curves are predictions obtained using eqn.(7.6) at different mean fibre inclination angles, while the points are measurements made at a mean temperature of 100 °C.

Using a slab model in series, the effective thermal conductivity of the overall sandwich structure becomes:

$$k_e = H\left[h_m\left\{fk_f\cos^2\theta+\left(1-f\cos\theta\right)k_a\right\}^{-1}+\frac{2h_b}{k_b}+\frac{2h_{fp}}{k_{fp}}\right]^{-1} \qquad (7.7)$$

where h is the thickness of various sandwich elements and H is the total sandwich thickness. The subscripts m, b and fp refer to mesh (felt), faceplate-to-core bond layer (adhesive or braze) and faceplate, respectively.

Figure 7-6 shows predictions and experimental data obtained for the different sandwich materials. For the MB sheet, using average values of 0.19 and 80° for f and θ respectively, an effective conductivity of about 0.2 W m^{-1} K^{-1} is predicted, which is consistent with experiment (0.22 ± 0.02 W m^{-1} K^{-1}). The conductivity of Ni-based braze (k_b) is taken as 14 W m^{-1} K^{-1} [151], and the bond layer thickness (h_b) is taken as about 100 μm (Figure 7-2). As for the MG sheet, assuming the fibres are inclined at a lower angle of about 75°, k_e is predicted to have a greater value of 0.34 W m^{-1} K^{-1}. This prediction also agrees with the experimental data (0.30 ± 0.03 W m^{-1} K^{-1}). The SF sheet is predicted to have the highest effective conductivity of 0.43 W m^{-1} K^{-1}, as compared with experimental value of 0.42 ± 0.04 W m^{-1} K^{-1}. Clearly, the higher conductivity is attributable to the use of braze for faceplate bonding and the lower mean fibre inclination angles (~70°).

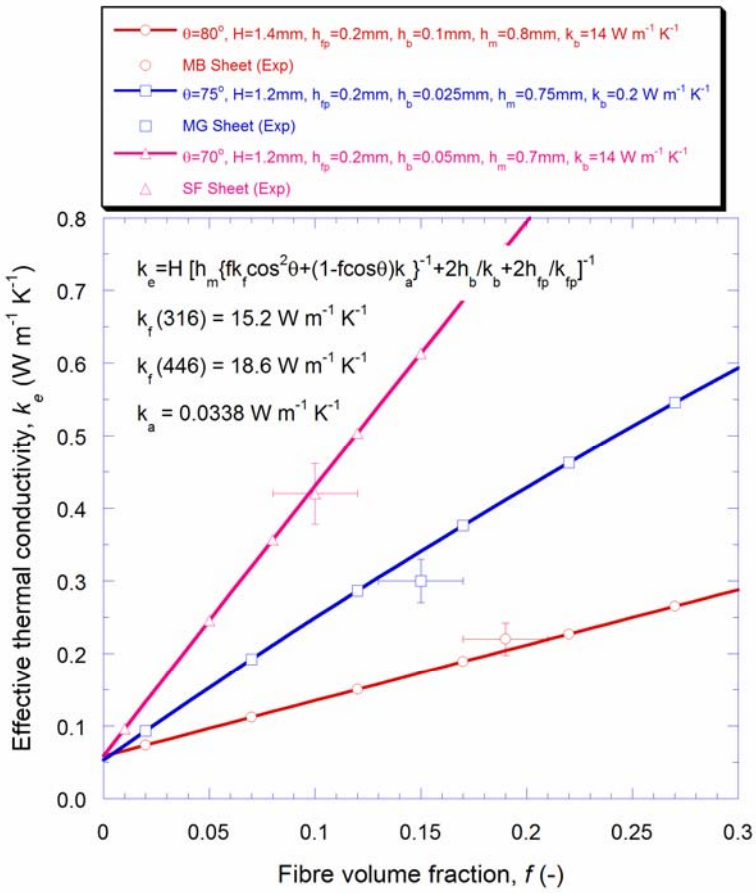

Figure 7-6. Effective thermal conductivity as a function of fibre volume fraction (f) for sandwich sheets incorporating a fibre mesh (felt) core. The curves are analytical model predictions, obtained using eqn.(7.7), while the three points with error bars (an average of five samples) correspond to measurements performed at a mean temperature of 100 °C.

The analytical model presented above can also be used to predict the effective conductivity of FG sheet. As a special case, if the fibres in the FG sheet are assumed as vertically aligned [1], then θ becomes 0° (see inset in Figure 7-7(a)). Hence, from eqn.(7.6) , the conductivity of the fibre and air column, k_{f+a}, can be written as:

$$k_{f+a} = fk_f + (1-f)k_a \tag{7.8}$$

The FG core is defined as the region containing the fibres, air column and adhesive. The core conductivity (k_c), can be predicted by incorporating the conductivity of the adhesive layer (k_b) with a thickness of h_b. Using a slab model in series, we can write:

$$k_c = h_c \left[h_f \left\{ fk_f + (1-f)k_a \right\}^{-1} + \frac{2h_b}{k_b} \right]^{-1} \tag{7.9}$$

where h_f is thickness of the flocked core. This expression can be extended to predict the effective thermal conductivity (k_e) of the overall sandwich structure:

$$k_e = H \left[h_f \left\{ fk_f + (1-f)k_a \right\}^{-1} + \frac{2h_b}{k_b} + \frac{2h_{fp}}{k_{fp}} \right]^{-1} \tag{7.10}$$

where H is the total thickness of the sandwich material.

Figure 7-7(a) shows the predicted plots of the core and effective conductivity, for various fibre volume fractions, when $\theta = 0°$. Using the values for f, k_f, k_a and k_b of 0.08, 15, 0.0338 and 0.3 W m^{-1} K^{-1} respectively, eqn.(7.9) predicts a core conductivity (k_c) of 0.42 W m^{-1} K^{-1}. The thermal conductivity of *Gurit Essex Betamate* epoxy (k_b) was found using the steady-state bi-substrate technique, from samples cured at conditions similar to the FG sheet. By employing eqn.(7.10), the effective conductivity (k_e) is predicted as 0.62 W m^{-1} K^{-1}, compared with the measured value of 0.48 ± 0.05 W m^{-1} K^{-1}. It is interesting to note that, although the conductivity of the fibre and air column (k_{f+a}) increases almost linearly with fibre volume fraction, the effective conductivity is less affected once f has exceeded 10%. This is due to the fact that k_e is dominated by the thick layer of low conductivity adhesive (h_b≈100 μm, k_e=0.3 W m^{-1} K^{-1}), which separates fibre ends from faceplates. However, fibre characterisation by micro-tomography has shown that the flocked fibres are not perfectly vertical, but inclined at a mean inclination angle of about 60º to the vertical axis (Figure 6-15). To consider the effect of fibre orientation, eqn.(7.6) is employed in predicting the conductivity of the flocked core (k_z). The predictions obtained are shown in Figure 7-4(b). It can be

seen that, at a volume fraction of 0.08, the effective conductivity is predicted as 0.42 W m^{-1} K^{-1}, as compared with an experimental value of 0.48 ± 0.05 W m^{-1} K^{-1}. The model that more closely resembles the actual core architecture is thus in general providing more reliable prediction.

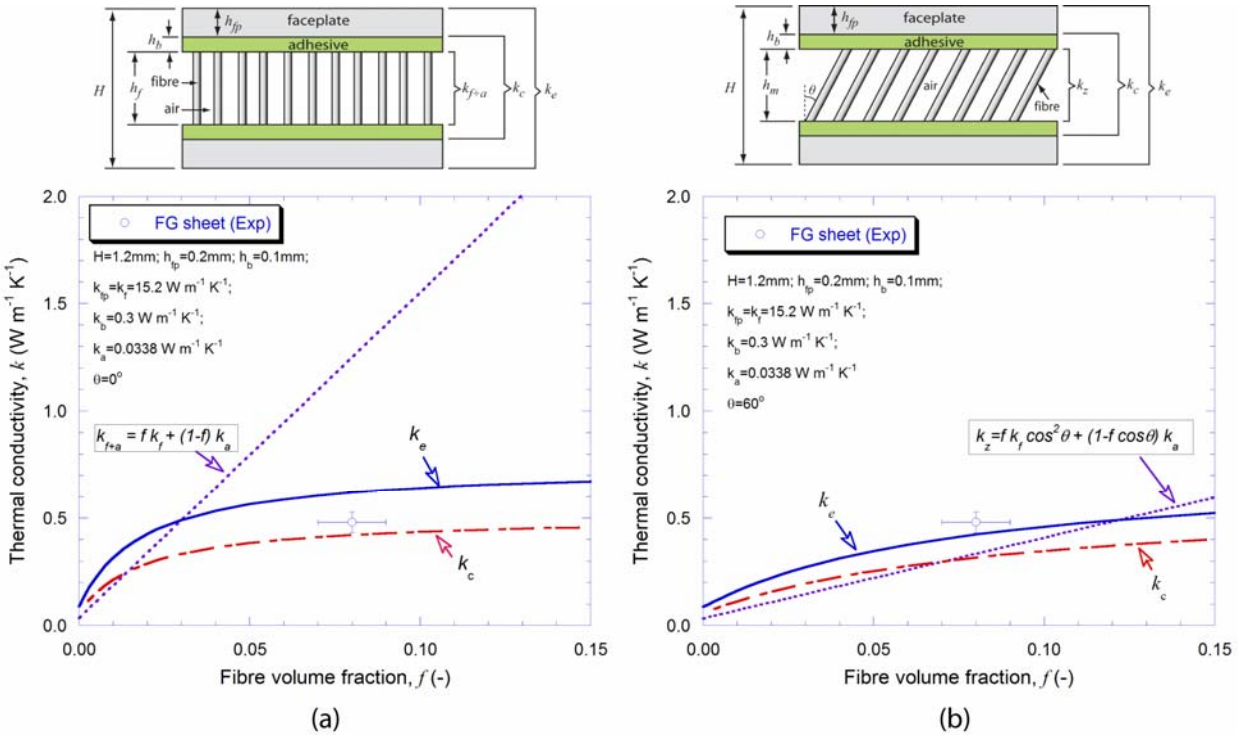

Figure 7-7. Core and effective thermal conductivities of the FG sheet, as a function of fibre volume fraction. Also shown here are the experimental data calculated from an average of five samples, measured at a mean temperature of 100 °C. (a) Assuming the flocked fibres at θ=0º, the curves (k_{f+a}, k_c and k_e) are predictions given by eqns.(7.8) to (7.10), (b) Assuming the fibres are inclined at θ=60º from the vertical axis, eqn.(7.6) is used to determine the combined conductivity of the inclined fibres and air (k_z).

7.2.1.2 In-plane conductivity

Based on the idealised unit cell model (Figure 7-4(b)), the resistances of fibre segments (R_f) and air column (R_a) in the in-plane directions (x and y) can be expressed as:

$$R_f = \frac{8L}{\pi D^2 k_f} \tag{7.11}$$

$$R_a = \frac{1}{Lk_a \cos\theta} \tag{7.12}$$

The total resistance of the sintered fibre felt in the x (or y) direction is given by:

$$R_x = \frac{8L}{8L^2 k_a \cos\theta + \pi D^2 k_f} \tag{7.13}$$

The in-plane conductivity can also be written as:

$$R_x = \frac{1}{k_x L \cos\theta} \tag{7.14}$$

Substituting eqn.(7.13) into (7.14), we obtain:

$$k_x = k_y = \frac{1}{2} f k_f \sin^2\theta + k_a \tag{7.15}$$

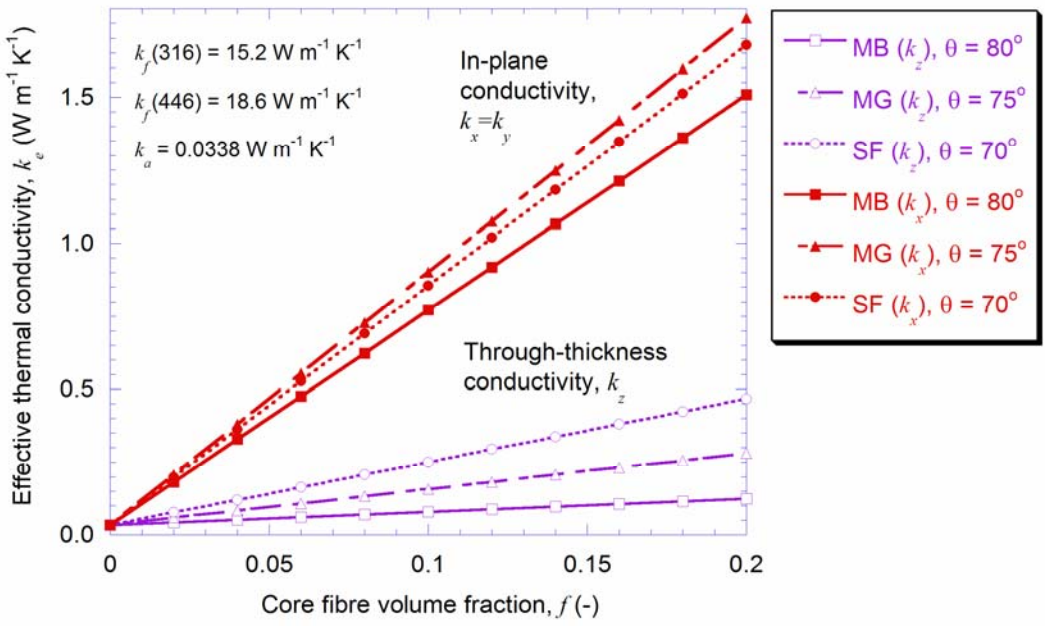

Figure 7-8. Effective thermal conductivity of MB, MG and SF cores as a function of core fibre volume fraction. The curves are predictions for through-thickness (k_z) and in-plane ($k_x \approx k_y$) conductivities, as given by eqns.(7.6) and (7.15), respectively. The mean fibre inclination angles (θ) of MB, MG and SF cores were assumed as 80º, 75º and 70º, respectively.

A comparison between through-thickness (k_z) and in-plane ($k_x \approx k_y$) conductivities of sintered fibre cores is shown in Figure 7-8. Clearly, the magnitude of in-plane conductivity is higher than the through-thickness conductivity, because of the more direct paths available for heat conduction in this direction. For the MB core, in-plane conductivity is predicted as about an order of magnitude greater than through-thickness conductivity, due to the higher inclination angle. In contrast, for both MG and SF cores, in-plane conductivities about five times greater are predicted. It is noted that, for cores made of stainless steel 446 fibres, because of higher inclination angle, MG is predicted as having higher in-plane conductivity, but lower through-thickness conductivity compared with SF.

7.2.2 Electrical Resistivity

Since thermal and electrical conductions are mathematically equivalent (§3.1), the thermal conduction model is also applicable for the prediction of electrical resistivity in highly porous fibre assemblies. The results presented in this section further extend the work of Markaki and Clyne (§3.3) [26].

7.2.2.1 Through-thickness (transverse) resistivity

From eqn.(7.6), since resistivity is the reciprocal of conductivity ($\rho = 1/k$) and $k_a = 0$ (electrical current only flows through the fibres), the resistivity of a unit cell of sintered fibre in through-thickness (transverse) direction simplifies to:

$$\rho_z = \frac{\rho_f}{f \cos^2 \theta} \tag{7.16}$$

where ρ_f is the fibre material resistivity. Using the same approach as above, the resistivity of faceplate-to-core bond layer can be expressed as:

$$\rho_b = \frac{\pi D^2 R_b}{h_b f \cos\theta} \tag{7.17}$$

By omitting the resistivity of faceplates, from eqn.(7.7), the resistivity of the whole sandwich sheet in through-thickness direction can be written as:

$$\rho_e = \frac{1}{fH \cos\theta}\left[\frac{\rho_f h_m}{\cos\theta} + 2\pi D^2 R_b\right] \tag{7.18}$$

where R_b is the electrical resistance of the braze or adhesive layer. Figure 7-9 shows a comparison between experimental data and model predictions. Eqn.(7.16) is valid only when a braze metal is used as core-faceplate bonding, which results in negligibly small contact resistance at the interface. For MB and SF sheets, good agreements with the model can be obtained when the fibres are assumed to incline at about 80° and 70°, respectively. The use of an adhesive for core-faceplate bonding in the MG sheet necessitates an additional contact resistance at the interface ($R_b \approx 5.6$ MΩ), to attain good agreement with experimental data.

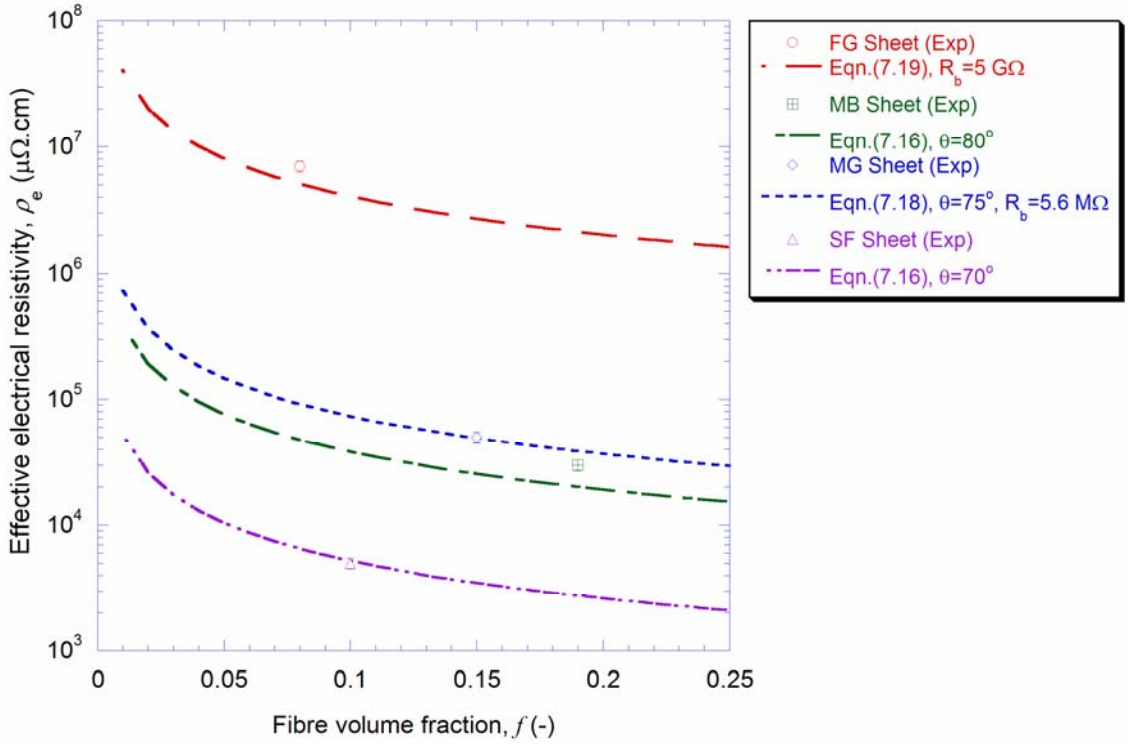

Figure 7-9. Through-thickness electrical resistivity as a function of fibre volume fraction. Curves are analytical model predictions while the points are experimental data. The electrical resistivity of stainless steel 316 and 446 is taken as 74 and 61 μΩ cm, respectively. Resistivities of brazed sandwich sheets (MB and SF) are predicted using eqn.(7.16), MG sheet predicted by eqn.(7.18) and FG sheet using eqn.(7.19).

In a similar fashion, eqn.(7.10) can be modified to predict the resistivity of a perfectly aligned flocked core ($\theta = 0°$). Since the resistance of the faceplate is negligible in comparison with that of adhesive, the effective resistivity can be expressed as:

$$\rho_e = \frac{1}{fH}\left[\rho_f h_f + 2\pi D^2 R_b\right] \tag{7.19}$$

where R_b is the contact resistance of the epoxy resin (*Gurit Essex Betamate*). From Figure 7-9, it is clear that the model is consistent with measurement only when a high contact resistance, of the order of $G\Omega$, is assumed.

Substituting eqn.(7.17) into (7.19), we obtain:

$$\rho_e = \frac{1}{H}\left[\frac{\rho_f h_f}{f} + 2\rho_b h_b\right] \tag{7.20}$$

Using eqn.(7.20), the adhesive resistivity (ρ_b) is estimated as 2×10^7 μΩ cm, which is within the range reported for a typical epoxy [151]. In any case, it is apparent that the effective resistivity of FG sheet is dominated by ρ_b, so, the contribution from the fibrous core is relatively small.

7.2.2.2 In-plane resistivity

Based on eqn.(7.15) and substituting $\rho = 1/k$, the in-plane electrical resistivity is given by:

$$\rho_x = \rho_y = \frac{2\rho_f}{f\sin^2\theta} \tag{7.21}$$

Figure 7-10 shows the predicted in-plane resistivity as a function of fibre volume fraction, shown here with experimental data for two of the sintered cores (MB and MG). Predictions were made by assuming that the MB, MG and SF cores have mean inclination angles of 80º, 75º and 70º, respectively. Using eqn.(7.21), their resistivities are predicted as 803, 872 and 1.38×10^3 μΩ cm, respectively. In comparison with experimental data, it can be seen that the model under-predicts the resistivities by as much as 20%. Nevertheless, a correct trend is observed, since the resistivity of MG is predicted to be higher than MB, which is consistent with the measurements.

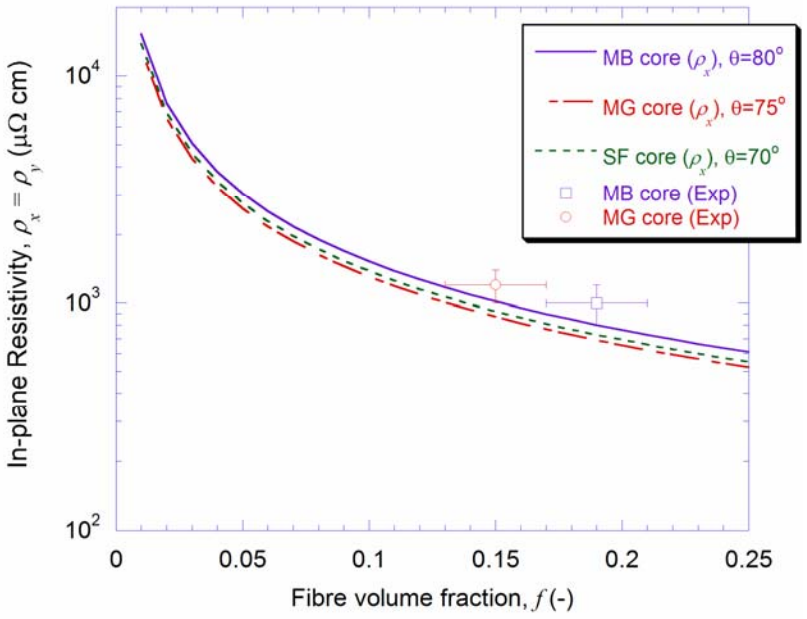

Figure 7-10. In-plane resistivity of MB, MG and SF sintered cores as a function of fibre volume fraction. The curves are predictions given by eqn.(7.21), while the two points are measurements. The electrical resistivity of stainless steel 316 and 446 is taken as 74 and 61 μΩ cm, respectively.

7.2.3 Effect of Fibre Orientation on Conductivities

The expressions derived in §7.2.1 and §7.2.2 can be used to study the effects of fibre inclination angle on conductivities in both through-thickness and in-plane directions. From Figure 7-11, it can be seen that through-thickness thermal conductivity decreases with increasing inclination angle, while in-plane conductivity increases with the angle. In contrast, the opposite is observed for the case of electrical resistivity (Figure 7-12). These changes in conductivities occur when the fibrous core undergoes compression in through-thickness direction, which leads to an increase in inclination angle. Also, it is noted that the core exhibits isotropic properties at $\theta \approx 55°$, i.e. when $k_x = k_y = k_z$ or $\rho_x = \rho_y = \rho_z$. However, for all the cores being investigated here, since θ is clearly greater than 55º (§6.2.2.4), they tend to be transversely isotropic and exhibiting higher in-plane conductivities.

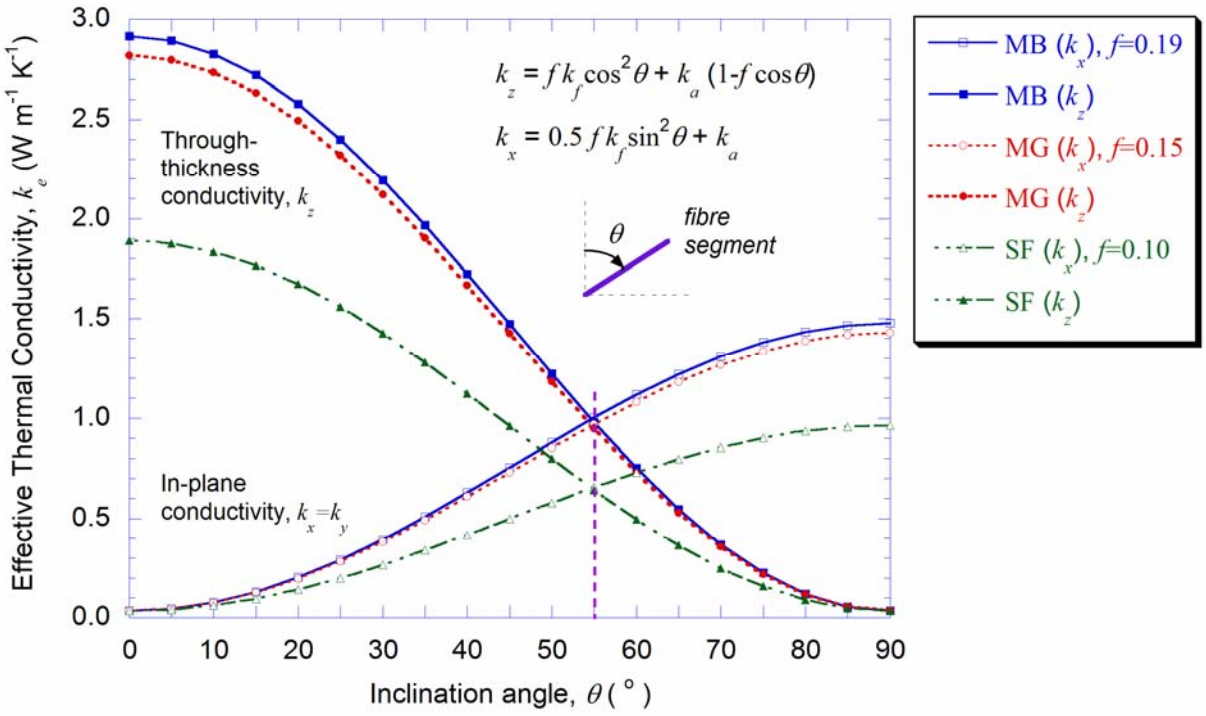

Figure 7-11. Effective thermal conductivity of transversely isotropic cores (MB, MG and SF), as a function of mean fibre inclination angle. The through-thickness and in-plane conductivities are predicted using eqns.(7.6) and (7.15), respectively.

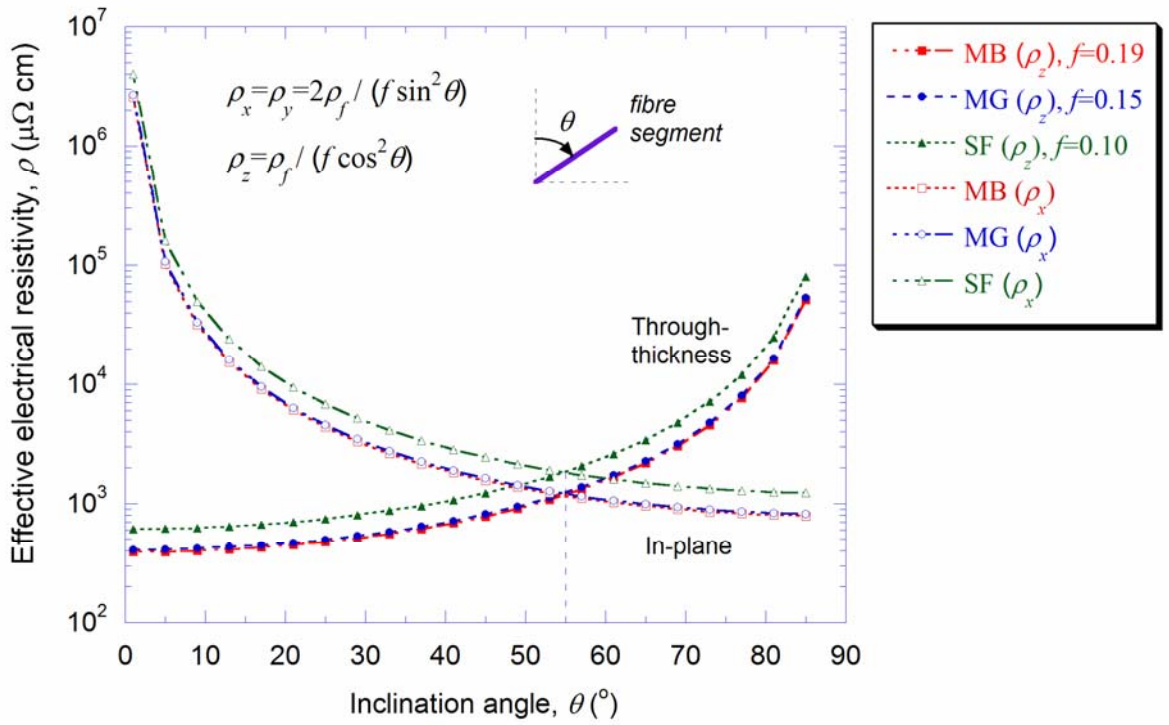

Figure 7-12. Electrical resistivity of MB, MG and SF cores in through-thickness and in-plane directions, as a function of fibre inclination angle. Predictions are obtained using eqns.(7.16) and (7.21), respectively.

7.3 Modelling of Through-thickness Conductivities using an Orientation Distribution Model

7.3.1 Model Formulation

The main limitation of the idealised unit cell model (§7.2) lies in its assumption of all fibres lying at the same inclination (θ) to the sheet normal. Of course, this simplifies the analysis and is useful when the statistical distribution is not available. However, it does not incorporate the effect of the actual fibre orientation distribution, which has been measured in the current work (§6.2.2.4).

In order to formulate an orientation distribution model, several assumptions are made. All fibre segments (Figure 6-6) are presumed to be interconnected from one end to the other. The contact resistance at the joint is assumed to be negligible. Since the thermal conductivity of stainless steel fibres (k_f: 15~18 W m^{-1} K^{-1}) is about three orders of magnitude greater than air (k_a : 0.0338 W m^{-1} K^{-1}), only solid conduction is considered.

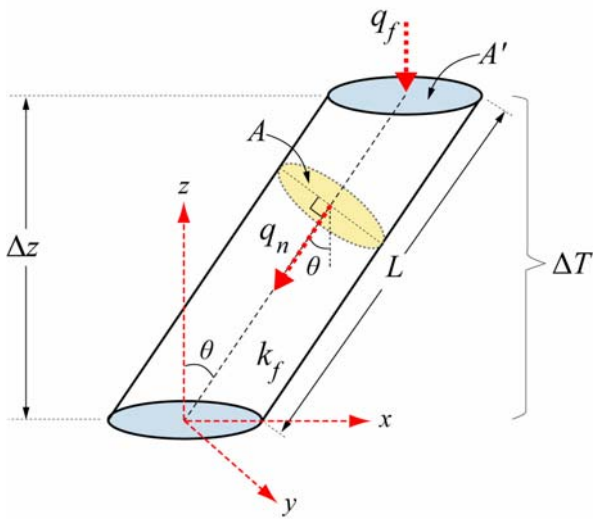

Figure 7-13. Schematic of a fibre segment of length L, orientated at an inclination angle of θ from the vertical axis. The temperature drop across the fibre segment is ΔT.

Consider a fibre segment of length L, inclined at an angle θ to the macroscopic heat flow direction (z-axis), as illustrated in Figure 7-13. The temperature gradient across the segment is $\Delta T/\Delta z$. The length (L) and cross-sectional area (A') of the inclined segment can be written as:

$$L = \frac{\Delta z}{\cos\theta} \tag{7.22}$$

$$A' = \frac{A}{\cos\theta} \tag{7.23}$$

The heat flux flowing along the segment normal axis, q_n, is given by:

$$q_n = \frac{q_f A'}{A} = \frac{q_f}{\cos\theta} \tag{7.24}$$

where q_f is the heat flux entering the segment at surface A'.

From Fourier's Law, q_n can also be expressed as:

$$q_n = k_f\left(\frac{\Delta T}{L}\right) = k_f \cos\theta\left(\frac{\Delta T}{\Delta z}\right) \tag{7.25}$$

By substituting eqn.(7.24) into (7.25), we obtain:

$$q_f = k_f \cos^2\theta \left(\frac{\Delta T}{\Delta z}\right) \tag{7.26}$$

The effective thermal conductivity, k_e, is related to q_f through the following expression:

$$q_f = k_e \left(\frac{\Delta T}{\Delta z}\right) \tag{7.27}$$

Substituting eqn.(7.26) into (7.27), the effective conductivity (k_e) of a single fibre segment inclined at θ is found as:

$$k_e = k_f \cos^2\theta \tag{7.28}$$

Consequently, for a core assembly with fibre volume fraction of f, we can write:

$$k_e = f k_f \cos^2\theta \tag{7.29}$$

The orientation distribution function $P(\theta)$, over the range 0 to $\pi/2$, must satisfy:

$$\int_0^{\pi/2} P(\theta)\ \sin\theta\ d\theta = 1 \tag{7.30}$$

Therefore, averaging the effective conductivity in eqn.(7.29) yields:

$$k_e = f k_f \int_0^{\pi/2} \cos^2\theta\ P(\theta)\ \sin\theta\ d\theta \tag{7.31}$$

However, the raw orientation distribution data obtained from skeletonisation analysis (§6.2.2.4) are generally in numerical, rather than functional form. So, in order to calculate the effective conductivity using eqn.(7.31), discretisation and normalisation of $P(\theta)$ are performed as follows:

$$\int_0^{\pi/2} P(\theta)\ \sin\theta\ d\theta \approx \sum_i^n P(\theta_i)\ \sin\theta_i\ \Delta\theta_i \tag{7.32}$$

$$P(\theta_i) = \frac{N_{\theta_i}}{\sin\theta_i\ \Delta\theta_i} \cdot \frac{1}{\sum_i^n N_{\theta_i}} \tag{7.33}$$

where N_{θ_i} designates the number of fibre segments falling into a bin size of $\Delta\theta_i$. By substituting eqns.(7.32) and (7.33) into eqn.(7.31), k_e can now be expressed as:

$$k_e = fk_f \cdot \frac{\sum_i^n N_{\theta_i} \cos^2 \theta_i}{\sum_i^n N_{\theta_i}} \tag{7.34}$$

For a core composed of randomly oriented (isotropic) fibres, since $P(\theta)$=1, its effective conductivity is given by:

$$k_e = fk_f \int_0^{\pi/2} \cos^2 \theta \ \sin\theta \, d\theta \tag{7.35}$$

Consequently,

$$k_e = \frac{1}{3} fk_f \tag{7.36}$$

Taking

$$\xi = \frac{\sum_i^n N_{\theta_i} \cos^2 \theta_i}{\sum_i^n N_{\theta_i}} \tag{7.37}$$

Comparing eqn.(7.36) with (7.34), we can conclude that, for an isotropic fibre distribution:

$$\xi = \frac{1}{3} \tag{7.38}$$

Hence, the coefficient ξ can serve as a parameter for evaluating the degree of anisotropy of the orientation distribution. The effective electrical resistivity (ρ_e) in the through-thickness direction can also be found from eqn.(7.34), by replacing ρ_f with $1/k_f$:

$$\rho_e = \frac{\rho_f}{f} \cdot \frac{\sum_i^n N_{\theta_i}}{\sum_i^n N_{\theta_i} \cos^2 \theta_i} \tag{7.39}$$

7.3.2 Model Predictions

Table 7-3 compares predictions from the orientation distribution model with corresponding experimental data. It can be seen that agreement is good, at least to an order of magnitude. For the SF core (f~0.10), agreement is excellent. However, discrepancies between prediction and measurement become more apparent as the core fibre volume fraction (f) increases. The conductivities of 316L and 446 fibre felts are over-predicted by about 150 and 200%, respectively. This can be explained in terms of the formulation of the model itself, which assumes that the ends of all fibre segments are interconnected. In fact, in an actual sintered fibre assembly (Figure 6-1), not all segments that come into contact are necessarily well-bonded. As a result of this, the model introduces conduction paths which are not actually present, particularly at higher volume fractions.

Since $\xi = 0.288$ for the flocked core, this structure exhibits the orientation distribution 'closest to' isotropic (random). This is expected, since flocked fibre segments are shorter, and not bonded to each other, so they experience less constraint from neighbouring fibres. In contrast, for the three other bonded fibre assemblies, it can be seen that ξ increases with the fibre volume fraction. This suggests that, an isotropic core is more difficult to attain as fibre segment aspect ratio (L/D) and fibre volume fraction go up.

Table 7-3. Through-thickness thermal conductivity and electrical resistivity of flocked (FG) core, sintered fibre felts and SF core. The thermal conductivity and electrical resistivity are predicted using eqns.(7.34) and (7.39), respectively. The orientation distributions presented in Figures 6-15 to 6-18 are used as inputs for the model calculations. Manipulation of the orientation distribution statistical data can be found in the Appendix. The material properties used are as follows:- 316L fibres (k_f=15.2 W m^{-1} K^{-1}, ρ_f=74 μΩ cm), 446 fibres (k_f=18.6 W m^{-1} K^{-1}, ρ_f=61 μΩ cm). The relevant experimental data are taken from Table 7-1 and Table 7-2.

Core type	Fibre vol. fraction, f	Orientation Distribution Model			Experimental Data	
		ξ (1/3 if random)	Thermal conductivity (W m^{-1} K^{-1})	Electrical resistivity (μΩ cm)	Thermal conductivity (W m^{-1} K^{-1})	Electrical resistivity (μΩ cm) ± 300
Flocked (FG) core	0.08	0.288	0.35	3.21×10^3	0.48±0.02*	-
316L pre-sintered felt (MB core)	0.19	0.145	0.42	2.69×10^3	0.14±0.02	1.6×10^3
446 pre-sintered felt (MG core)	0.15	0.154	0.43	2.65×10^3	0.17±0.02	1.8×10^3
Short fibre 3-D array (SF) core	0.10	0.196	0.36	3.11×10^3	0.42±0.04	$3.0\times10^{3*}$

*Measurements were performed on an assembled sandwich structure, since it was not possible to detach the core without first destroying the original structure.

7.4 Modelling of Effective Conductivities using the Finite-Element (FE) Method

For both idealised unit cell and orientation distribution models, in order to make the prediction of conductivities possible, various assumptions are necessary to simplify the actual fibrous core architecture. Despite being easy to implement, more complex features of the core, such as connectivity and tortuosity of long fibres, cannot be fully represented using these simplified models. In order to predict the conductivities of real fibre assemblies, a numerical method such as the finite-element (FE) method is required. The FE method has been previously used by several workers who investigated the effective thermo-elastic properties of woven fabric composites [152-154] and short fibre composites [155, 156]. However, their structures are far less complex than bonded fibre assemblies, and in some instances can be modelled using a unit cell.

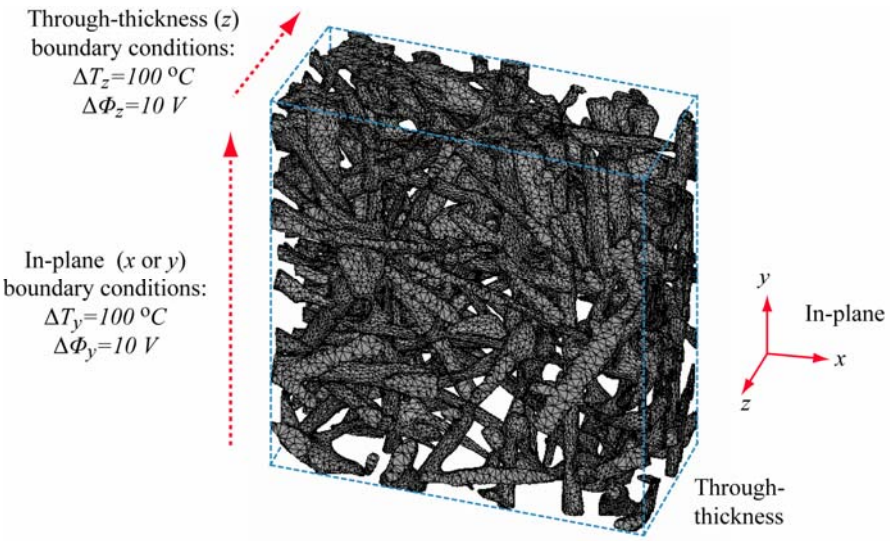

Figure 7-14. A typical FE mesh generated for a short fibre 3-D array (SF) core. The mesh has about 300,000 tetrahedral elements. Also shown here are the thermal and electrical boundary conditions applied to through-thickness (z) and in-plane (x or y) conduction simulations.

A three-dimensional FE mesh was generated using the reconstructed fibre assembly surfaces obtained from X-ray micro-tomography scans, similar to those depicted in Figure 6-5. Figure 7-14 depicts a typical mesh of a SF core used in the FE simulation, showing the 3-D tetrahedral elements and the relevant boundary conditions for thermal and electrical conduction simulations. Because of the high thermal conductivity of steel fibres, compared with air, only solid conduction was modelled and the contribution from the gaseous phase was assumed negligible. All models were solved using the ANSYS finite-element code (Release 8.1). The type of element used was *SOLID69* [157], which has 3-D thermal and electrical conduction capabilities. For heat conduction simulation, the

temperature boundary conditions were applied by assigning a temperature drop (ΔT) of 100 ºC through the model. On the other hand, for electrical conduction simulation, a potential drop $(\Delta \Phi)$ of 10 V was applied. In all cases, all lateral faces located parallel to the macroscopic fluxes were assumed to be perfectly insulating ($q = 0$ or $J = 0$).

Table 7-4 lists the details of all fibrous sandwich core FE models employed in the analyses. Volume of fibre (V_f) present in the model is calculated by summing up the volume of each individual tetrahedral element (V^e), that is:

$$V_f = \sum_i^n V_i^e \tag{7.40}$$

where the superscript *e* denotes a particular element, while *n* is the total number of elements. The total volume of the model (V_{tot}), is defined as volume of the outer boundaries enclosing the 3-D mesh, consisting of both fibres and air gaps. The volume fraction (*f*) of the model is therefore given by:

$$f = \frac{\sum_i^n V_i^e}{V_{tot}} \tag{7.41}$$

Table 7-4. Details of the 3-D finite-element mesh of sandwich cores used in this study.

Core type	V_f (mm^3)	V_{tot} (mm^3)	f (-)	Number of 3-D elements
Flocked (FG) core	0.097	1.989	0.049	~80,000
316L pre-sintered felt (MB core)	0.265	1.349	0.197	~300,000
446 pre-sintered felt (MG core)	0.284	1.772	0.160	~300,000
Short fibre 3-D array (SF) core	0.738	4.735	0.156	~300,000

Figure 7-15 shows the temperature and potential fields developed in a SF core at steady-state conditions, using the applied boundary conditions. Similar fields were obtained for the other cores.

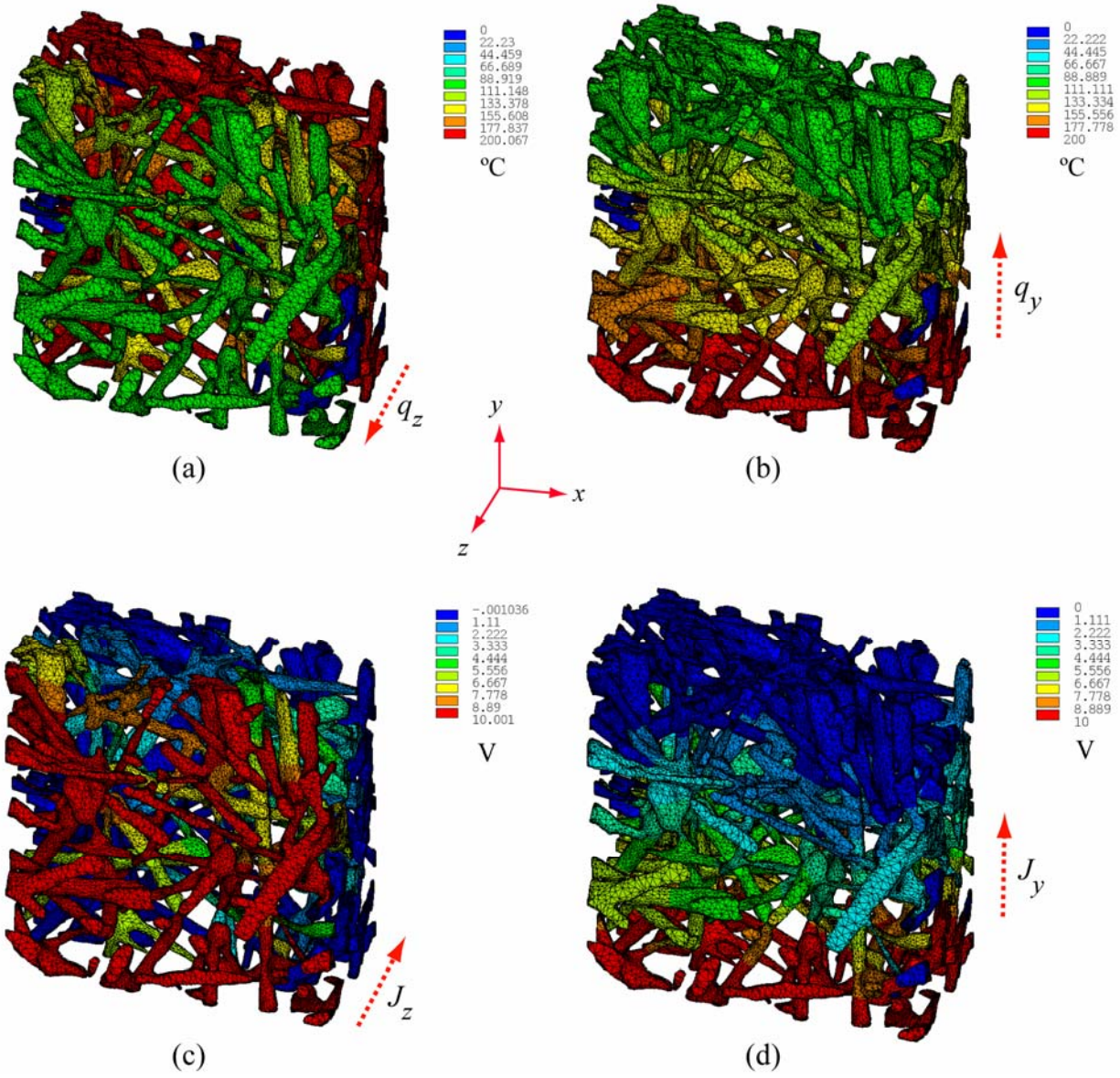

Figure 7-15. Thermal and electrical potential fields obtained from finite-element simulations of heat and electrical conductions in a short fibre 3-D array (SF) core. The through-thickness (z) profiles are shown in (a) and (c), while the in-plane (y) profiles are depicted in (b) and (d). A temperature drop (ΔT) of 100 ºC was used in heat conduction simulations while a potential drop ($\Delta \Phi$) of 10 V was used for electrical conduction simulations. q and J designate the macroscopic heat and electrical charge flow directions, respectively. All lateral faces parallel to the fluxes were modelled as perfectly insulating (q=0 or J=0).

The steady-state heat conduction model solves for the nodal temperatures, which were then used to calculate the heat flux flowing across every individual element (q^e). By assuming that the fibrous core is a continuum, the volume average heat flux, $\langle q \rangle$, is defined as:

$$\langle q \rangle = \frac{1}{V_{tot}} \int_V q^e dV = \frac{\sum_{i=1}^{n} q_i^e V_i^e}{V_{tot}} \tag{7.42}$$

The volume averaging method of eqn.(7.42) is similar to that used by Dasgupta and Agarwal [152]. Subsequently, $\langle q \rangle$ is used to determine the effective thermal conductivity, k_e:

$$k_{e(z)} = \frac{\sum_{i=1}^{n} q_i^e V_i^e}{V_{tot}} \cdot \frac{\Delta z}{\Delta T} \tag{7.43}$$

where the subscript (z) designates the through-thickness direction, while Δz is the thickness in that direction. In a similar fashion, the volume average electric charge flux, $\langle J \rangle$, and the effective electrical resistivity, ρ_e, can be calculated as follows:

$$\langle J \rangle = \frac{1}{V_{tot}} \int_V J^e dV = \frac{\sum_{i=1}^{n} J_i^e V_i^e}{V_{tot}} \tag{7.44}$$

$$\rho_{e(z)} = \frac{V_{tot}}{\sum_{i=1}^{n} J_i^e V_i^e} \cdot \frac{\Delta \Phi}{\Delta z} \tag{7.45}$$

The conductivities and resistivities predicted using the FE models are tabulated in Table 7-5 and Table 7-6, respectively. It can be seen that, for the SF core, all model predictions agree well with the experimental data. However, for cores containing higher volume fraction of fibres (MG and MB), the thermal conductivities are over-predicted, while electrical resistivities are under-predicted. In fact, the accuracy of the FE analysis is strongly dependent on the quality of the reconstructed fibres (from tomography) used in creating the 3-D finite-element meshes. Because of the limited resolution available in tomographic imaging (~10 μm), surface reconstruction tends to produce many spurious bonds (joints) among fibre surfaces lying in close proximity. These act as additional conduction paths, leading to an increase in conductivities. Unfortunately, there is no easy way to distinguish real bonds from spurious ones using the tomography technique. In general, the chances of introducing spurious bonds will increase with fibre length and core fibre volume fraction, which probably was the case in both MB and MG finite-element meshes. Despite these complications, the predicted values were broadly consistent with measurements, both in through-thickness and in-plane directions.

Table 7-5. Finite-element (FE) predictions of through-thickness and in-plane thermal conductivities. The temperature drops across all models were 100 ºC. The experimental data of through-thickness conductivities are included here for comparison.

Core type	Through-thickness (z)					In-plane ($x \approx y$)			
	$\left.\sum_{i=1}^{n} q_i^e V_i^e\right\|_z$ $\times 10^{-3}$ (W m)	$\langle q_z \rangle$ $\times 10^4$ (W m^{-2})	Δz (mm)	FE model $k_{e(z)}$ (W m^{-1} K^{-1})	Experimental data (W m^{-1} K^{-1})	$\left.\sum_{i=1}^{n} q_i^e V_i^e\right\|_y$ $\times 10^{-3}$ (W m)	$\langle q_y \rangle$ $\times 10^4$ (W m^{-2})	Δy (mm)	FE model $k_{e(y)}$ (W m^{-1} K^{-1})
Flocked (FG)	0.167	8.392	0.386	0.32	0.48±0.02*	-	-	-	-
316L pre-sintered felt (MB core)	0.303	22.478	0.467	1.05	0.14±0.02	0.149	10.920	1.705	1.86
446 pre-sintered felt (MG core)	0.180	10.174	0.606	0.62	0.17±0.02	0.157	8.873	1.729	1.53
Short fibre 3-D array (SF)	0.181	3.827	0.928	0.36	0.42±0.04	0.232	4.900	2.184	1.07

*Measurement was performed on an assembled sandwich structure, instead of on the core itself.

Table 7-6. Results from finite-element (FE) calculations to determine the through-thickness and in-plane electrical resistivities. The voltage drops across all FE models ($\Delta\Phi$) were 10 V. The experimental data are included for comparison.

(a) Through-thickness Electrical Resistivity, ρ_z

Core type	$\left.\sum_{i=1}^{n} J_i^e V_i^e\right\|_z$ (A m)	$\langle J_z \rangle$ $\times 10^8$ (A m^{-2})	Δz (mm)	FE model $\rho_{e(z)}$ (μΩ cm)	Experimental data (μΩ cm) ± 300
Flocked (FG)	1.463	7.354	0.386	3.52×10^3	-
316L pre-sintered felt (MB core)	2.659	19.713	0.467	1.09×10^3	1.6×10^3
446 pre-sintered felt (MG core)	1.296	7.314	0.606	2.26×10^3	1.8×10^3
Short fibre 3-D array (SF)	1.565	3.306	0.928	3.26×10^3	$3.0\times10^{3*}$

*Measurement was performed on an assembled sandwich structure.

(b) In-plane Electrical Resistivity, $\rho_x \approx \rho_y$

Core type	$\left.\sum_{i=1}^{n} J_i^e V_i^e\right\|_y$ (A m)	$\langle J_y \rangle$ $\times 10^8$ (A m^{-2})	Δy (mm)	FE model $\rho_{e(y)}$ (μΩ cm)	Experimental data (μΩ cm) ± 200
316L pre-sintered felt (MB core)	1.171	8.682	1.705	677.5	1000
446 pre-sintered felt (MG core)	1.102	6.220	1.729	929.8	1200
Short fibre 3-D array (SF)	1.953	4.125	2.184	1100.0	-

Chapter 8: Modelling of the Resistance Spot Welding (RSW) of Thin Sandwich Sheets

A finite-element (FE) numerical model has been developed to simulate resistance spot welding (RSW) of thin stainless steel sandwich sheets. Such sheets have a collapsible core, with relatively low thermal and electrical conductivities, compared with monolithic materials. The model is based on a sequential-coupling formulation to simulate mechanical and thermal-electrical effects. The fibrous core is treated as an isotropic continuum. For simulation of the mechanical effects, it is shown that a crushable foam constitutive relationship can be successfully employed to model the large strain deformation taking place during the squeeze stage. The transient thermal-electrical finite-element solution takes into account temperature-dependent properties of the collapsed core, phase transformation and interfacial contact resistances. The model incorporates complex interplays between various factors (mechanical, thermal, electrical & metallurgical) and is useful for investigating the effects of welding parameters (welding force, current & time) and the welding characteristics (weld pool formation and nugget evolution). Comparisons between model predictions and experiments are presented in Chapter 9.

8.1 RSW Finite-Element Model Formulation

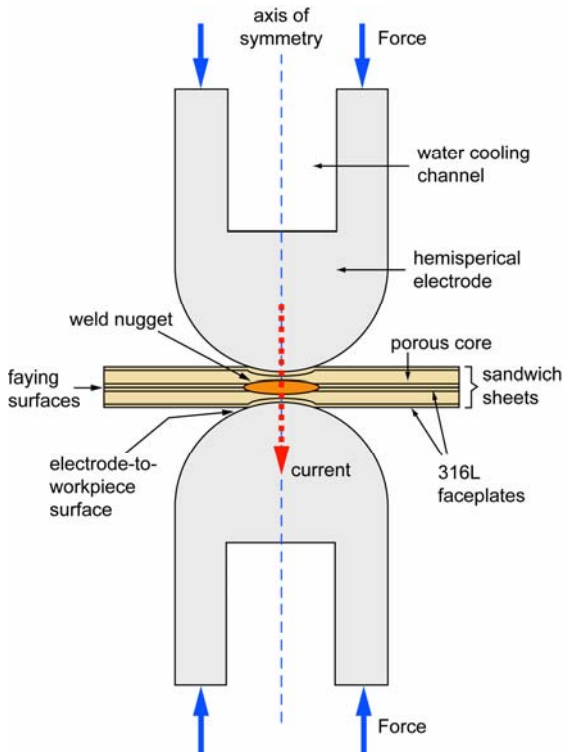

Figure 8-1. Schematic representation of resistance spot welding (RSW) of thin stainless steel sandwich sheets. Shown here are the hemispherical face electrodes (type-F) used in the welding experiments. As a result of electrode compression, the porous sandwich sheets exhibit much more substantial mechanical deformation (collapse), compared with monolithic (dense) sheets.

Modelling the RSW of sandwich sheets with a highly porous core requires simulation of mechanical deformation, coupled with current and heat flow (Figure 8-1). The process is initiated with a squeeze stage, during which two sandwich sheets are compressed between a pair of electrodes. This is

followed by a weld period, when a high current (kA) is passed through the electrodes for several hundred milliseconds, to generate intense heating at the faying surfaces, resulting in the formation of a weld pool. Current flow is then discontinued during a hold time, while the electrode force is maintained, to promote rapid heat dissipation and solidification of the weld nugget. These important changes occurring at different stages of the process must be incorporated into the numerical model.

Compared with the welding of monolithic sheets, several major differences can be observed. In terms of mechanical deformation, more significant changes to the porous core are expected during the process. In terms of transport properties, the porous cores have considerably lower thermal and electrical conductivities (Chapter 7). Moreover, the core deformation alters the fibre volume fraction and fibre orientation distribution, leading to changes in conductivities.

In order to simulate the RSW process rigorously, a fully-coupled mechanical-thermal-electrical FE model would be desirable. However, this is computationally intractable due to the high degree of non-linearity involved in the analysis, as a consequence of large plastic mechanical deformation of the sandwich cores, interfacial contact changes (mechanical contacts, interfacial thermal and electrical contact conductances), phase transformations during nugget formation, temperature-dependent material properties etc. Therefore, a more manageable approach has been employed, based on a sequentially-coupled mechanical-thermal-electrical finite-element formulation. Furthermore, by exploiting the radial symmetry of the RSW set-up (Figure 8-1), a 2-D axisymmetric finite-element model is expected to be satisfactory (Figure 8-2). The mechanical and thermal-electrical models are depicted in Figure 8-2(a) and (b), respectively. The mesh is refined in regions subject to high stresses and/or high thermal/potential gradients, which include the electrode-workpiece (E-W) interfaces, faceplates and cores in the vicinity of the hemispherical tips. The mechanical problem is first solved using appropriate load and displacement boundary conditions to obtain the stress and strain fields. Subsequently, the deformed geometry from mechanical analysis is assigned a new mesh, with appropriate thermal and electrical boundary conditions, and then solved for the potential and temperature fields.

This sequentially-coupled model does not take into account the effects of thermo-mechanical coupling. However, the additional mechanical deformation caused by softening (reduction in yield strength) and thermal expansion as the temperature increases, should be small, compared with the large deformation attributed to core collapse (in squeeze stage).

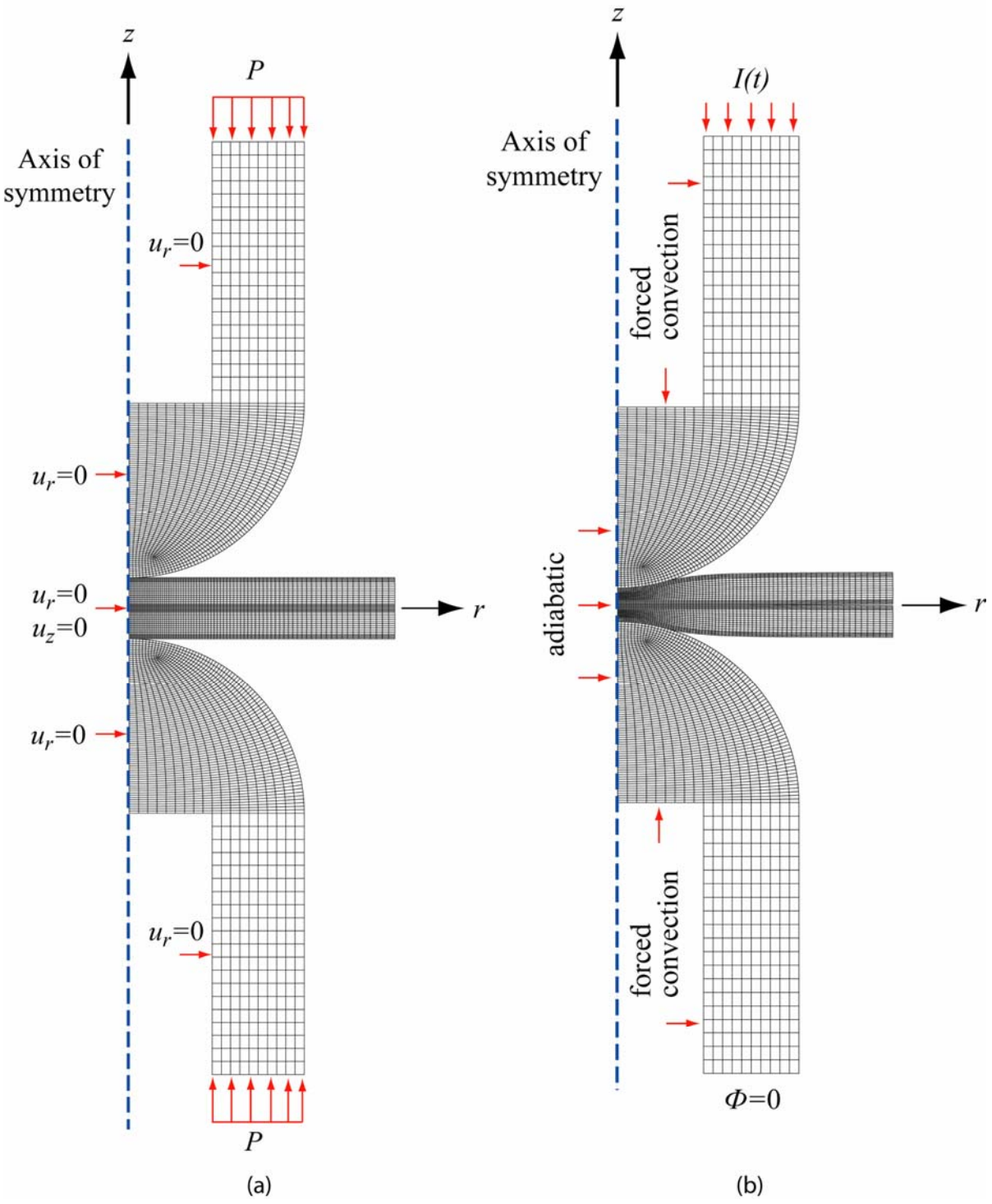

Figure 8-2. Axisymmetrical finite-element meshes with the relevant boundary conditions assigned, for (a) mechanical and (b) thermal-electrical analyses. The thermal-electrical analysis uses the deformed geometry of mechanical analysis. P is the uniformly distributed pressure boundary condition, u_r and u_z are displacements in the radial and axial directions, respectively. $I(t)$ is the time-dependent current and Φ=0 is the voltage boundary condition.

8.2 Mechanical Modelling

A quasi-static mechanical model has been developed to simulate the core collapse induced by electrode compression, occurring at the start of the welding process. The electrodes and sandwich sheets are modelled using 4-node bilinear axisymmetric quadrilateral elements (*CAX4R*) in ABAQUS/Explicit [158]. Each node has two degrees of freedom – translations in the nodal x and y directions. The ABAQUS/Explicit solver is chosen due to its capability in resolving complicated mechanical contact problems and simulating large strain deformations. The FE solutions predict the geometry of the collapsing sandwich structure, apparent contact area and stress-strain fields.

The FE mesh and the applied boundary conditions are depicted in Figure 8-2(a). The electrode force (2.5 kN) is assigned via a uniformly distributed pressure boundary condition ($P \approx 16.6$ MPa) at both electrode ends. Axial and radial displacement boundary conditions are applied to the relevant model boundaries to satisfy the symmetrical conditions. The mechanical contacts at the electrode-to-workpiece (E-W) and faying (W-W) interfaces are modelled using a 'penalty contact' algorithm with 'finite-sliding' formulation [158]. Each pair of interfaces is treated as two deformable surfaces - a 'master' and a 'slave' surface, which can separate, slide or rotate with respect to each other. To prevent penetration of contacting pairs into each other, the element size has to be sufficiently small and of comparable dimensions. Coulomb friction is modelled between the contacting pairs, by assuming a typical value for the coefficient of friction ($\mu = 0.2$). It is assumed that all faceplate-to-core interfaces are perfectly bonded, so the braze or polymeric adhesive layers are not incorporated into the model. In addition, since the porous core can undergo substantial deformation, an 'adaptive meshing' technique [158] is applied to the cores to prevent excessive element distortion during loading.

The stainless steel (316L) faceplates are modelled using elastic-plastic constitutive relationships, with isotropic hardening and a von Mises yield criterion. The nominal stress-strain curve of 316L is shown in Figure 8-3(a). The copper (Cu-Cr-Zr) electrode is modelled as an elastic-perfectly plastic material, with Young's modulus, yield strength and Poisson's ratio of 130 GPa, 350 MPa and 0.33, respectively [159]. Figure 8-3(b) depicts the compressive stress-strain curves of MG and SF sandwich sheets. It may be noted that the compressive response is similar to those of other highly porous cellular solids (e.g. foams), and exhibit a plastic plateau prior to densification at higher strains [80]. It can be seen that both cores have similar plateau stresses, but SF exhibits higher flow stresses after densification ($\varepsilon > 35\%$). Evidently, the strengths of the porous cores are significantly lower than that of monolithic (316L) sheet. In the tested samples, the core elastic constants are not accurately known, since the elastic regime was difficult to trace when testing a thin sample (~1 mm). The data

collected prior to 5% strain are mainly due to bedding-down of the compression platens onto the faceplates at the start of the compression test. However, since the plastic strain is orders of magnitude greater than elastic strain, this is not important.

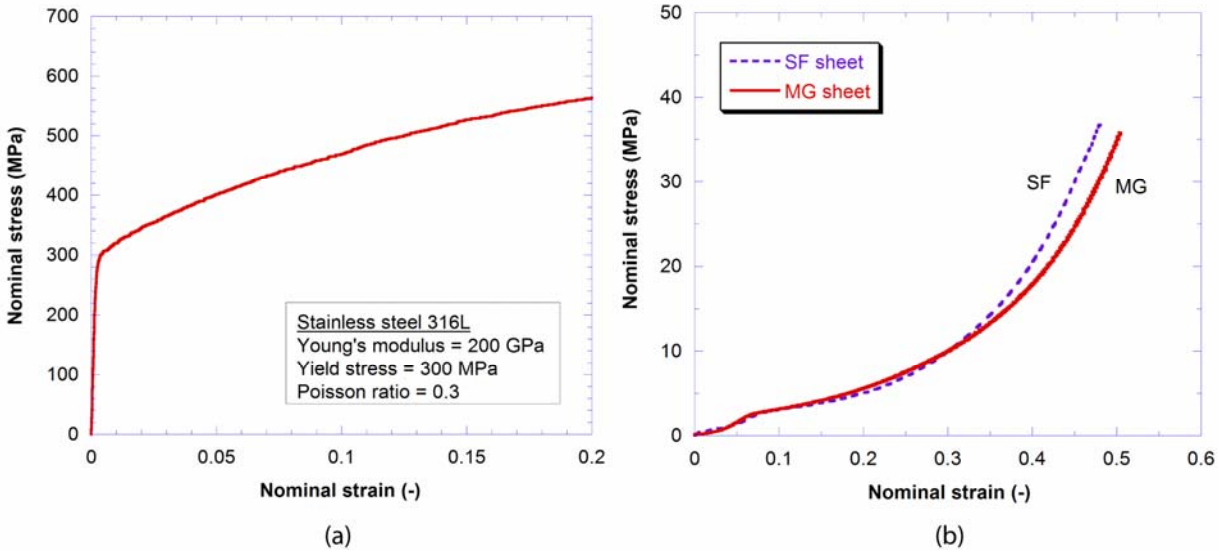

Figure 8-3. Typical nominal stress-strain curves of (a) stainless steel 316L [160] and (b) MG and SF sandwich sheets (cores) in uniaxial compression.

In the model, the fibrous core is treated as an isotropic continuum. The compressive response curves are consistent with the use of a crushable (compressible) foam plasticity constitutive relationship [161] to represent the porous core. The strain-rate dependency is presumed to be small and so, not taken into account. The core hardening behaviour is assumed to be isotropic, as depicted in Figure 8-4. The yield surface is an ellipse centered at the origin in the meridional (p-q) stress plane, evolving in a self-similar manner (constant α) and governed by the equivalent plastic strain ($\bar{\varepsilon}^{pl}$). Only a concise description of the model is included here. The complete FE formulation and implementation into ABAQUS/Explicit code can be found in commercial literature [158].

The yield surface (F) is defined by:

$$F = \sqrt{q^2 + \alpha^2 p^2} - B = 0 \tag{8.1}$$

with

$$B = \alpha p_c = \sigma_c \sqrt{1 + \left(\frac{\alpha}{3}\right)^2} \tag{8.2}$$

where p is the hydrostatic stress (or mean stress), q is the Mises stress, α is the shape factor of the yield ellipse, p_c and σ_c are yield stresses in hydrostatic and uniaxial compression, respectively. The use of this yield function allows yielding to occur under both hydrostatic and deviatoric loadings.

The magnitude of α is related to p_c and σ_c, through the following expressions:

$$\alpha = \frac{3\omega}{\sqrt{9-\omega^2}} \qquad \text{with} \qquad \omega = \frac{\sigma_c^0}{p_c^0} \tag{8.3}$$

where the superscript 0 denotes the initial condition and ω is the compression yield strength ratio.

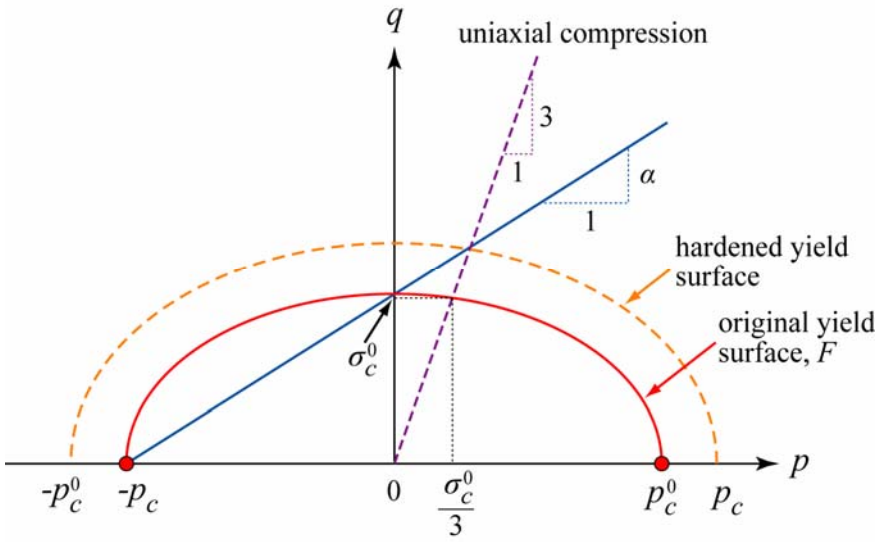

Figure 8-4. Crushable foam constitutive relationship with isotropic hardening. The yield surface (F) is plotted in the p-q stress plane [158].

The crushable foam constitutive relationships in ABAQUS/Explicit are calibrated for both elastic and plastic responses in compression. In the elastic regime, the Young's moduli (E) of MG and SF cores are approximated as 50 MPa and 100 MPa, respectively (§2.4.2.3). These are small values compared with the stiffness of 316L faceplates (200 GPa). For the fibrous cores, the actual values of initial yield stresses (p_c^0 and σ_c^0) are not accurately known. In practice, these are difficult to determine experimentally, since the yield points are not easily identified from the stress-strain response curves. For this model, we assume that the compression yield strength ratio (ω) is about 1, i.e. $p_c^0 \simeq \sigma_c^0$. Also, previous work by Schluppkotten [162] indicated that the magnitude of p_c^0 is similar to σ_c^0, for a low density foam material. The Poisson ratio (ν) is assumed as 0, since the lateral deformation is generally negligible for compression of highly porous materials, particularly under constraint conditions such as those during RSW. In the plastic regime, the evolution of the

yield surface is governed by a hardening law (Figure 8-4). This defines the compressive yield stress (σ_c) as a function of axial plastic strain (ε_{axial}^{pl}), which is obtained from uniaxial compression test data (Figure 8-3(b)).

In order to assess the suitability of the assumptions made for different material relationships, a quasi-static uniaxial compression simulation was performed. Figure 8-5(a) shows the axisymmetric FE mesh and the boundary conditions applied. The cylindrical compression platens (indenters) have flat tips (r=6 mm) and were modelled as a pair of analytical rigid surfaces. The sandwich sheets had an initial core thickness of 1.0 mm. To simulate the indentation process, a prescribed displacement boundary condition (u_2=±0.5 mm) was assigned to the indenters. Figure 8-5(b) shows the deformed geometry and nominal strain contours developed in the compression direction. As expected, due to the use of flat indenters, a uniform contour was attained in the vicinity of the indenter face, with a nominal strain of ~0.5 found in the collapsed core.

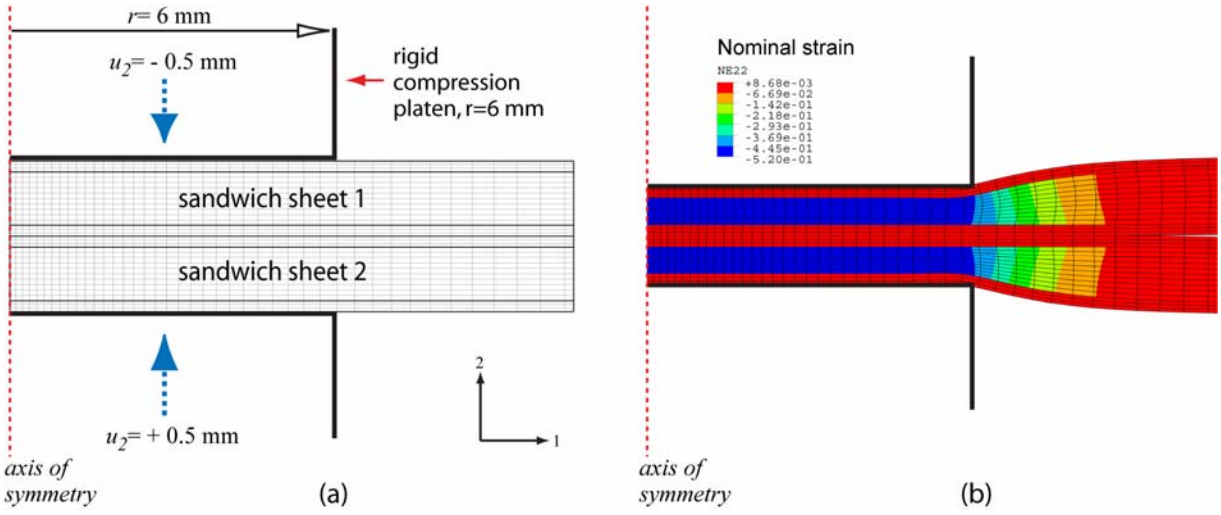

Figure 8-5. (a) Finite-element model for the uniaxial compression of sandwich sheets with (MG) porous cores, using a pair of rigid cylindrical indenters (r=6 mm). (b) The deformed mesh and nominal strain fields (in direction 2) developed at the end of compression simulation.

The stress-strain response predicted by this model is shown in Figure 8-6, together with the experimental data. It can be seen that the predictions are generally in good agreement with measurements. The model over-predicts the stresses by about 10% within the strain level of 0.1 to 0.45. This is probably attributable to the various assumptions made in setting up the core constitutive relationships. Firstly, the model assumes an isotropic core, whereas the actual material is expected to be transversely isotropic. Taking the compression yield strength ratio ($\omega = \sigma_c^0 / p_c^0$) as about 1, may also be inaccurate. Despite these assumptions, the constitutive relationship formulated here is

considered adequate to describe the collapse behaviour experience by sandwich cores during welding.

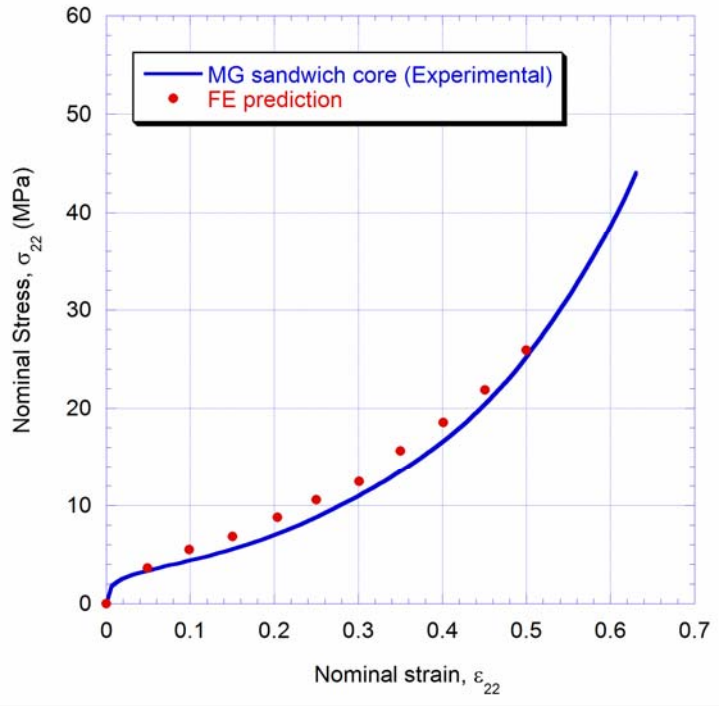

Figure 8-6. Nominal stress-strain response of the MG core. The points are finite-element model predictions while the continuous line is based on experiment data.

Simulations of the squeeze stage were performed on a pair of monolithic 316L stainless steel sheets and MG sandwich sheets, using a pair of hemispherical electrodes. A constant pressure of 16.6 MPa was assigned to the electrode ends (2.5 kN axial load). Figure 8-7 shows the deformed geometries and predicted plastic strain contours. It can be seen that the sandwich sheets have undergone more substantial deformation, compared with monolithic sheets. The maximum equivalent plastic strain in the core approaches 39%, whereas it is only ~4% in the monolithic sheets. This is expected, since the strength and stiffness of the sandwich material are much lower than that of the monolithic counterparts (Figure 8-3). For the case of monolithic sheets, some plastic deformation (1~2%) can be observed in the periphery of the hemispherical tips. In contrast, the electrodes for compressing sandwich sheets remained elastic until the end of the process. A similar response is expected from the SF core, since both porous cores exhibit similar stress-strain responses under compression. Further discussion and comparisons with experimental observations are presented in §9.1.

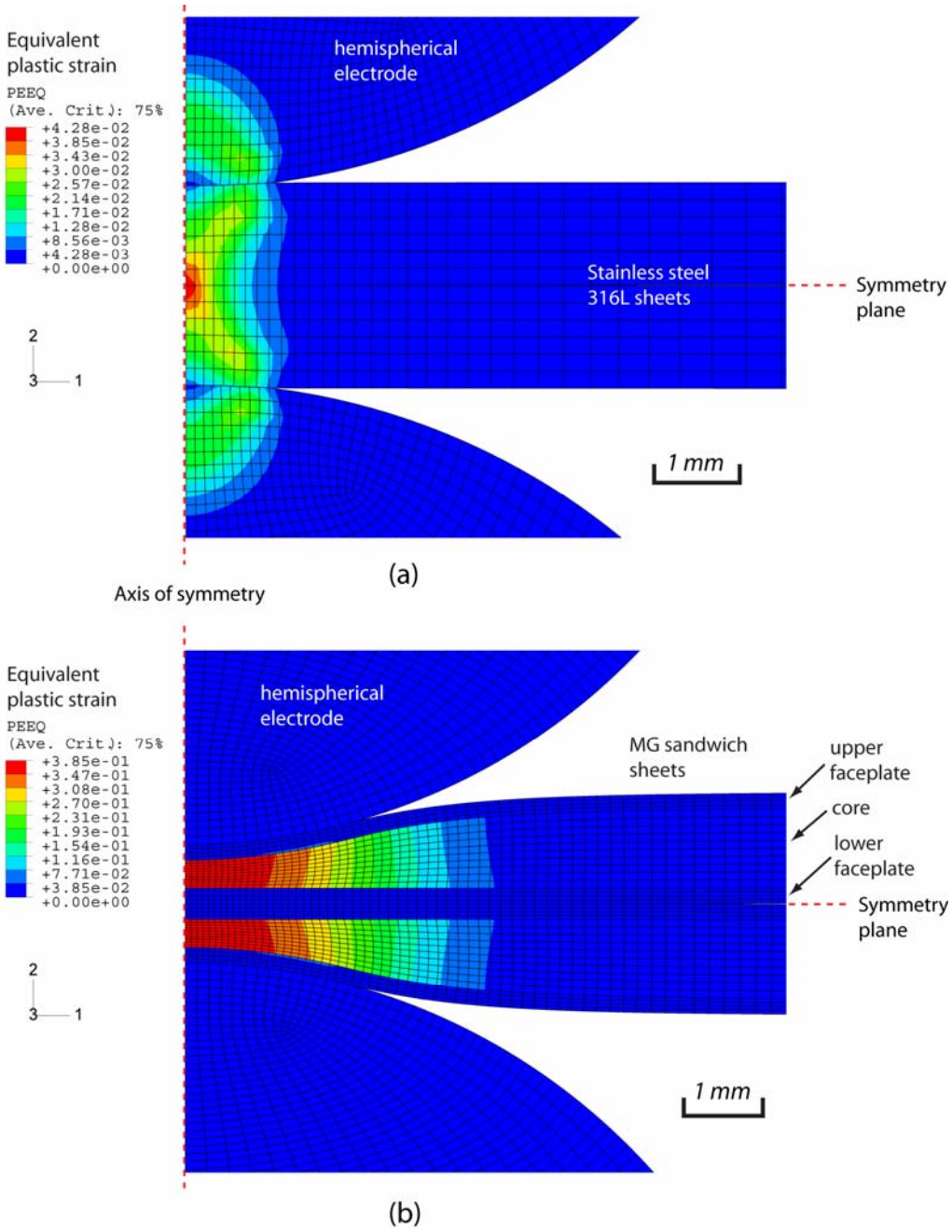

Figure 8-7. Axisymmetric finite-element models showing the deformed meshes, when indenting a pair of (a) monolithic stainless steel 316L sheets (1.2 mm thickness), and (b) MG sandwich sheets (1.25 mm thickness). In both cases, a constant pressure of 16.6 MPa (2.5 kN) was applied at the electrode ends as boundary conditions. The copper (Cu-Cr-Zr) electrodes were modelled as elastic-perfectly plastic bodies. The hemispherical electrodes have radii of 8 mm.

The use of contact elements at E-W and W-W interfaces also enables the prediction of contact pressure distribution and contact area. The normal pressures and contact areas (radii) attained at the end of the squeeze stage are depicted in Figure 8-8. For 316L monolithic sheets, the average pressure at the E-W interface is ~850 MPa, with a contact radius of ~1 mm (measured from the axis of symmetry). A maximum pressure of ~1 GPa is predicted at the vicinity of the outer radius, probably due to plastic hardening near the electrode tips. The contact radius at the W-W interface is much

larger (~1.5 mm) and the normal pressure gradually decreases to zero as the radius increases. In contrast, for the MG sheets, the contact pressures are more than an order of magnitude lower than for monolithic sheets. However, the contact radii at both E-W (~2.1 mm) and W-W (~5.4 mm) interfaces are relatively large, clearly due to more extensive core deformation. Unlike 316L sheets, the normal pressure predicted at the E-W interface appears to be unstable, with high pressures (~65 MPa) seen close to the electrode centre and outer radius. This could be related to the complicated contact conditions established (at each pair of master-to-slave surface contact elements) between the hemispherical electrode face and the faceplate. Since the electrode remained purely elastic (Figure 8-7(b)), the high stresses may be attributable to faceplate yielding, when forced to conform to the electrode face geometry (see §9.1). However, such instability in contact pressure is not observed at the W-W interface. It can be seen that the normal pressure gradually decreases from ~30 MPa to zero, over a radius of ~5.2 mm.

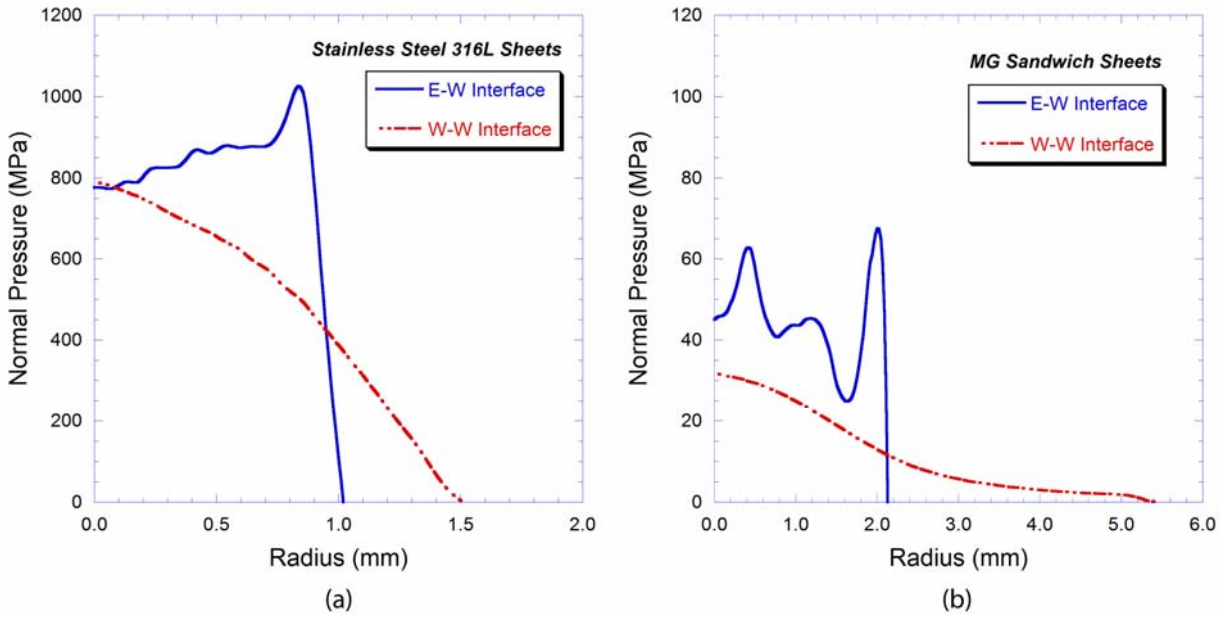

Figure 8-8. Predicted normal contact pressure distributions along E-W and W-W (faying) interfaces: (a) monolithic stainless steel 316L sheets and (b) MG sandwich sheets. The loading conditions and deformed geometries are as depicted in Figure 8-7. The radius corresponds to the lateral distance measured from the electrode axis of symmetry.

8.3 Thermal-Electrical Modelling

The changing geometry arising from the mechanical analysis is used in the thermal-mechanical analysis. The thermal-electrical finite-element model is solved using an implicit and fully-coupled finite-element formulation, which provides transient predictions of current density, potential field, heat generation and temperature profiles. The electrode and deformed workpiece are meshed with 4-node axisymmetric quadrilateral elements (*PLANE 67*) in ANSYS [157]. The element has two

degrees of freedom at each node – temperature and voltage, and takes into account Joule heating attributed to current flow. The ANSYS (implicit) finite-element code has been chosen for this analysis, because of its robustness in solving transient heat and electrical conduction problems involving multiple interfacial contacts, which can be time-, temperature- and/or pressure-dependent. In contrast, the ABAQUS/Standard code [163] is limited in this respect.

The relevant thermal and electrical boundary conditions are depicted in Figure 8-2(b). To simulate electrical current flow, the weld current, $I(t)$ in RMS, is assigned as a time-dependent load boundary condition at the upper electrode end, while the potential of the lower electrode end is set to zero, $\Phi = 0$. The inner free boundaries of the electrodes that are water-cooled are assigned forced convection boundary conditions, by assuming a heat transfer coefficient of 10^4 W m^{-2} K^{-1} [164] and constant water temperature of 10 ºC. Geometrical boundaries located along the axis of symmetry are modelled as perfectly insulating (adiabatic). Since convective and radiative heat losses are presumably small and insignificant compared with heat conduction into the electrodes (§4.3.2.3), these effects are not incorporated into the model.

To model current and heat conduction across contacting interfaces (E-W and W-W), surface-to-surface contact elements (*CONTA 172* and *TARGE 169*) [157] are applied to the matching surfaces (contact and target pairs). The interfacial contact resistances are modelled using electrical and thermal contact conductances, σ_{ecc} (Ω^{-1} m^{-2}) and σ_{tcc} (W m^{-2} K^{-1}), respectively. Both can be defined as temperature- and/or pressure-dependent. At each pair of contact interfaces, the electrical current density, J (A m^{-2}), is calculated from:

$$J = \sigma_{ecc} \cdot (\Phi_t - \Phi_c) \tag{8.4}$$

where $(\Phi_t - \Phi_c)$ is the potential drop across the contact points of a surface pair. The subscripts t and c denote target and contact, respectively.

The heat flux, q (W m^{-2}), generated at the interface due to the passage of current (Joule heating) is given by:

$$q = f_q \cdot J \cdot (\Phi_t - \Phi_c) \tag{8.5}$$

where f_q is the fraction of electric dissipated energy being converted into heat (assumed as 1 in this analysis). Subsequently, the heat being dissipated into the contact and target surfaces is found as:

$$q_c = f_j \cdot q \tag{8.6}$$

and

$$q_t = (1 - f_j) \cdot q \tag{8.7}$$

where f_j is the Joule dissipation weight factor. In practice, the actual magnitude of f_j is often not known or difficult to determine [121]. In this model, it is assumed that the generated heat is equally distributed among the two adjacent surfaces, so f_j=0.5.

The conductive heat transfer across the interface is governed by:

$$q = \sigma_{tcc} \cdot (T_t - T_c) \tag{8.8}$$

where T_t and T_c are temperatures of the target and contact surface, respectively.

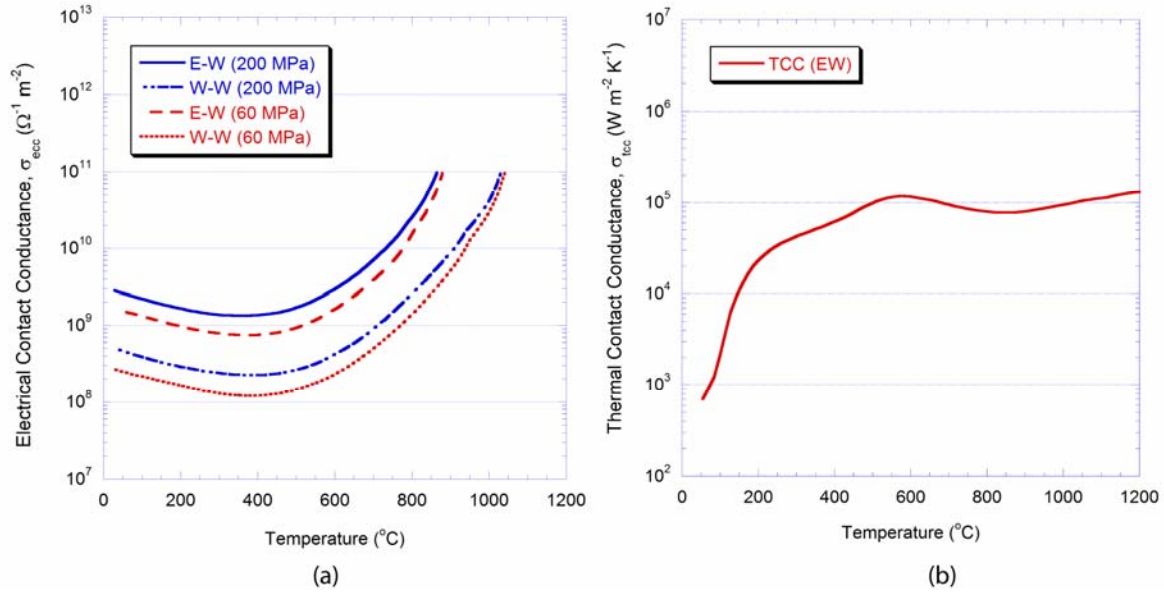

Figure 8-9. Temperature-dependent (a) electrical and (b) thermal contact conductances at E-W (electrode-workpiece) and W-W (faying) interfaces. Electrical conductance curves are predictions from eqn.(4.3) [109], at contact pressures of 60 and 200 MPa. The E-W thermal conductance curve as measured at ~70 MPa [121].

Both contact conductances at W-W and E-W interfaces are assumed to be only temperature-dependent. Since the model does not incorporate thermo-mechanical coupling effects, pressure-dependency is not taken into account. The electrical contact conductance (σ_{ecc}) is calculated based on the empirical model proposed by Babu *et al* [109]. Two (initial) contact pressures, P=60 MPa and 200 MPa were considered. Data used for the model (eqn.(4.3)), i.e. temperature-dependent bulk resistivity (ρ), temperature-dependent yield strength (σ_Y) and number density of contacting

asperities (η), are obtained from [109]. The predictions for both E-W and W-W surfaces at two different contact pressures, expressed as a function of temperature, are shown in Figure 8-9(a). It can be seen that higher pressure leads to better contact conductances at lower temperatures (below ~800 ºC). Also, conductance at E-W interface is predicted as about one order of magnitude higher than W-W (faying) interface. A similar trend was observed from contact resistance measurements performed by several workers [117, 124, 165]. This is because better metal-to-metal contact is easier to establish at an interface consisting of two materials of different yield strengths. Up to about 450 ºC, σ_{ecc} decreases with temperature, since it is dominated by the increase of bulk resistance with temperature. However, above 450 ºC, a rapid increase in σ_{ecc} is predicted, due to substantial reduction in the material yield strength at higher temperatures. The effect of contact pressure on σ_{ecc} also becomes less apparent as temperature rises. For the current RSW model, contact conductance curves predicted at 60 MPa were assumed.

The temperature-dependent thermal contact conductances (σ_{tcc}) used in the model is shown in Figure 8-9(b). The E-W thermal conductance is based on the measurements performed at ~70 MPa, by Le Meur *et al* [121] (§4.4.2). The rapid increase in σ_{tcc} up to ~600 ºC is attributed to the increase in interfacial contact area as the material softens. It stabilises at ~100 kW m^{-2} K^{-1} (E-W), when a force balance is attained. Since neither experimental data nor model predictions can be found in the literature for W-W interface conductance, it is assumed to be similar to that of E-W interface. In the current model, contact conductances, as shown in Figure 8-9, are applicable only when the local temperature is lower than the liquidus temperature (T_L). When the interfacial temperature exceeds T_L, both conductances are assumed to become infinite (ideal contact), since the solid interface boundary effectively disappears after melting.

The incorporation of temperature-dependent material properties into the model is essential, because the thermal-electrical analysis involves large temperature changes and phase transformation during weld nugget formation. In addition, since the squeeze stage results in large strain deformation in the porous core, the changes in effective conductivities also become important. Figure 8-10 depicts the cross-sectional views of MG and SF sheets at the end of the squeeze stage, using a compression force of 2.5 kN. It can be seen that regions near the vicinity of electrode tips have been substantially deformed, as compared with the original core structure (away from the tip). The volume fractions of fibres found in the crushed zones of MG and SF sheets are about 0.5 and 0.4, respectively; corresponding to maximum axial strains of ~0.65 and ~0.6.

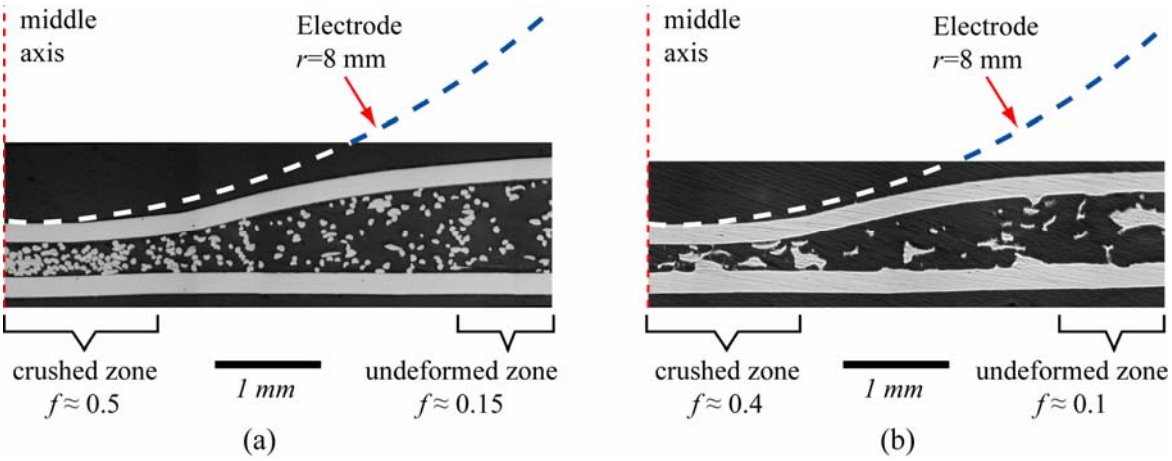

Figure 8-10. Cross-sectional views showing the cold collapse profiles obtained at the end of squeeze stage (2.5 kN), for (a) MG and (b) SF sheets. The porous regions have been impregnated with resin.

Table 8-1. Thermal conductivities and electrical resistivities of MG and SF sandwich cores, before (as-received) and after squeeze stage. Each data is an average of measurements performed on at least five different samples.

Core type	Fibre vol. fraction *f*		Thermal conductivity* at 100 ºC (W m^{-1} K^{-1})		Electrical resistivity at 23 ºC (±300 μΩ cm)			
					Through-thickness		*In-plane*	
	Before	After	Before	After	Before	After	Before	After
MG	0.15	~0.5	0.17 ±0.02	1.05 ±0.10	1800	1200	1200	1100
SF	0.10	~0.4	0.42 ±0.04	0.85 ±0.07	3000	1000	-	-

*In through-thickness direction only.

Uniaxial compression tests were performed on sandwich test coupons, to similar strain levels as those observed in the actual squeezing process. These samples were then used in determining the thermal conductivities and electrical resistivities of the crushed cores. The experimental procedures used for testing are explained in §5.5 and §5.6. The results obtained are shown in Table 8-1. The collapsed cores exhibit a clear increase in through-thickness conductivities (or reduction in resistivities). This is probably attributable to the higher core fibre volume fraction (*f*), as oppose to increasing fibre inclination angles (squashed fibres are lying more in-plane). Moreover, in a collapsed core, more fibres are brought into contact with each other in through-thickness direction, hence raising the number of available conduction paths. Unfortunately, only limited in-plane measurements were obtained (MG). Since the SF core is manufactured together with the faceplates, measuring the property of the crushed core alone is not feasible using the existing experimental set-up (Figure 5-10(b)). However, the limited data available suggest that changes in in-plane properties

may be relatively small, compared with through-thickness direction. For the case of a collapsed MG core, both through-thickness and in-plane resistivities appeared to be similar (~10% decrease). Therefore, for the modelling of RSW process, the crushed core thermophysical properties are assumed isotropic.

Figure 8-11 shows the temperature-dependent conductivities of monolithic stainless steel sheets (316 and 446) and collapsed fibre cores (MG and SF). The elevated-temperature conductivity, $k(T)$, and resistivity , $\rho(T)$, of the fibre felts up to the solidus temperatures (T_s), are approximated using the empirical relationships proposed by Koh and Fortini [57]:

$$k(T) = k_{373}\left[1+\left\{\gamma_1 \cdot (T-373)\right\}\right] \quad \text{,where } \gamma_1 = 0.00089 \text{ K}^{-1} \tag{8.9}$$

$$\rho(T) = \rho_{300}\left[1+\left\{\gamma_2 \cdot (T-300)\right\}\right] \quad \text{,where } \gamma_2 = 0.000544 \text{ K}^{-1} \tag{8.10}$$

The conductivity at 373 K (k_{373}) and resistivity at 300 K (ρ_{300}) were used as reference values (Table 8-1) in eqns.(8.9) and (8.10). Since both correlations only take into account the increase in parent material conductivities as a function of temperature, the coefficients (γ_1 & γ_2) are independent of core fibre volume fractions [166]. During solidus to liquidus transition, the effective conductivities are assumed to gradually increase to that of monolithic materials. After exceeding T_L, conductivities of the melts are used for subsequent calculations.

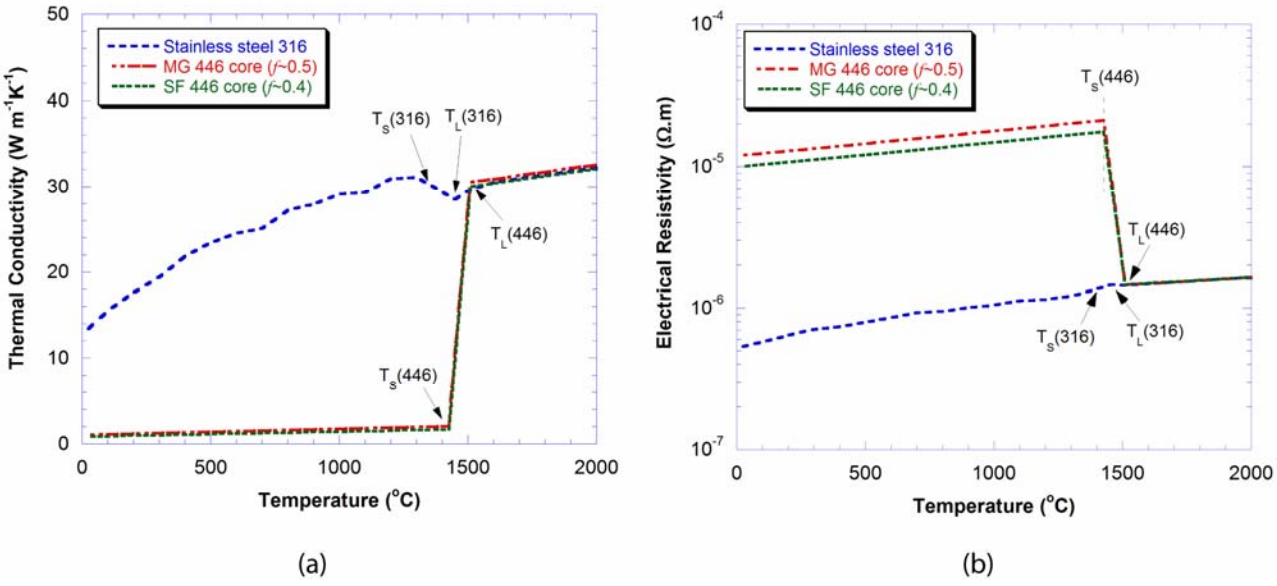

Figure 8-11. Temperature-dependent thermophysical properties of monolithic stainless steel 316 and effective conductivities of collapsed fibre felts (MG and SF cores): (a) thermal conductivity and (b) electrical resistivity. The monolithic (316) curves are obtained from experimental data [145, 167, 168]. The lower temperature properties of the felts are based on measurements (Table 8-1), while eqns.(8.9) and (8.10) are employed for predictions up to the solidus temperature (T_s).

The formation and solidification of a weld nugget involve phase changes in the weld pool. During a phase change process, the latent heat of fusion is taken into account by ANSYS using the enthalpy method [157]. The specific enthalpy at a temperature T, $\hat{h}_T$ (J m^{-3}), is defined as [167]:

$$\hat{h}_T - \hat{h}_{298} = \int_{298}^{T} \rho(T)\, C_p(T)\, dT \tag{8.11}$$

where $\rho(T)$ and $C_p(T)$ are temperature-dependent density (kg m^{-3}) and specific heat capacity (J kg^{-1} K^{-1}), respectively, while $\hat{h}_{298}$ is the reference enthalpy at 298 K. The temperature-dependent specific enthalpy of stainless steels 316 and 446, calculated using the data found in [167] and [145], are shown in Figure 8-12. Results of thermal-electrical model predictions and comparisons with experimental observations are presented in §9.2 and §9.3.

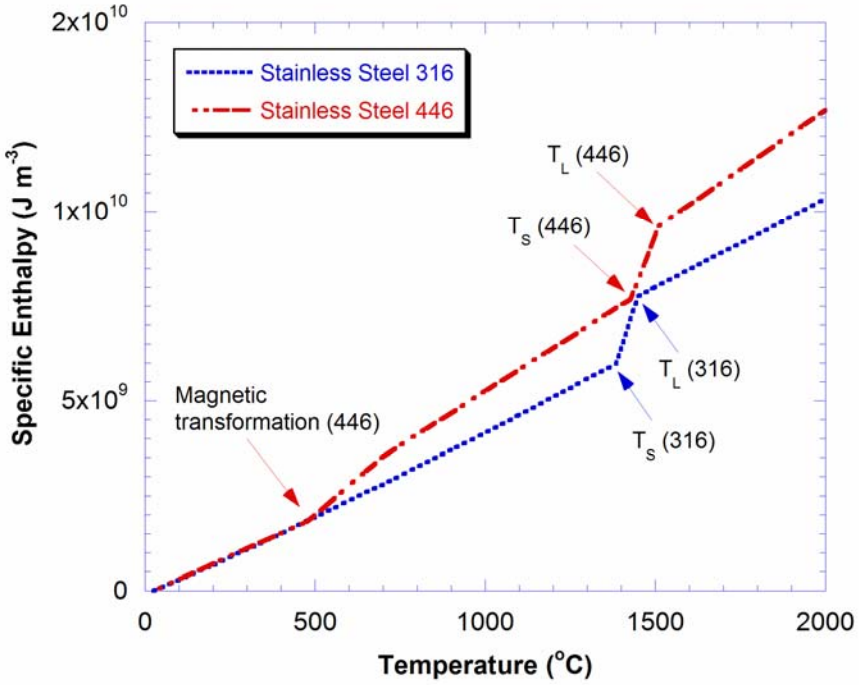

Figure 8-12. Temperature-dependent specific enthalpy of stainless steels 316 [167] and 446 [145].

Chapter 9: Welding Characteristics of Thin Sandwich Sheets

The welding characteristics of two variants of thin stainless steel sandwich materials incorporating a highly porous core – glued in-plane mesh (MG) and short fibre 3-D array (SF) sheets have been investigated. Welding experiments were conducted to study the effects of different welding parameters (i.e. electrode force, current and weld time) on nugget development. Using suitable parameters, both variants were found to be readily weldable, producing good quality joints (weld nuggets). The resistance spot welding (RSW) finite-element model described in Chapter 8 is applied here to explain and predict the experimental observations. The model provides important information that cannot be readily obtained from experiments, such as transient thermal fields. Despite the complex interplays of various factors (mechanical, electrical and thermal), the model gives a reliable indication of the behaviour, at least up to the current levels at which melt expulsion is likely to occur.

9.1 Squeeze (Cold Collapse) Stage

The squeeze stage involved compressing two sandwich materials under a pair of electrodes, at a constant force of 2.5 kN (Figure 5-14). The deformed shapes of the glued in-plane mesh (MG) and short fibre 3-D array (SF) sandwich sheets at the end of the squeeze stage, from welding experiments and finite-element (FE) models (§8.2), are depicted in Figure 9-1. It can be seen that the agreement is good, although not perfect, in terms of specimen shape.

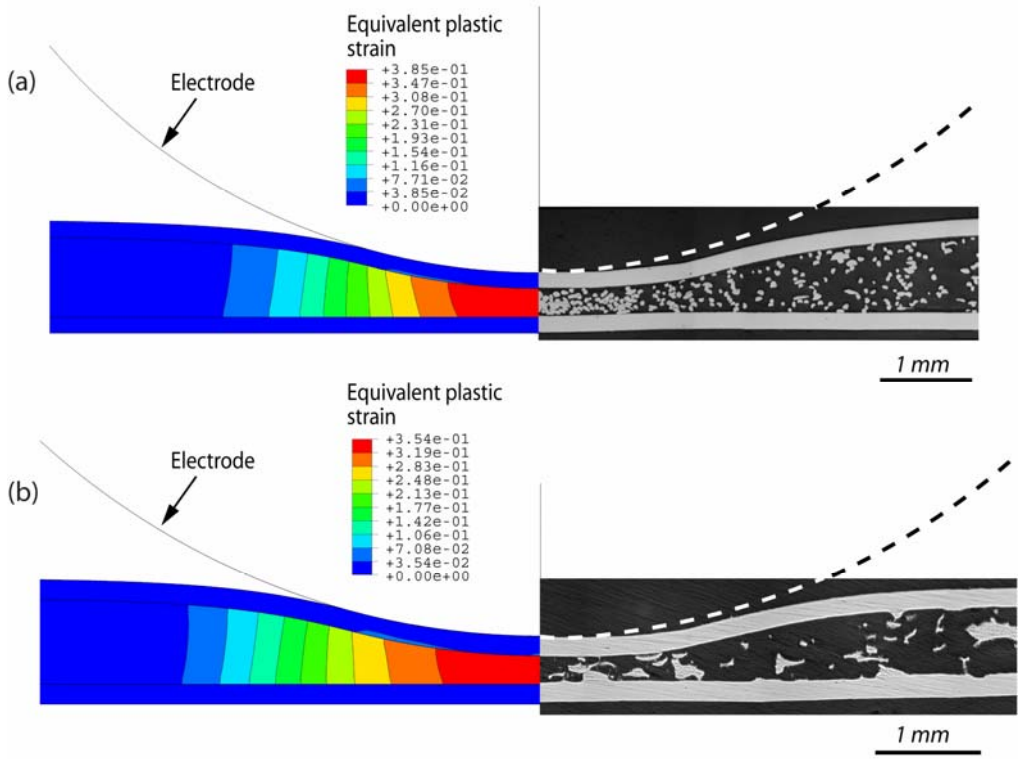

Figure 9-1. Cold collapse profiles at the end of squeeze stage (2.5 kN), obtained from the finite-element model (left) compared with the experiments (right), for (a) MG and (b) SF sandwich sheets. The model estimates the equivalent plastic strain fields of the collapsed structures.

For both variants, it is clear that the regions located directly under the hemispherical electrode tips have undergone large plastic deformations. The FE model predicts a maximum equivalent plastic strain ($\bar{\varepsilon}^{pl}$) of ~39% for the MG core and a lower value of ~35% for the SF core. This difference is due to the fact that SF exhibits a higher flow stress after core densification (Figure 8-3(b)). Core regions and faceplates located remote from the crushed zone (electrode tip) remain elastic.

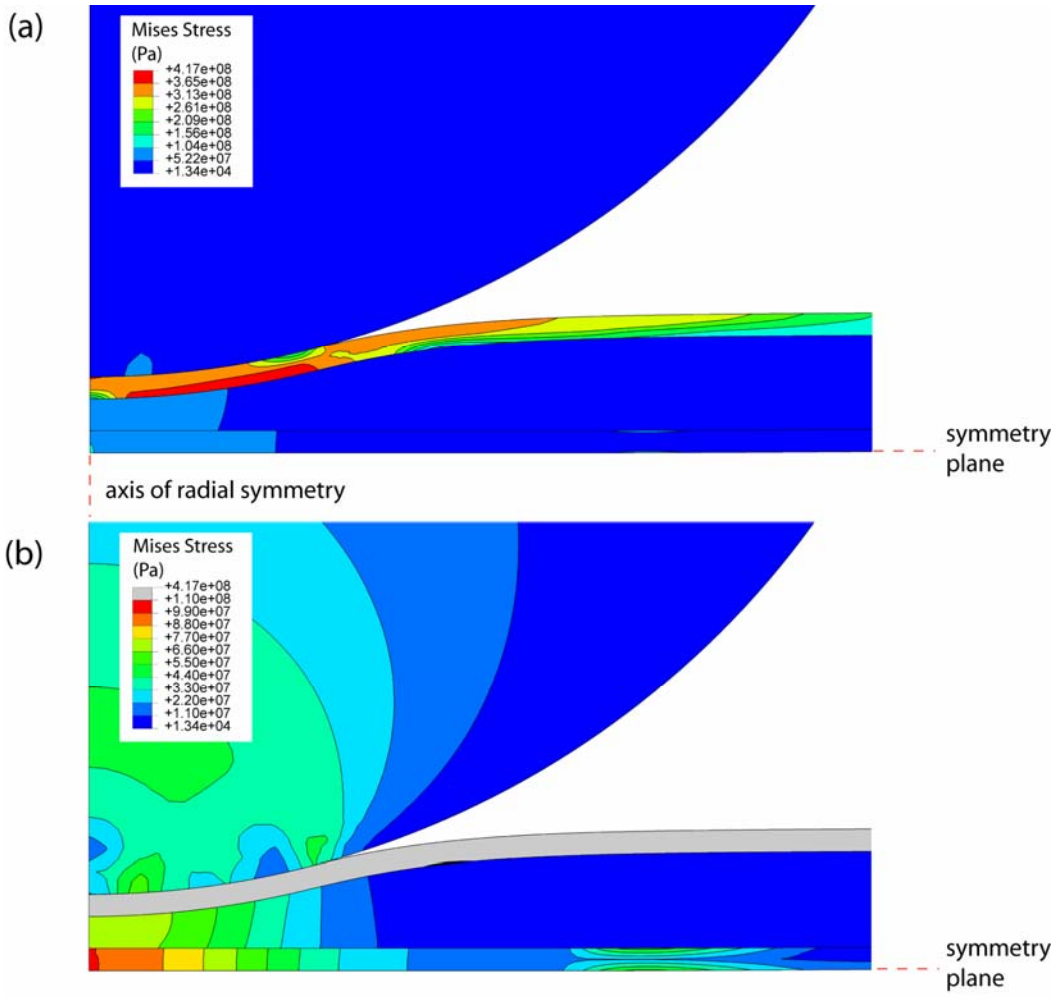

Figure 9-2. Mises stress fields developed in SF sandwich materials at the end of squeeze stage, as predicted by the FE model. Mises stresses in the (a) upper faceplate and (b) for all other regions.

Figure 9-2 shows the von Mises (equivalent) stress fields predicted for the electrode and SF sheet. From Figure 9-2(a), it can be seen that certain regions of upper faceplate under the electrode tip have yielded (>300 MPa), with stresses ranging from about 300 to 410 MPa. In contrast, both the electrode and lower faceplate remain elastic, as shown in Figure 9-2(b). Within the collapsed core, the maximum stress is predicted as ~70 MPa, which is about an order of magnitude lower than that in the upper faceplate. The stress fields predicted for the core of the MG sheet are similar to those of

SF, but at lower magnitudes. Maximum stresses of ~420 MPa and ~33 MPa are predicted in the upper faceplate and core, respectively.

9.2 Voltage and Current Profiles

The voltage and current profiles measured during welding experiments are useful for analysing the welding characteristics of sandwich sheets. Figure 9-3 depicts typical plots for MG and SF sheets, as obtained from experiments, together with corresponding FE predictions. The welding current incorporates a 2 kHz ripple. This ripple is apparent in the measured voltage signal. Both welds were made under similar conditions: ~4 kA (RMS) current, for 200 ms and 2.5 kN electrode force. Similar current responses were observed for the different materials. It can be seen that, initially, the weld current increases rapidly from zero to values above the nominal current settings. However, the current gradually decreases to the set levels within ~30 ms, at which point they were maintained until the end of the weld cycle. This is a result of the sudden fall in resistance during the first part of the weld (Figure 9-4), causing an overshoot in the feedback control of current. The current level eventually stabilised at the set level. The experimental current profiles were assigned as time-dependent load boundary conditions, $I(t)$, in the thermal-electrical model (Figure 9-3(b)).

At the start of the weld period, MG sheets displayed a relatively high peak voltage, representing a high initial resistance. This can be attributed to the limited electrical contact between the fibre ends and faceplates, through the poorly conducting adhesive or via the occasional fibre in direct contact with the faceplate (Figure 7-3(a)). As the core was compressed and the adhesive decomposed, contact improved and the resistance (and thus voltage levels) fell. Lower peak voltage was observed with the SF sheets, which is attributable to the presence of the (high conductivity) nickel-based braze. However, the voltage signals for the two materials displayed no significant differences after ~50 ms, suggesting that the adhesive in the glued variant has been largely decomposed by that point. As shown in Figure 9-3(b), the model can predict the observed increase in voltage response, but not the voltage ripples. This is because a ‘smooth’ direct current (DC) profile was assumed as a boundary condition, instead of applying the actual current waveforms (ripples or oscillations) observed in the experiments. The reliable predictions of voltage history during steady-state flow (>50 ms) indicate that the transport properties of the collapsed core have been adequately modelled.

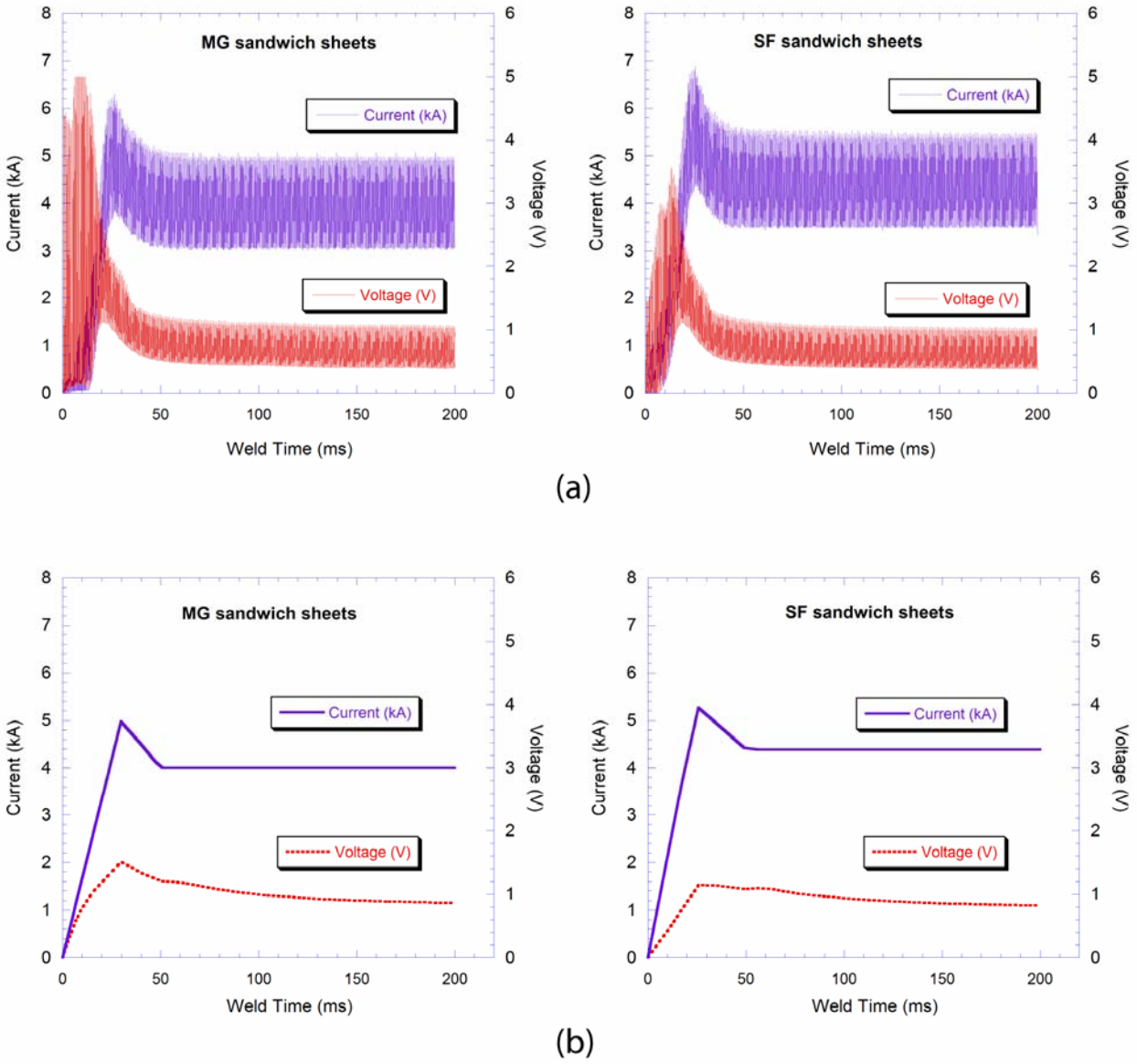

Figure 9-3. Typical voltage and current histories throughout the 200 ms weld time for a pair of MG and SF sheets. The applied RMS currents were 4 kA and 4.39 kA, respectively. Shown here are the V-I plots, as obtained from (a) welding experiments, and (b) finite-element model predictions, where time-dependent current (purple curve) is set as the boundary condition and voltage (red curve) is the prediction.

After ~30 ms, the voltage plots show a progressive reduction with increasing weld time, even though the current (RMS) remained virtually constant. This indicates a reduction in the total electrical resistance. Figure 9-4 shows the variation of both measured and predicted total resistances throughout the weld time (200 ms). The total resistance was measured across the pair of electrodes and was the sum of copper electrode bulk resistance, interfacial contact resistances (E-W and W-W) and effective resistance of sandwich sheets. At the start of welding (0 ms), the initial resistance was clearly higher for the MG material, due to the presence of the adhesive layer. However, it decreased rapidly within the first 30 ms and remained at a magnitude of ~200 μΩ until the end of the weld time. The gentle fall in resistance, however, is attributed to the rising core electrical conductance

(decreasing resistance) as temperature increased (Figure 8-9(a)). In the resistance welding of monolithic sheets, such as steel and aluminium, the drop in voltage is primarily caused by the reduction in interfacial resistance (collapse of faying surface asperities) [100], since the resistivity of solid metal rises with temperature. In contrast, for these thin sandwich sheets, since the porous core has a higher resistivity (Figure 8-11(b)), which substantially drops upon melting, the resistance and voltage across the electrodes also decrease as melting commences. This effect is captured by the thermal-electrical model. Nevertheless, the rapid resistance changes observed in the first 30 ms are not predicted, because the model does not incorporate the decomposition of adhesive or softening of brazing materials present at the faceplate-to-core interfaces. These properties are generally difficult to isolate and quantify, especially as a function of temperature. More importantly, it can be seen that omitting these factors does not affect the predictions at steady-state conditions (>50 ms).

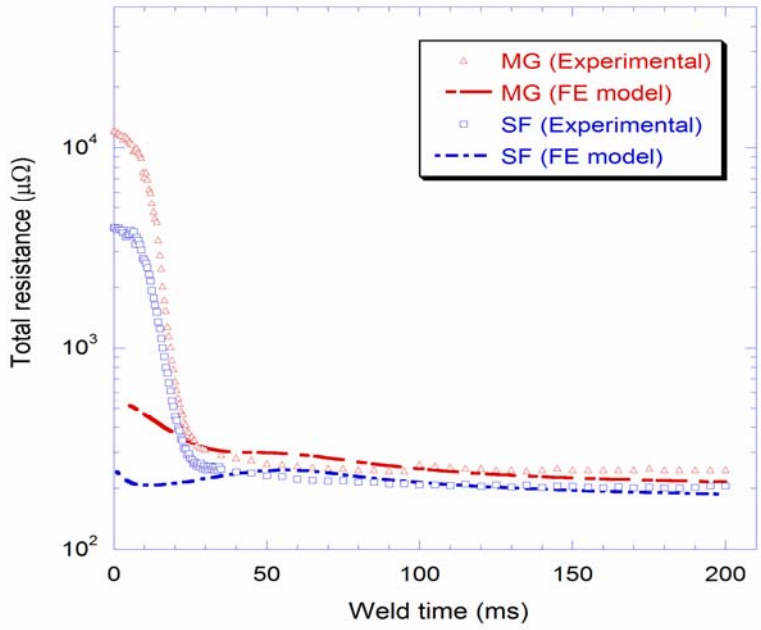

Figure 9-4. Total resistances (measured and predicted) across the electrode pairs as a function of weld time (200 ms), for (a) MG and (b) SF sandwich sheets.

Evidently, both glued and brazed variants are resistance weldable, since they allow the passage of high amperage current (of the order of kA) through the collapsed cores. It is noted that the glued variant (MG) is readily weldable without using a shunt, an important development when compared with FG sandwiches (§4.6.1). This is expected, since the effective electrical resistivity of the collapsed MG core is of the same order of magnitude as that of the brazed (SF) material (Table 8-1).

9.3 Weld Nugget Development

Figure 9-5 compares the nugget geometry and size (diameter) of weld nuggets, as obtained from experiment and FE model. They agree well. The boundary of the nugget is defined as the isotherm of the liquidus temperature (T_L=1510 ºC for stainless steel 446 [145]). Also, it should be noted that, for the current model, the 'molten' nugget is assumed to be thermally active, but mechanically inactive, so fluid flow effects are not simulated. Maximum temperatures of ~1800 ºC are predicted at the centre of the molten nuggets.

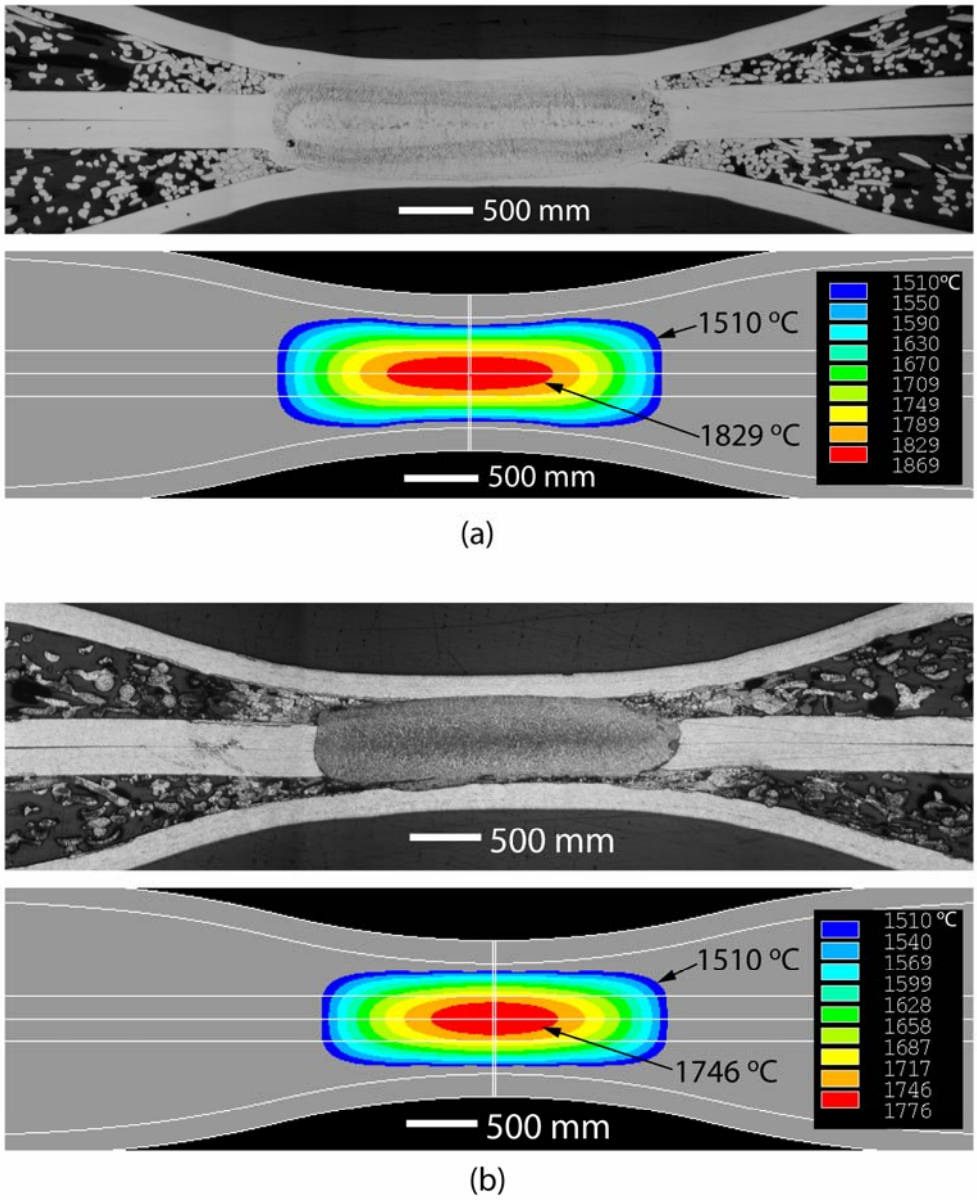

Figure 9-5. Cross-sectional views showing the actual spot weld nuggets, in comparison with predictions, for (a) MG and (b) SF sheets. The welding conditions are as shown in Figure 9-3. The boundary of the nugget is defined by the liquidus temperature (T_L=1510 ºC). The grey regions are below the liquidus temperature (unmelted zones).

The changes in temperature field as a function of weld time, as predicted by the model, are useful for tracking and explaining the different stages of weld nugget development. Figure 9-6 depicts the predicted nugget growth at four different stages, when welding a pair of MG sheet. The welding conditions were 4 kA for 200 ms, at an electrode force of 2.5 kN. Figure 9-7 shows the predicted temperature histories of the faying surfaces (T_1), core-to-faceplate interfaces (T_2 and T_4), centre of core (T_3) and electrode-to-workpiece (E-W) interfaces (T_5).

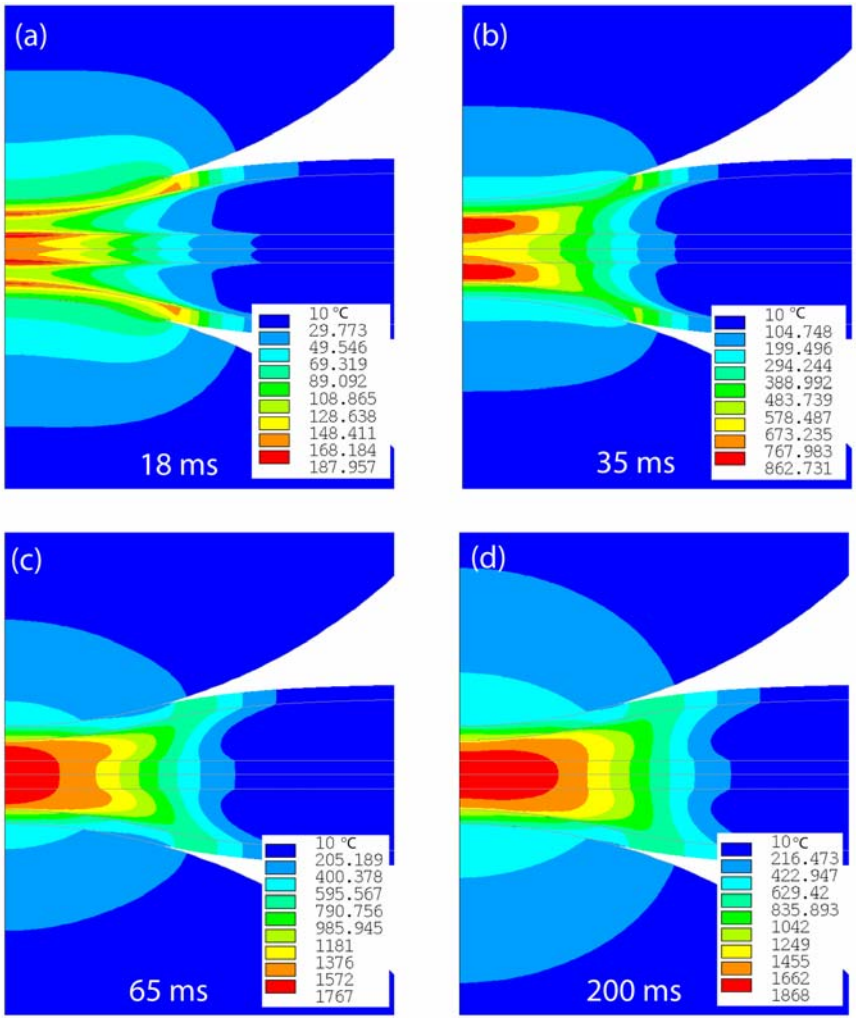

Figure 9-6. Predicted temperature fields (in ºC) for the MG sandwich sheets, at different stages of weld time: (a) 18 (b) 35 (c) 65 and (d) 200 ms. The voltage and current histories are depicted in Figure 9-3.

Figure 9-6(a) indicates that, at an early stage (~18 ms), heat generation is concentrated at the core-to-faceplate interfaces. This arises from the initially low interfacial electrical contact conductance (σ_{ecc}), associated with the low temperature (Figure 8-9). In the actual welding process, heating of these localised regions leads to softening and decomposition of the adhesives (Figure 7-3(a)). In the thermal-electrical model, this effect is simulated by increasing both thermal and electrical contact

conductances as temperature rises. It can be seen that the temperature at the E-W interface remains low at all times, as a result of efficient heat dissipation into the water-cooled copper electrodes. The E-W temperature is predicted to be below 800 ºC until the end of weld time, as shown by T_5.

At the end of ~35 ms (Figure 9-6(b)), the maximum temperatures are within the collapsed cores. This is attributed to the significantly higher core resistivity (Figure 8-11(b)), which in turn, generates high current density in those regions. At this point, there is clearly a greater thermal gradient at T_3 than at T_1 (faying surfaces). This behaviour differs from that of monolithic sheets, where the highest temperature is initially found at the faying surfaces, where the molten pool is first developed (Figure 4-6) [100, 104]. In contrast, for the case of sandwich sheets, melting commences in the vicinity of the collapsed cores, prior to the melting of faceplates. As observed in Figure 9-7, the core (T_3) first reaches the solidus temperature (T_S), closely followed by the inner face of lower faceplate (T_2), and subsequently the faying surfaces (T_1).

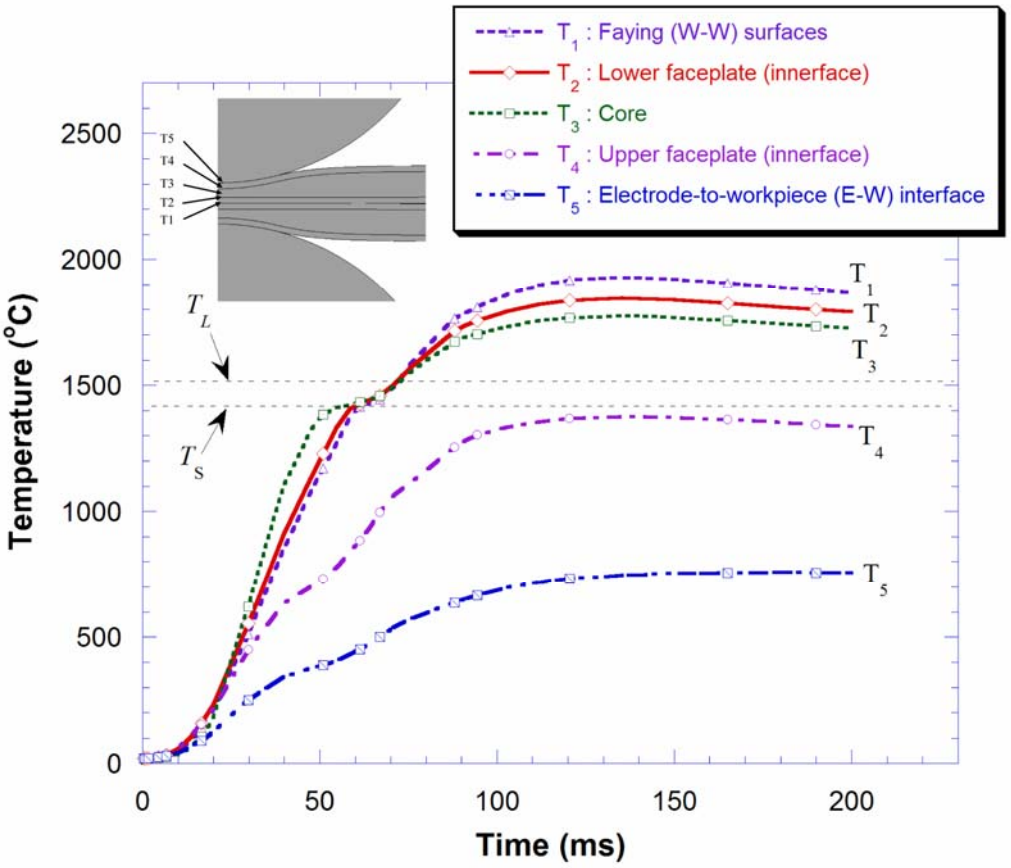

Figure 9-7. Predicted temperature histories of the MG sheets, at different locations indicated by the inset schematic. The welding conditions are 4 kA (RMS) for 200 ms. T_S and T_L are the solidus and liquidus temperatures, respectively.

After the temperature of the collapsed core reaches T_S, the faying surface becomes the dominant heat generation source. Within the solidus-to-liquidus transition regime, the core resistivity decreases dramatically (Figure 8-11). Melting of the faceplates initiates after ~65 ms, forming a 'molten' pool contained between the two outer faceplates, as shown in Figure 9-6(c). The highest temperature is now located in the central region of the molten nugget. So, T_1 exceeds T_3 after the liquidus temperature (T_L) is attained. As weld time progresses, the molten pool grows in the radial directions, since growth in the axial direction is impeded by rapid heat losses into the electrodes (Figure 9-6(d)). A similar temperature history plot was obtained for the welding of SF sheets, but, lower electrical resistivity (Figure 8-11(b)) results in less Joule heating, so lower overall temperatures were predicted (Figure 9-5(b)).

9.4 Model Validation

The FE model was validated by conducting a series of welding experiments, at increasing welding currents, ranging from 3.5 to 5.5 kA. All tests were performed at the same preset electrode force of 2.5 kN. The nugget diameters (in lateral direction) were measured from the metallographic samples and compared with predicted nugget sizes, as shown in Figure 9-8.

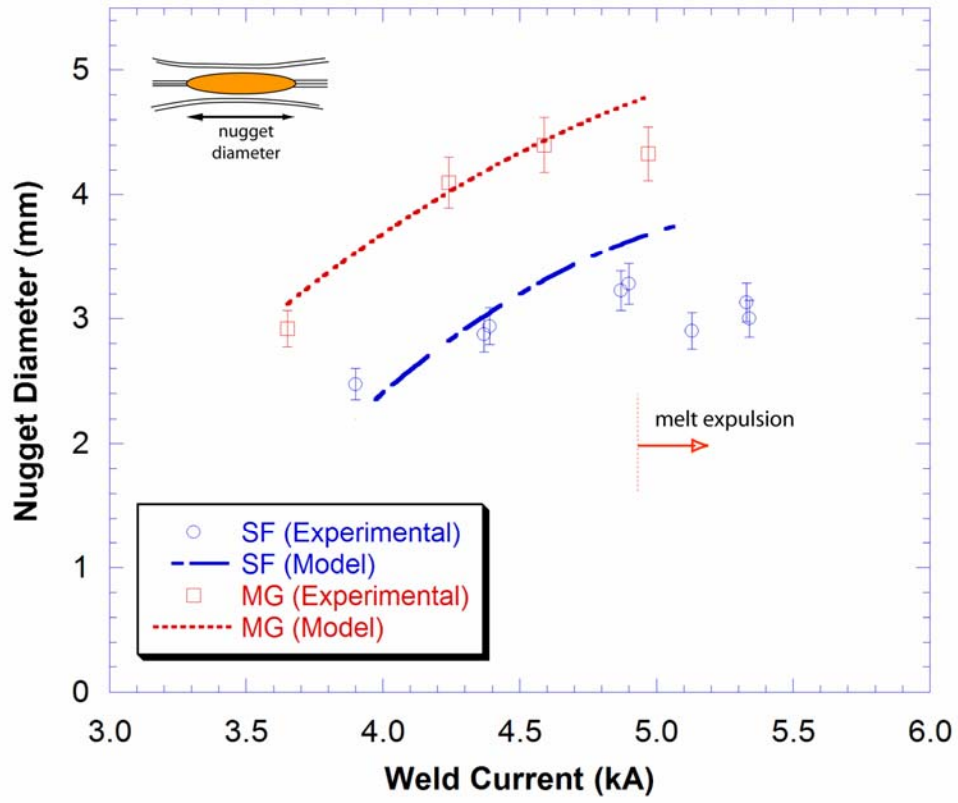

Figure 9-8. Weld nugget diameter versus weld current for MG and SF sandwich materials. The lines are FE predictions while the points are experimental data.

It can be seen that, at current levels below ~5 kA, the nugget diameter rises steadily with increasing current, as a result of increasing heat generation (Joule heating). However, beyond ~5 kA the weld diameter starts to decrease, which is contradictory to the model predictions. At high current levels, as a result of faceplate cracking, the molten weld pool can no longer be fully contained, leading to melt expulsion (weld splash). This phenomenon is depicted in Figure 9-9(a) and (b). Melt expulsion reduces the nugget size and results in shrinkage cracking and porosity, since the molten nugget is not sufficiently forged during cooling (Figure 9-9(c)). In addition, porosity formation may also be exacerbated by the evaporation of adhesive and its decomposition products. Prior to melt expulsion (below ~5 kA), the model predictions are generally in good agreement with experimental observations. However, beyond this current level, agreement becomes poor, since the model does not incorporate the effects of melt expulsion. Despite this, and having to take into account the interplays of different factors (mechanical-thermal-electrical-metallurgical interactions), the model gives a reliable representation of the resistance welding behaviour, at least up to the current levels at which melt expulsion is likely to occur.

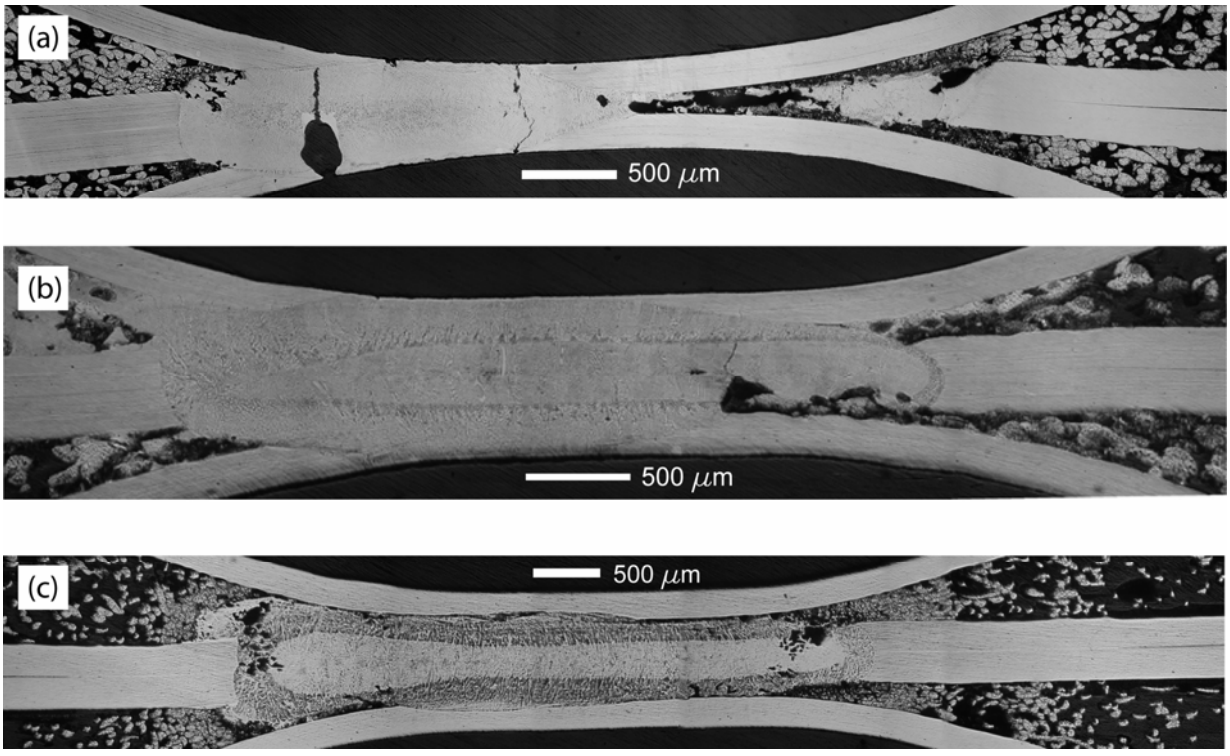

Figure 9-9. Resistance welded sandwich sheets with various defects: (a) MG sheets welded at 5.32 kA, showing faceplate cracking leading to melt expulsion (b) SF sheets welded at 5.57 kA, with a defective nugget due to expulsion and (c) MG sheets welded at 4.24 kA, showing an asymmetric weld nugget containing porosity. All welds were performed at a weld time of 200 ms.

Figure 9-8 also shows that, under similar welding conditions, the nugget diameter in welded MG sheets is consistently larger than SF (~30%). This may be attributed to the higher electrical resistivity and thermal conductivity of a collapsed MG core. More heat gets generated and conducted in the core, leading to the development of larger nuggets.

Chapter 10: Summary and Conclusions

This work investigates the core architecture, transport properties and welding characteristics of a novel stainless steel sandwich sheet material incorporating a fibre network core. Three different variants of thin (~1 mm) sandwich sheets have been produced and studied; flocked and glued (FG) sheet, long fibre in-plane mesh – brazed (MB) and glued (MG) sheets and short fibre 3-D array (SF) sheet. All sandwiches consist of 316L faceplates, while the cores are composed of either 316L or 446 fibres. A systematic study was carried out to characterise the complex core architecture, which was then correlated with their thermal and electrical conductivities. Resistance welding experiments were performed to access the weldability of these sheets. The experimental observations were compared with predictions from a numerical model, which takes into account changes in the core transport properties as it collapses and temperature rises. Main conclusions can be drawn in the following areas.

10.1 Architecture of Bonded Metallic Fibre Networks

- Computed X-ray micro-tomography (μCT) is demonstrated to be a powerful non-destructive technique for visualising the 3-D structure of the complex fibre networks. By employing a skeletonisation algorithm, important statistical data, such as fibre segment lengths, fibre orientation distributions and fibre tortuosity have been extracted. This technique is expected to be widely applicable to bonded fibre materials.

- Fibre segment lengths were found to increase with decreasing fibre volume fraction and fibre length. Although such an increase is expected as fibre fraction falls, the expected effect of fibre length is less obvious. However, for shorter fibres, fewer entanglements may be expected, which in turn, result in longer segment length. Details of the processing technique may be relevant in this context.

- The orientation distribution data indicate that all cores are transversely isotropic. Compared with a flocked core (FG), all sintered cores (MG, MB and SF) have fibres that are lying more in-plane (higher inclination angles, 70~75°). Evidently, long fibres (>10 mm) when constrained in a core of thickness less than 1 mm, will tend to be oriented at higher angles.

- It was noted that determination of fibre volume fractions from segmented tomography slices may be subject to relatively large errors (>20%), due to the small sample size (a few mm) and the limitations of the image analysis method, which is very sensitive to segmentation errors. Therefore, density measurement is recommended instead, as a more accurate method.

10.2 Thermal and Electrical Properties of Sandwich Sheets with Fibrous Cores

- A steady-state bi-substrate technique has been developed to measure the through-thickness thermal conductivities of thin sandwich sheets. The setup is designed to generate a one-dimensional heat flow across the sample. Estimation of heat flux is carried out by the averaging of fluxes through upper and lower substrates, taking into account the temperature dependence of thermal conductivity. The interfacial contact resistance can also be estimated if samples of different thicknesses are tested. This method is also potentially useful for other materials with low thermal conductivities (~1 W m^{-1} K^{-1}), e.g. ceramic coatings [169].

- The effective thermal conductivities of pre-sintered fibre felts and assembled sandwich sheets have been measured, with a mean temperature of ~100 ºC. They were found to be of the order of 0.1 W m^{-1} K^{-1}. Such low conductivities can be attributed to the highly porous cores, with porosity levels exceeding 80 vol.%. Also, the incorporation of low conductivity adhesives (in FG and MG) lowers the effective conductivities.

- The effective electrical resistivities (reciprocal of conductivities) of pre-sintered felts and sandwich sheets were measured in both through-thickness and in-plane directions. Because of the transversely isotropic core architecture, the in-plane resistivity is lower (~40%) than that in the through-thickness direction.

- The through-thickness electrical resistivity of FG sheet is a few orders of magnitude higher than that of other sandwiches, due to the thick epoxy adhesive separating fibre ends from faceplates. However, by employing low viscosity adhesive and curing under moderate pressure, it is possible to produce a sandwich (MG) with resistivity comparable to that of brazed (MB) sheets.

- A simple analytical model, based on an idealised unit cell structure, has been developed to predict the through-thickness and in-plane conductivities. It assumes a mean fibre inclination

angle (θ), which strongly affects the overall conductivity. Raising the inclination angle effectively lengthens the conduction path, which in turn lowers the effective conductivity (thermal and electrical). Also, the conductivity is predicted to increase with fibre volume fraction, which is rather self-evident. Its primary limitation lies in the assumption of all fibres lying at the same inclination angle to the faceplate normal. Nevertheless, this model is useful when the statistical distribution of the actual fibre orientation is not available.

- The orientation distribution model takes into account the actual fibre segment orientation distribution, obtained using tomography. This model gives excellent agreement with experiments when the core volume fraction is low (~10 vol.%), but over-predictions become apparent for denser cores. The assumption that all segment ends are interconnected leads to the introduction of extra conduction paths, not physically present, which raises the conductivity.

- In an attempt to capture the complex features of the fibre networks, such as fibre connectivity and tortuosity, 3-D finite-element (FE) models were constructed to simulate heat and electrical charge flows. Again, good agreement was obtained for low volume fraction cores (SF), while over-predictions were seen as the volume fraction increases. The use of an FE model is limited here, because the predictions are over-sensitive towards the quality and accuracy of the mesh. The limited resolution (~10 μm) of the current tomographic imaging facility may result in the generation of spurious bonds among fibre surfaces lying in close proximity, increasing the conductivities. The use of a higher resolution (1 μm) micro-tomography scanner may alleviate this problem.

10.3 Simulating the Resistance Spot Welding of Thin Sandwich Sheets

- A sequentially-coupled 2-D axisymmetric finite-element (FE) model for resistance spot welding (RSW) has been developed to simulate mechanical and thermal-electrical interactions occurring during welding of thin stainless steel sandwich sheets. The collapsed fibrous core is treated as an isotropic continuum. The model can capture the complex interplay of mechanical, electrical, thermal and metallurgical effects.

- The quasi-static (explicit) mechanical model gives good predictions of the geometry of collapsed sandwich structures, obtained at the end of the squeeze stage. It implements a ‘crushable foam’ constitutive relationship to simulate the large strain deformation. The core exhibits more extensive deformation, compared with the faceplates, due to its low yield

strength. The model also predicts the contact areas and normal contact pressures at the electrode-to-workpiece (E-W) and workpiece-to-workpiece (W-W) interfaces.

- The transient (implicit) thermal-electrical model takes into account temperature-dependent transport properties (of the collapsed core), interfacial contact resistances (thermal and electrical) and phase transformations (via enthalpy method). The 'molten' nugget is assumed to be thermally active, but mechanically inactive, so, the effects of fluid flow in the molten weld pool are not simulated. The model predicts the potential fields and Joule heat generation, which are used in determining the transient thermal profiles (weld nugget growth).

10.4 Welding Characteristics of Thin Sandwich Sheets

- The weldability of two variants of thin sandwich sheets, glued (MG) and brazed (MB), has been investigated. Both variants were found to be weldable, allowing high amperage currents to flow through the cores, forming good quality weld nuggets at appropriate welding conditions; electrode force ~2.5 kN, weld current ~4 kA and weld time ~200 ms.

- At the end of the squeeze stage (cold collapse), the core regions located directly under the electrode tips had sustained large plastic deformations (equivalent plastic strain of 35~40%). This is expected, since highly porous cores have significantly lower yield strengths than monolithic faceplates. However, both core and faceplate remotely located from the vicinity of electrode tips remain elastic (mechanical model predictions).

- The voltage and current history plots exhibit large fluctuations in voltage at the start of the weld period, before stabilising at the preset level (>50 ms). However, MG sheets showed a higher peak voltage, compared with SF, due to the high initial interfacial resistance of the low electrical conductivity adhesive layers. The breakdown of adhesive as temperature increases gradually lowers the voltage. This is also reflected in the rapid fall in total resistance, seen in the first 30 ms of weld time. Under steady-state conditions, the total resistance was found to remain at ~200 μΩ. The RSW model successfully predicts the voltage history and resistance in this period, implying that the core transport properties are being adequately modelled.

- It is noted that, due to its lower electrical resistivity, the newly developed glued sheet (MG) can be welded without requiring a shunt. The use of a low viscosity adhesive and curing under pressure help to promote better contact between the fibre ends and faceplate. This is an important improvement compared with FG sheets, which are not readily weldable.

- By examining the cross-sections of weld nuggets, it was observed that both the nugget geometry and size agreed well with model predictions. This suggests that the thermal fields have been correctly predicted, with maximum temperatures of ~1800 °C found at the centre of the molten pool.

- The weld nugget development in sandwich sheets can also be explained by following the evolution of transient thermal fields. Initially, heat generation is concentrated at the core-to-faceplate interfaces, arising from the initially low interfacial electrical contact conductance (at low temperature). However, as temperature rises, the maximum temperature shifted to the collapsed core, due to the higher core resistivity. Melting is predicted to commence in the vicinity of the core, followed by the inner faceplates melting. The molten nugget subsequently grows in the radial direction, since heat is constantly dissipated in the axial direction into the water-cooled electrodes.

- Welding experiments conducted at current levels below ~5 kA exhibited a direct increase of nugget diameter with increasing current. This is because of the increasing contribution from Joule heating. However, at higher currents (>5 kA), the measured nugget size starts to fall, as a result of melt expulsion. Clearly, welding at higher currents can potentially lead to various weld defects, such as faceplate cracking, shrinkage cracking and formation of porosity (due to decomposition of adhesive). These defects are generally associated with poor mechanical properties.

10.5 Future Work

- The resistance spot welding model does not currently incorporate thermo-mechanical coupling effects, so the changing stress states as weld time progresses cannot be predicted. The effect of thermal expansion is also not taken into account, but this may not be significant, due to the extensive core deformation. The existing FE model could be extended to incorporate these features (via a user subroutine).

- The temperature-dependent thermal and electrical interfacial contact resistances used in the current welding model (§8.3) need to be more carefully examined, since they can strongly influence the potential drops and heat generation at the interfaces (W-W and E-W). The mechanism of weld nugget development (§9.3) may also be sensitive to these resistances. However, measurement of interfacial resistances is generally complicated and requires elaborate setups (customised resistance welding machines). Systematic experimental studies, such as those reported by [110, 120, 170], may be useful.

- This work did not involve any investigations into the mechanical properties of the solidified welds. It is certainly important to correlate the quality of the weld nugget (experimental and model predictions) with its performance under combined loading conditions (especially under tensile and shear stresses).

APPENDIX

(A) Orientation Distribution Data of a FG Core

Angle at centre of bin, θ_i (º)	Number of fibre segment, N_{θ_i}	Number of fibre segment (corrected), $\frac{N_{\theta_i}}{\sin\theta_i}$	$N_{\theta_i}\cos^2\theta_i$	$P(\theta_i)=\frac{N_{\theta_i}}{\sin\theta_i\ \Delta\theta_i}\cdot\frac{1}{\sum_i^n N_{\theta_i}}$
4.5	0	0	0	0.0000
13.5	1	4.2836	0.9455	0.0635
22.5	3	7.8393	2.5607	0.1163
31.5	14	26.7943	10.178	0.3976
40.5	31	47.7328	17.925	0.7083
49.5	106	139.399	44.709	2.0686
58.5	122	143.0850	33.307	2.1233
67.5	81	87.6737	11.862	1.3010
76.5	37	38.0513	2.0164	0.5646
85.5	34	34.1051	0.2093	0.5061
$\Delta\theta_i$ $= 9^\circ = \frac{\pi}{20}$ rad	$\sum_i^n N_{\theta_i}$ = 429		$\sum_i^n N_{\theta_i}\cos^2\theta_i$ = 123.71	

(B) Orientation Distribution Data of a MB Core

Angle at centre of bin, θ_i (º)	Number of fibre segment, N_{θ_i}	Number of fibre segment (corrected), $\frac{N_{\theta_i}}{\sin\theta_i}$	$N_{\theta_i}\cos^2\theta_i$	$P(\theta_i)=\frac{N_{\theta_i}}{\sin\theta_i\ \Delta\theta_i}\cdot\frac{1}{\sum_i^n N_{\theta_i}}$
4.5	6	76.473	5.9631	0.8007
13.5	6	25.702	5.6730	0.2691
22.5	14	36.584	11.950	0.3830
31.5	17	32.536	12.359	0.3406
40.5	19	29.256	10.986	0.3063
49.5	28	36.822	11.810	0.3855
58.5	38	44.567	10.374	0.4666
67.5	61	66.026	8.9332	0.6913
76.5	152	156.32	8.2835	1.6367
85.5	267	267.83	1.6436	2.8043
$\Delta\theta_i$ $=9^\circ=\frac{\pi}{20}\text{rad}$	$\sum_i^n N_{\theta_i}$ $=608$		$\sum_i^n N_{\theta_i}\cos^2\theta_i$ $=87.98$	

(C) Orientation Distribution Data of a MG Core

Angle at centre of bin, θ_i (º)	Number of fibre segment, N_{θ_i}	Number of fibre segment (corrected), $\frac{N_{\theta_i}}{\sin\theta_i}$	$N_{\theta_i}\cos^2\theta_i$	$P(\theta_i)=\frac{N_{\theta_i}}{\sin\theta_i\ \Delta\theta_i}\cdot\frac{1}{\sum_i^n N_{\theta_i}}$
4.5	1	12.745	0.99384	0.2732
13.5	3	12.851	2.8365	0.2755
22.5	7	18.292	5.9749	0.3921
31.5	13	24.88	9.4509	0.5333
40.5	6	9.2386	3.4693	0.1980
49.5	18	23.672	7.5921	0.5074
58.5	26	30.494	7.0981	0.6536
67.5	29	31.389	4.247	0.6728
76.5	58	59.648	3.1608	1.2786
85.5	136	136.42	0.83719	2.9242
$\Delta\theta_i$ $=9^\circ=\frac{\pi}{20}\text{rad}$	$\sum_i^n N_{\theta_i}$ $=297$		$\sum_i^n N_{\theta_i}\cos^2\theta_i$ $=45.66$	

(D) Orientation Distribution Data of a SF Core

Angle at centre of bin, θ_i (º)	Number of fibre segment, N_{θ_i}	Number of fibre segment (corrected), $\frac{N_{\theta_i}}{\sin\theta_i}$	$N_{\theta_i}\cos^2\theta_i$	$P(\theta_i)=\frac{N_{\theta_i}}{\sin\theta_i\ \Delta\theta_i}\cdot\frac{1}{\sum_i^n N_{\theta_i}}$
4.5	2	25.490	1.9877	0.6819
13.5	6	25.701	5.673	0.6875
22.5	8	20.905	6.8284	0.5592
31.5	9	17.224	6.543	0.4607
40.5	11	16.937	6.3604	0.4531
49.5	16	21.041	6.7485	0.5628
58.5	21	24.629	5.7331	0.6588
67.5	25	27.059	3.6612	0.7238
76.5	47	48.335	2.5613	1.2929
85.5	93	93.287	0.57249	2.4953
$\Delta\theta_i$ $=9^\circ=\frac{\pi}{20}\text{rad}$	$\sum_i^n N_{\theta_i}$ $=238$		$\sum_i^n N_{\theta_i}\cos^2\theta_i$ $=46.669$	

REFERENCES

1. Gustafsson, R.N.-G., *Formable Sandwich Construction Material and Use of the Material as Construction Material in Vehicles, Refrigerators, Boats etc*. Patent WO 98/01295. 1998, AB Volvo: International.

2. Markaki, A.E., Westgate, S.A., and Clyne, T.W. *The Stiffness and Weldability of an Ultra-Light Steel Sandwich Sheet Material with a Fibrous Metal Core*. in *Processing and Properties of Lightweight Cellular Metals and Structures*. Ghosh, A.K., Claar, T.D., and Sanders, T.H., Editors. 2002. Seattle: TMS. p. 15-24.

3. Williams, N.T. and Parker, J.D., *Review of Resistance Spot Welding of Steel Sheets. Part 1-Modelling and Control of Weld Nugget Formation.* International Materials Reviews, 2004. **49**(2): p. 45-75.

4. Allen, H.G., *Analysis and Design of Structural Sandwich Panels*. 1969, London, UK.: Pergamon Press Ltd.

5. Corden, J., *Honeycomb Structure*, in *Engineered Materials Handbook*, Dostal, C.A., Editor. 1990, ASM Int.: Ohio, USA. p. 721-728.

6. Bitzer, T., *Honeycomb Technology*. 1997, London, U.K.: Chapman & Hall.

7. Davies, J.M., ed. *Lightweight Sandwich Construction*. 2001, Blackwell Science Ltd.: Cornwall, U.K.

8. Graham, R. *Sandwich Structures for Space Applications*. in *Proc. of the 3rd Inter. Conf. on Sandwich Construction*. Allen, H.G., Editor 1995. Southampton, UK: EMAS Ltd. p. 129-138.

9. Olsson, K.-A. and Lonno, A. *Sandwich Constructions - Recent Research and Development: GRP-Sandwich Technology for High-speed Marine Vessels*. in *Proc. of the 2nd Inter. Conf. on Sandwich Construction*. Weissman-Berman, D. and Olsson, K.-A., Editors. 1992. Florida, USA.: EMAS Ltd. p. 807-823.

10. Karlsson, K.F. and Astrom, B.T., *Manufacturing and Applications of Structural Sandwich Components.* Composites Part A, 1997. **28**: p. 97-111.

11. Braziel, K.R. and Cartwright, C.L. *Commercial Aircraft Nose Radomes Using Rigid Foam Core Sandwich Construction*. in *Proc. of the 2nd Inter. Conf. on Sandwich Construction*. Weissman-Berman, D. and Olsson, K.-A., Editors. 1992. Florida, USA.: EMAS Ltd. p. 825-841.

12. Sato, M., Tanaka, Y., Yutori, Y., Nishikawa, H., and Miyahara, M. *Development of Conductible Type Vibration Damping Composite Steel Sheet for Automotive Use*. in *International Congress and Exposition, SAE Technical Paper Series*. 1991. Detroit, Michigan.: SAE , Inc. p. 1-8.

13. Muroga, O., Nishimoto, A., Watanabe, Y., Fujii, Y., Yamazaki, Y., and Kabasawa, M., *Properties of Vibration Damping Steel Sheet and Its Application.* NKK Technical Review, 1989(57): p. 1-8.

14. Makinouchi, A., Ogawa, H., and Hashimoto, K. *Computational Methods for Predicting Material Processing Defects*. in *STRUCMAT 87*. Predeleanu, M., Editor 1987. Cachan, France: Elsevier Science Publishers B.V., Amsterdam. p. 221-230.

15. Fatt, M.S.H., Lin, C., Revilock, D.M., and Hopkins, D.A., *Ballistic Impact of GLARE Fiber-Metal Laminates.* COMPOS STRUCT, 2003. **61**: p. 73 - 88.

16. Wadley, H.N.G., Fleck, N.A., and Evans, A.G., *Fabrication and Structural Performance of Periodic Cellular Metal Sandwich Structures.* Comp Sci & Tech, 2003. **63**(Special Issue on Porous Materials): p. 2331-2343.

17. Sypeck, D.J. and Wadley, H.N.G., *Multifunctional Microtruss Laminates: Textile Synthesis and Properties.* J. Mater. Res., 2001. **16**(3): p. 890-897.

18. Kooistra, G.W., Deshpande, V.S., and Wadley, H.N.G., *Compressive Behavior of Age Hardenable Tetrahedral Lattice Truss Structures Made From Aluminium.* Acta Materialia, 2004. **52**(14): p. 4229-4237.

19. Banhart, J., *Manufacture, Characterisation and Application of Cellular Metals and Metal Foams.* Progress Mater. Sci., 2001. **46**: p. 559-632.

20. NASA, *Fact Sheet 2000-06-29-KSC: Orbiter Thermal Protection System*. 1997, NASA.

21. Lee, S.C. and Cunnington, G.R., *Heat Transfer in Fibrous Insulations: Comparison of Theory and Experiment.* J. Thermophysics and Heat Transfer, 1998. **12**(3): p. 297-303.

22. Daryabeigi, K., *Thermal Analysis and Design Optimization of Multilayer Insulation for Reentry Aerodynamic Heating.* J. Spacecraft & Rockets, 2002. **39**(4): p. 509-514.

23. Daryabeigi, K., *Heat Transfer in High Temperature Fibrous Insulation.* J. Thermophysics & Heat Transf., 2003. **17**(1): p. 10-20.

24. Delannay, F. and Clyne, T.W. *Elastic Properties of Cellular Metals Processed by Sintering Mats of Fibres*. in *MetFoam '99*. Banhart, J., Ashby, M.F., and Fleck, N.A., Editors. 1999. Bremen, Germany: Verlag MIT Publishing. p. 293-298.

25. Gustafsson, R.N.-G. *Ultralight Stainless Steel Sandwich Materials*. in *Proceedings of the 5th International Conference on Sandwich Construction*. Meyer-Piening, H.-R. and Zenkert, D., Editors. 2000. ETH Zurich: Emas Publishing. p. 169-176.

26. Markaki, A.E. and Clyne, T.W., *Mechanical and Electrical Properties of Stainless Steel Sandwich Sheets with Fibrous Metal Cores, Designed for Automotive Applications*, in *'Metal and Ceramic Composites: Automotive Applications', Oxford-Kobe Materials Seminar*, Grant, P., Johnston, C., and Cantor, B., Editors. 2005, IoP Publishing Ltd. p. in press.

27. Markaki, A.E., Gergely, V., Cockburn, A., and Clyne, T.W., *Production of a Highly Porous Material by Liquid Phase Sintering of Short Ferritic Stainless Steel Fibres and a Preliminary Study of its Mechanical Behaviour.* Comp. Sci. & Techn., 2003. **63**: p. 2345-2351.

28. Wadley, H., *Cellular Metals Manufacturing.* Adv. Eng. Mater., 2002. **10**(4): p. 726-733.

29. Landrock, A.H., *Adhesives Technology Handbook*. 1985: Noyes Publications.

30. Gauthier, M.M., *Types of Adhesives*, in *Engineered Materials Handbook*, Dostal, C.A., Editor. 1990, ASM Int.: USA. p. 74-93.

31. Schwartz, M.M., *Fundamentals of Brazing*, in *ASM Handbook: Welding, Brazing and Soldering*, Olson, D.L., Siewert, T.A., Liu, S., and Edwards, G.R., Editors. 1993, ASM International: Ohio. p. 114-125.

32. Lucas, M.J., *Brazing of Stainless Steels*, in *Welding Brazing and Soldering*, Olson, D.L., Siewert, T.A., Liu, S., and Edwards, G.R., Editors. 1993, ASM International. p. 911-923.

33. duBois, S., *Brazing Fundamentals - Metallurgy of Nickel-Based Brazing Filler Metals*. 2004, Wall Colmonoy Corporation: USA.

34. Hanebuth, H., Dotzer, A., Nielsen, K., and Sorensen, K.G., *Joining of Cellular and Stratified Laminates for Lightweigh Construction and Thermal-Acoustic Insulation.* J. Mat. Proc. Tech., 2001. **115**(1): p. 31-37.

35. Chen, C., Harte, A.M., and Fleck, N.A., *The Plastic Collapse of Sandwich Beams with A Metallic Foam Core.* Int. J. Mech. Sci., 2001. **43**(6): p. 1483-1506.

36. Lok, T.S. and Chen, Q.H., *Elastic Stiffness Properties and Behavior of Truss-Core Sandwich Panel.* J. Structural Engineering - ASCE, 2000. **126**(5): p. 552-559.

37. McCormack, T.M., Miller, R., Kesler, O., and Gibson, L.J., *Failure of Sandwich Beams with Metallic Foam Cores.* Int. J. of Solids and Structures, 2001. **38**(28-29): p. 4901-4920.

38. Markaki, A.E. and Clyne, T.W., *Mechanics of Thin Ultra-Light Stainless Steel Sandwich Sheet Material: Part I - Stiffness.* Acta Mater., 2003. **51**(5): p. 1341-1350.

39. Markaki, A.E. and Clyne, T.W., *Mechanics of Thin Ultra-Light Stainless Steel Sandwich Sheet Material: Part II - Resistance to Delamination.* Acta Mater., 2003. **51**(5): p. 1351-1357.

40. Cockburn, A., *Certificate of Postgraduate Studies (CPGS):- Production of 3D Fibre Array Sandwich Sheet Material*. 2003, University of Cambridge.

41. Markaki, A.E. and Clyne, T.W., *Ultra Light Stainless Steel Sheet Material*. Patent no. 10/000117 (US 6,764,772 B2). 2001, Cambridge University: US.

42. Tan, J.C., *Certificate of Postgraduate Studies (CPGS):- Thermal, Electrical and Resistance Welding Characteristics of a Novel Sandwich Sheet Material*. 2002, University of Cambridge: Cambridge.

43. Mohr, D. and Wierzbicki, T., *Crushing of Soft-Core Sandwich Profiles: Experiments and Analysis.* Int. J. Mech. Sciences, 2003. **45**: p. 253-271.

44. Incropera, F.P. and Dewitz, D.P., *Fundamentals of Heat and Mass Transfer*. Fifth ed. 2002: John Wiley & Sons.

45. Markaki, A.E., Colombo, P., and Clyne, T.W., *Highly Porous Cellular Metals and Ceramics: Thermo-Mechanical Properties*, in *Encyclopedia of Condensed Matter Physics*, Bassani, F., Liedl, J., and Wyder, P., Editors. 2005, Elsevier. p. in press.

46. Powell, R.W., *Correlation of Metallic Thermal and Electrical Conductivities for Both Solid and Liquid Phases.* Int. J. Heat & Mass Transf., 1964. **8**: p. 1033-1045.

47. Boomsma, K. and Poulikakos, D., *On the Effective Thermal Conductivity of a Three-Dimensionally Structured Fluid-Saturated Metal Foam.* Int. J. Heat Mass Transfer, 2001. **44**: p. 827-836.

48. Mantle, W.J. and Chang, W.S., *Effective Thermal Conductivity of Sintered Metal Fibers.* J. Thermophysics & Heat Transf., 1991. **5**(4): p. 545-549.

49. Bhattacharya, A., Calmidi, V.V., and Mahajan, R.L., *Thermophysical Properties of High Porosity Metal Foams.* International Journal of Heat and Mass Transfer, 2002. **45**(5): p. 1017-1031.

50. Schuetz, M.A. and Glicksman, L.R. *Proceedings of the Society of Plastics Industry*. in *6th International Technical/Marketing Conference*. 1983. San Diego, California. p. 341-347.

51. Gibson, L.J. and Ashby, M.F., *Cellular Solids: Structure and Properties*. 2nd ed. 1997, Cambridge: Cambridge University Press. 357.

52. Clyne, T.W., *Thermal and Electrical Conduction in MMCs*, in *Comprehensive Composite Materials, Vol. 3 : Metal Matrix Composites*, Clyne, T.W., Editor. 2000, Elsevier: Amsterdam. p. 447-468.

53. Bauer, T.H., *A General Analytical Approach Toward the Thermal Conductivity of Porous Media.* Int. J. Heat Mass Transfer, 1993. **36**(17): p. 4181-4191.

54. Collishaw, P.G. and Evans, J.R.G., *An Assessment of Expressions for the Apparent Thermal Conductivity of Cellular Materials.* J. Mat. Sci., 1994. **29**: p. 486-498.

55. Dawson, D.M. and Briggs, A., *Prediction of the Thermal Conductivity of Insulation Materials.* J. Mat. Sci., 1981. **16**: p. 3346-3356.

56. Calmidi, V.V. and Mahajan, R.L., *Effective Thermal Conductivity of High Porosity Fibrous Metal Foams.* J. Heat Transf., Trans. ASME, 1999. **121**(2): p. 466-471.

57. Koh, J.C.Y. and Fortini, A., *Prediction of Thermal Conductivity and Electrical Resistivity of Porous Metallic Materials.* Int. J. Heat & Mass Transfer, 1973. **16**(11): p. 2013-2022.

58. Aivazov, M.I. and Domashnev, I.A., *Influence of Porosity on the Conductivity of Hot-Pressed Titanium Specimens.* Soviet Powder Metallurgy and Metal Ceramics, 1968. **7**(67): p. 708-710.

59. Acton, A., *Correlating Equations for the Properties of Metal Felt Wicks*, in *Advances in Heat Pipe Technology*, Reay, D.A., Editor. 1982, Pergamon Press: New York. p. 279-288.

60. Koh, J.C.Y., Casal, E.P.d., Evans, R.W., and Deriugin, V., *Fluid Flow and Heat Transfer in High-Temperature Porous Matrices for Transpiration Cooling*. 1966, Air Force Flight Dynamics Lab., Research and Development Div., Wright-Patterson AFB: OH.

61. Semena, M.G. and Zaripov, V.K., *Influence of the Diameter and Length on Material Heat Transfer of Metal-Fibre Wicks of Heat Pipes.* Teploenergetika, 1977. **24**(4): p. 82-84.

62. Soliman, M.M., Graumann, D.W., and Berenson, P.J., *Effective Thermal Conductivity of Dry and Liquid-Saturated Sintered Fiber Metal Wicks*, in *American Society of Mechanical Engineers*. 1970: New York.

63. Alexander, E.G., *Structure-Property Relationships in Heat Pipe Wicking Materials*. 1972, North Carolina State University: Raleigh, NC.

64. Januszewski, J., Khokhar, M.I., and Mujumdar, A.S., *Thermal Conductivity of Some Porous Materials*. Letters in Heat and Mass Transfer, 1977. **4**: p. 417-423.

65. Holman, J., *Heat Transfer*. 7th ed. 1992, London: McGraw-Hill.

66. Skochdopole, R.E., *The Thermal Conductivity of Foamed Plastics.* Chem. Eng. Prog., 1961. **57**(10): p. 55-59.

67. Bhattacharyya, R.K., *Heat Transfer Model for Fibrous Insulations, Thermal Insulation Performance*, in *ASTM STP 718*, McElroy, D.L. and Tye, R.P., Editors. 1980, American Society for Testing and Materials. p. 272-286.

68. Lu, T.J., Stone, H.A., and Ashby, M.F., *Heat Transfer in Open-Cell Metal Foams.* Acta Mater., 1998. **46**(10): p. 3619-3635.

69. Angirasa, D., *Forced Convective Heat Transfer in Metallic Fibrous Materials.* J. Heat Transf. -Trans. ASME, 2002. **124**(4): p. 739-745.

70. Angirasa, D., *Experimental Investigation of Forced Convection Heat Transfer Augmentation with Metallic Fibrous Materials.* Int. J. Heat & Mass Transf., 2002. **45**(4): p. 919-922.

71. Tong, T.W. and Tien, C.L., *Radiative Heat Transfer in Fibrous Insulations. Part 1: Analytical Study.* Journal of Heat Transfer-Transactions of the ASME, 1983. **105**(1): p. 70-75.

72. Tong, T.W., Yang, Q.S., and Tien, C.L., *Radiative Heat Transfer in Fibrous Insulations. Part 2: Experimental Study.* Journal of Heat Transfer-Transactions of the ASME, 1983. **105**(1): p. 76-81.

73. Lee, S.C., *Effect of Fiber Orientation on Thermal-Radiation in Fibrous Media.* International Journal of Heat and Mass Transfer, 1989. **32**(2): p. 311-319.

74. McIntire, O.R. and Kennedy, R.N., *Styrofoam for Low-Temperature Insulation.* Chem. Eng. Prog., 1948. **44**(9): p. 727-730.

75. Stark, C. and Fricke, J., *Improved Heat-Transfer Models for Fibrous Insulations.* International Journal of Heat and Mass Transfer, 1993. **36**(3): p. 617-625.

76. Lee, S.C. and Cunnington, G.R., *Conduction and Radiation Heat Transfer in High Porosity Fiber Thermal Insulation.* J. Thermophysics & Heat Transf., 2000. **14**(2): p. 121-136.

77. Petrov, V.A., *Combined Radiation and Conduction Heat Transfer in High Temperature Fiber Thermal Insulation.* Int. J. Heat Mass Transf., 1997. **40**(9): p. 2241-2247.

78. Glicksman, L., Schuetz, M., and Sinofsky, M., *Radiation Heat Transfer in Foam Insulation.* Int. J. Heat Mass Transfer, 1987. **30**(1): p. 187-197.

79. Schuetz, M.A. and Glicksman, L.R., *A Basic Study of Heat-Transfer Through Foam Insulation.* Journal of Cellular Plastics, 1984. **20**(2): p. 114-121.

80. Ashby, M.F., Evans, A.G., Hutchinson, J.W., and Fleck, N.A., *Metal Foams: A Design Guide*. 1998, Cambridge University, Engineering Department: Cambridge.

81. Dharmasena, K.P. and Wadley, H.N.G., *Electrical Conductivity of Open-Cell Metal Foams.* J. Mater. Res., 2002. **17**(3): p. 625-631.

82. Williams, N.T., *Resistance Spot Welding*, in *ASM Handbook: Welding, Brazing and Soldering*. 1993, ASM International: Ohio. p. 226-230.

83. Natale, T. and Irving, B., *Automakers Set the Pace for Spot Welding the New Galvanized Steels.* Welding J., 1992. **71**(3): p. 47-52.

84. Harlin, N., Jones, T.B., and Parker, J.D., *Weld Growth Mechanisms During Resistance Spot Welding of Two and Three Thickness Lap Joints.* Sci. Tech. of Welding and Joining, 2002. **7**(1): p. 35-41.

85. Hardin, W., *Spot Welding: Still in the Driver's Seat.* Welding J., 2003. **82**(11): p. 46-49.

86. Kearns, W.H., ed. *AWS Welding Handbook*. 7th ed. Vol. 3: Resistance and solid-state welding and other joining processes. 1980, The Macmillan Press Ltd.: UK.

87. Hill, R., *The Mathematical Theory of Plasticity*. 1950, London: Oxford University Press.

88. Ishlinsky, A.J., *Theoretical Research Translation no. 2/47*, in *J. Appl. Math. Mech. (USSR)*. 1947, Ministry of Supply.

89. Feng, Z., Gould, J.E., Babu, S.S., Santella, M.L., and Reimer, B.W. *An Incrementally Coupled electrical-Thermal-Mechanical Model for Resistance Spot Welding*. in *Proc. 5th Inter. Conf. Trends in Welding Research*. J.M. Vitek, S.A.D., J.A. Johnson, H.B. Smartt, T. DeRoy, Editor 1998. Georgia, USA: ASM Int. p. 599-604.

90. Khan, J.A., Xu, L.J., Chao, Y.J., and Broach, K., *Numerical Simulation of Resistance Spot Welding Process.* Numerical Heat Transfer Part A-Applications, 2000. **37**(5): p. 425-446.

91. Xu, L. and Khan, J.A. *The Finite Element Modeling of Axisymmetric Nugget Development during Resistance Spot Welding*. in *Proc. 5th Inter. Conf. Trends in Welding Research*. J.M. Vitek, S.A.D., J.A. Johnson, H.B. Smartt, T. DeRoy, Editor 1998. Georgia, USA: ASM Int. p. 616-621.

92. Bowers, R.J., Sorensen, C.D., and Eagar, T.W., *Electrode Geometry in Resistance Spot Welding.* Welding J., 1990. **69**(2): p. 45s-51s.

93. Nied, H.A., *The Finite Element Modeling of the Resistance Spot Welding Process.* Welding J., 1984. **63**(4): p. 123s-132s.

94. Williams, N.T. and Parker, J.D., *Review of Resistance Spot Welding of Steel Sheets. Part 2-Factors Influencing Electrode Life.* International Materials Reviews, 2004. **49**(2): p. 77-108.

95. Fukumoto, S., Lum, I., Biro, E., Boomer, D.R., and Zhou, Y., *Effects of Electrode Degradation on Electrode Life in Resistance Spot Welding of Aluminum Alloy 5182.* Welding Journal (Miami, Fla), 2003. **82**(11): p. 307-312.

96. Rice, W. and Funk, E.J., *An Analytical Investigation of the Temperature Distributions during Resistance Welding.* Welding J., 1967. **46**(4): p. 175s-186s.

97. Thornton, P.H., Krause, A.R., and Davies, R.G., *Contact Resistances in Spot Welding.* Welding J., 1996. **75**(12): p. 402s-412s.

98. Xu, L. and Khan, J.A., *Nugget Growth Model for Aluminum Alloys during Resistance Spot Welding.* Welding J., 1999. **78**(11): p. 367s-372s.

99. Kaiser, J.G., Dunn, G.J., and Eagar, T.W., *The Effect of Electrical Resistance on Nugget Formation during Spot Welding.* Welding J., 1982. **61**(6): p. 167s-174s.

100. Cho, Y. and Rhee, S., *Experimental Study of Nugget Formation in Resistance Spot Welding.* Welding Journal (Miami, Fla), 2003. **82**(8): p. 195-201.

101. Alcini, W.V., *Experimental Measurement of Liquid Nugget Heat Convection in Spot Welding.* Welding J., 1990. **69**(4): p. 177s-180s.

102. Sun, X. and Dong, P., *Analysis of Aluminum Resistance Spot Welding Processes Using Coupled Finite Element Procedures.* Welding J., 2000. **79**(8): p. 215s-221s.

103. Wei, P.S. and Yeh, F.B., *Factors Affecting Nugget Growth with Mushy-Zone Phase Change during Resistance Spot Welding.* J. Heat Transfer (Trans. ASME), 1991. **113**: p. 643-649.

104. Kim, E.W. and Eagar, T.W., *Measurement of Transient Temperature Response during Resistance Spot Welding.* Welding J., 1989: p. 303s-312s.

105. Wei, P.S. and Ho, C.Y., *Axisymmetric Nugget Growth during Resistance Spot Welding.* J. Heat Transfer (Trans. ASME), 1990. **112**: p. 309-316.

106. Yeung, K.S. and Thornton, P.H., *Transient Thermal Analysis of Spot Welding Electrodes.* Welding J., 1999. **78**(1): p. 1s-6s.

107. Greenwood, J.A., *Temperatures in Spot Welding.* British Welding Journal, 1961. **6**: p. 316-322.

108. Civelek, M.S., Erdogan, F., and Cakiroglu, A.O., *Interface Separation for an Elastic Layer Loaded by a Rigid Stamp.* Int. J. Engr. Sci., 1978. **16**: p. 669-679.

109. Babu, S.S., Santella, M.L., Feng, Z., Riemer, B.W., and Cohron, J.W., *Empirical Model of Effects of Pressure and Temperature on Electrical Contact Resistance of Metals.* Science and Technology of Welding and Joining, 2001. **6**(3): p. 126-132.

110. Gedeon, S.A., Sorensen, C.D., Ulrich, K.T., and Eagar, T.W., *Measurements of Dynamic Electrical and Mechanical Properties of Resistance Spot Welds.* Welding J., 1987. **66**(1): p. 1s-10s.

111. Crinon, E. and Evans, J.T., *The Effect of Surface Roughness, Oxide Film Thickness and Interfacial Sliding on the Electrical Contact Resistance of Aluminium.* Mater. Sci. & Eng., 1998. **A242**: p. 121-128.

112. Richard, D., Fafard, M., Lacroix, R., Clery, P., and Maltais, Y., *Carbon to Cast Iron Electrical Contact Resistance Constitutive Model for Finite Element Analysis.* Journal of Materials Processing Technology, 2003. **132**(1-3): p. 119-131.

113. Greenwood, J.A., *Constriction Resistance and the Real Area of Contact.* Br. J. Appl. Phys., 1966. **17**: p. 1621-1632.

114. Wang, S.C. and Wei, P.S., *Modeling Dynamic Electrical Resistance during Resistance Spot Welding.* J. Heat Transfer - Trans. ASME, 2001. **123**(3): p. 576-585.

115. Savage, W.F., Nippes, E.F., and Wassell, F.A., *Dynamic Contact Resistance of Series Spot Welds.* Welding J., 1978. **57**(2): p. 43s-50s.

116. Dickinson, D.W., Franklin, J.E., and Stanya, A., *Characterization of Spot Welding Behavior by Dynamic Electrical Parameter Monitoring.* Welding J., 1980. **59**(6): p. 170s-176s.

117. Vogler, M. and Sheppard, S., *Electrical Contact Resistance under High Loads and Elevated Temperatures.* Welding J., 1993. **72**(6): p. 231s-239s.

118. Lee, A. and Nagel, G.L. *Basic Phenomenon in Resistance Spot Welding*. in *SAE Inter. Congress and Exposition*. 1988. Detroit, Mich. p.

119. Fletcher, L.S., *Recent Developments in Contact Conductance Heat-Transfer.* Journal of Heat Transfer-Transactions of the ASME, 1988. **110**(4B): p. 1059-1070.

120. Loulou, T. and Bardon, J.P., *Estimation of Thermal Contact Conductance during Resistance Spot Welding.* Experimental Heat Transfer, 2001. **14**: p. 251-264.

121. Le Meur, G., Bourouga, B., and Dupuy, T., *Measurement of Contact Parameters at Electrode/Sheet Interface during Resistance Spot Welding Process.* Science and Technology of Welding and Joining, 2003. **8**(6): p. 415-422.

122. Tsai, C.L., *Advances in the Resistance Welding of Automotive Aluminum.* JOM, 1997. **49**(5): p. 28-30.

123. Sakuma, Y. and Takahashi, Y., *Spot Weldability of Galvannealed Steel Sheets with a Tensile Strength of 590 MPa.* JSAE Review, 2002. **23**(1): p. 142-144.

124. James, P.S., Chandler, H.W., Evans, J.T., Wen, J., Browne, D.J., and Newton, C.J., *The Effect of Mechanical Loading on the Contact Resistance of Coated Aluminium.* Mater. Sci. & Eng., 1997. **A230**: p. 194-201.

125. Oberle, H., Commaret, C., Magnaud, R., Minier, C., and Pradere, G., *Optimizing Resistance Spot Welding Parameters for Vibration Damping Steel Sheets.* Welding Journal, 1998. **77**(1): p. 8S-13S.

126. Nishimoto, A., Watanabe, Y., Fujii, Y., Kabasawa, S., and Matsuda, Y., *Weldable Vibration Damping Steel Sheet.* NKK Technical Review, 1988(53): p. 10-18.

127. Tsai, C.L., Dai, W.L., and Dickinson, D.W. *Analysis and Development of a Realtime Control Methodology in Resistance Spot Welding*. in *International Congress and Exposition, Feb 25-Mar 1 1991*. 1991. Detroit, MI, USA: Publ by SAE, Warrendale, PA, USA. p. 44.

128. Jou, M., *Realtime Monitoring Weld Quality of Resistance Spot Welding for the Fabrication of Sheet Metal Assemblies.* Journal of Materials Processing Technology, 2003. **132**(1-3): p. 102-113.

129. Khan, J.A., Broach, K., and Kabir, A.A.S.A., *Numerical Thermal Model of Resistance Spot Welding in Aluminum.* J. Thermophysics and Heat Transfer, 2000. **14**(1): p. 88-95.

130. Gould, J.E., *An Examination of Nugget Development during Spot Welding, Using Both Experimental and Analytical Techniques.* Welding J., 1987. **66**(1): p. 1s-10s.

131. Bentley, K.P., Greenwood, J.A., Knowlson, P.M., and Baker, R.G., *Temperature Distributions in Spot Welds.* British Welding J., 1963. **12**: p. 613-619.

132. Tsai, C.L., Jammal, O.A., Papritan, J.C., and Dickinson, D.W., *Modeling of Resistance Spot Weld Nugget Growth.* Welding J., 1992. **71**(2): p. 47s-54s.

133. Cho, H.S. and Cho, Y.J., *A Study of the Thermal Behavior in Resistance Spot Welds.* Welding J., 1989. **68**(6): p. 236s-244s.

134. Han, Z., Orozco, J., Indacochea, J.E., and Chen, C.H., *Resistance Spot Welding: A Heat Transfer Study.* Welding J., 1989. **73**(9): p. 362s-371s.

135. Browne, D.J., Chandler, H.W., Evans, J.T., and Wen, J., *Computer Simulation of Resistance Spot Welding in Aluminum: Part I.* Welding J., 1995. **74**(10): p. 339s-344s.

136. Browne, D.J., Chandler, H.W., Evans, J.T., James, P.S., Wen, J., and Newton, C.J., *Computer Simulation of Resistance Spot Welding in Aluminum: Part II.* Welding J., 1995. **74**(12): p. 417s-422s.

137. Khan, J.A., Xu, L., and Chao, Y.-J., *Prediction of Nugget Development during Resistance Spot Welding using Coupled Thermal-Electrical-Mechanical Model.* Sci. Tech. of Welding and Joining, 1999. **4**(4): p. 201-207.

138. De, A., *Finite Element Modelling of Resistance Spot Welding of Aluminium with Spherical Tip Electrodes.* Sci. Tech. of Welding and Joining, 2002. **7**(2): p. 119-124.

139. Long, X. and Khanna, S.K., *Numerical Simulation of Residual Stresses in a Spot Welded Joint.* Trans A.S.M.E., 2003. **125**: p. 222-226.

140. Leffler, B., *Stainless Steels and Their Properties*. 2001, Avesta Polarit AB: Degerfors.

141. Feldkamp, I.A., Davis, L.C., and Kress, J.W., *Practical Cone Beam Algorithm.* 1984. **1**(6): p. 612-619.

142. Lindquist, W.B., *3DMA General Users Manual*. 1999, State University of New York at Stony Brook: New York. p. 1-47.

143. Lindquist, W.B. and Venkatarangan, A., *Investigating 3D Geometry of Porous Media from High Resolution Images.* Physics and Chemistry of the Earth Part A: Solid Earth and Geodesy, 1999. **24**(7): p. 593-599.

144. Yang, H., *A Geometric and Statistical Analysis of Fibrous Materials from Three-Dimensional High Resolution Images (PhD Thesis)*, in *Department of Applied Mathematics and Statistics*. 2001, State University of New York at Stony Brook: New York. p. 1-162.

145. Peckner, D. and Bernstein, I.M., *Handbook of Stainless Steels*. 1977: McGraw-Hill Book Company.

146. *Nimonic Alloy 80A Material Datasheet: Physical and Mechanical Properties*, Special Metals Corporation: Hereford, UK.

147. *Heraeus Quarzglas - Quartz Glass for Optics: Data and Properties*. 2004, Heraeus: Germany.

148. Whitehouse, A.F., Warwick, C.M., and Clyne, T.W., *The Electrical Resistivity of Copper Reinforced with Short Carbon Fibres.* J. Mat. Sci., 1991. **26**: p. 6176-6182.

149. Perona, P. and Malik, J., *Scale-space and Edge Detection using Anisotropic Diffusion.* IEEE Transactions on Pattern Analysis and Machine Intelligence, 1990. **12**(7): p. 629-639.

150. Yang, H. and Lindquist, B.W. *Three-Dimensional Image Analysis of Fibrous Materials*. in *Applications of Digital Image Proceeding XXIII, Jul 31-Aug 3 2000*. 2000. San Diego, CA, USA: Society of Photo-Optical Instrumentation Engineers, Bellingham, WA, USA. p. 275-282.

151. Shackelford, J.F. and Alexander, W., *CRC Materials Science and Engineering Handbook*. 3rd ed. 2001, N.Y., USA: CRC Press.

152. Dasgupta, A. and Agarwal, R.K., *Orthotropic Thermal Conductivity of Plain-weave Fabric Composites using a Homogenization Technique.* Journal of Composite Materials, 1992. **26**(18): p. 2736-2758.

153. Dasgupta, A., Agarwal, R.K., and Bhandarkar, S.M., *Three-Dimensional Modeling of Woven-fabric Composites for Effective Thermo-Mechanical and Thermal Properties.* Composites Science and Technology, 1996. **56**(3): p. 209-223.

154. Goo, N.S. and Woo, K., *Measurement and Prediction of Effective Thermal Conductivity for Woven Fabric Composites.* International Journal of Modern Physics B, 2003. **17**(8-9): p. 1808-1813.

155. Lusti, H.R., Hine, P.J., and Gusev, A.A., *Direct Numerical Predictions for the Elastic and Thermoelastic Properties of Short Fibre Composites.* Composites Science and Technology, 2002. **62**(15): p. 1927-1934.

156. Hine, P.J., Lusti, H.R., and Gusev, A.A., *Numerical Simulation of the Effects of Volume Fraction, Aspect Ratio and Fibre Length Distribution on the Elastic and Thermoelastic Properties of Short Fibre Composites.* Composites Science and Technology, 2002. **62**(10-11): p. 1445-1453.

157. ANSYS, *ANSYS Release 8.1 Documentation.* Ansys Inc., 2004.

158. ABAQUS, *ABAQUS/Explicit User's Manuals, version 6.3.* Hibbitt, Karlsson & Sorensen, Inc., 2003.

159. Li, G., Thomas, B.G., and Stubbins, J.F., *Modeling Creep and Fatigue of Copper Alloys.* Metall. Mater. Trans. A, 2000. **31A**(10): p. 2491-2502.

160. Landert, M., *Personal communication*. 2003.

161. Deshpande, V.S. and Fleck, N.A., *Isotropic Constitutive Models for Metallic Foams.* Journal of the Mechanics and Physics of Solids, 2000. **48**(6-7): p. 1253-1283.

162. Schluppkotten, J., *Investigation of the ABAQUS/Crushable Foam Plasticity Model.* Internal Report of BMW AG, 1999.

163. ABAQUS, *ABAQUS/Standard User's Manuals, version 6.3.* Hibbitt, Karlsson & Sorensen, Inc., 2003.

164. Rohsenow, W.M., Hartnett, J.P., and Cho, Y.I., eds. *Handbook of Heat Transfer*. 3rd ed. 1998, McGraw-Hill: New York, London.

165. Savage, W.F., Nippes, E.F., and Wassell, F.A., *Static Contact Resistance of Series Spot Welds.* Welding J., 1977. **56**(11): p. 365s-370s.

166. Koh, J.C.Y. and Fortini, A., *Thermal Conductivity and Electrical Resistivity of Porous Materials*. NASA CR-120854, 1972.

167. Mills, K.C., *Recommended Values of Thermophysical Properties for Selected Commercial Alloys*. 2002, UK: Woodhead Publishing Ltd.

168. Goldsmith, A., Waterman, T.E., and Hirschhorn, H.J., *Handbook of Thermophysical Properties of Solid Materials*. 1961, New York: McMillan.

169. Tan, J.C., Golosnoy, I.O., Tsipas, S.A., Paul, S., Curran, J.A., and Clyne, T.W., *Use of a Steady State Bi-substrate Technique for Measurement of the Thermal Conductivity of Thick Ceramic Coatings.* Surf. Coat. Techn., 2004: p. submitted.

170. Dupuy, T. and Ferrassee, S. *Influence of the Type of Current and Materials properties on Resistance Spot Welding, using a Finite Element Model*. in *Proc. 5th Inter. Conf. Trends in Welding Research*. J.M. Vitek, S.A.D., J.A. Johnson, H.B. Smartt, T. DeRoy, Editor 1998. Georgia, USA: ASM Int. p. 610-615.